

University of Alberta

Entrained Flow Gasification of Oil Sand Coke

by

Farshid Vejahati

A thesis submitted to the Faculty of Graduate Studies and Research
in partial fulfillment of the requirements for the degree of

Doctor of Philosophy

In

Chemical Engineering

Department of Chemical and Materials Engineering

©Farshid Vejahati

Spring 2012

Edmonton, Alberta

Permission is hereby granted to the University of Alberta Libraries to reproduce single copies of this thesis and to lend or sell such copies for private, scholarly or scientific research purposes only. Where the thesis is converted to, or otherwise made available in digital form, the University of Alberta will advise potential users of the thesis of these terms.

The author reserves all other publication and other rights in association with the copyright in the thesis and, except as herein before provided, neither the thesis nor any substantial portion thereof may be printed or otherwise reproduced in any material form whatsoever without the author's prior written permission.

This work is dedicated to my wife, Mehrdokht and my parents, for their unconditional support and love.

Abstract

The effect of blending woody biomass material with fluid coke and coal on the co-pyrolysis process was investigated in an entrained flow gasifier. The SEM results showed a particle size decrease and shape change from needle to spherical as the temperature was increased. Agglomeration between particles occurred above 1250°C due to the low ash fusion temperature of biomass. The results were verified by particle size distribution analysis. Reactivity of pyrolyzed blended and pure fuels decreased with increasing temperature. No agglomeration was found for blends of coal and coke. Pyrolysis at high temperatures also showed a significant surface area development for coke.

The combined effects of the steam and oxygen concentrations and coal/coke blending ratio were investigated in gasification of fluid coke with sub-bituminous and lignite coals using Response Surface Methodology (RSM). Six response variables were considered: H₂, CO and syngas production, H₂/CO ratio, gasification efficiency, and carbon conversion. Experiments were conducted over a temperature range of 1000-1400°C, using steam and oxygen to carbon weight ratios of (0.9-4.3) and (0-0.4), respectively. Using RSM, the interactions between different factors were determined. The response variable correlations were employed to determine the experimental conditions under which the H₂ production was maximized.

The intrinsic rates for Char-O₂, char-CO₂, and char-H₂O reactions were developed for coke. The validity of thermogravimetric determination of kinetics was discussed in depth. Four surface area measurement techniques were used to

normalize the specific reaction rate: N₂-BET, GCMC-NLDFT and DR models, and active surface area measured by CO₂ chemisorption. The objective was to find the specific surface area which gives the best reduction in the variability of reaction rate $r(X)$ using the regressor variable $S(X)$. Overall ASA was found to be the best regressor.

A numerical simulation was developed for entrained flow gasifier using the underlying physics and the intrinsic rates. The intrinsic rates were successfully implemented into the Fluent CFD code via user defined functions. The energy content of particle on a dry basis was conserved by properly calculating the formation enthalpy of volatile matter. The results were compared to the experiment data for carbon conversion, H₂, CH₄, CO and CO₂ concentrations. In general, a fair agreement between simulation and experiment results were found.

Acknowledgement

I wish to take this opportunity to express my gratitude to my wonderful mother who has nurtured and supported me through the whole years of my life.

I shall always remain indebted to my lovely wife for her encouraging attitude and unconditional love.

I am very grateful to my supervisor, Dr. Rajender Gupta, for his invaluable guidance over the course of my studies.

I contentedly express my gratitude to Dr. Murray Grey and Dr. Zhenghe Xu as the members of supervisory committee for their valuable contributions toward accomplishing this study.

Special thanks are also extended to Dr. Hassan Katalambula and Mrs. Chen Gao for their help toward completing part of this work.

The technicians and staff at National Institute for Nanotechnology (NINT) and University of Alberta are well appreciated for providing laboratory resources and services.

The financial support from Natural Science and Engineering Research Council (NSERC), Helmholtz-Alberta Initiative (HAI) centre, Faculty of Graduate Studies and Research and Faculty of Engineering at the University of Alberta, and Dr. Rajender Gupta is also well appreciated.

Table of Contents

CHAPTER 1:	Introduction to gasification.....	1
1.1	Overview of Gasification Technology	1
1.2	Gasification Fundamentals.....	3
1.3	Types of Gasification Technologies.....	5
1.4	Economy of Gasification.....	7
1.4.1	Gasification Incentives in Alberta/Canada	9
1.5	Research Objectives	12
CHAPTER 2	Literature review.....	16
2.1	Oil Sands	16
2.2	Properties of oil sand coke	17
2.3	Properties of coal.....	21
2.4	Gasification studies on oil sand coke	22
2.5	Review of related works on co-gasification.....	31
2.6	Gasification kinetic of oil sand coke	38
2.7	Review of related works on char gasification kinetics.....	40
2.7.1	Effect of temperature on reactivity of chars	44
2.7.2	Effect of temperature on the reaction mode.....	45
2.7.3	O ₂ gasification rates	47
2.7.4	CO ₂ gasification rates	50

2.7.5	Steam gasification rates	50
2.8	Numerical modeling of entrained flow gasifier	51
2.9	Chapter overview and findings	55
CHAPTER 3	Co-Pyrolysis of fluid coke with biomass and coal	58
3.1	Experimental setup.....	58
3.2	Pyrolysis results and discussions	61
3.2.1	Fuels characterization	62
3.2.2	Char preparation.....	63
3.2.3	Surface area development.....	64
3.2.4	Char Reactivity	67
3.2.5	Morphological analysis of pyrolyzed chars	68
3.2.6	Variations in particle size distribution	73
3.3	Chapter findings and Conclusions.....	74
CHAPTER 4	Entrained flow gasification of fluid coke with coal.....	76
4.1	Introduction	76
4.2	Raw Materials	77
4.3	Experimental procedure	78
4.4	Methodology	79
4.4.1	Response surface Methodology (RSM)	80
4.4.2	Response variables.....	81

4.4.3	ANOVA tests	82
4.5	Results and discussions	85
4.5.1	Model validation	85
4.5.2	H ₂ production analysis	86
4.5.3	CO production analysis	91
4.5.4	Syngas (CO+H ₂) production analysis	94
4.5.5	H ₂ /CO ratio analysis	96
4.5.6	Gasification efficiency	100
4.5.7	Conversion	104
4.5.8	Numerical optimization	107
4.5.9	Synergy	109
4.6	Chapter findings and conclusions	112
CHAPTER 5 Intrinsic reaction kinetics of fluid coke char with O ₂ , CO ₂ and H ₂ O		115
5.1	Introduction	115
5.2	Raw material	115
5.3	Experimental procedure	116
5.3.1	Thermogravimetric analyzer	116
5.3.2	Total surface area characterization	120
5.3.3	Active surface area characterization	123
5.3.4	Treatment of TGA results	127

5.4	Char-O ₂ reaction.....	127
5.5	Char-CO ₂ reaction.....	137
5.6	Char-H ₂ O reaction.....	141
5.7	Chapter findings and conclusions	145
CHAPTER 6 CFD simulation of entrained flow gasifier		147
6.1	Introduction	147
6.2	Numerical models	148
6.2.1	Drying and devolatilization.....	148
6.2.2	Liquid droplets	151
6.2.3	Volatile oxidation.....	152
6.2.4	Gasification reactions.....	153
6.2.5	Gas phase reactions.....	158
6.2.6	Continuous phase equations.....	159
6.2.7	Radiation model	162
6.2.8	Particle transport equations.....	163
6.2.9	Stochastic tracking of particles	169
6.3	Computational schemes.....	170
6.4	Results and discussions	175
6.4.1	Atmospheric pressure entrained flow gasifier	176
6.5	Chapter findings and conclusions	186

CHAPTER 7 Conclusions and Recommendations	188
7.1 Conclusions	188
7.2 Recommendations for future work.....	193
References.....	195
APPENDIX A Collection probe sketch.....	210
APPENDIX B Surface area measurement.....	211
B1. BET method	211
B2. Multipoint BET Method.....	211
B3. Dubinin-Radushkevich (DR) Method	212
B4. Density Functional Theory (DFT) method.....	213
APPENDIX C Response surface methodology	215
C1. Methodology	215
C2. Estimation of the parameters.....	216
C2.1 properties of least square estimators and estimation of σ^2	218
C3. Hypothesis testing in multiple regression	219
C3.1 Test for significance of regression.....	219
C4. Model adequacy checking.....	220
C4.1 Residual analysis	220
C4.2 Scaling residual.....	220
C5. Standard error of predicted response.....	222

C6.	Design moment and property of rotatability	223
C7.	Practical Design optimality	224
C8.	Computer-generated designs in RSM	225

List of Tables

Table 1.1	Alberta's Energy Resources	9
Table 2.1	Typical properties of oil-sand bitumen	17
Table 2.2	Analysis of Suncor (delayed) and Syncrude (fluid) cokes	18
Table 2.3	Ash properties of fluid and delayed coke	19
Table 2.4	Typical analysis of various coals	22
Table 2.5	Typical activation energies of carbonaceous chars.....	48
Table 2.6	Typical activation energies of CO ₂ -char reaction.....	50
Table 2.7	Relative rate of gasification with O ₂ , CO ₂ , and steam for variety of chars at 1073K and 0.2 atm	51
Table 3.1	Proximate and ultimate analyses of fuels	62
Table 3.2	Major and minor composition and fusion temperature analyses of fuels ash	63
Table 3.3	Pore structure development for fuels and their blends as a function of temperature.....	66
Table 4.1	Design space and experimental values of response variables for RSM created using IV-optimal design and coordinate exchange algorithm	82
Table 4.2	Analysis of Variance (ANOVA).....	83
Table 4.3	Matrix of coefficients estimated for the proposed response models as a function of decoded operating factors	84
Table 4.4	Optimization results for hydrogen response variable	108
Table 4.5	Proximate and ultimate analyses of Boundary Dam lignite coal...	109
Table 4.6	Major and minor composition and fusion temperature analyses of lignite ash	109
Table 4.7	Comparison of gasification performance between pure coke and 50/50 blend of pure coke and lignite ash	110
Table 5.1	Variation of total Surface area with conversion for fluid coke char.....	135

Table 5.2	Variation of active surface area with conversion for fluid coke char.....	135
Table 6.1	Yield of volatile gases.....	149
Table 6.2	Expressions of a for different size of fuel particle.....	154
Table 6.3	Kinetics of reaction R_4 - R_9	154
Table 6.4	Solid phase properties.....	156
Table 6.5	Generated mesh quality	176
Table 6.6	Gasification operating conditions	178
Table 6.7	Particle tracking history (Run# 3).....	180
Table 6.8	Comparison of gas composition between experiment and simulation.....	186

List of Figures

Figure 1.1	Poly-generation IGCC plant	3
Figure 1.2	Power production cost comparison	8
Figure 1.3	Cost of hydrogen production between IGCC and steam methane reforming (SMR)	11
Figure 1.4	Cost of power production	11
Figure 2.1	Surface area of fluid coke versus Log mean particle diameter	21
Figure 2.2	Effect of temperature and lignite ash on carbon conversion for delayed and fluid cokes.....	24
Figure 2.3	Effect of temperature, char recycling and addition of catalyst on carbon conversion of fluid coke.....	26
Figure 2.4	Effect of temperature on carbon conversion of fluid coke ($D_p=0.14$ mm) and delayed coke ($D_p=2$ mm).....	27
Figure 2.5	Effect of particle size on conversion of delayed coke	27
Figure 2.6	Surface area of delayed coke as a function of carbon conversion	28
Figure 2.7	Scanning electron microscopy of fluid cokes.....	29
Figure 2.8	Effect of CO_2 and N_2 conveying gases on syngas production and conversion	30
Figure 2.9	Typical plot representing the change of reaction rate with temperature	47
Figure 2.10	Region (hatched area) of valid steady state assumption for O_2 -char reaction	49
Figure 3.1	Schematic diagram of entrained flow gasification system	60
Figure 3.2	Collection probe (left) and furnace (right)	61
Figure 3.3	Pyrolysis temperature effect on the surface area for fuels	64
Figure 3.4	TGA results for Genesee coal and sawdust (GCS 1-1) blended char pyrolyzed at 700, 1100, 1250, and 1400°C.....	67
Figure 3.5	TGA results for fluid coke and sawdust (FCS 1-1) blended char pyrolyzed at 700, 1100, 1250 and 1400°C.....	68

Figure 3.6	SEM images of 50/50 blend ratio of sawdust and Genesee coal at 4 different temperatures: (a) 700°C, (b) 1100°C, (c) 1250°C, and (d) 1400°C.....	69
Figure 3.7	SEM images of 50/50 blend ratio of sawdust and Genesee coal representing particle agglomeration at two temperatures: (a)&(b):1250°C, (c)1400°C	70
Figure 3.8	Effect of temperature on the porosity development of particles in a 50/50 blend of Genesee coal and sawdust	71
Figure 3.9	Pores development in fluid coke at 700°C, 1250°C and 1400°C....	72
Figure 3.10	SEM image of fluid coke-Genesee coal 50/50 blend at 1400°C	72
Figure 3.11	Effect of pyrolysis temperature on the particle size distribution...	74
Figure 4.1	Normal probability and Residuals plot for H ₂ response variable ...	84
Figure 4.2	Predicated response values versus experimental values. (□) experimental design points used for fitting the models (●) Additional experimental points.....	86
Figure 4.3	Effect of blending ratio on H ₂ production	87
Figure 4.4	Perturbation plot representing the effects of experimental factors on H ₂ production: (a) Genesee coal, (b) 50-50 wt. % blend of coal and coke, (c) pure coke	88
Figure 4.5	Interaction plots for hydrogen response variable: (a) steam-temperature interaction, (b) coke ratio-temperature interaction, (c) oxygen-steam interaction.....	90
Figure 4.6	Contour plot representing the combined effect of Coke ratio and temperature on H ₂ Production.....	91
Figure 4.7	Perturbation plot representing the effects of experimental factors on CO production.....	92
Figure 4.8	Interaction plot for carbon monoxide production (mol/kg fuel, daf)	93
Figure 4.9	Contour plots representing the combined effect of Coke ratio and temperature on CO production.....	94
Figure 4.10	Perturbation plot representing the effects of experimental factors on syngas production	95

Figure 4.11	Interaction plots for hydrogen response variable: (a) steam-temperature interaction, (b) coke ratio-temperature interaction, (c) oxygen-steam interaction.....	95
Figure 4.12	Contour plot representing the combined effect of Coke ratio and temperature on syngas production	96
Figure 4.13	Perturbation plot representing the effects of experimental factors on H ₂ /CO ratio	97
Figure 4.14	Temperature-oxygen interaction plots for H ₂ /CO ratio: (a) 15 vol. % steam, (b) 32.5 vol. % steam, (c) 50 vol. % steam.....	98
Figure 4.15	Steam-oxygen interaction plots for H ₂ /CO ratio: (a) 1000°C, (b) 1400°C.....	99
Figure 4.16	Contour plot representing the combined effect of Coke ratio and temperature on H ₂ /CO ratio	100
Figure 4.17	Perturbation plot representing the effects of experimental factors on gasification efficiency	101
Figure 4.18	Effect of blending ratio on gasification efficiency at the midpoints of operating variables.....	102
Figure 4.19	Interaction plots for gasification efficiency: (a) steam-temperature interaction, (b) oxygen-steam interaction, (c) coke ratio-temperature.....	103
Figure 4.20	Contour plot representing the combined effect of Coke ratio and temperature on gasification efficiency.....	103
Figure 4.21	Perturbation plots representing the effects of experimental factors on carbon conversion: (a) 1000°C, (b) 1400°C, (c) pure coal, (d) pure coke	105
Figure 4.22	Effect of blending ratio on carbon conversion at the midpoints of operating variables.....	106
Figure 4.23	Contour plot representing the combined effect of Coke ratio and temperature on carbon conversion	106
Figure 4.24	Regime of char-slag micromechanical interaction: E=entrapment; S= segregation, and SC= segregation and coverage	111
Figure 5.1	Schematic design of TA SDT Q600 thermogravimetric analyzer ...	117

Figure 5.2	Performance comparison of SDT Q600 and Thermax 400 units.....	118
Figure 5.3	Rate of mass loss vs. conversion for two TGA units	119
Figure 5.4	Diffuser configuration for steam injection in TGA.....	119
Figure 5.5	Original and modified sample pans	120
Figure 5.6	CO ₂ isotherm for Fluid coke at 273 K.....	123
Figure 5.7	TG plot of fluid coke representing the ASA measurement	126
Figure 5.8	Arrhenius plot for char-O ₂ reaction at 3% O ₂ and 50% carbon conversion level in the range of 475°C-550°C	131
Figure 5.9	The temporal variation of carbon conversion as a function of temperature at 3% O ₂	132
Figure 5.10	Variation of activation energy with conversion	132
Figure 5.11	The temporal variation of carbon conversion at 500°C	133
Figure 5.12	Porosity distribution in fluid coke char at X=0%	135
Figure 5.13	Specific rate as a function of different measures of surface area at 500°C and 3% O ₂	136
Figure 5.14	Specific rate as a function of different temperatures.....	137
Figure 5.15	Arrhenius plot for char-CO ₂ reaction at 100% CO ₂ and 50% carbon conversion level in range of 950°C-1025°C	138
Figure 5.16	The temporal variation of carbon conversion as a function of temperature at 100% CO ₂	139
Figure 5.17	Specific rate as a function of different measures of surface area at 1025°C and 100% CO ₂	140
Figure 5.18	Specific rate as a function of different temperatures.....	141
Figure 5.19	Arrhenius plot for char-H ₂ O reaction at 50% H ₂ O and 50% carbon conversion level in the range of 900°C-975°C	142
Figure 5.20	The temporal variation of carbon conversion as a function of temperature at 50% H ₂ O	143
Figure 5.21	Specific rate as a function of different measures of surface area at 950°C and 40% H ₂ O	144

Figure 6.1	Schematic of computational domain	177
Figure 6.2	Coke particle trajectories at 1400°C (Run# 3)	179
Figure 6.3	Contour plot of several parameters (Run#3)	182
Figure 6.4	Contour plot of gas composition in mass fraction (Run#3)	183
Figure 6.5	Contour plot of homogenous and heterogeneous gasification reactions (Run#3).....	184

CHAPTER 1:

Introduction to gasification

1.1 Overview of Gasification Technology

Management and reduction of greenhouse gas (GHG) emissions from fossil fuels have emerged as top priorities within the last decade. Governments and Industry have already started to respond as both investors and the public awareness of the concepts of global warming and global air pollution has been built up. Despite the GHG emissions issues associated with the fossil fuels, they are anticipated to remain as a major contributor to the world's energy markets for the foreseeable future. According to U.S energy information administration, fossil fuels are predicated to provide 78 percent of total energy use by 2035[1]. Structural change in economy, higher prices and stricter GHG emission regulations in future demand more energy efficient technologies. Among a number of cleaner and energy efficient technologies available today, energy cycles based on gasification technology of solid fuels, such as Integrated Gasification Combined Cycle (IGCC) are considered as one of the promising alternatives to secure the energy supply in the future. Carbon capture and

sequestration (CCS)-enabled gasification cycles are considered as a potential pre/post combustion carbon capture technology due to their multiple benefits vs. traditional PC plants: (1) because of pre-combustion treatment of syngas (CO , H_2) in IGCC, nitrogen is mainly absent from combustion process which results in smaller gas volume treatment and consequently lower treatment cost than pulverized coal plants. For the same reason CO_2 capture can be achieved at a significantly lower cost, (2) Sulfur and nitrogen oxides and particulates from IGCC are at least an order of magnitude less than those from pulverized coal plants, (3) IGCC overall efficiency of as high as 43% has been reported compared to 34% for pulverized coal with sulfur and nitrogen oxides control, (4) Syngas produced from gasification can be converted to variety of valuable products such as electricity, steam, hydrogen, ammonia, methanol, synthetic natural gas, and transportation fuels, (5) gasification can utilize a multiplicity of fuels or blends such as coal, biomass, petroleum coke, etc., (6) Mercury removal in an IGCC plant has been estimated to cost $< \$0.25/\text{MWh}$, an order of magnitude less than PC plants, (7) Slag from IGCC is inert and marketable. Sulfur or sulfuric acid from IGCC has a positive market value. Contrarily, ash and scrubber effluent (gypsum) from a PC plant have some minimal value but in most cases incur a cost for disposal, (8) since IGCC does not require scrubber for sulfur capture, water consumption is almost 40% lower than PC plants, (9) separation of H_2 and CO_2 is comparatively easier than combustion based cycles and CO_2 from this process is already at high pressure required for enhanced oil recovery or sequestration processes, (10) and the last but not the least, the poly-generation aspect of IGCC in hydrogen and chemicals production combined with power generation [2-4]. Figure 1.1 shows a schematic of poly-generation IGCC plant.

On the other hand, IGCC is regarded by PC plant operators as a complex chemical process. This opinion has been originated from the low availability figures for the large demonstration plants. A large proportion of the unavailability is because of combined cycle issues and basically not the gasification process itself. In this respect, gas turbine problems at Beggenum (Netherland) and Puertollano (Spain) IGCC plants can be cited. Due to the fact that compressed air

necessary for Air Separation Unit (ASU) is supplied from combustion turbine, any problems with combustion turbine will effectually shut down the whole process. Some other unavailability issues have been resulted from contractual obligations for the demonstration sponsors.

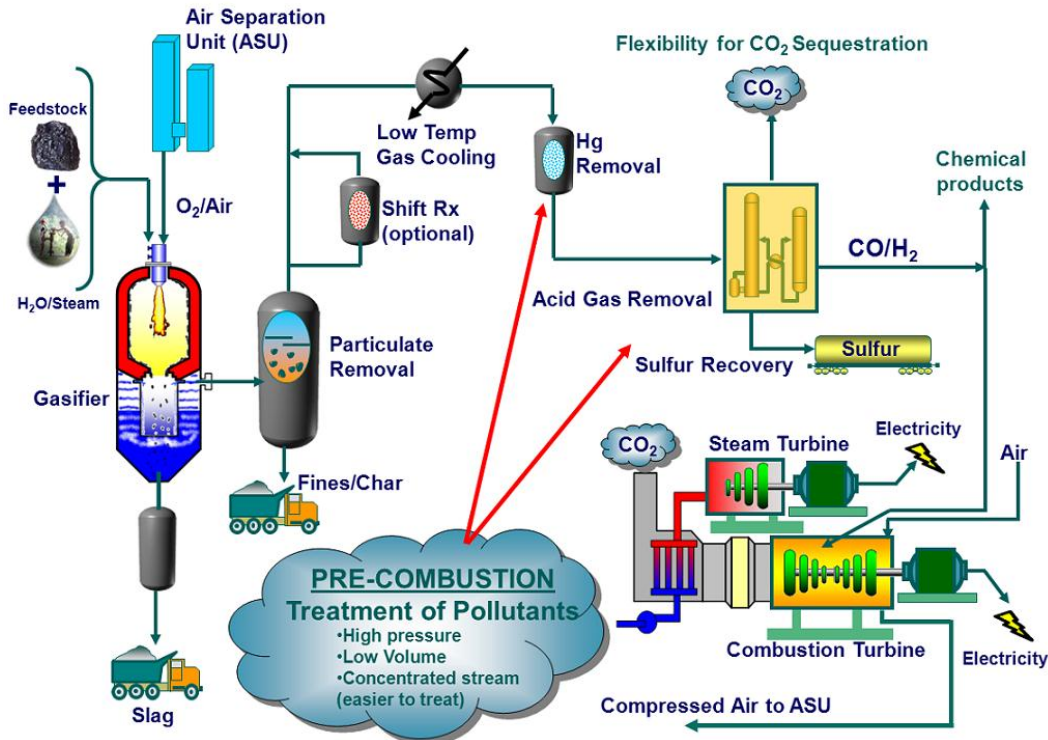


Figure 1.1 Poly-generation IGCC plant

1.2 Gasification Fundamentals

In its widest sense, gasification is defined as conversion of carbonaceous fuels to gaseous products with a usable heating value in an oxygen deficient ambient using air, oxygen, steam, carbon dioxide or a mixture of these gases at temperatures exceeding 700°C.

The conversion of solid fuel to gases can be described in three steps: pyrolysis, char combustion, and char gasification.

Pyrolysis happens at temperatures above 350°C depending on fuel quality. As a result of pyrolysis, hydrogen-rich volatile matter, tars, and hydrocarbon gases are released. Parallel with pyrolysis, char gasification reactions start which

yield the final products, such as gases (e.g. syngas) and solid residues (ash, slag). Char gasification can be summarized in 7 basic reactions[5]:

- *Combustion with oxygen:*



This reaction consumes most of the injected oxygen to provide heat required to dry the feed, breaking the chemical bonds, and increasing the temperatures of solid particles to start the gasification reaction.

- *Gasification with oxygen:*



- *Gasification with carbon dioxide (Boudouard reaction):*



In the absence of catalyst, this reaction is much slower than combustion reaction at the same temperature.

- *Gasification with steam:*



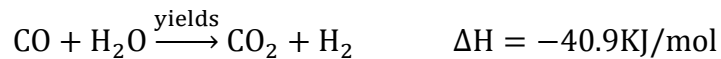
This reaction is favored by elevated temperature and reduced pressure and in the absence of catalysts occurs slowly at temperatures below 900°C.

- *Gasification with hydrogen (hydrogasification reaction):*



This reaction is very slow except at high pressures.

- *The water-gas shift reaction:*



This reaction is very important if syngas is to be used for production of H₂ by changing the ratio of CO/H₂.

- *The methanation reaction:*



This reaction increases the calorific value of the syngas but normally is very slow at high temperatures normally encountered in an entrained flow gasifier.

Studies at high temperatures have shown that the gas phase composition can be estimated with a reasonable accuracy from thermodynamics equilibrium considerations, when the assumption of full carbon conversion holds. However, to perform the equilibrium calculations it is essential to know the amount of carbon that has been converted to the gas phase at any given time. This subject has been studied in details by Harris *et al.* [6].

Several factors determine the composition of produced gas: feedstock chemical composition, particle size, gasifying agents used (oxygen/air, steam), temperature, pressure, heating rate and residence time in the gasifier, coal feeding system (dry or slurry), contact pattern between gasifying agent and feed (flow geometry), mineral content of solid fuel, heat transfer mechanism, and syngas clean up (i.e. sulfur removal, nitrogen removal, other pollutants removal)[5].

1.3 Types of Gasification Technologies

During the course of gasification process development, different types of gasifiers have been emerged that can generally be classified into three categories based on the flow geometry: fluidized bed, fixed bed, and entrained flow gasifiers.

Fluidized bed gasifiers normally operate on a dry feedstock at low temperatures (600–1000°C). To prevent agglomeration of ash particles, that causes defluidization of the bed, feedstock must have an ash fusion temperature higher than operating temperature of the gasifier. Low temperature operating feature of this class of gasifiers favors the reactive and high volatile content feedstocks such as lignite and brown coal. Also due to the low operating temperatures all mineral matter contents are discharged as dry ash.

Fixed bed gasifiers could be operated either in low temperature dry ash or slagging mode. In the dry ash mode requirements for the feedstock ash properties are almost the same as for fluidized bed gasifiers. Due to the large particle size used, slagging fixed bed gasifiers are very sensitive to the reactivity of feedstock. Physical strength and coking behavior of feed particles to maintain the

permeability of the fixed bed are also effective parameters in this class of gasifiers. Compared to other types of gasifiers, this class has comparatively small throughput and very limited variations in feedstock specifications.

In the entrained bed gasifiers, the concurrent gases and particles flow typically implies a short residence time of feed particle inside the reaction zone. This short residence time requires feedstock to be pulverized to ensure high carbon conversion. High operating temperatures (flame temperatures above 1800°C) in this type of gasifier maximizes the carbon conversion. Entrained flow gasifiers allow both high coal throughput and usage of a wide range of less reactive feedstocks such as high rank coals and petroleum coke. These unique characteristics make this class of gasifiers the most suitable type for bituminous coal and oil sand coke. They can accept either dry or slurry fed fuels. However, the slurry fed gasifier operates in lower range of temperatures due to the additional energy requirements for evaporation of water. For this reason, dry fed gasifiers are more efficient and less oxygen consuming. On the other hand, design of dry fed systems is more complex to build and operate than slurry fed systems, particularly at high pressures. For the same reason, the operating pressure in dry fed gasifiers (up to 4 MPa) is normally lower than slurry fed gasifiers (7 MPa) which results in a larger size of dry fed gasifier compared to slurry fed one. Overall, there is a trade-off between higher efficiency of dry-fed gasifiers and simpler and cheaper design of slurry fed systems and also higher operating pressures of slurry-fed gasifiers. Due to the high operating temperatures above ash fusion temperature (AFT), mineral content of the feedstock is discharged through a slag tap system. Smooth operation of an entrained flow gasifier depends on the steady removal of slag through a slag tap device. Therefore, slag flow behavior is one of the central keys in assessing the suitability of the feedstock in this type of gasifiers [7, 8].

1.4 Economy of Gasification

The recent trend of natural gas prices within the range of \$3-\$5/GJ, due mainly to the advent of shale gas in North America has given a setback to IGCC projects. IGCC is economically sensible only at high prices of power and carbon emission penalties. IGCC plants release about 60% more carbon dioxide than conventional natural gas combined cycles (NGCC). One recent study shows that carbon penalties of \$100/t are required in order for IGCC plants to be economically competitive with NGCC [9].

Guillermo *et al.* [10] performed a comparative techno-economic study on 4 different IGCC scenarios: (1) no CO₂ capture, (2) 60% CO₂ capture, (3) 80% CO₂ capture, (4) and H₂S/CO₂ co-capture (80% CO₂ and complete H₂S capture) and a NGCC plant based on natural gas and coal prices of \$3/GJ and \$1.14/GJ, respectively. Figure 1.2 represents their results on power production cost. For IGCC with 60% CO₂ capture (NGCC CO₂ emission parity), the capital cost is a significant fraction of all-in cost (about 60%) while fuel cost is relatively low and stable. On the contrary, NGCC has a relatively low capital cost (around 15% of all-in cost) but natural gas has had a highly volatile price in the recent past years. So, power generated by NGCC is by far more sensitive than the corresponding IGCC plants to the fuel cost. Their study sets the contribution of natural gas price to electricity cost to over 50% of all-in cost. Nevertheless, significant lower capital cost of NGCC makes it a more feasible option than IGCC in view of the plant owners and investors further supported with the recent relatively low and stable prices of natural gas.

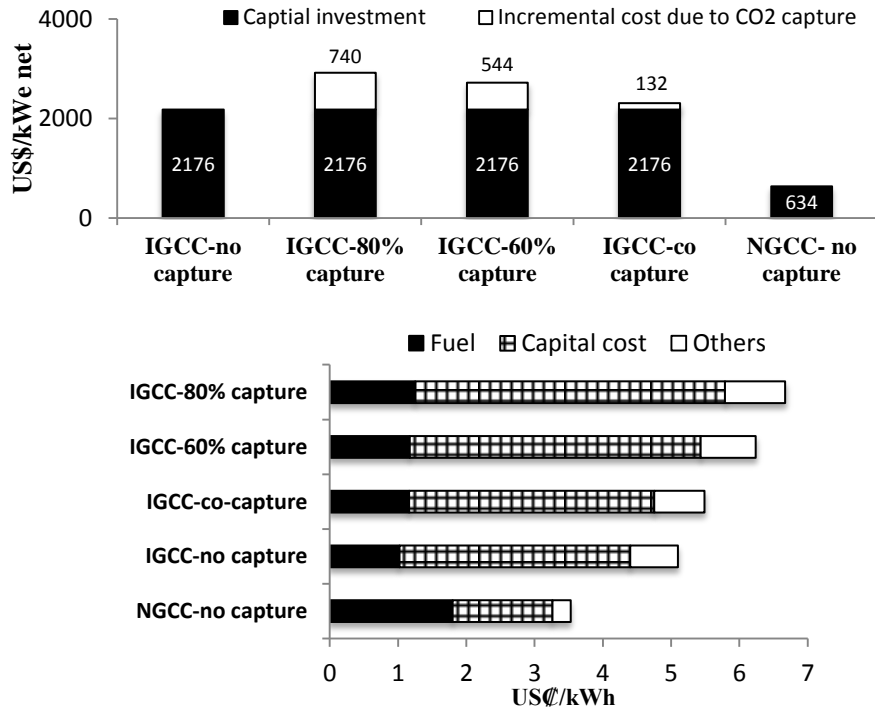


Figure 1.2 Power production cost comparison[10]

Another technology review [11] shows that in order for IGCC complexes to be economically justifiable, natural gas prices higher than \$8/GJ have to be in place. It is worth noting that the review is solely based on the conventional NGCC plants. However, the production of unconventional shale gas, which seems to be responsible for the low natural gas prices particularly in North America, has not been thoroughly investigated yet with respect to the sustainability and environmental acceptability. For the time being, production of shale gas raises some serious issues [12]:

1. Production of shale gas requires a considerable amount of chemical injections in fracturing process which raises the issue of underground water contamination.
2. Formation water in production is typically very saline (3 times as salty as seawater) so disposal is an issue.
3. Shale formation water can have significant levels of Benzene and other light hydrocarbons.

4. Raw shale gas basin contains about 10-12% CO₂ which is much higher than the 2-4.5% of the conventional gas.
5. Production from shale gas wells declines rapidly, with a drop of 60% to 80% in the first year compared to 25% to 40% decline in conventional reservoirs.
6. Shale gas production has relatively short track record so we may not have all the answers to the long term environmental impacts.

The above mentioned issues could potentially incur extra costs on production of shale gas in near future which in turn might result in elevated prices of natural gas. Tougher carbon emission penalties and elevated natural gas prices in foreseeable future once again could turn the investors and governments attentions to the alternative clean energy technologies, where IGCC stands of prime importance.

1.4.1 Gasification Incentives in Alberta/Canada

Alberta is known as the “energy province” in Canada due to the fact that more than 80% of Canada’s energy resources are located in this province. Table 1.1 represents Alberta’s established and ultimate potential energy resources [13].

Table 1.1 Alberta's Energy Resources [13]

2010 Reserves	Oil (Billion barrel)	Gas (trillion cf)	Oil Sands (Billion barrels)	Coal (Billion tonnes)
Remaining Established	1.6	40	174	33
Ultimate potential	19.7	223	315	620

Alberta’s vast resources of coal and petcoke makes it a perfect location for utilization of different conversion technologies such as coal bed methane, oxy fuel combustion, chemical looping combustion, IGCC, and underground coal gasification. For the time begin, Alberta generates 60 % of its power from coal.

Alberta's Production of bitumen from oil sands is expected to double by 2020 from its production rate of 1.5 million barrels per day in 2009. Bitumen upgrading produces petroleum coke as by-product which can be utilized as low-cost feedstock for further value-added operation such as gasification. The current rate of petroleum coke production estimates about 20,000-30,000 tonnes per day. At the end of 2009, close to 57 million tonnes of coke was stockpiled which is one of the largest inventory available worldwide. Inventories of these sizes can sustain world-scale IGCC poly-generation complex with potential economies of scale [13].

Alberta has the highest hydrogen demand and production per capita in North America. The demands for Steam Assisted Gravity Drainage (SAGD) steam, process steam, hydrogen, and power is expected to experience an explosion till 2030. The demands for SAGD steam are predicted to triple between 2012 and 2030. The H₂ demands of the oil sands industry in Alberta is poised to grow by a factor of 2.7 from 2012 onward. Process steam demands are expected to increase by a factor of 2.4 by 2030 [14]. IGCC is considered a potential technology which can be utilized to produce hydrogen and steam necessary.

The Western Canadian sedimentary basin is ideal for permanent CO₂ storage. So, Alberta's strategic location makes it a perfect candidate for different CCS-enabled technologies including IGCC with the minimum cost of pipeline transportation for CO₂.

As far as the economy of IGCC complex is concerned, a recent study conducted by Jacobs Consultancy for the Alberta Government [11] has reviewed the different competing technologies and products in order to find the optimal economic configuration which maximizes the value of the resources. The study shows that hydrogen and methanol production using gasification technology become competitive at intermediate gas prices (>\$8/GJ). Figure 1.3 represents the comparative cost of hydrogen production between IGCC and steam methane reforming technologies.

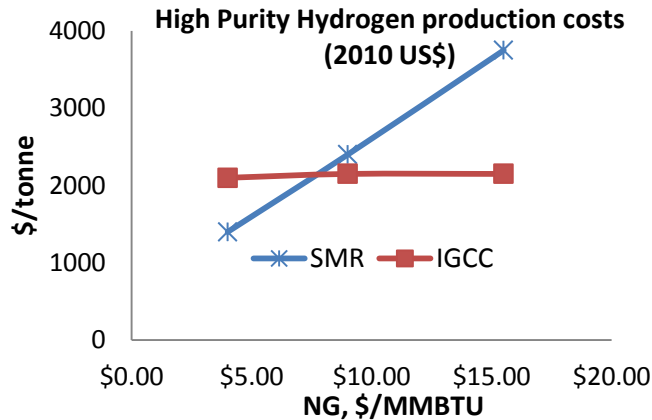


Figure 1.3 Cost of hydrogen production between IGCC and steam methane reforming (SMR) [11]

However, IGCC is not a competitive technology in power generation compared to NGCC and conventional coal fired power plants due mainly to its high capital cost. Figure 1.4 represents the comparative costs of power generation by IGCC compared to two other technologies. Natural gas prices of even \$20/GJ do not justify the economy.

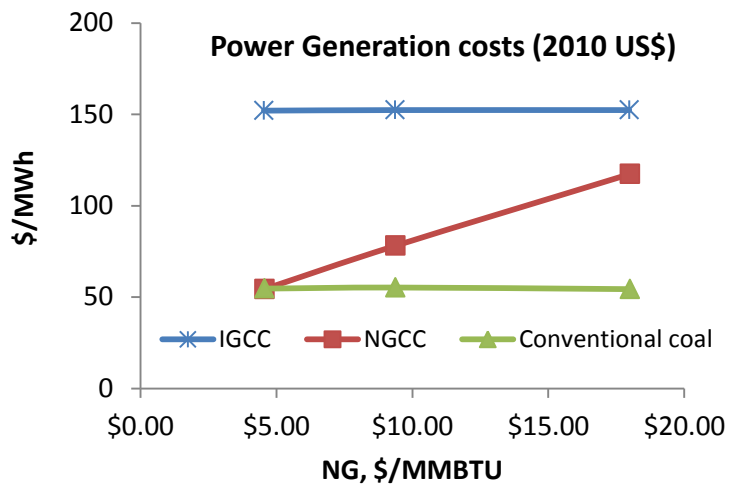


Figure 1.4 Cost of power production [11]

In conclusion, the study demonstrates that high capital cost of gasification complex with the current state of technology masks the potential synergies and poly-generation options.

The high capital cost of IGCC complex is partially linked to low availability figures of the technology. In addition, advancement in gasification technology such as the development of new generation of compact gasifiers known as Pratt and Whitney Rocketdyne (PWR) gasifier with high pressure dry solid pump and proven potential of lowering gasification systems costs up to 50%, warm gas cleanup options for sulfur and CO₂ removal, membrane technologies for oxygen and hydrogen separation, and process innovation and optimization could potentially cut down the total IGCC complex costs. However, further research and technology development in these fields require a long term plan to achieve a great step forward.

1.5 Research Objectives

As pointed out earlier in this chapter, Alberta's strategic location creates a unique situation for demonstration of world class IGCC complexes. In the heart of the IGCC technology lies the gasification process, which its cost and reliability is largely influenced by feed quality and operating conditions. Adoption of this new technology is inevitably linked to the full appreciation of gasification behavior of Canadian oil sand coke, coal, and/or their blends. Nonetheless, there are little fundamental studies and experiences with Canadian coke and its blend with coal available [9, 15]. The commercial entrained bed licensors such as shell have also claimed to have experience with Canadian oil sand cokes, however, the results are not in public domains and more importantly fundamental studies at commercial scale units are much more difficult than small scale lab reactors, if not impossible at all.

Oil sand cokes are high in sulfur content (between 5.5 and 7.5 wt. %), vanadium and nickel content (EPA regulated elements), whereas Alberta's coals are high in moisture and ash content and low in sulfur. Blending coke with coal is regarded as a promising option to improve the slag flow difficulties of high ash content coals due to the relatively low ash content of oil sand coke which reduces the risk of slag plugging the reactor tapping system. Mixing coke with coal also

helps to reduce the sulfur loading in flue gas which in turn results in lowering downstream processing requirements. Blending also helps to alleviate the high Ni and V difficulties of oil sand coke gasification such as destroying the refractory binder, slagging and fouling on economizer heat transfer-surfaces, problems with burners and syngas cooler, and formation of low melting point sodium vanadate which deposits in syngas cooler [5]. Furthermore, there is a chance that blending coke with coal can enhanced the conversion through catalytic activity of alkali metals in coal ashes although the results reported in literature are not consistent in this respect. And the last but not the least, blending is one of the promising options which can further help to reduce the environmental impacts and footprints of oil sands industry. Given these advantages, however, there are little gasification experiences with Canadian oil sand coke and coal-coke blends available particularly at high temperature ($>1000^{\circ}\text{C}$) which normally occurs in entrained flow gasifiers. More studies are required to address the morphological and structural changes of blends in high heating rate, high temperature pyrolysis process. It is well known that treatment condition in pyrolysis strongly affects the yield and the reactivity of the char, which consequently influences the solid-gas reaction rates. Pyrolysis has an important effect on particle swelling and agglomeration, char reactivity, char physical structure and surface area [16].

Furthermore, the design and scale up of gasifiers suitable for oil sand coke demands accurate and reliable data on the intrinsic reaction rates, which are currently missing from the literature. Almost all the data available in the literature are at best in the form of extrinsic rates or reported reactivities which cannot be effectively used for the purpose of reactor design.

Computational fluid dynamics (CFD) has been extensively utilized as a powerful tool to simultaneously solve all the governing equations, pertaining to the physics of the chemical reactors, using a minimum set of assumptions. Despite the profusion of works devoted to computational fluid dynamic simulation of gasification process, few have dealt with the modeling of the entrained flow gasifiers, having the majority of works focused on fluidized bed reactors. Also, of those studies dedicated to the modeling of entrained flow gasifiers, neither has

focused on the use of intrinsic reaction rates nor has tried to model the gasification of fuel blends. Also, majority of the studies are lacking a proper solid fuel mass and energy conservation.

To this respect, the underlying objectives of this research study are fourfold:

1. Assessing the effect of pyrolysis temperature and high heating rates normally encountered in entrained flow gasifier, on the morphology and structural development of produced chars from individual fuels and their blends.
2. Assessing the combined effects of the operating variables (i.e. temperature, oxygen and steam concentrations) and coal/coke blending ratio on high-temperature entrained flow gasification process, where the focus is to quantify the relationships between the response variables and vital factors and also to look for the possible synergies in co-gasification of coal and coke. These results will further help in finding the desirable location in the design space where H_2 production is maximized by finding the optimum values of the operating variables. In this regard, a new statistical methodology called, Response surface methodology, will be employed in lieu of classical “one-factor-at-a-time” which is well known to fail to detect the interactions between operation variables.
3. Developing the intrinsic reaction rates for oil sand coke using a thermogravimetric analyzer in combination with variety of char surface area characterization techniques including physisorption and chemisorption techniques to find the proper measure in order to normalize the apparent or specific rates.
4. Computational fluid dynamics simulation of the entrained flow gasification process to cover the underlying phenomenological aspects of reactor including the development of a new calculator scheme for Discrete Particle Modeling (DPM) option of Ansys Fluent software to check the elemental mass and

energy conservation in the solid fuels, multiple User Defined Functions (UDF) for modeling devolatilization and char gasification/combustion using intrinsic reaction rates. The model is built upon the assumption that slag-char micromechanical interactions are negligible.

CHAPTER 2

Literature review

2.1 Oil Sands

The word "Oil sand" is referred to naturally occurring mixtures of sand, clay, water, and a dense and viscous substance called bitumen. Oil sand is found in large amounts in many countries throughout the world, and huge quantities in Canada and Venezuela. Overall 1.7 trillion barrels of bitumen has been proven to be in place in three major areas (Fort McMurray, Peace River, and Cold Lake) with a proven 173 billion barrels of recoverable oil from the oil sand. Bitumen is recovered from the mixture by surface mining combined with mixing with hot water and in-situ production via using heat and steam. Only 20% of bitumen is recoverable by surface mining and the rest has to be produced via in-situ production techniques [17]. Both Suncor and Syncrude plants use surface mining and hot water extraction process to recover the bitumen [18]. Oil sands have been the subject of a series of detailed characterization studies over time which has resulted in the emergence of several structural models which are

broadly accepted among researchers in the field [19]. The typical properties of oil sand bitumen are represented in Table 2.1.

The extracted bitumen contains roughly about 5% sulfur and 15-20% asphaltenes, which are higher than typical values of those found in conventional crude oil. The extracted bitumen is then passed to upgrading plants to produce synthetic crude oil by thermal cracking or hydrocracking. The former process is being used by both Suncor and Syncrude. Upgrading process results in the production oil and gas as main products and pet coke as by product where the nature of coke formation is related to the coking process utilized.

Table 2.1 Typical properties of oil-sand bitumen [18]

<i>Elemental analysis</i>		<i>Metals (PPM)</i>	
Carbon	83.3	Vanadium	250
Hydrogen	10.3	Nickel	90
Nitrogen	1.1	Iron	75
Oxygen	0.4	Copper	5
Sulfur	4.9	<i>High heating value (MJ/kg)</i>	41
<i>Molecular weight</i>	540-800	<i>Specific gravity</i>	1.01

2.2 Properties of oil sand coke

Suncor and Syncrude plants use two different coking processes. Suncor uses a batch delayed coking process where the thermal cracking occurs by heating bitumen to 400-500°C followed by charging hot feed to a coke drum where all cracked products are separated as vapor and leave behind porous coke matter in the drum. Most of the sulfur and metals content of bitumen are retained in the coke. The yield of coke in this process is estimated about 20 wt. % of the bitumen feed. On the other hand, Syncrude plant uses a continuous fluid coking process where the thermal cracking occurs by spraying liquid feed into a bed of hot coke particles. Coke particles are fluidized in steam at 475-600°C, where steam helps to strip the distillate oil from the coke particles. Fluid coking results in higher yields of liquid hydrocarbons and lower coke yields compared to delayed coking

process. Coke particles are continuously redirected to a secondary burner where approximately 5% of coke production is burnt in air to heat up the rest of the coke particles to about 650°C, before being partially recycled back to the coker. The rest of produced coke is separated and stockpiled [18]. Over the years, the properties of different oil sand cokes have been thoroughly investigated for their chemical compositions and structural properties. Furimsky [20] provides a detailed review of the research studies on oil sand coke. A typical compositional analysis of delayed coke and fluid coke is represented in Table 2.2.

Table 2.2 Analysis of Suncor (delayed) and Syncrude (fluid) cokes [20]

Fluid Coke		Delayed coke	
<i>Proximate analysis</i>		<i>Proximate Analysis</i>	
Moisture	0.44	Moisture	0.1
Ash	5.4	Ash	4.04
Volatile matter	4.85	Volatile matter	12.15
Fixed carbon	89.3	Fixed carbon	83.71
<i>Ultimate Analysis</i>		<i>Ultimate Analysis</i>	
Carbon	82.7	Carbon	84.02
Hydrogen	1.72	Hydrogen	3.67
H/C	0.25	H/C	0.5
Nitrogen	1.75	Nitrogen	1.38
Sulfur	6.78	Sulfur	5.73
Oxygen	1.81	Oxygen	1.21

An important property of oil sand coke is its relatively low ash content compared to many coals (between 10 and 40%). The high carbon content of these cokes results in high heating value of feedstock and higher electricity and final production per unit weight of coke. Also data shows that volatile matter content of Suncor coke is higher than Syncrude which results in higher reactivity of delayed coke. Studies have shown a similar ash fusion temperature for both cokes due to the similarities in ash compositions.

Table 2.3 represents the ash chemical composition and fusion temperature of two oil sand cokes.

With respect to physical properties, particle size distribution (PSD) and grindability index have been studied for both cokes. The results show that Suncor coke is produced in the form of large lumps whereas coke produce by Syncrude is in powder form. For this reason application of Suncor coke in an entrained flow gasifier needs an extensive grinding. Same data shows that almost 40% of Syncrude cokes do not need any further grinding which results in significant saving compared to Suncor coke in the design of grinding systems [20].

Table 2.3 Ash properties of fluid and delayed coke[20, 21]

composition	Delayed Coke	Fluid Coke
SiO ₂	44.67	42.77
Al ₂ O ₃	26.70	25.85
Fe ₂ O ₃	9.78	12.58
TiO ₂	6.15	5.02
P ₂ O ₅	0.29	0.36
CaO	1.63	1.69
MgO	1.11	1.45
SO ₃	3.47	1.94
Na ₂ O	0.79	1.20
K ₂ O	1.13	2.00
BaO	0.48	0.15
SrO	0.40	0.06
V ₂ O ₅	1.96	3.33
NiO	1.21	1.20
MnO	0.12	0.30
Cr ₂ O ₃	0.11	0.09
Gross Heating Value (MJ/kg)	35.20	32.41
Ash Fusion Temperature (°C)		
Initial	1074	1082
Softening	1285	1293
Hemispherical	1338	1335
Fluid	1446	1418

The porosity and structural properties of both cokes has also been the subject of several studies [19, 22-26]. Delayed coke particles have been characterized by the irregularity in shape whereas fluid coking is characterized as dense spherical particles with layered “onion-like” internal structure. With respect

to the porosity, there is not an agreement in the reported value for delayed coke. Some authors found no porosity in the particles [22] whereas Hall [26] found a relatively high porosity. Similar discrepancies exist for fluid coke porosity as well. Some authors have reported a non-porous particle whereas some other works have reported surface area values of 10-12 m²/gr for fluid coke [18]. The main reason for the disparity in the reported values should be sought in the characterization techniques used to study the coke porosity and its surface area. The prolonged exposure of coke particles to temperatures higher than 500°C creates graphite-like structures, which can be detected in both cokes using the X-ray diffraction technique. It is well established that coke is a micro-porous material with the majority of its pores sizes distributed well below 50Å. So, the data reported by mercury porosimetry will underestimate the pore volume in the coke. Also, traditionally pore size distribution of a porous solid is evaluated from the analysis of nitrogen adsorption isotherms measured at 77K. It is very well known, however, that at these low temperatures diffusion of nitrogen molecules into micro-pores is practically very slow [27-30]. The use of other adsorbate molecules such as Ar and CO₂ have been recommended and widely used to characterize the pore size distribution of micro-porous coke particles [31, 32]. Furimsky [33] studied the variation of surface area and porosity with the fluid coke particle size. Figure 2.1 shows the effect of particle size on the surface area. N₂ BET method determines surface area associated with macro- and meso-pores, whereas CO₂ BET and Dubinin-Polanyi reflect the micro-porosity.

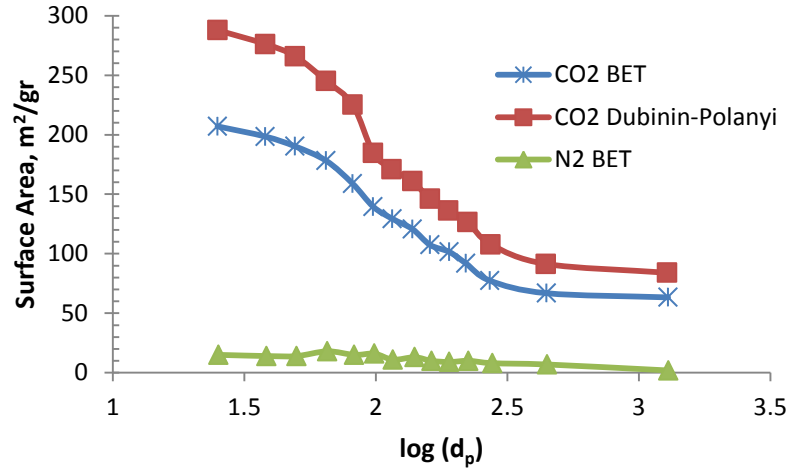


Figure 2.1 Surface area of fluid coke versus Log mean particle diameter [33]

From the figure it is clear that most of the porosity of the coke is associated with the micro-pores.

2.3 Properties of coal

The formation of coal began some 400 million years ago, following the first appearance of terrestrial plants on earth and has since formed in every geological era from the debris of vegetation. Overburdened plants convert to brown coal or lignite over time, under the influence of pressure and temperature. This low rank coals subsequently convert to sub-bituminous, then into bituminous coal and finally into anthracite. Coal is often classified in terms of its rank, increasing from brown coal to anthracite. Brown coal, lignite, and sub-bituminous coals are known as low rank coals, whereas higher rank coals are often called hard coals. Table 2.4 shows the variation of proximate and ultimate analysis and heating value with the coal rank [5, 34].

Table 2.4 Typical analysis of various coals [5]

Coal	Proximate analysis				Ultimate analysis					LHV MJ/kg, maf
	Rank	FC	VM	M	A	C	H	O	N	
Lignite	27.8	24.9	36.9	10.4	71.0	4.3	23.2	1.1	0.4	26.7
Sub-bituminous	43.6	34.7	10.5	11.2	76.4	5.6	14.9	1.7	1.4	31.8
Bituminous	51.3	32.7	2.2	13.8	83.8	4.8	8.4	2.0	1.0	34.0
Anthracite	81.8	7.7	4.5	6.0	91.8	3.6	2.5	1.4	0.7	36.2

FC: fixed carbon, VM: volatile matter, M: moisture, A: ash

All sorts of minerals and heavy metal trace elements can be found in coal. The occurrence of elements highly depends on the geological site that coal has been formed. In fact, coals of the same rank could be entirely different in the ash components. Coals from different countries have been the subject of detailed characterization and analysis for their rank, mineralogy and trace elements chemistry. One can easily find enormous number of literature in this respect [34-43].

2.4 Gasification studies on oil sand coke

Several years of investigations on coal, biomass and conventional petroleum coke gasification has resulted in an enormous number of publications and assortment of reaction models in this field. In this regard, reviews by Johnson [44], Kristiansen [45] and Basu [46] could be referred. However, compared to coal, biomass and conventional petroleum coke, very few fundamental studies have been conducted on Canadian oil sand coke. There is some confusion regarding similarities of oil sand coke and conventional petroleum coke and sometimes these two terms have been used interchangeably. However, it is quite important to notice that the conventional petroleum cokes have lower metal, silica and sulfur content compared to Canadian oil sands coke. These factors can have a significant role on the technology screening and also they can affect the performance and reactivity of the fuel in the gasification or combustion systems.

Scott and Carpenter [47] investigated the effect of fuel quality in advanced power systems. According to their study the high sulfur content of fuels such as oil sand coke (above 3.3%) favors IGCC systems over pressurized fluidized bed combustion technology. Additionally, the low reactivity of coke as explained in section 1.3 also favors entrained bed gasification systems over fluid bed and fixed bed technologies.

Almost all the available studies on oil sand coke have been conducted at low temperatures (below 1000°C) usually encountered in fluid bed or fixed bed reactors.

The early studies on gasification of Suncor and Syncrude cokes date back to 1980s in a fixed bed reactor to assess the reactivity of the samples using steam as gasifying agent [48]. A maximum operating temperature of 930°C used was. In this work, the synergy in blending lignite coal with coke and lignite ash with coke was also investigated separately. Figure 2.2 represents the effect of temperature and lignite ash on the carbon conversion of the cokes.

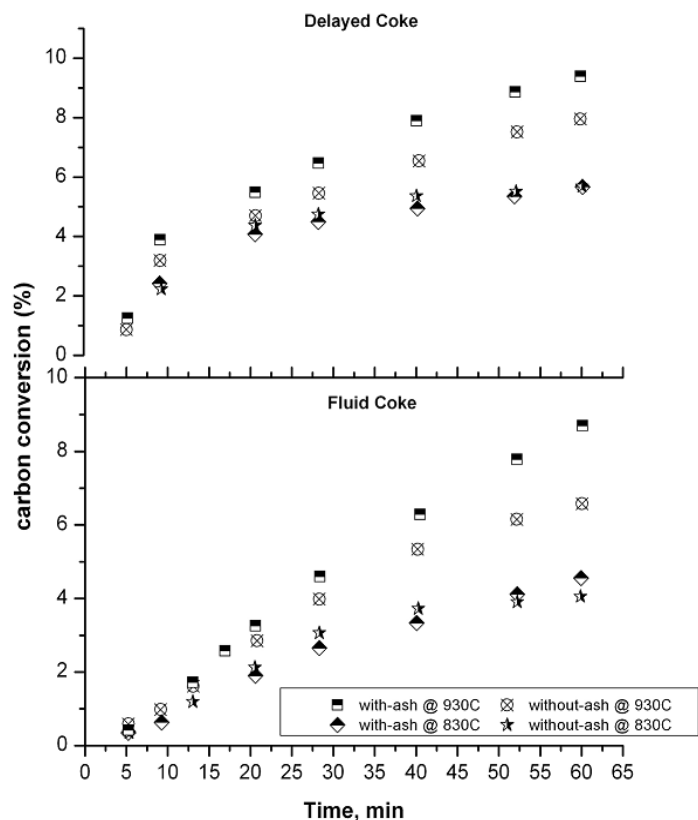


Figure 2.2 Effect of temperature and lignite ash on carbon conversion for delayed and fluid cokes [48]

The results of this study revealed an initial rapid carbon conversion for Suncor coke compared to Syncrude coke which was the direct effect of higher volatile content of delayed coke. It was observed that in case of Suncor coke, H_2 formation during the devolatilization almost accounted for 50% of the total H_2 formed in the whole process. However, the estimate of gasification rates showed that Syncrude coke has a higher reactivity than Suncor Coke in later stages of the experiments when heterogeneous gasification reactions started. The authors found that a direct blending of cokes with lignite coal did not yield in any catalytic synergy. On the contrary, the addition of lignite ash to coke resulted in a notable increase in carbon conversion. They postulated that in case of coal the access of coke to the catalytic sites is hindered by organic portion of coal. However, the catalytic effect of lignite ash was not evident at temperatures lower than $900^\circ C$. Figure 2.2 clearly shows the lack of catalytic effect at $830^\circ C$ for both delayed and

fluid cokes. The catalytic observations were attributed to calcium and iron content of lignite ash. The authors further discussed that the high content of inorganic sulfur in lignite coal traps all the Fe in the form of pyrite which are not catalytically active for steam gasification reaction.

Furimsky [49] further extended the work to gasification with air and steam. The results revealed that carbon conversion of Syncrude coke was reliably 15% higher than Suncor one. However, they argued that the observed reactivity differences should disappear at higher temperatures normally encountered in entrained flow reactors. Experiments at high temperatures need to be conducted to check their claim though. They also compared the reactivity of both cokes with lignite and a bituminous coal. After 30 min of gasification under the same conditions, the reactivity of the lignite and bituminous coals were found to be five times and two times greater than that of oil sand coke. Nevertheless, oil sand cokes were found to be slightly more reactive than anthracite and semi-anthracite coals.

Watkinson *et al.* [50] investigated the gasification behavior of Syncrude fluid coke and Suncor delayed coke in fluidized bed reactor and spouted bed reactors, respectively, using steam and oxygen as gasifying agents. The objective was to study the effects of oxygen/coke ratio and temperature on gas composition, heating value and carbon conversion. The choice of reactor was dictated by the particle size distribution of the cokes. The Suncor coke particle size was on average 10 times the size of Syncrude coke. At about 950°C and a feed rate of 20 kg/hr, carbon conversions of 90% and 80% were obtained for Suncor and Syncrude cokes, respectively. Gasifying fluid coke in fluidized bed and recycling the char particles using cyclone resulted in lower carbon conversion and heating values compared to delayed coke. They reported that to attain conversions above 80 wt. %, temperatures exceeding 1000°C is required. However, for both cokes, recycling fine particles significantly improved the overall carbon conversion. Application of potassium carbonate catalyst either by spraying onto the particle followed by drying or feeding as powder into the bed, increased the carbon

conversion and heating value of producer gas. Figure 2.3 shows their finding in this respect.

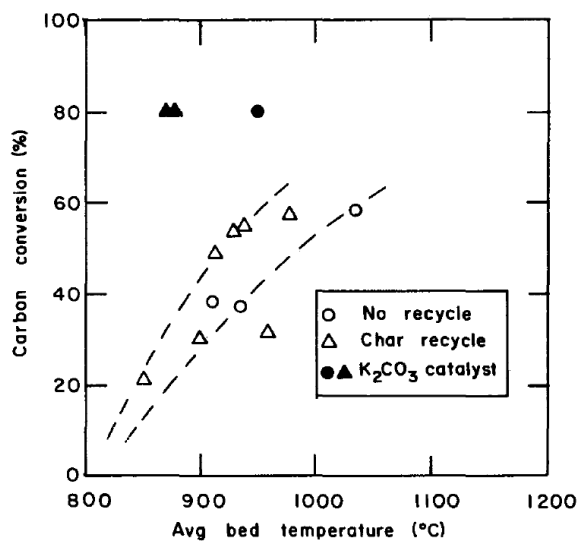


Figure 2.3 Effect of temperature, char recycling and addition of catalyst on carbon conversion of fluid coke [50]

Using dolomite for adsorption of sulfur from flue gas, more than 95% of H₂S reduction was achieved. Using thermodynamic calculations they were also able to approximately predict the flue gas heating values, however, their thermodynamic model failed to predict the H₂/CO ratio.

Nguyen and Watkinson [51] studied the kinetics of steam gasification of delayed and fluid cokes in the range of 800°C to 930°C in an atmospheric pressure stirred-bed semi batch reactor. Coke particle sizes were sieved to the cut-size of 0.1-3.5 mm. Steam partial pressure was varied between 15.2 to 60.6 kPa. They also characterized the structural changes in coke particles as a function of conversion using SEM, BET surface area analyzer, and mercury porosimetry techniques. Figure 2.4 shows the effect of temperature on the carbon conversion of both cokes. The data again showed similar reactivity for both cokes with fluid coke being more reactive than delayed coke at later stages of gasification which resulted in a higher conversion compared to delayed coke.

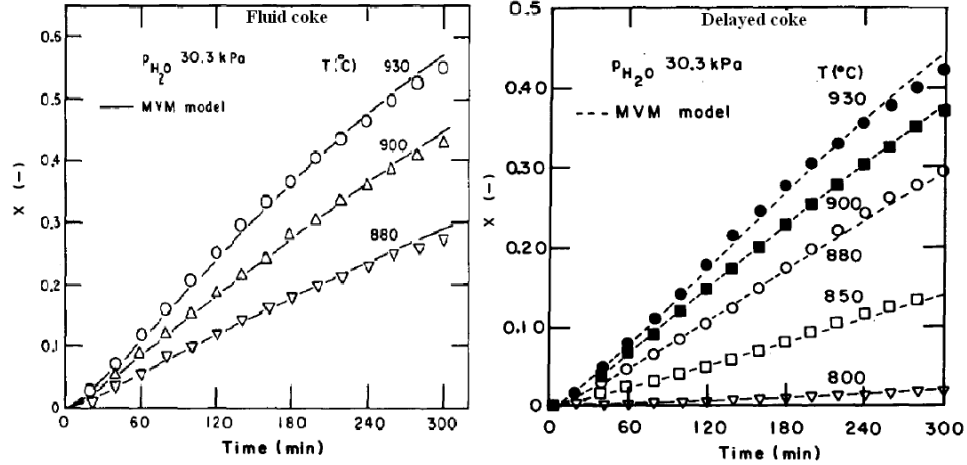


Figure 2.4 Effect of temperature on carbon conversion of fluid coke ($D_p=0.14 \text{ mm}$) and delayed coke ($D_p=2 \text{ mm}$) [51]

They also observed that reactivity of Suncor coke at 930°C increased with decreasing particle size. Figure 2.5 delineates their findings.

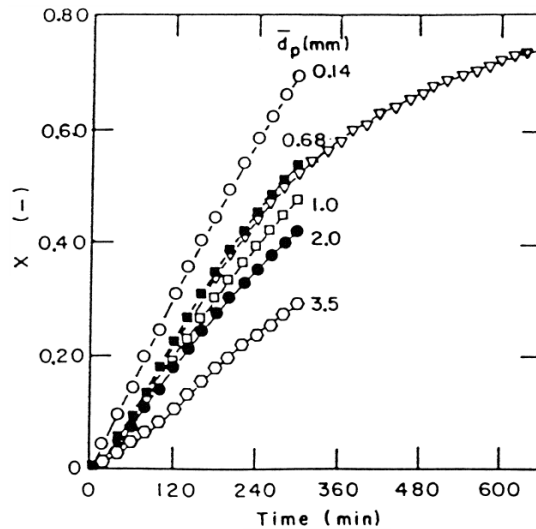


Figure 2.5 Effect of particle size on conversion of delayed coke [51]

Using BET surface area analyzer they observed that surface area increased with carbon conversion reached a maximum around 30% conversion and then declined. This is a typical behavior reported by many authors working on gasification of microporos carbons. In fact the well-known Random Pore Model (RMP) has been developed based on the same assumptions. The rapid initial

increase in surface area is attributed to the reopening of micro-pores closed during heat treatment; however, as the gasification reactions proceed micro-pores will gradually grow in size and coalesce to form meso- and macro-pores which manifests itself in reduction of surface area in the later stages of gasification. Figure 2.6 represents the variation of surface area at different levels of conversion for delayed coke particle.

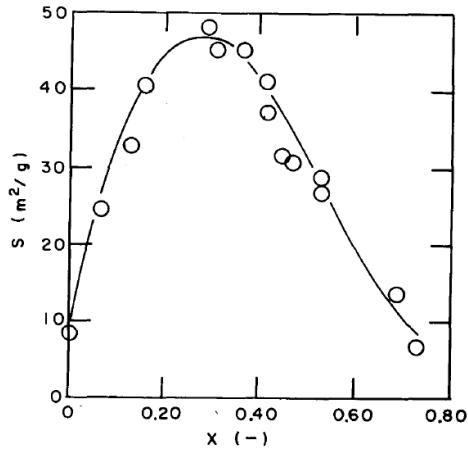


Figure 2.6 Surface area of delayed coke as a function of carbon conversion [51]

These results were further confirmed with pore size distribution determined with mercury porosimetry. They also examined the morphology of chars at different level of conversion using SEM. Figure 2.7 shows the SEM images of fluid coke and delayed coke at 55% and 57% carbon conversion, respectively. The images clearly show the different structural properties of the oil sand cokes. The “onion-like” structure of fluid coke can be easily noticed in the images. It is worth noting, however, that the surface of fluid coke despite the claim of some authors is not very smooth. Even in the image scale of 50 micron one can easily notice development and rough edges and fine pore structure development. This partly explains why BET surface area measurements using N_2 highly underestimates the total surface area of the cokes. This was earlier explained in section 2.2 by significant difference in surface area values measured using N_2 and CO_2 .

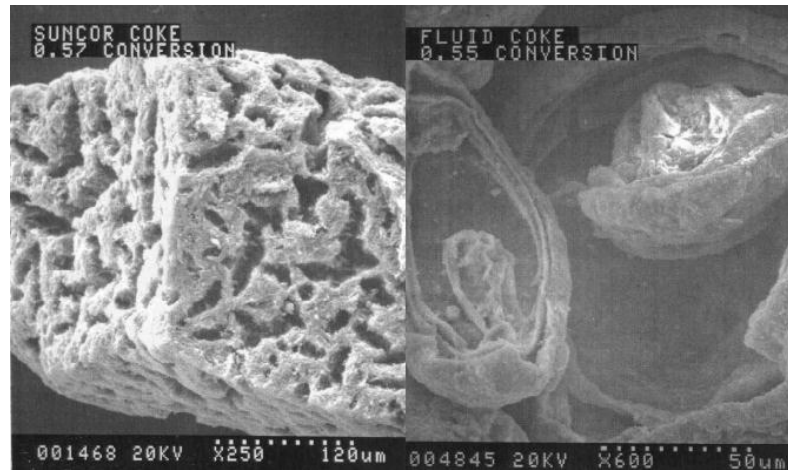


Figure 2.7 Scanning electron microscopy of fluid cokes [51]

The only publicly available high temperature gasification study on oil sand coke was conducted by Cousins *et al.* [21] in CANMET energy technology centre in Ottawa. They investigated the effect of blending delayed coke with sub-bituminous and lignite coal in a pilot scale high pressure entrained flow gasifier at CETC-Ottawa using CO₂ and steam as gasifying agents within temperature ranges of 1200-1400°C. Using CO₂ to transfer fuel to the gasifier they did not observe any significant influence in carbon conversion and syngas production compared to that achieved using N₂ as conveying gas. Figure 2.8 delineates the effect of N₂ and CO₂ conveying gases on the carbon conversion and syngas production in their study. They reported that blends of coke and coals resulted in higher carbon conversion and cold gas efficiencies than runs conducted using coke alone. However, the reported gain in conversion and gasification efficiencies between 5-10% could be well within the range of experimental errors particularly that the statistical significance of the reported data has not been discussed. They also found out that while CO₂ addition does not affect the conversion considerably, steam has a significant effect on CO and H₂ content of syngas. Using thermogravimetric analysis and SEM images they also observed that majority of the residual carbon in chars collected after gasification of coke/coal blends were from the coke component of blends. Overall, a limited number of parameters were

based on SEM and EDX analyses. KCl was also found to be effective only at temperatures higher than 800°C. Its catalytic effect, however, was found to be weaker than K_2CO_3 and Na_2CO_3 . They concluded that the enhanced catalytic activity of alkali metal catalysts is linked to their higher mobility and their penetration into the coke structure compared to alkaline earth compounds.

2.5 Review of related works on co-gasification

Majority of co-gasification studies are concentrated on biomass and coal with the objective to produce gaseous and liquid end products. Among them few have also investigate the catalytic effects in blending coal, biomass and petroleum coke as well:

Collot *et al.* [53] studied the pyrolysis and gasification of coal and biomass blends in bench-scale fixed- and fluidized-bed reactors. They found that, neither intimate contact between fuel particles nor their relative segregation led to synergistic effects in pyrolysis experiments. However mineral matter residues from the wood appeared to have a catalytic effect during combustion. Overall, they concluded that there was no evidence of synergy in fluidized-bed reactor.

Sjostrom *et al.* [54] studied the gasification reactivity of chars from blends of biomass and coal. Mixtures of the fuels and their chars showed a higher reaction rate of gasification under studied conditions compared to that of coal alone. Further, both the formations of tar and nitrogen compounds also seemed affected synergistically in the co-gasification experiments of the fuels. The yields of tar and of ammonia were lower than expected. Although not very certain, they reported the occurrence of synergetic effects in the co-gasification of birch wood with two different types of coal in experiments performed in the pressurized fluidized-bed reactor. The reactivity of the fuels in the mixtures and the formed chars was seen to have increased, leading to promoted gas production.

Pinto *et al.* [55] studied the effect of experimental conditions on co-gasification of coal, biomass and plastics wastes with air and steam in a fluidized bed reactor. They observed that rising temperature promoted the reactions of

hydrocarbon, and resulted in a drop in tars and hydrocarbons content and increased the H₂ production. For a mixture of 60% (w/w) of coal, 20% of pine and 20% of PE wastes, increasing temperature, from 750 to 890°C, decreased the methane and other hydrocarbons concentration in flue gas by 30% and 63%, respectively. However, hydrogen production increased by 70%. They also reported that increasing air flow resulted in reduction of hydrocarbons as well by switching partial oxidation to full combustion; however, higher oxygen concentration reduced the heating value of flue gas. Increasing steam on the other hand, led to an increase in H₂ production via reforming hydrocarbons.

Vuthaluru [56] investigated the thermal behavior during co-pyrolysis of coal, biomass materials and coal/biomass blends prepared at different ratios (10:90, 20:80, 30:70 and 50:50) using a thermogravimetric analysis (TGA) apparatus. They did not find any interactions between coal and biomass on thermal behavior of coal/biomass blends during co-pyrolysis. The 50/50 coal/biomass blend showed the highest reaction rate, ranging from 1×10^9 to 2×10^9 min⁻¹. The reaction orders in these experiments were found to be in the range of 0.21-1.60, thus having a significant effect on the overall reaction rate.

Kumabe *et al.* [57] carried out a study on the co-gasification of woody biomass and coal using air and steam in a downdraft fixed bed gasifier at 1173K with the objective of supplying syngas for synthesis of liquid fuels. With variation of biomass to coal ratios from 0% to 100% on a carbon basis, they observed that conversion to gas increased with increasing the biomass ratio whereas both char and tar yield decreased. Also an increase in biomass ratio led to a decrease in H₂ production, and a rise in CO₂ content of flue gas. Nonetheless, they found that CO content did not change with biomass ratio. They speculated that synergy in co-gasification of biomass and coal, if present at all, might be due to the extent of water-gas shift reaction per se rather than catalytic effect influencing gas-solid reactions.

Zhang *et al.* [58] studied co-pyrolysis of legume straw and Dayan lignite in a free-fall reactor under atmospheric pressure in nitrogen environment, over a temperature range of 500-700°C. The results showed that the compositions of the

gaseous products from the blended samples are not all in accordance with those of their parent fuels. Moreover, under the higher blending ratio conditions, the char yields were lower than the theoretical values calculated on pyrolysis of each individual fuel and consequently the liquid yields were higher. The results indicated that there exists a synergetic effect in the co-pyrolysis of biomass and coal and might be explained by the fact that biomass in blends offers plenty of hydrogen donors and plays a hydrogenation role on coal pyrolysis.

Despite the proven catalytic effects of alkali metal salts, such as potassium and Sodium salts, in carbon gasification, they are too expensive to be applied on industrial scale. Blending high potassium content biomass materials such as Wheat Straw is considered a promising additive as a source of catalyst. In this respect, Zhu *et al.* [59] used an herbaceous type of biomass, with a high content of potassium to act as a source of catalyst in co-processing with coal. The co-pyrolysis chars revealed higher gasification reactivity than that of char from coal, especially at high levels of carbon conversion. They observed that increasing temperature in pyrolysis lessens the catalytic activity of biomass ash. Experimental results showed that the co-pyrolyzed chars prepared at 750°C had the highest alkali concentration and reactivity as compared to the char prepared at 850°C. However, no explanation was provided.

Fermoso *et al.*, [60] co-gasified coal, biomass and petroleum coke at high pressure in a fixed bed reactor. A synergistic effect was observed for blends of coal with pet-coke. They also observed a positive deviation from linear additive behavior in both the H₂ and CO production for blends of coal and coke. Addition of up to 10% biomass into the blend of 50%/50% coal and coke blend showed that both H₂ and CO production increased accordingly. Further, blending biomass with coal/pet-coke blends did not produce any significant change in H₂ production, although slight variations were observed in the production of CO and CO₂. The maximum temperature studied in their work was around 1000°C.

Lu and Yan [61] investigated the co-gasification of biomass (pine sawdust or rice straw) and coal using air/steam mixture in a bubbling fluidized bed for the blending ratio effect on gas component, LHV, gasification efficiency and carbon

conversion rate. Results indicated that increasing sawdust blending ratio from 0% to 100% led to an increase in H₂ and CO production by 4.6% and 4.4%, respectively, whilst the CO₂ production reduced by 3%. Whereas when the blending ratio of rice straw rose from 0% to 100%, the volume concentration of CO increased from 25.8% to 27.5% and then dropped to 25.3%. Variation of other gas components during co-gasification of rice straw and coal is similar to that of the pine sawdust. They also reported a synergy in gasification efficiency and carbon conversion for blends of both biomass feedstocks.

Wang *et al.* [62] studied the effect of operating variables such as temperature, biomass/coal and steam/biomass ratios on hydrogen production in a series co-gasification experiments conducted in a fluidized bed reactor. Two-step gasification process in a fluidized bed was adopted in their experiment. They also investigated the tar content under different conditions. The results showed that hydrogen yield is mainly affected by temperatures and steam. Using the reactor temperature between 950 to 1000°C, and steam to biomass ratio of 0.9, and the biomass to coal ratio of 4/1, the hydrogen yield of about 68.25 g per kilogram dry ash-free biomass and coal was obtained. Also, the highest hydrogen yield potential was estimated as 138.01 g per kilogram dry ash-free biomass and coal.

Hernández *et al.* [63] conducted a series of air-blown entrained flow co-gasification of biomass and a coal-coke mixture in order to evaluate the effect of the relative fuel/air ratio (ranging between 2.5 and 7.5), the reaction temperature (ranging between 750 and 1150 °C), and the biomass content in the fuel blend on the producer gas composition and the process performance. The results showed that an increase of the biomass content in the fuel blend promotes the producer gas quality and improves the cold gas efficiency. Some signs of synergy between biomass and coal-coke was found, particularly at low fuel/air ratios and low reaction temperatures, which was linked to catalytic effects of ash (especially due to the catalytic effects of Ca and K coming from the biomass ash, and the Fe, Ni, and Zn contents of the coal-coke ash). However, no interaction was found in thermogravimetric analyses between biomass and coal-coke. This fact will make their observed synergy in entrained flow reactor unreliable due to the fact that the

contact mode in TGA is much higher than entrained flow beds. The reported synergies could be in the order of experimental error, which have not been reported in their study.

A series of high-temperature drop tube pyrolysis and gasification tests were conducted by Kajitani *et al.* [64]. In this work, two bituminous coals, cedar bark, and their blends were pyrolyzed in nitrogen gas or gasified with carbon dioxide at high temperature. The results did not reveal any synergy between coal and cedar bark in the co-gasification tests at 1400°C. The co-pyrolysis product yields at high temperatures agreed with the equilibrium yields, and the char reactivity of the blends of coal and biomass was almost the same as that of single fuels at the high temperatures. However, the reactivity of the blend was reported to be greater than pure coal at 1200°C or lower. Overall they concluded that synergy is only possible to be improved at lower temperatures and high contact modes as far as co-gasification is concerned.

Li *et al.* [65] also investigated the effect of blending coal and biomass on syngas production in a fluidized bed reactor. They were able to gain a continuous stable operation with the maximum biomass ratio of 33 wt%. The highest gasification efficiency obtained was 60.92%. Corresponding syngas yield and carbon conversion were 1.00 Nm³/(kg fuel) and 88.89%, respectively. In their study, the hydrogen content in the flue gas product decreased with the increase of oxygen equivalent ratio, but increased almost linearly with the biomass ratio. Similar trend was observed for carbon monoxide concentration and syngas yield with variations of oxygen equivalent ratio and biomass ratio. They also reported that there is a maximum value in syngas yield curve versus steam/carbon ratio.

The co-gasification of coal and wood in a dual fluidized bed gasifier was also conducted by Aigner *et al.* [66] with the main focus directed to investigate the effect of blending ratio on the producer gas quality. Their results did not show any signs of synergy in co-gasification either, even at low temperatures. Hydrogen concentration rose with increasing coal ratio, while CO concentrations dropped. However, adding wood to coal reduced the levels of the impurities NH₃ and H₂S in the producer gas due to the lower sulfur and nitrogen content of wood.

Steam co-gasification of coal and biomass derived chars in an atmospheric pressure fixed bed reactor was investigated by Howaniec *et al.* [67]. Temperature of bed was varied from 700°C to 900°C. The effectiveness of co-gasification of coal/biomass blends of 20, 40, 60 and 80% w/w biomass content was tested in terms of gas flows, composition, carbon conversion and chars reactivity. A synergy effect in the co-gasification tests, consisting of an increase in the volume of hydrogen produced, when compared to the tests of coal and biomass gasification, was observed at all tested temperatures. The observed synergy effect was attributed to the catalytic effect of K₂O present in blend ash (6-10 wt.%). Moreover, an increase in the total gas yield was observed for blends of 20 and 40% w/w biomass. However, for higher biomass content (i.e. 60 and 80% w/w) blends, a slight decrease in the total volume of product gas was observed.

The effect of mixing coal liquefaction residue with petroleum coke for their co-gasification potentialities was studied by Liu *et al.* [68] using a thermogravimetric analyzer. The blends of fuels were co-gasified with carbon dioxide in a TGA. The isothermal (at 1273K) kinetics was compared to evaluate the effect of blending coal liquefaction residue on gasification reactivity of petroleum coke. They found that the gasification reactivity of petroleum coke enhanced significantly by the catalytic components in coal liquefaction residue. They also showed that the catalytic effect of coal liquefaction residue was influenced by the temperature and loading. Under the condition of reaction kinetic control, higher temperature promoted the catalytic effect of coal liquefaction residue, and the catalytic effect also increased with the loading.

Recently, Shen *et al.* [69] studied the co-gasification performance of coal and petroleum coke blends in a pilot-scale pressurized entrained-flow gasifier. Two subbituminous and bituminous coals were individually blended with a coke. They found that the slagging problem due to high ash content of subbituminous coal was improved when 70% or more coke was mixed with the coal. They also observed that higher oxygen to carbon ratios resulted in a drop in syngas production with O₂/C ratio between 0.6 and 0.65 Nm³/kg resulting in maximum syngas production. The best blending ratio for syngas production in their study

was found to be 50% coal/coke combined with an O₂/C ratio of 0.61 Nm³/kg. However, the study did not consider the effect of steam in gasification performance. Furthermore, a long term gasification operation requires a much closer attention to ash composition of coke for elements such V and Ni which cause refractory failure and fouling in economizer and shift reactor as well. So, the recommended 50% blending ratio might not be feasible in thereality of the gasifier.

Xu and sun [70] also investigated the co-gasification behavior of biomass and petroleum in a fixed-bed reactor to determine the effect of the blending ratio and particle size of petroleum coke on the tar yield and gas heat value. For the case biomass fuel gasification alone at 700°C, the results showed that the gas heat value decreases up to 15% from 2.37 MJ/m³ with a 13% increase in oxygen content. The average tar yield was 6.4%. For the co-gasification case, the average tar yield was found about 2.9%, with corresponding gas heat value of 5.19 MJ/m³ compared to biomass case under similar conditions. At the temperature of 700°C, the best ratio of the petroleum coke to biomass was 1:1 with the oxygen content of 4%. The largest and smallest tar yields obtained for the gasification with petroleum coke alone, and the co-gasification case. They also observed that as the particle size of petroleum coke increased, the tar decomposition rate gradually decreased. Also, they reported that the tar yield decreased with temperature in all cases.

And finally, Zhan *et al.* [71] investigated the influence of blending method on the co-gasification reactivity of a blend of petroleum coke and lignite in a thermogravimetric analyzer using CO₂ as gasifying agent. They claimed that blending method has a significant effect on the co-gasification reactivity. They used two methods of blending, wet grinding and dry grinding and their results showed that wet grinding was much more effective than dry grinding. They also reported that co-gasification reactivity increases linearly with a rise of BET specific area. However, their results is in contrast with the recent work of Karimi *et al.* [72] which showed that admixing catalysts with coke or adding them to

liquid vacuum residue prior to coke formation did not make any difference in the reactivity of samples.

2.6 Gasification kinetic of oil sand coke

Compared to the studies on gasification performance of Canadian oil sand coke, much less is known about their kinetic rates with different reactant gases. Also, to the author's best knowledge, there are no intrinsic rates available for Canadian oil sand coke.

Perhaps the most detailed study on gasification of oil sand coke was conducted by Nguyen and Watkinson [51] where they studied the kinetic of steam gasification of delayed and fluid coke at atmospheric pressure and temperatures between 800°C to 930°C. A generalization of the uniform reacting porous particle model was used to fit the experimental data in the following form:

$$\frac{dX}{dt} = k(X)(1 - X)P_{H_2O}^n \quad (2.1)$$

Where, $k(X)$ was defined using three different models: random pore model of Gavalas [73], random capillary model of Bhatia and Perlmutter [74], and modified volumetric model of Kasaoka *et al.* [75]. They also showed that $k(X)$ in all three models could be expressed as:

$$k(X) = [a - b \cdot \ln(1 - X)]^m \quad (2.2)$$

Parameters a , b and m can be estimated for each model by fitting models to experiment data. For random pore model and random capillary $m = 1/2$ and a , b must be estimated whereas in modified volumetric model $a = 0$ and m , b has to be estimated. Overall, in this study modified volumetric model gave the best fit to the experimental data. Because of the particle size they used in their experiments (in the order of millimeter), their results suffered from diffusional effects. Therefore, they represented the reaction rate constants as a function of particle diameter. For instance, they found the following rate constant for delayed coke:

$$K = \frac{3.204 \times 10^4}{d^{0.26}} \exp\left(-\frac{162350}{RT}\right) \quad (2.3)$$

Additionally, using the N₂ BET surface area, they normalized the reaction rates. However, their results at best can be considered as extrinsic rates. There are two basic problems with this study (1) there are no distinction between molecular diffusion and Knudsen diffusion or any discussion about the effective diffusivity. So as far as the modeling is concerned, the proposed rates and activation energies are not reliable to be used, (2) for a micro-porous materials such as coke, application of N₂ BET to normalize the specific rate is not acceptable without proper justification. No attempts were made to measure the micro-pore surface area or active surface area. So, the formal reaction rates proposed in this study with the units of g/m².s have no relation with intrinsic reaction rates whatsoever.

Karimi *et al.* [72] further studied the kinetic of catalytic steam gasification of bitumen coke in a thermogravimetric analyzer with steam partial pressures in the range of 60 kPa to 85 kPa. The activation energy was notably decreased from 2.1×10^5 J/mol for the uncatalyzed steam gasification reaction to 1.2×10^5 J/mol and 1.3×10^5 J/mol, for K₂CO₃ and Na₂CO₃ catalyzed reactions, respectively. A Langmuir-Hinshelwood rate model was proposed for the steam gasification reaction, however, a first order power law model was found to be sufficiently accurate to fit the rate data. Using Secondary Ion Mass Spectrometry, it was shown that a fraction of alkali metals penetrate into the coke structure. Diffusion continues till coke becomes saturated. Using this depth profiling results, the lower reactivity of the metals at low catalyst loadings was explained by the inaccessibility of active metals to the gaseous reactant. Given the fact that surface area decreases after a certain level of conversion, an increasing trend of specific rates at higher conversion levels was justified by an increase in the catalyst loading as coke is consumed. Normalizing the predicted specific rates with the instantaneous surface loading of catalyst, they also rejected the previously suggested model where gradual increase in absolute rates was explained by gradual release of the potassium atoms from the K-O-C structures.

2.7 Review of related works on char gasification kinetics

As discussed in the section 1.2 after devolatilization, the slowest step is the reactions of the char with oxygen, carbon dioxide, and steam. So access to reliable solid-gas reactions rates is crucial in determining the required char residence times or recycling rates which in turn affect the gasifier design and operating conditions.

Due to the heterogeneous nature of the solid fuels, almost all the attempts which were directed to correlate gasification reactivity of coal and coke to chemical composition, or macerals of coal have failed. Even coals with very similar compositional analysis represent a wide range of reactivities. Several comprehensive reviews have been dedicated to the kinetic of char gasification reactions (ref. [76, 77]). The reactivity of fuels to reactant gases has found to be a complex function of (1) the properties of coal, (2) the condition during pyrolysis and (3) the condition during gasification. Furthermore, for a single char under study, char gasification reactivity is affected by three factors: (a) the active surface area (ASA) of the char, (b) the degree of access of the gaseous species to the active sites located on micropore surfaces of particle, and (c) the potential catalytic effects of the mineral impurities in ash [78].

For the case of a porous solid catalyst, where the surface is not consumed by reaction, factor (b) is reasonably well understood. Its quantitative treatment has been established from the pioneering work of Thiele [79]. However, chars from carbonaceous materials undergo various structural changes as the reactions proceed. So, realistic models need to be developed to take into account the complicated underlying physics such as porosity development, surface area and effective diffusivity during reaction. In the past years, various such models have been proposed [44, 77], for instance, random pore model, and capillary model. Even when all effects of mass and heat transfer limitation are accounted for, the carbon from various origins show a wide range of reactivities [80]. This in fact shows the importance of factor (a) and (c) in determining the intrinsic reaction rates.

The intrinsic reactivity is defined by kinetic data measured under conditions where chemical processes alone control the conversion rates. So practically influence of mass and heat transfer are minimized. These data are usually normalized to some measure of the surface area of the char, to make them an inherent property of the carbon. Intrinsic reactivity is normally developed by kinetic parameters determined from reaction rate measurements (apparent or specific rates) normalized to the char active surface area. This requires tests to be conducted at relatively low temperatures: below 500°C for char-O₂ reaction and temperatures less than 1000°C for char-CO₂ and char-H₂O reactions. The intrinsic rates are of prime importance in modeling and simulation of gasification processes. Combination of intrinsic rates with underlying heat and mass transfer physics will allow the development of predictive models which are extremely helpful in detail design or improving the available design of gasifiers.

Gasification of a porous char requires the transport of gaseous reactant from gas to the surface of particle, diffusion through the pores and onto the active sites, reaction between gaseous reactant and solid followed by desorption and removal of product gases. Under the chemically controlled conditions, the intrinsic reaction rate is defined as:

$$\hat{R} = \hat{k} P^m = \frac{k}{A_g} * P^m \quad gr/m^2.s \quad (2.4)$$

Where $\hat{k} = A \exp(-\hat{E}/RT)$ is the intrinsic reaction rate constant and k is the specific rate constant. The term A_g is a measure of char surface area. Despite the abundance of works in this field, there still is a lack of unanimous agreement between researchers on what has to be used to normalize the specific reaction rates. Some have tried to use N₂ BET surface area as the normalizing parameter whilst other have criticized the limitation of N₂ in characterizing the true surface area of chars, particularly micro-porous chars, so there has been attempts to replace N₂ with Ar and CO₂ gases and BET method with more sophisticated techniques called Density Functional theory (DFT) and Grand Canonical Monte Carlo (GCMC) modeling [27, 81]. On the other hand, some researchers believe the underlying assumption in using Total Surface Area (TSA) as a normalizing

parameter is questionable due to the fact that it inherently implies that the ratio of Active Surface Area (ASA) to TSA is constant, which has been proven to be invalid in several cases. So this group has perhaps used the most promising normalizing factor based on ASA determined from chemisorption of oxygen or CO₂ via different techniques such as thermogravimetric, Temperature Desorption (TPD), and Transient Kinetic (TK) studies. A detail review of work in this field can be found in ref. [82].

It is well known that char reactivity also changes with carbon conversion. A monotonic increase in reactivity with carbon conversion (up to 35%) for graphitized carbon black was reported by Lain et al. [83] in early 60's. A normalized reactivity versus conversion, based on a dimensionless time parameter of $t/t_{0.5}$ (instantaneous time normalized by the time required to reach 50% carbon conversion) for gasification of lignite with oxygen was presented by Mahajan et al. [84]. Their plot clearly showed that reactivity was not constant. The non-constant behavior of plot was qualitatively explained by opening up the closed pores as reaction proceeds and finally the open pores are enlarged until they finally coalesce. However, they failed to provide a quantitative explanation of this behavior.

Char gasification reactivity is usually treated to be proportional to the total surface area of the carbon. As a result, numerous models have emerged in the literature based on this assumption trying to relate the variation of observed reactivity to the structural changes of carbon. These studies are intended to represent the evolution of Total Surface Area (TSA) as a function of time (or conversion) under the kinetically controlled regime. Here, physisorption of gases such as N₂, Ar, or CO₂ have been extensively used to measure the total surface area in combination with BET, Dubinin-Polanyi (DP), and Dubinin-Radushkevich (DR) equations or more recently DFT and GCMC models. Despite all the efforts in this area, in general poor correlation between TSA and reactivity particularly for microporous carbons has been gained so far.

An alternative approach has also been introduced which uses the concept of Active Surface Area (ASA) instead of TSA. This basic concept was first

introduced by Taylor [85] stating that for surface reactions, some sites are more active than the others and reactions mostly take place on these sites. Later on, the concept of availability extended the primary idea of activity by taking into consideration that the sites with high energy and potential to bind with reactant gases are not necessarily the sites that participate in reactions due mainly to the fact that very few of them are accessible where some other sites with weak affinity for the reactant are mostly available. So, the optimum sites lie somewhere between these two sites.

Similar to heterogeneous catalysis, ASA is determined by low temperature chemisorption commonly using oxygen as the adsorbate. However, in contrast to heterogeneous catalysis where ASA is essentially constant (in absence of poisoning), ASA of carbons is a function of conversion [86]. A complete review of the related works in this field can be found in ref. [82]. In general, studies based on ASA seem to be more promising compared to TSA. Nonetheless, there are limitations associated with studies focused on ASA [86]. For instance, both Lain et al. [83] and Tong et al. [87] found a good correlation between ASA and specific gasification rate for a graphitized carbon black and pyrolytic carbon film, respectively. However, using the same experimental technique, the results were not satisfactory for Saran char, a highly disordered carbon [83]. Jenkins and Piotrowski [88] studied the variation of ASA with conversion for demineralized coal chars of varying rank. Their results did not show a good correlation between ASA and reactivity either. The problem with determining ASA using oxygen chemisorption at low temperatures is that active sites measured in this way, may or may not be reactive during the gasification. There have been reports of formation of stable complexes which can resist to temperatures of up to 1300K and consequently unavailable for reaction, whilst other adsorbing sites form the reaction intermediates very slowly [89-91]. So, the active sites definition were revisited and modified as the sites which are sufficiently active to dissociatively chemisorb the oxygen but not that strong to form a so-called “stable complex” [92]. A specific carbon can exhibit different chemisorption capacities at different temperatures. This reflects the distribution of active sites with different affinities

in formation of surface complexes [83, 93]. Radovic [86] suggested that low temperature oxygen chemisorption needs some modification to take into consideration the formation of stable complexes. In this respect, he has introduced the concept of Reactive Surface Area (RSA) where traditional experimental technique for O₂ chemisorption is modified in such a way that enables one to quantitatively measure the formation of stable complexes and total complexes where difference gives the known RSA which he has shown to be more appropriate for normalizing the reactivity of carbons from different sources. He has also shown that O₂ chemisorption can be effectively replaced with CO₂ chemisorption for measuring the active surface area due to the simple fact that measurements using CO₂ are conducted at higher temperatures where the formation of stable complexes are much less than the case of O₂. Klose and Wolki [94] have successfully used the CO₂ technique for developing the intrinsic rate of a biomass char.

Despite all the efforts in this area, still no clear conclusions can be drawn about the effect of mineral matter and added catalysts on active sites in coal chars.

In summary, studies suggest that development of gasification reactivities of coal and coke as an inherent property of carbon are not possible with the current state of knowledge. So, intrinsic rates have to be developed separately for different fuels. However, as far as a single char of interest is concerned, ASA and RSA are much more promising measures of surface area in order to normalize the specific rates, than commonly used TSA [82].

2.7.1 Effect of temperature on reactivity of chars

Effect of thermal annealing on reactivity of carbons, of particular interest, high heating rates and high temperatures normally encountered in entrained flow gasifiers, has been given much less attention compared to low temperature studies. It is well known that thermal annealing can result in micropore collapse, structural ordering of the carbon on a molecular level, and catalyst deactivation [77, 95]. In general chars prepared at higher temperatures during pyrolysis exhibit

lower gasification reactivity [96]. A complete review of the works in this field covering O₂ and CO₂ reactions and temperatures as high as 2500K has been provided by Suuberg [82]. The author covers available studies and models involved in determining high temperature reactivity of carbon. However, he concludes that we are still limited by the lack of fundamental understanding of gasification mechanisms. For instance, there is still no fundamental answer to the question of why the effect of annealing process on carbon reactivity is reactant dependent.

In addition to temperature, residence time of particles at high temperatures also plays an important role on the reactivity of the produced chars. Radovic et al. [92] investigated the reactivity of chars subjected to different residence times at a temperature of 1000C°. They observed that reactivity of chars dropped after residence times of a few seconds, reached a minimum after 5 minutes and could not be reduced any further. This reduction was attributed to the ordering of the carbon lattice at higher temperatures resulting in the loss of active sites.

Heating rate during pyrolysis also has an important role on the reactivity of the produced char. Gale et al. [97] have reported a decrease in reactivity of char with increasing heating rate. The higher heating rates results in greater volatile yield from the particle, so the remaining particle has lower H/C ratio and consequently has lower reactivity.

Effect of temperature, residence time and heating time could be quite different depending on the fuels studied. Some coals have shown to undergo drastic changes during pyrolysis such as coals with strong coking properties, whereas other might not change much such as anthracite coals [98].

2.7.2 Effect of temperature on the reaction mode

At relatively low temperatures the diffusion rate of reactants, both to the surface and within the pores of particle, are much faster than chemical reaction rate. This is defined as chemical reaction rate controlled regime or “Regime I”. Under these conditions, the true reaction order and activation energies can be

measured. As the temperature rises, the reaction rate increases until the chemical reaction rate is limited by the diffusion of reactants through the pore structure of char particle. This is called “Regime II” where a combination of pore diffusion and chemical reaction rate is controlling the particle conversion rate. The diffusion in this regime is usually characterized by the mean of so-called ‘effective diffusivity’ which is a combination of bulk diffusion and Knudsen diffusion resulting from concentration gradient and frequent collisions of gas molecules with the walls of pore structure, respectively. The activation energy in this regime is roughly half of that in Regime I [77, 99, 100]. The measured rate exponent also departs from the corresponding intrinsic value. Under these conditions the measured rate exponent (n) is approximately related to the intrinsic one (m) as [77]:

$$n = \frac{m + 1}{2} \quad (2.5)$$

Further increase in the particle temperature results in an even faster reaction rates to the extent that the concentration of reactant gas literally approaches zero at the particle surface. This is known as “Regime III” or the regime which bulk diffusion to the surface of particle alone controls the rate of carbon consumption. Under these conditions, the observed activation energy becomes very small, and close to zero which means that temperature effect on reaction rate is trivial. The rate, however, is affected by gas composition and particle size and fluid flow properties. Particles in this regime are normally characterized by continues shrinking in size as reaction proceeds whilst density remains constant [77].

Figure 2.9 represents the theoretical dependence of specific reaction rate to temperature in combination with the relations between true (E_T) and measured (E_a) activation energies and also true reaction rate exponent (m) and measured one (n). It also demonstrates how the concentration profile of reactant gas changes from the bulk of gas to the centre of char particle with radius R .

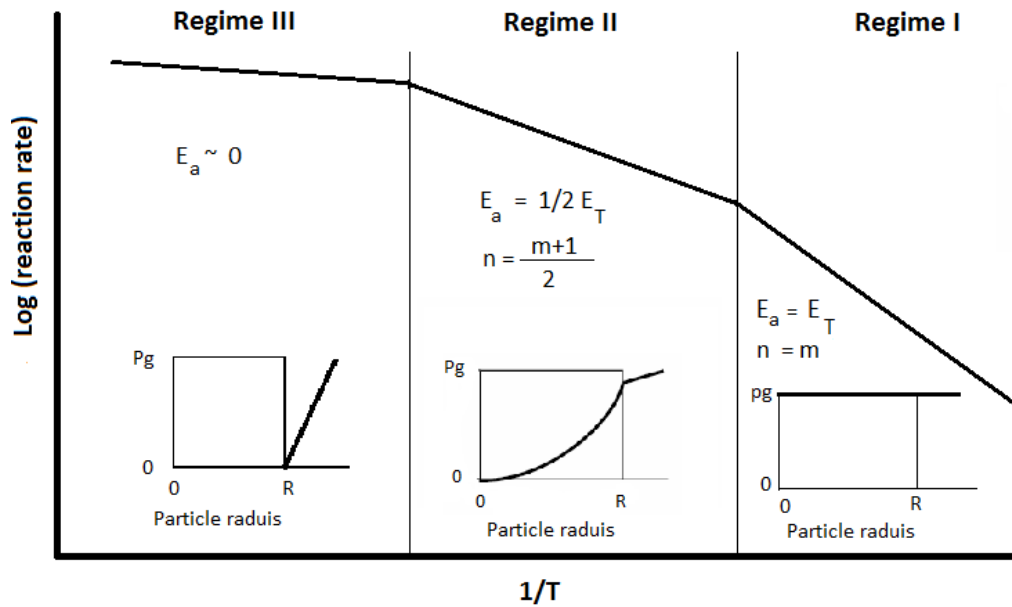


Figure 2.9 Typical plot representing the change of reaction rate with temperature [77]

The extent to which chemical reaction rates are affected by pore diffusion is usually expressed in term of effectiveness factor, η [100]. For Regime I the effectiveness factor is theoretically equal to unity which means that reactant gas concentration is uniform through the solid particle. For Regime II, however, the effectiveness factor drops below unity ($\eta < 1$) and this indicates that there is gradient of concentration inside the particle. And finally for Regime III, effectiveness factor is much smaller than unity ($\eta \ll 1$) and approaches to zero.

2.7.3 O₂ gasification rates

The oxygen gasification rate is much faster than steam and CO₂ gasification rate. The oxygen in gasifier is rapidly depleted through volatile combustion and some char combustion to supply heat for the rest of reaction and also to dry the feed. The rapid reaction of carbonaceous materials with oxygen makes the determination of reaction rates very difficult. Furthermore the oxidation reactions are highly exothermic, so measuring the particle temperature is very difficult in practice. The temperature gradients of 45K can be easily

calculated even within very fine particles (this will be discussed in a later chapter).

At high temperatures encountered in entrained flow gasifiers, the reaction is mainly limited by diffusion. Depending on how high is the temperature, either Regime II or Regime III are the prevailing modes [77, 100]. In Regime III, O₂-char reaction rates can be estimated from diffusion theory knowing the gas composition, temperature, pressure and size of particle [101]. However, chemical reaction rate data still are needed in order to determine that to what extent oxidation reaction is limited by mass transfer [102].

Numerous studies have been devoted to measure the intrinsic rate of O₂-char reaction of variety of fuels. Some typical values of activation energies extracted from literature are represented in Table 2.5. Typically the activation energy of oxidation reaction falls between 110-180 KJmol⁻¹.

Table 2.5 Typical activation energies of carbonaceous chars [81]

Carbon Type	E_a (kJ mol⁻¹)	Reference
Petroleum Coke	155	[103]
Bituminous Coal Char	142	[100]
Brown Coal Char	127	[103]
Various	130	[104]

Reviews of Johnson [44], Laurendeau [77] and Smith [99] can be referred in this respect for more comprehensive summary tables.

As far as the reaction order is concerned, after reviewing all the available data in literature, Laurendeau [77] suggested the following approximation for a wide range of carbons:

$$\begin{aligned}
 m &\approx 0 && \text{for } T < 900K \\
 m &\approx 0.5 && \text{for } 900 < T < 1500K \\
 m &\approx 1 && \text{for } T > 1500K
 \end{aligned}$$

His suggestion is reasonably well supported by the adsorption/desorption mechanism. However, further works [103, 105] have suggested that under

atmospheric pressures the reaction order is better characterized within the range of 0.5 to 0.7.

Majority of the reaction rate parameters have been determined using thermogravimetric analysis. However, the recent work of Feng and Bhatia [106] clearly shows that majority of previous studies are not reliable due to the effect of chemisorption and its dynamics. In this study they theoretically determined the criteria under which weight change profiles obtained from TGA can be used to derive intrinsic kinetics for CO₂ and O₂ gasification by examining the region in which the chemisorption dynamics can be assumed pseudo-steady. Figure 2.10 represents the theoretical region (hatched area) of temperature-O₂ partial pressure domain where thermogravimetric results can be used to obtain intrinsic rates. It is worth mentioning that the calculation of this theoretical region is solely based on physics of mass transfer, however, if one takes into account the physics of heat transfer (this will be dealt with later) the region is even more limited than the one shown in Figure 2.10 due mainly to extremely exothermic nature of combustion reaction which can result in temperature gradient of as big as 45K within the solid particle.

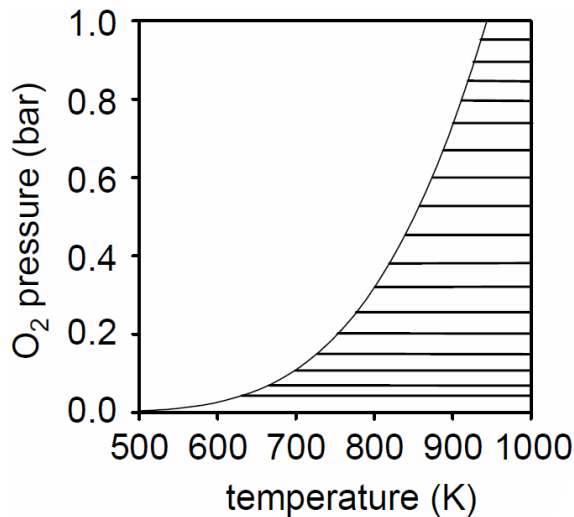


Figure 2.10 Region (hatched area) of valid steady state assumption for O₂-char reaction [106]

2.7.4 CO₂ gasification rates

As mentioned earlier the rate of CO₂-char reaction is several orders of magnitude lower than O₂-char reaction [103]. The slower reaction rate makes the determination of kinetic parameters more convenient than oxygen. Even at temperatures as high as 2000K, typical of dry fed entrained flow gasifier, the combination of pore diffusion and chemistry controls the carbon conversion rate. Table 2.6 represents the activation energies for variety of carbonaceous material for CO₂-char reaction. It can be seen that the typical range of activation energies for CO₂ are greater than those of oxygen.

Table 2.6 Typical activation energies of CO₂-char reaction [81]

Coal Type	Ea (KJ mol-1)	Reference
Various	399 ¹	[107]
subbituminous	286	[108]
bituminous	247	[109]
bituminous	239	[110]
petroleum coke	214	[103]
metallurgical coke	216	[103]
brown coal char	214	[103]
brown coal char	230	[103]
bituminous	229	[111]

¹Value at high temperature corrected for diffusion

However, reaction orders reported for CO₂ are similar to O₂ with the accepted values in the range of 0.5-0.7 [77, 103]. This could be expected from similar surface adsorption /desorption mechanisms for oxygen and carbon dioxide.

2.7.5 Steam gasification rates

The rate of char-steam reaction has been reported to be of similar order of magnitude of that of char-CO₂ reaction. The steam gasification rate is usually faster than CO₂-char rate (there are some cases that this statement does not hold

such as [111]) and the surface area created by steam is also higher than CO₂ [81]. Table 2.7 compares the reaction rate of chars from different sources for O₂, CO₂, and steam reactions. It is clear that oxygen rates are several orders of magnitude greater than CO₂ and H₂O. It is worth noting that steam gasification rates for the two petroleum coke is smaller than CO₂ rates whereas for coal and carbon it is par for the course.

Table 2.7 Relative rate of gasification with O₂, CO₂, and steam for variety of chars at 1073K and 0.2 atm [81]

Char Type	O₂	H₂O	CO₂	Reference
Petroleum Coke	9e+4	0.2	1	[103]
Petroleum Coke	5e+4	0.1	1	[81]
Brown coal	1e+4	2	1	[103]
Carbon	1e+5	3	1	[112]

The reported activation energies and reaction orders for steam-char reaction are similar to carbon dioxide reaction [81]. Some studies suggest that steam reaction competes for the same reactive sites as the CO₂ reaction [113, 114], however there are some studies that show steam and CO₂ does not compete for the same reactive sites [115, 116].

2.8 Numerical modeling of entrained flow gasifier

Over the years, a wide range of computational models have been developed for modeling gasification processes with different levels of complexity, such as zero order models using equilibrium calculations (e.g. using ASPEN PLUS) with no flow field characterization, 1D plug flow models, 2D flow/axisymmetric flow models, and the full featured 3D CFD models which can incorporate fluid dynamics, reactor geometry, thermodynamics, heat and mass

transfer and reaction modeling. Models based on equilibrium require a priori knowledge about the carbon conversion, which is a major disadvantage of this category. 1D plug flow models can predict carbon conversion but they suffer from the poor particle residence time estimation due to the absence of gas and particle dynamics and more importantly their interaction. The more realistic models for entrained flow gasifier where high levels of turbulence and/or swirl exist are two-dimensional CFD flow model where particle-gas flow dynamics and their interaction can be modeled with reasonable accuracy. Complex turbulence models and mixing can also be modeled incorporating the turbulent reaction models. Three-dimensional models are used where the level of flow geometry complexity cannot be simplified using a 2D model, or where there are a number of burners operating in a pattern that would be unsuitable for 2D modeling [117]. With the current level of sophistication in CFD codes almost all the features of gasifiers such as 3D gas flow, particulate trajectories and the interaction with continuous phase, particle characteristics, convective and radiative heat transfer, Maxwell-Stefan mass transfer problems, different reaction models and more can be modeled. CFD models as a tool for engineering assessments are being widely used and their acceptance for modeling industrial gasifiers is continuously increasing.

The computational fluid dynamics (CFD) modeling of entrained flow gasifiers dates back to early 1980's [116, 118]. Celik and Chattree [119] used a publicly available code PCGC-2 to model the gasification of a subbituminous coal in an entrained flow reactor and compared the results to experiment. The main finding was that particle residence time was substantially different from the gas residence time.

Govind and Shah [120] developed a 1D mathematical model to simulate the Texaco down flow entrained-bed gasifier using coal liquefaction residues and coal-water slurries as feedstocks. They described complex gasification reactions in the gasifier including devolatilization and heterogeneous reactions with the equilibrium assumption of gas phase reactions. Solid surface reactions were modeled using unreacted-core shrinking model. In this model effects of ash layer

diffusion, gas film, diffusion and chemical reaction are considered. However, no reaction is considered to occur within the pore structures. Using this model they were able to provide a better understanding of the reactor performance for different inlet feed conditions.

Vamvuka et al. [121] developed a one-dimensional steady state model for an entrained flow gasifier. The gas phase was assumed to be at equilibrium and heterogeneous reaction were calculated using extrinsic data collected from a TGA using external surface area of coal as the effective reactive surface. They found out that realistic conversions of carbon could not be obtained if the devolatilization and surface reactions between coal and O_2 and H_2O were assumed to proceed sequentially.

Fletcher et al. [122] developed a model to simulate the flow and reaction in an entrained flow biomass gasifier. The model was based on CFX commercial package. Biomass particulates were modeled using a Lagrangian approach. Transport equations were solved for the concentration of CH_4 , H_2 , CO , CO_2 , H_2O and O_2 and heterogeneous reactions between fixed carbon and O_2 , CO_2 , and H_2O were modeled. They also used a first order extrinsic rate model for simulating the surface reactions.

A three-dimensional simulation model for entrained flow gasifier was developed by Chen et al. [123]. The model implemented coal devolatilization, char- O_2 , char- CO_2 , and char- H_2O reactions sub-models. They performed a series of simulations for a 200 tpd two-stage air blown entrained flow gasifier designed for an IGCC plant with varying operation conditions. Their results showed that devolatilization and char oxidation were responsible for up to 80% of carbon conversion in gasifier. They also found that devolatilization model did not have a notable effect on carbon conversion whereas conversion was very sensitive to reaction rates of heterogeneous reactions. Their model also predicted that increasing the average size of particle reduces the carbon conversion which in turn results in an increase in the exit gas temperature and lower gasification efficiency. They also studied the effect of pressure on the system and found out

that increasing pressure increases the average particle residence time due to the lower gas velocity and this will result in an increase in carbon conversion.

Bockelie et al. [124] developed a CFD model for two gasifier configurations: single-stage down fired system and two-stage updraft system with multiple feed inlets. In this model, the basic combustion flow field was established using thermodynamics equilibrium. Gas properties were calculated from local mixing calculations and were allowed to fluctuate randomly according to a statistical probability density function (PDF) which is characteristic of the turbulent. The gas phase reactions were assumed to be governed by mixing rates rather than chemical kinetic rates. A local instantaneous equilibrium was assumed for gaseous reactions. The particle reaction processes included coal devolatilization, char oxidation, particle energy, particle liquid vaporization and gas-particle interchange. The model also includes a flowing slag sub-model.

Watanabe and Otaka [125] modeled CRIEPI (Central Research Institute of Electric Power Industry) 2 tpd research scale entrained flow coal gasifier. They investigated the effect of air ratio on gasification performance. The model results were in good agreement with experimental results. They used a typical RPM reaction rate model developed in a high temperature entrained flow gasification experiments [126]. Increasing air resulted in reduction of gasification efficiency.

Choi et al. [127] studied the parametric analysis of flow field in an entrained flow reactor with changing the gas injection angle, gas inlet diameter, gas inlet velocity, extending the burner length, and geometry of gasifier. Their result showed that regardless of the modifications mentioned above, the flow field in the gasifier was almost parabolically distributed and changing the burner parameters only influences the flow field at the inlet in proximity of burner.

Liu et al. [128] perhaps developed the most comprehensive gasification model for a pressurized entrained flow coal gasifier. They studied the effect of reaction kinetics and char structure in their model. They performed a sensitivity analysis to reaction kinetics and char structure and also compared the model predictions with published atmospheric and high pressure gasification data. They found out that gasification performance is very sensitive to reaction kinetics and

char structure with initial surface area being more influential than intrinsic reaction for bituminous coal. They also concluded that low pressure carbon conversion cannot be extrapolated to high pressure conditions. They also used different char structural development models and suggested that random pore model gives the best predictions. Overall, their model showed reasonable agreement with the published data. They also used the intrinsic rate models based on a high pressure thermogravimetric analysis in conjunction with pore structure model. This structural models convey a lot of assumptions and as it has been discussed earlier they might not be a reasonable substitute for intrinsic rates developed based on active surface area which is a better representative of the reality of the reactive surface. Furthermore, the reaction rates used in this model are not taking into account the effect of high heating rates and temperatures in char structural development.

There are several other studies available in the literature, but in terms of reaction kinetics and models used they are mostly similar [129-133].

2.9 Chapter overview and findings

The large inventories of oil sand coke and proximity to geological formation suitable for CO₂ storage in Alberta, Canada creates a unique situation for demonstration of world class IGCC complexes. Adoption of gasification as an alternative clean technology is inevitably linked to the full appreciation of gasification behavior of Canadian oil sand coke, coal, and their blends. Nonetheless, there are little fundamental studies and experiences with Canadian coke and its blend with coal available.

A brief review of literature makes it clear that there are little gasification experiences with Canadian oil sand coke and coal-coke blends available particularly at high temperature (>1000°C) which normally occurs in entrained flow gasifiers. Very less is known about the morphological and structural changes of blends in high heating rate, high temperature pyrolysis process. It is well

known that treatment condition in pyrolysis strongly affects the yield and the reactivity of the char, which consequently influences the solid-gas reaction rates. Pyrolysis has an important effect on particle swelling and agglomeration, char reactivity, char physical structure and surface area.

Almost all the gasification studies conducted so far, have taken into consideration the effects of few operating variables and within a limited range of conditions using classical “one-factor-at-a-time”. This methodology has been long known to be problematic in true characterization of the system under study due mainly to the fact that it cannot detect the effect of interaction between different factors or combined effects of experimental factors. Furthermore, classical methodology gives at best a qualitative representation of gasifier performance. This is a serious disadvantage of these types of studies in as much as the gasification operating conditions can hardly be optimized, and also the full potentiality of a feedstock for the optimum gain in the response variable of interest (e.g. electricity generation or H₂ production) will not be fully understood. Application of statistical experimental design methodology such, Response Surface Methodology, can further help to avoid these shortcomings.

The design and scale up of gasifiers suitable for oil sand coke and Albertan coals requires the accurate and reliable data on the intrinsic reaction rates of these fuels, which are currently missing from the literature. Almost all the data available in the literature are at best in the form of extrinsic rates or reported reactivities which cannot be effectually used for the purpose of reactor design and modeling. Even studies which have focused on similar feedstocks with the objective of finding the intrinsic reaction rates are mostly concerned with total surface area of char as a function of carbon conversion in order to normalize the specific reaction rates. The more appropriate method which is based on active surface area or reactive surface area has not been employed effectually in majority of the cases.

Computational fluid dynamics (CFD) has been extensively utilized as a powerful tool to simultaneously solve all the governing equations, pertaining to the physics of the chemical reactors, using a minimum set of assumptions. Despite

the profusion of works devoted to computational fluid dynamic simulation of gasification process, few have dealt with the modeling of entrained flow gasifiers with the majority of works focused on fluidized bed reactors. Also, of those studies dedicated to the modeling of entrained flow gasifiers, neither has focused on the use of intrinsic reaction rates nor has tried to model the gasification of fuel blends. Also, majority of the studies are lacking a proper solid fuel mass and energy conservation which needs to be addressed for the proper simulation of gasifiers.

CHAPTER 3

Co-Pyrolysis of fluid coke with biomass and coal¹

3.1 Experimental setup

The experimental atmospheric pressure entrained flow gasifier (AEFG) setup used for pyrolysis and gasification studies is shown in Figure 3.1. The setup consists of an electrically heated vertical core of Mullite tube (6.5 cm ID, 153 cm height). The furnace is equipped with molybdenum disilicide heating elements (Moly-D33) with a maximum working temperature of 1800°C. However, the maximum working temperature of setup is limited by Mullite tube (MV-30) to 1500°C. The temperature of the reactor is fixed along the tube length using three PID temperature controllers (Omron E5CK) in three different zones. The controllers are hooked up to a PC which can remotely communicate with the controllers using Lab View interface. A screw feeder (Schenck AccuRate volumetric feeder) with pulsating walls and a flight free auger with stirring rod

¹ This work has been published in Journal of Energy and Fuels, 24 (1), pp. 232-240.
Authors: Gao C., Vejahati F., Katalambula H., Gupta R.

and poly nozzle is used to feed the solid feedstock into the reaction tube through a custom designed feeder probe. The nominal capacity of the feeder ranges from 8 to 150 g/hr. Feeder is volumetrically calibrated for each sample; however, the real gravimetric rate is determined by weighing feeder both before and after experiments. For different samples under study, the actual solid loading rate was found to be within $\pm 1.5\%$ of the volumetrically calibrated values. A primary flow of N_2 is also used to entrain the particles into the reaction tube. It also helps to avoid particles from sticking to the inner surface of the feeder probe. In order to minimize the cooling effect of the gases entering from the top of the gasifier, all gases and vapors are preheated to $400^\circ C$ in a heater before entering the gasifier. The gases are further heated up before reacting with samples to temperatures close to the set point of furnace by passing through a column of porous honeycomb ceramics fitted to the top of the reaction tube. The flow of primary N_2 gas is also set to a minimum value (approximately $1/8$ of the total gas flow rate). Gas flow rates are adjusted using high precision mass flow controllers (AALBORG instruments). A custom designed steam generator in combination with a high precision water metering pump (Eldex, Opto series with a flow range of 0.002-80 ml/min, and reproducibility 0.3%) is used to supply the steam for the setup. Gasification products were collected through a water-cooled collection probe, shown in Figure 3.2 (ref. APPENDIX A for design details). To prevent condensation of gasification products on the inner shell of the collector probe, the probe is equipped with a sintered stainless steel inner shell through which gas (N_2) is passed. There are two gas inlet ports on the collector probe: the quench gas inlet, which quenches the products in the top section of the collector and Stops the reactions progress, and wall gas inlet, which prevents condensation and deposition of particles in the lower section of the probe. Following the collection probe, the cooled stream is passed through a cyclone where char and ash samples are separated from flue gas and collected. Then, the flue gas is passed through a bag filter to trap sub-micron particles and a condenser to take out the remaining water vapor. The pressure in the gasifier is fixed in proximity of ambient pressure via a vacuum pump and two regulating valves using feedback signals from a pressure

transducer mounted on top of the gasifier. The flue gases are analyzed in real time using an Agilent micro-GC (CP-4900) with integrated thermal conductivity detector. The micro-GC is equipped with two columns molecular sieve, Molsieve 5 Å, and PPU columns. Multiple calibration points were used and the measurements are reproducible in low ppm levels.

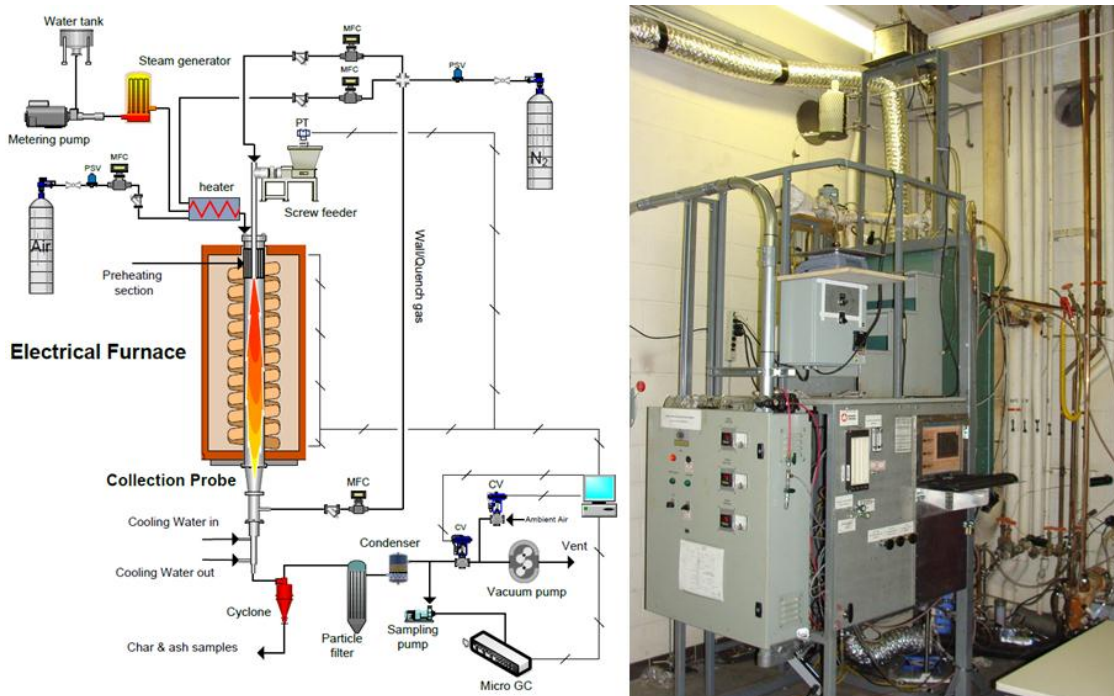


Figure 3.1 Schematic diagram of entrained flow gasification system



Figure 3.2 Collection probe (left) and furnace (right)

3.2 Pyrolysis results and discussions

Char samples were prepared using the experimental setup in N_2 atmosphere. The objective was to assess the effect of pyrolysis temperature and high heating rates, on the morphology and structural development of produced chars from individual fuels and their blends. Variations in morphology of different char samples were studied with the help of a Scanning Electron Microscope (SEM). Scanning electron microscopy was performed using a Hitachi S-2700 SEM (Hitachi High-Technologies, Toronto). The particles were carbon-coated prior to analysis. Particle size distribution was determined using a laser diffraction Mastersizer (Malvern Inc.). Also, surface area and pore structure was studied by Brunauer-Emmett-Teller (BET) and Density Functional Theory (DFT) analyses using both N_2 and CO_2 as adsorbate. CO_2 reactivity of produced chars was assessed using a thermogravimetric analyzer (TA STD Q600).

3.2.1 Fuels characterization

Three different raw materials, Genesee coal (Sherritt Co.), fluid coke (Syncrude coke), and woody biomass from a carpentry shop (sawdust), were used in this study. Fuels were pulverized, sieved and classified to a cut-size range of 53-75 micron using a ball mill (Retsch PM100) for both coal and fluid coke. The original size of sawdust was reduced to a range of 250-300 micron using a cutting mill. These are the particle size range normally used in practical cases. In order to avoid particle agglomeration and also to have a uniform solid feed rate using the screw feeder, samples were oven-dried for 2 hours at 105°C.

Table 3.1 shows the proximate, ultimate, ash composition and fusion temperature analyses of the feedstocks. Proximate analysis of fuels was determined according to ASTM D3172 for coal and coke and ASTM E870-82 for sawdust. The ultimate analyses tests were determined by a Vario MICRO cube elemental analyzer.

Table 3.2 shows the composition and fusion temperature analyses of ash for all three fuels. Ash composition was determined according to ASTM D4326 using X-ray fluorescence. Ash fusion temperature was determined according to ASTM D-720.

Table 3.1 Proximate and ultimate analyses of fuels

Sample	Proximate analysis (wt.%, AR)				Ultimate analysis (wt.% daf)				
	FC	VM	ash	M	C	H	N	S	O*
Genesee coal	50.26	29.89	15.4	4.45	78.98	4.33	1.33	0.67	14.69
Fluid coke	85.81	6.6	6.22	1.37	88.13	2.02	2.14	5.9	1.81
Sawdust	12.38	84.17	0.43	3.02	49.15	6.54	0.27	0.51	43.53

* by difference, FC: Fixed carbon, VM: volatile matter, M: moisture

Table 3.2 Major and minor composition and fusion temperature analyses of fuels ash

composition	Genesee coal	Fluid Coke	Sawdust
SiO ₂	57.36	42	38
Al ₂ O ₃	22.45	25.58	9.41
Fe ₂ O ₃	5.74	10.01	5.89
TiO ₂	0.44	7.2	0.91
P ₂ O ₅	0.09	0.3	3.05
CaO	6.28	2.1	24.22
MgO	1.41	1.15	6.26
SO ₃	3.15	4.1	-
Na ₂ O	2.19	0.92	4.51
K ₂ O	0.51	1.5	7.43
BaO	0.23	0.3	-
SrO	0.08	0.8	-
V ₂ O ₅	0.0065	2.5	-
NiO	0.0042	1.33	-
MnO	0.054	0.11	0.32
Cr ₂ O ₃	0.0073	0.1	-
Gross Heating Value (MJ/kg)	35.20	32.41	18.13
Ash Fusion Temperature (°C) (reducing condition)			
Initial	1200	1295	850
Softening	1211	1302	963
Hemispherical	1223	1335	1097
Fluid	1245	1401	1182

3.2.2 Char preparation

The pyrolysis of samples was conducted at four different temperatures 700°C, 1100°C, 1250°C, and 1400°C. Sawdust was blended with coal or fluid coke at three different blending ratios (33%, 50% and 67%).

The furnace was heated up under air flow over night. The maximum heating and cooling rate of furnace was limited to 100°C/hr due to the material characteristics of Mullite tube. After reaching the set point temperature, the air was replaced with a high purity N₂ (99.99%) and flow rate was set to 10 lit/min. The nitrogen concentration at the outlet of gasifier was analyzed with Micro-GC every 10 minutes till the concentration of nitrogen reached the purity level of gas cylinder. One hour purging with nitrogen was shown to be enough to purge the

oxygen out of the reaction tube. The feeder was separately calibrated for each sample. The solid feed rate and flow of N₂ was fixed for all the tests.

3.2.3 Surface area development

The surface area and pore volume of chars were determined from N₂ BET measurements conducted in Quantachrome Autosorb1 instrument. Samples were degassed at 350°C for 8 hours. The outgassing was tested by isolating the sample cell and monitoring the pressure rise due to outgassing over the course of 1 minute. Degassing was continued till sample pressure rise fell below 50 micron (μHg) per minute at degassing temperature. The micro-pore surface area of samples was also determined using N₂ adsorption isotherms at low relative pressures in the order of 10⁻⁵ using DFT technique (APPENDIX B). Figure 3.3 shows the effect of pyrolysis temperature on BET and micro-pore surface area of the produced chars measured using N₂.

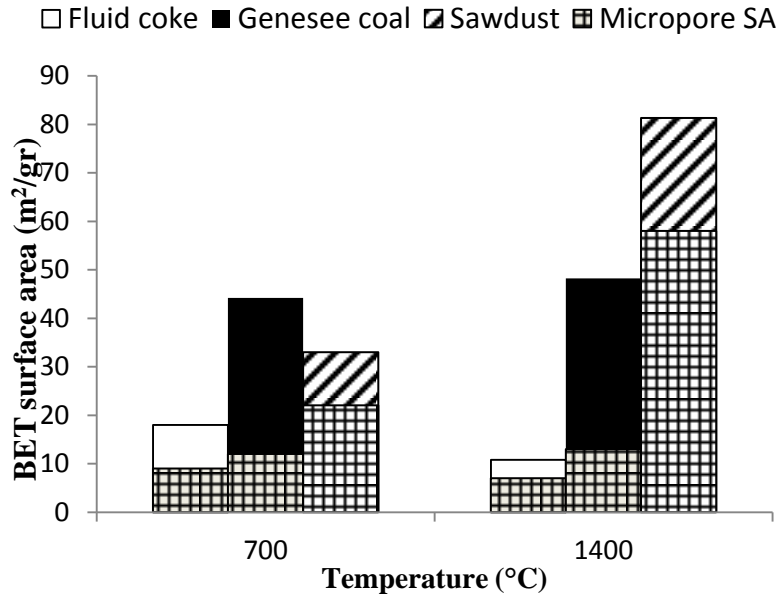


Figure 3.3 Pyrolysis temperature effect on the surface area for fuels

For coal and biomass it was observed that an increase in the pyrolysis temperature results in an increase in both mesoporous and microporous surface

area due to the removal of volatile matters. However, it is worth noting that for biomass materials majority of pores are distributed over higher range of microporosity (above 15 Å). This range of porosity can be easily measured using N₂ adsorption isotherms. So in case of biomass we will observe a substantial rise in both mesopore and micropore surface area. The higher volatile matter content of biomass also enhances the pore structure development in biomass. However, for coal with significant fractions of pores in low range of microporosity (less than 15 Å), N₂ adsorption isotherms is not able to correctly characterize the pore structure of fuels. So, the results do not show a significant difference in surface area. It is worth noting that due to the short residence time in AEFG (less than 7 sec), at low temperature (700°C) pyrolysis was not complete. Samples from 700°C further showed a release of volatile matter in TGA tests under N₂ atmosphere. This behavior was not observed for samples prepared at 1400°C. Considering that the difference in BET surface area of partly devolatilized coal (700°C) and fully devolatilized coal (1400°C) was not significant, once more demonstrates that BET and micropore surface area measurements using N₂ is not representative of the total surface area in coal. This fact was more obvious for the case of fluid coke which is a microporous material. Fluid coke has very low volatile matter content. So, no major structural development in pyrolysis is expected to occur. However, high temperature heat treatment (HHT) is known to further organize the crystallite structure of coke and increase the organized carbon content in coke [82]. This can further shift the mesoporosity in coke toward the microporosity which is not detectable with N₂ isotherms as already stated in section 2.2. These structural changes manifest themselves in reduction of both meso and micro pore surface area in Figure 3.3.

Table 3.3 represents the value of BET surface area and microporosity volume of fuels and their blends at two different temperatures. The surface area for 1:1 blending ratio of Genesee coal and fluid coke with sawdust prepared at 700°C was smaller than that of pure coal and coke chars prepared under same condition. This might be due to thermal cracking of volatile contents of fuel into gases and liquid phases at 700°C. The thermal cracking of high volatile content

sawdust results in release of gases and light to moderate molecular weight liquid phases at low temperatures. Due to the short residence times and low temperatures a portion of the liquid phases might condense on the surface or within pore structure of solid particles. When blended with coke, collection of these particles from the bottom of AEFG using collection probe brings the biomass and coke particles in close contact where they can agglomerate as the surface of particles is still cooling down. A portion of these liquid can penetrate into surface and pore structure of coke and partially block the pores. However, it is worth noting that when reporting the surface area, the weighed char mostly contains coke and coal with majority of biomass initial weight already evaporated. So the blend ratio of char is no longer 50/50 wt%. This is why the reported surface areas for blends are much closer to that of coke and coal values. At higher temperatures almost all the volatile matter content of fuels crack into gas phase so the surface area reported for blends is higher than that of pure coal and coke, considering the char yields of fuels. From the surface area analyses, it can be pointed out that, even though the surface area of both pure and biomass blended chars increase with increasing pyrolytic temperature, the increase in blended chars is much more pronounced when compared to that of the corresponding pure chars. This might be due to the strong physical or chemical agglomeration that occurs at high pyrolytic temperatures between biomass and other fuel.

Table 3.3 Pore structure development for fuels and their blends as a function of temperature

<i>Sample</i>	<i>BET surface area (m²/g)</i>		<i>Micropore cm³/g</i>	
	700°C	1400°C	700°C	1400°C
Sawdust (S)	33.0	81.3	0.00675	0.01461
Genesee coal (GC)	44.2	48.2	0.00452	0.00519
Fluid coke (FC)	18.0	10.8	0.00575	0.00311
GC-S (1-1 wt%)	12.8	64.0	0	0.02282
FC-S (1-1 wt%)	6.6	12.5	0	0.00382

3.2.4 Char Reactivity

Reactivity of different co-pyrolyzed samples was measured using CO₂ as gasifying agent at 800°C.

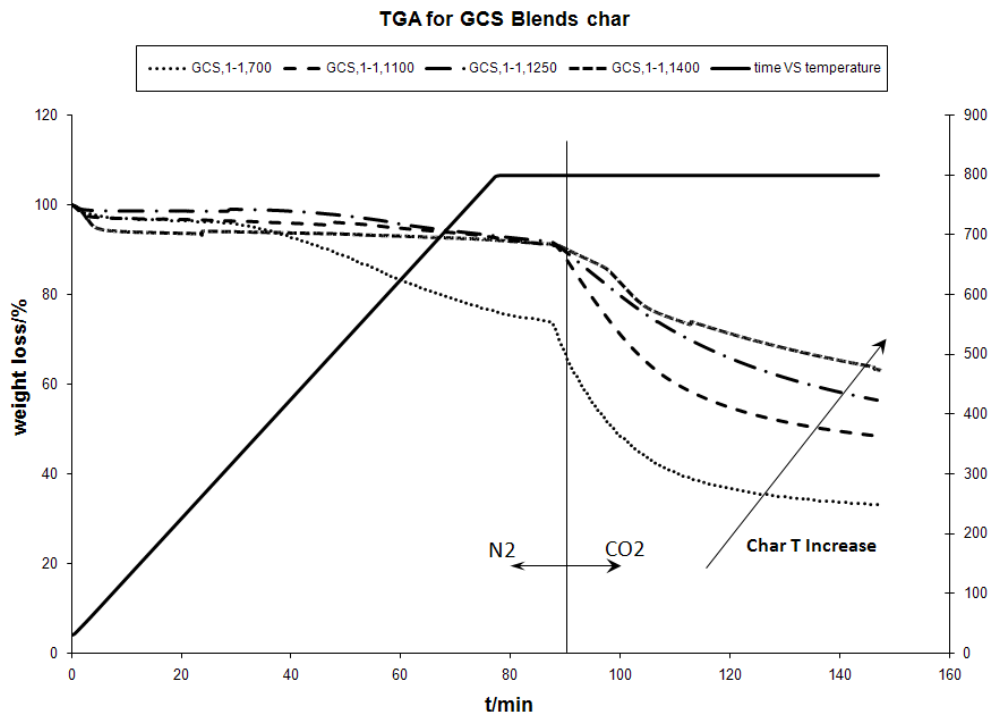


Figure 3.4 TGA results for Genesee coal and sawdust (GCS 1-1) blended char pyrolyzed at 700, 1100, 1250, and 1400°C.

Figure 3.4 shows the weight loss curves for the pyrolyzed Genesee coal and sawdust 1:1 blend ratio chars produced at four different temperatures. Char produced at 700°C are the most reactive, and reactivity drops with increasing the pyrolysis temperature. This can be explained by the fact that with increasing the temperature the volatiles yield increases, and hence, rendering the remaining chars less reactive. Higher temperatures and higher heating rates will also promote the annealing process of carbon which further results to the low reactivity chars through the reorganization of carbon crystallite structure [82, 134-136]. For the char produced at 700°C, the weight loss starts much earlier at a temperature of about 450°C in N₂ atmosphere. This is due to the fact that at 700°C devolatilization is not complete in AEFG so the rest of volatile content comes off upon heating in TGA.

Similar trend was observed for blend of fluid coke-sawdust (1:1 ratio) as shown in Figure 3.5. Again the char produced at 700°C had the most weight loss, indicating its high reactivity. The early weight loss for the 700°C char was again observed here, and an almost similar trend was observed for the char produced at 1100°C, although the onset of the weight loss was at a much higher temperature. The same explanation as the one given for the coal-sawdust blend above is valid in this case as well.

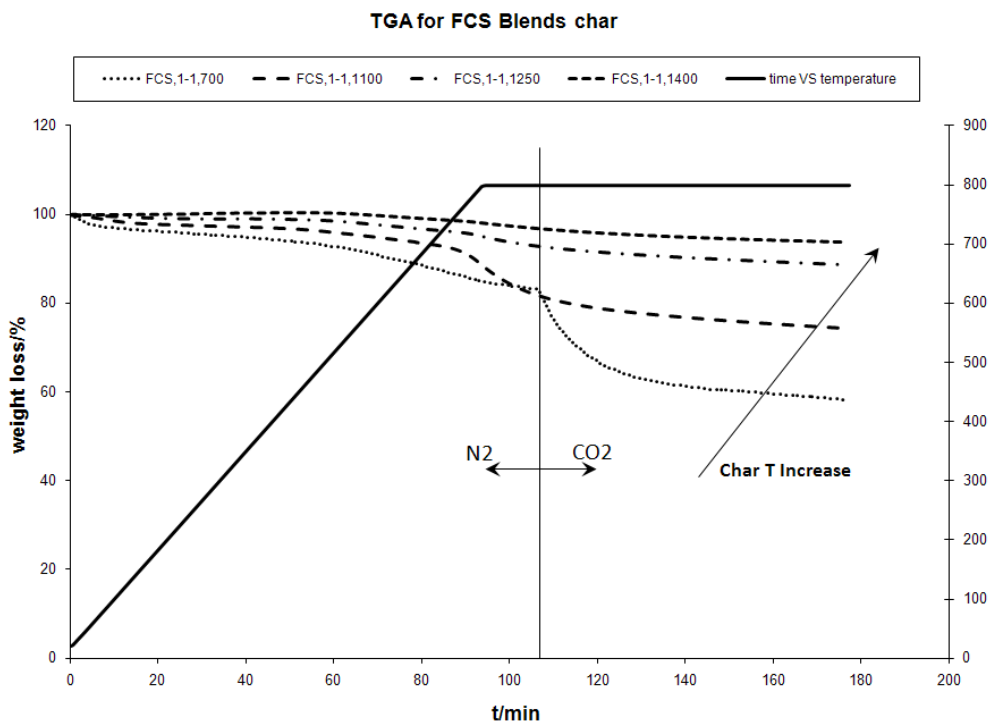


Figure 3.5 TGA results for fluid coke and sawdust (FCS 1-1) blended char pyrolyzed at 700, 1100, 1250 and 1400°C.

3.2.5 Morphological analysis of pyrolyzed chars

The morphological variation of the chars was examined using SEM. Figure 3.6 represents the SEM images of 50/50 blend ratio of sawdust and Genesee coal at four different temperatures.

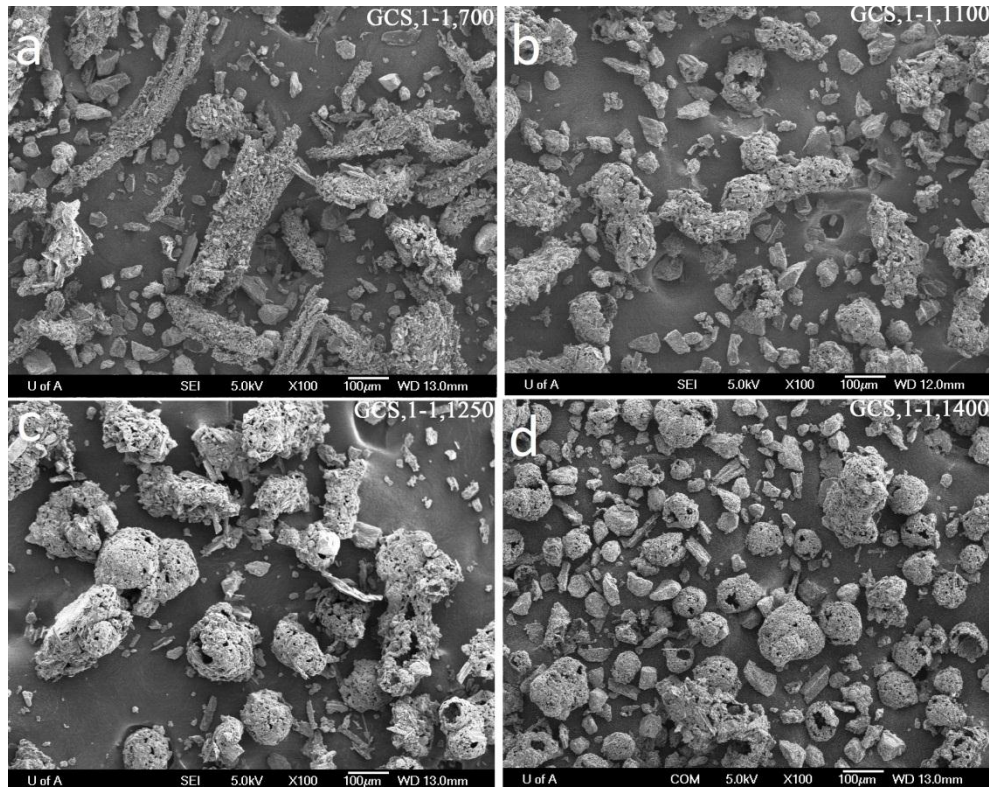


Figure 3.6 SEM images of 50/50 blend ratio of sawdust and Genesee coal at 4 different temperatures: (a) 700°C, (b) 1100°C, (c) 1250°C, and (d) 1400°C

As the temperature rises, a transition from needle-like to spherical particles are observed. The needle-like particles are mostly sawdust biomass materials which are composed of softwood materials. Due to the high volatile content of biomass the resultant chars are very porous compared to smaller particles which are mainly coals. This is in agreement with the observations of Cetin et al. [137].

Further increase in temperature resulted in accelerated agglomeration of coal to biomass, particularly at temperatures above 1250°C. The agglomeration is caused by low melting point silicate compounds in biomass. We believe that this mainly happens at the top of the collection probe where a close contact between particles is achieved on the conical surface while particles are still hot. Figure 3.7 clearly shows the entrapment of coal particles at the surface of biomass for temperatures exceeding 1250°C.

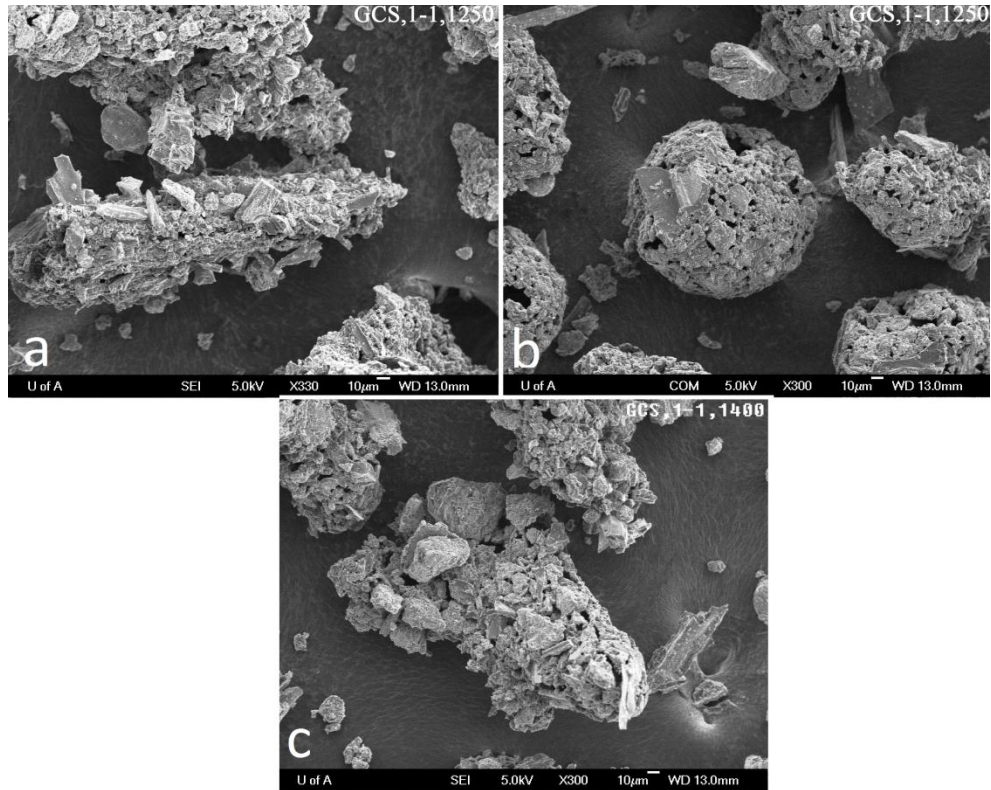


Figure 3.7 SEM images of 50/50 blend ratio of sawdust and Genesee coal representing particle agglomeration at two temperatures: (a)&(b):1250°C, (c)1400°C

As the temperature rises, the volatile yield of fuels also increases. The enhanced release of volatile yield could result in development of more porous particles at higher temperatures. This has been exhibited in Figure 3.8 for four different temperatures. The formation of hollow char particles is obvious in the figure.

Similar morphology changes were observed for the fluid coke-sawdust blend.

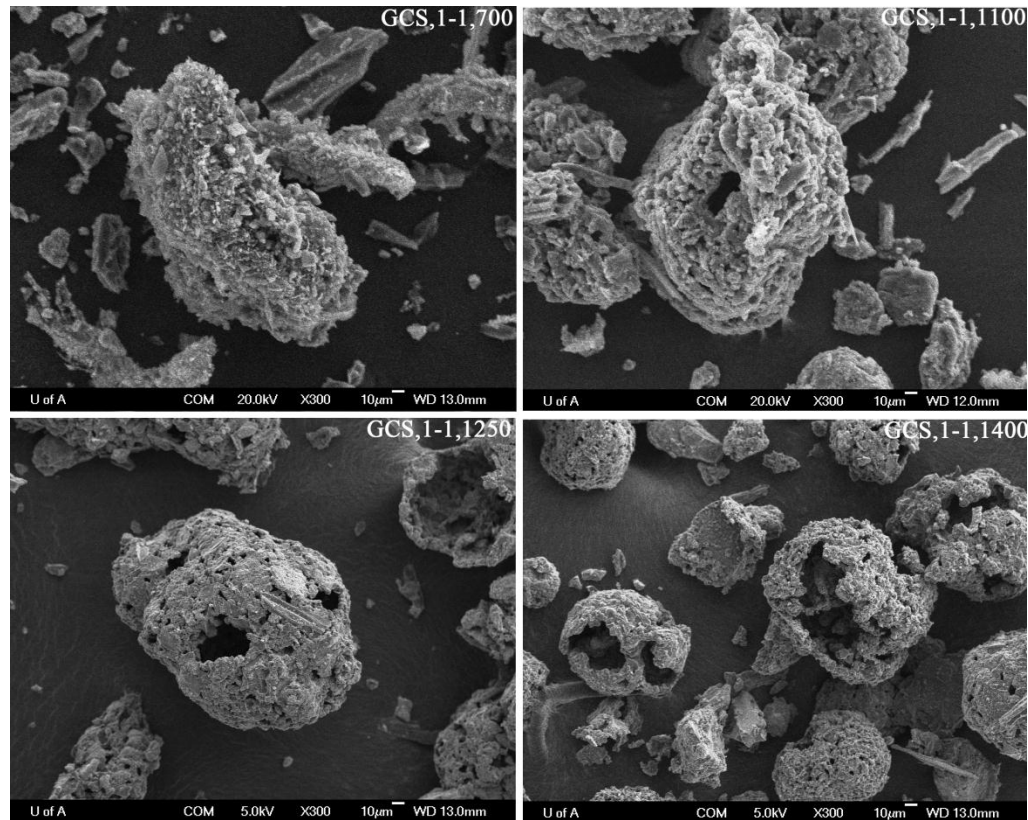


Figure 3.8 Effect of temperature on the porosity development of particles in a 50/50 blend of Genesee coal and sawdust

The SEM studies on pure fluid coke, however, showed a significant pore development in chars prepared at high temperatures compared to low temperatures. At 700°C coke char particles look like non-porous solid particles. As the temperature increases, a porous structure develops and at highest temperature studies in this work (i.e. 1400°C) frothy and or spongy shape particles also appear within the chars as shown in Figure 3.9.

For the blends of fluid coke and Genesee coal, as stated before, no significant particle agglomeration was observed compared to the sawdust blends. This is due mainly to the higher ash fusion temperatures indicated in Table 3.2.

Figure 3.10 shows the SEM image of 50/50 blend of coke and coal which further explains the insignificant particle agglomeration even at temperatures as high as 1400°C.

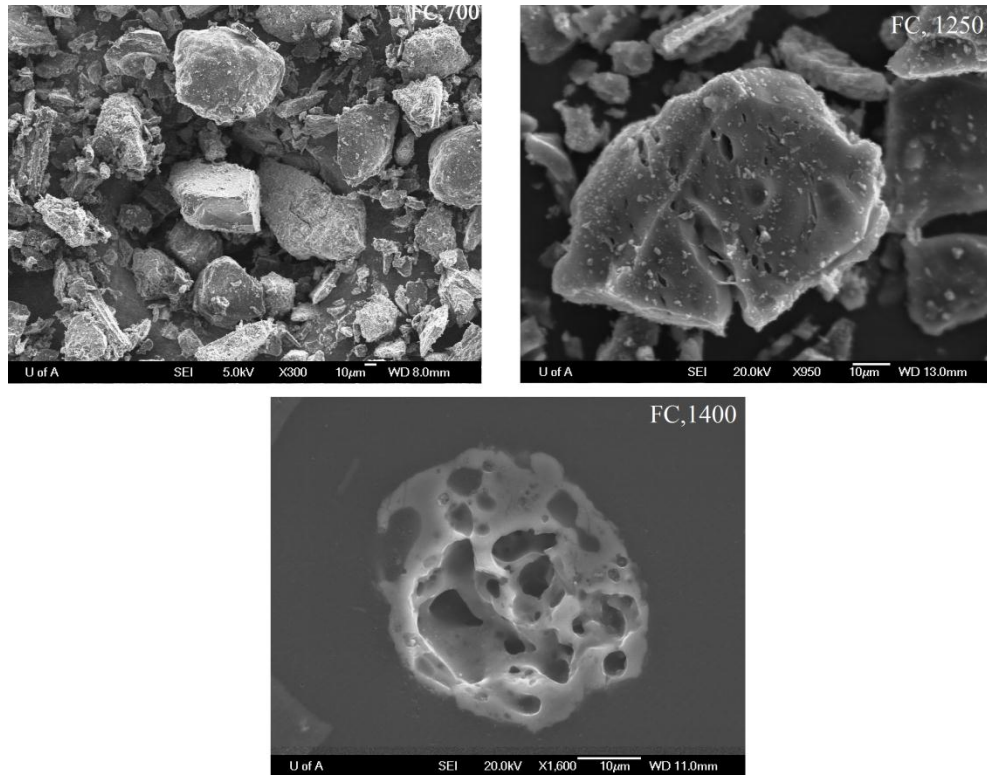


Figure 3.9 Pores development in fluid coke at 700°C, 1250°C and 1400°C.

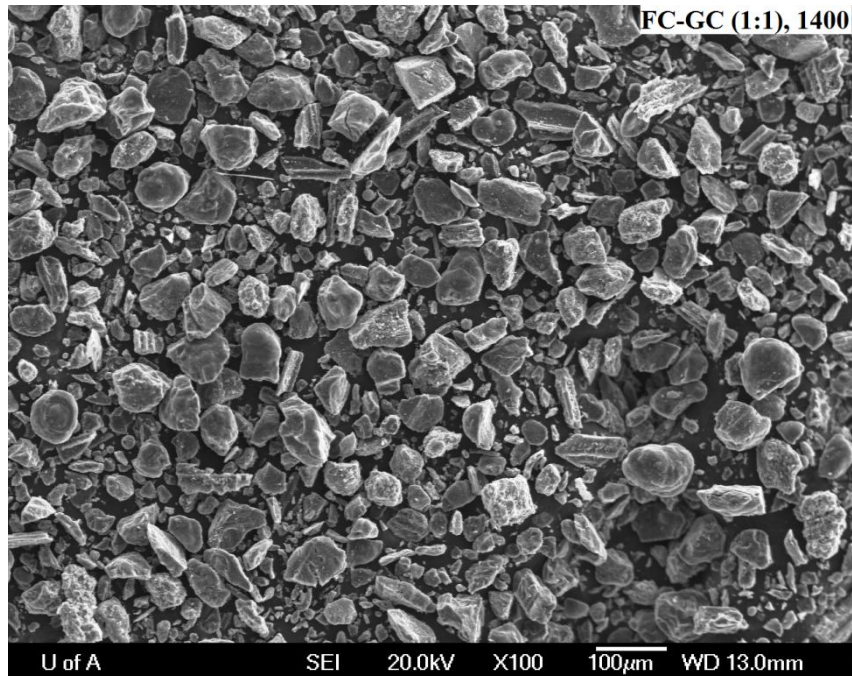


Figure 3.10 SEM image of fluid coke-Genesee coal 50/50 blend at 1400°C

3.2.6 Variations in particle size distribution

The effect of co-pyrolysis temperature on particle size and size distribution was investigated using a laser diffraction Mastersizer 2000 instrument. For this particular analysis, 50/50 blends of both coal and fluid coke were used.

Figure 3.11 shows the variation of particle size with char pyrolysis temperature for 50/50 blends of sawdust with both fluid coke and Genesee coal. The particle size variation is explained by using d_{10} and d_{90} which represent, respectively, the size where 10% and 90% of the particles are smaller of. The bars at 25°C belong to the pure sample before pyrolysis. The figure shows that d_{90} monotonically decreases with increasing temperature up to 1250°C. Any further increase above this temperature will result in the increase of d_{90} . In contrast to d_{90} , for d_{10} starts with very fine particles at 25°C, however, the d_{10} size increases with increasing temperature. The initial drop in d_{90} size as discussed earlier could be related to the morphology transformation of sawdust from needle-shape to spherical particles as the temperature increases. However, as the temperature is increased further, agglomeration between particles takes place which results in larger particles. The shrinking and agglomeration phenomena are consistent with SEM results discussed in the previous section and supports further reactivity results. On the other hand, the increase in d_{10} particle size reflects the decrease in the proportion of fines in the blend. One possibility is the early onset of agglomeration. And the other possibility which seems to be more justifiable is that some particles could likely be lost during pyrolysis and sample collection in cyclone and filter hence raising the size of d_{10} .

A closer look at Figure 3.11 shows particle sizes of over 450 μm while the particle sizes used in experiments were 53-75 μm , and 250-300 μm for coal/coke and biomass, respectively. This could be explained by the sieving method used for separation of solid particles in sample preparation stage. In sieve analysis, pin shaped particles could vertically sift through the sieves whereas in Mastersizer they can be detected with their longest dimension. The difference between the two

measuring techniques could be the reason for the discrepancy. The Mastersizer measurements however are purely for comparison purposes.

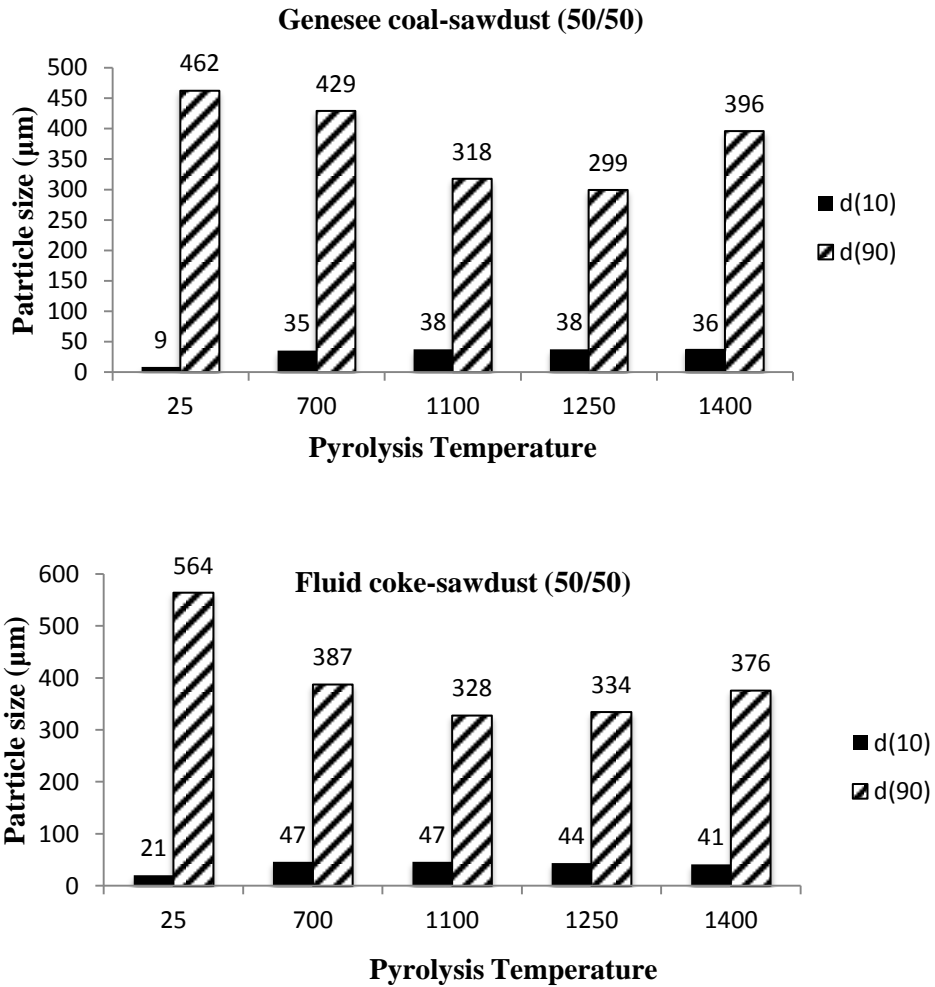


Figure 3.11 Effect of pyrolysis temperature on the particle size distribution

3.3 Chapter findings and Conclusions

The effect of blending woody biomass material with fluid coke and coal on the co-pyrolysis process was investigated in an atmospheric pressure entrained flow gasifier.

The morphological study using SEM showed a particle size decrease and shape change from needle to spherical shape as the pyrolysis temperature was increased which was mainly linked to the biomass material. Further investigation revealed that, as the pyrolysis temperature was increased beyond 1250°C, agglomeration seemed to start occurring. The reason for the agglomeration could be due to the low ash fusion temperature of biomass which is related to the melting of alkali silicates in biomass. The molten layer on the surface enables coal and coke particles to attach themselves to sawdust particles, leading to the particle agglomeration at higher temperatures. The shrinking and agglomeration phenomena were also verified by the particle size distribution analysis.

It was further observed that reactivity of pyrolyzed blended and pure fuels decreased with increasing the temperature. This is due to the reorganization of carbon crystallite structure in carbonaceous fuels.

A series of tests were conducted on blends of sub-bituminous coal and fluid coke. No agglomeration was found in SEM analysis even at highest temperature studied in this work.

From the surface area analyses, it can be pointed out that, even though the surface area of both pure and biomass blended chars increase with increasing pyrolytic temperature, the increase in blended chars is much more pronounced when compared to that of the corresponding pure chars. This might be due to the strong physical or chemical agglomeration that occurs at high pyrolytic temperatures between biomass and other fuel.

Despite the fact that fluid coke originally looked mostly as non-porous particles, pyrolysis at high temperatures showed a significant surface area development corroborated with scanning electron microscopy.

CHAPTER 4

Entrained flow gasification of fluid coke with coal²

4.1 Introduction

The importance and incentives of oil sand coke gasification in Alberta, Canada and the advantages of blending coke with coal was discussed with detail in chapter 1. Despite the studies conducted in gasification of all sorts of fuels and their blends, all the attempts to predict the gasification performance of a blend from the performance of its components has not been successful, especially for those fuels which are markedly different in their properties [21, 138]. Furthermore, all of the above studies have used a classical “one-factor-at-a-time” methodology to study the effect of operating variables and also blending ratio. The known shortcomings of this method in identifying the effect of experimental factors and their interactions can be resolved using a statistical design of experiment based on Response Surface Methodology (RSM) [139, 140].

² This work has been accepted for publication in Journal of Energy and Fuels (DOI: 10.1021/ef201277y).

Authors: Vejahati F., Katalambula H., Gupta R.

Response surface methodology (RSM) explores the relationship between several factors and one or more response variables using experimental design and multiple regression analysis. Having fewer experimental runs, detailed identification of experimental factors and their interactions, and ability to optimize the desired response variables within a range of operating variables of interest are the RSM's main advantages. RSM can be used for developing, improving, and optimizing the process or experiment with a comparatively large number of factors. RSM has been successfully employed in research to investigate complex processes [141-143]. The Recent work of Fermoso et al. [144] has also shown how this statistical technique can be successfully adopted to assess the effect of operating variables on high-pressure fixed bed coal gasification .

In this study co-gasification of oil sand fluid coke with sub-bituminous coal was performed in an atmospheric entrained flow gasifier using steam and oxygen as gasifying agents using RSM technique. The underlying objective of this work was to assess the combined effects of the operating variables (i.e. temperature, oxygen and steam concentrations) and coal/coke blending ratio on high-temperature entrained flow gasification process, where the focus was to quantify the relationships between the response variables and vital operating factors.

4.2 Raw Materials

In this work, the solid fuels, fluid coke and Genesee sub-bituminous coal were supplied by Syncrude Co. and Sherritt Co., respectively. The proximate and ultimate analyses of fuels were already presented in previous chapter in section 3.2.1. The bulk samples were crushed using a jaw crusher and then pulverized and sieved to a particle cut-size of 53-75 μm . Retsch planetary ball mills and ASTM (D4749–87) wet sieving procedure were used for this purpose. The samples were then dried in an Oven for 2 hours at 105°C before blending and feeding into the gasifier. The Blends were prepared by mixing required

proportions of samples in a plastic bottle with 1 kg capacity and vigorously shaking the bottle for 5 minutes. Adequate headspace above the sample was considered for proper mixing. The sample size was analyzed by laser diffraction Mastersizer as well. The d_{50} of blended samples was about 63 μ m.

4.3 Experimental procedure

The atmospheric entrained flow gasifier was introduced in section 3.1 of chapter 3. In order to compare the results obtained for different samples, a fixed 60 gr/hr nominal flow rate of carbon was maintained for all runs. Experiments were conducted over a temperature range of 1000°C -1400°C, using steam and oxygen to carbon weight ratios of (0.9-4.3) and (0-0.4), respectively, equivalent to a (15-50 vol. %) of steam and (0-3 vol. %) of oxygen in N₂ carrier gas. The volumetric flow rate of producer gas was estimated from a N₂ balance, since the amount of nitrogen in inlet and composition of N₂ at outlet are known. A fixed residence time of about 5 sec recommended Wen and Chaung [145] was used for the current study. The residence time in gasifier was estimated using CFD simulation (Ansys Fluent) in combination with a parametric study via “Design Explorer” in Ansys workbench to set the residence time to 5 sec by varying the total volumetric flow rate of gas. Analysis of flue gas with micro-GC showed that 15-20 minutes was enough to obtain a steady gas production.

The performance of the gasifier was determined by means of “gasification efficiency” defined as the ratio of the energy content of the syngas to that of the original fuel:

$$GE = \frac{(283[CO] + 888[CH_4] + 286[H_2]) \times Q}{F \cdot SE} \quad (4.1)$$

Where the gas concentrations in square brackets are on a molar basis (mol/m³) and the prefixes are their molar heats of combustion (MJ/mol), SE is the specific energy of the feed (MJ/kg), F is the feed rate of fuel (kg/hr), and Q is the normal volumetric flow rate of flue gas (m³/hr).

The carbon conversion was calculated using gas analysis method as:

$$X(\%) = \frac{(\dot{m}_{CO} + \dot{m}_{CO_2} + \dot{m}_{CH_4}) * 12}{\dot{m}_{c,feed}} \quad (4.2)$$

Where \dot{m}_j is the molar flow rate of gas species and $\dot{m}_{c,feed}$ is the mass flow of carbon in the feed. Other form of carbon leaving the gasifier (e.g. HCN, COS) were measured with Micro-GC and in all cases they were small enough to be considered not having any effect on the conversion calculations. Sulfur content of oil sand coke was mainly released in the form of H₂S.

Currently the setup has no mean of measuring the total flow rate of gas leaving the gasifier. As a result, the total flow rate was calculated by a mass balance on N₂ across the gasifier. The total molar nitrogen flow entering the gasifier was set equal to that leaving the reactor. To check whether N₂ leaves the reactor in other forms such as HCN, NH₃, NO₂ and NO, the Micro-GC was calibrated for these gases and all the compositions were found to be at low ppm levels which could be safely ignored compared to the concentration of N₂ in flue gas.

4.4 Methodology

Almost all the gasification studies available have used the classical “one-factor-at-a-time” method by singling out a limited number of experimental factors. There are two main issues with these types of studies. First, one cannot get a through sense of the process due to the limited number of factors chosen. Second, the classical design chosen does not allow the identification of the effect of experimental factors and their interactions on the system under study. Considering these inherent shortcomings of the classical method, a statistical design of experiment based on Response Surface Methodology (RSM) was utilized in this work which allows a full investigation of experimental factors and their interactions in a systematic way which is otherwise impossible using classical methodology.

4.4.1 Response surface Methodology (RSM)

In RSM use is being made of mathematical and statistical techniques in order to quantify the relationships between one or more measured response variables and vital factors with the objective being to find the desirable location in the design space. This can be thought of an area where a response is stable and optimized over a range of the factors. It might also include a set of criteria for several responses simultaneously [140]. The general form of response variable is represented as:

$$y = f(x_1, x_2, \dots) \pm \epsilon \quad (4.3)$$

Where y is response variable (dependent variable), f is the function (response surface), x_i are the factors (independent factors), and ϵ is the fit error.

The required data for fitting the response surface is generally collected from a series of design points generated by a proper experimental design technique. Amongst a number of design techniques available, RSM optimal design was adopted for this study. The design space was generated by the statistical software package Design-Expert 8.0.5. Coordinate exchange algorithm was used to select the actual design points. Using RSM optimal design, Design-Expert generates the minimum number of design points needed for the specified model. To obtain a better prediction across the entire design space, an IV-optimal design was employed which minimizes the integral of the prediction variance across the design space. More details about RSM have been provided in APPENDIX C. A second-order polynomial equation was used for the response surface. The general form of quadratic function is represented by:

$$y = \beta_0 + \sum \beta_i x_i + \sum \beta_{ii} x_i^2 + \sum \sum \beta_{ij} x_i x_j \pm \epsilon \quad (4.4)$$

The independent factors selected for this study and their ranges are as follows: temperature (1000-1400°C), oxygen concentration (0-3 vol. %), steam concentration (15-50 vol. %) and coke to coal blend ratio (0, 1/3, 1/2, 2/3, 1).

4.4.2 Response variables

Six response variables were chosen in this study were: H₂, CO, CO+H₂, H₂/CO, gasification efficiency (GE), and conversion (X). By far the most important response is hydrogen production, particularly for upgrading process in oil sands industry which needs a cheap and reliable source of hydrogen. Conversion always needs to be maximized in gasification process. CO can be shifted to CO₂ and H₂ using water-gas shift reaction. So both CO and syngas (CO+H₂) productions have to be considered. Additionally, electricity generation and chemicals synthesis are best analyzed using gasification efficiency and H₂/CO ratio as response variables, respectively.

The analysis of variance (ANOVA) calculations may often be made more easily or accurately by coding the observations. Once the factor values are coded all the coefficients in the model will have the same unit which makes the comparison of the effects of factors and their interactions more convenient. Coding is a simple transformation of factors from original domain to a new domain changing from [-1 1]. The transformation function is:

$$x_{\text{new}} = \frac{x_{\text{old}} - [\max(x_i) + \min(x_i)]/2}{[\max(x_i) - \min(x_i)]/2} \quad (4.5)$$

So for temperature changing from 1000°C to 1400°C, in new domain it changes from -1 to 1. So, 1200°C in original domain is equivalent to 0 in new domain.

Table 4.1 shows the design space generated by Deign-expert together with the experimental values of the response variables. Overall, 25 observations were considered for a total of 4 factors with a minimum of 5 levels for each factor. This systematically includes 5, 5, and 15 degree of freedom (DF) for lack-of-fit, pure error and model, respectively. Three additional center points were added to the design space to better resolve the possible curvature in response variables. Both decoded and coded (in parentheses) independent variables are indicated in the Table 4.1.

Table 4.1 Design space and experimental values of response variables for RSM created using IV-optimal design and coordinate exchange algorithm

factors	A:Temp	B: H ₂ O	C: O ₂	D:coke%	H ₂	CO	H ₂ /CO	GE	X
Run	[°C]	[vol. %]	[vol. %]	[wt. %]	mol/kg fuel, daf			%	
1	1000 (-1)	15 (-1)	3 (1)	0 (-1)	38.40	24.20	1.59	61.79	61.23
2	1400 (1)	18.5 (-0.8)	0 (-1)	100 (1)	30.40	12.40	2.45	37.09	24.90
3	1000 (-1)	50 (1)	0 (-1)	100 (1)	15.17	3.23	4.69	16.40	9.97
4	1400 (1)	15 (-1)	1.49 (-0.01)	0 (-1)	43.67	40.10	1.09	77.41	63.17
5	1200 (0)	31.28 (-0.07)	1.59 (0.06)	100 (1)	23.19	7.22	3.21	26.39	24.94
6	1400 (1)	50 (1)	0 (-1)	0 (-1)	63.10	39.02	1.62	95.01	73.03
7	1200 (0)	15 (-1)	2.1 (0.4)	50 (0)	28.73	21.25	1.35	45.29	41.74
8	1000 (-1)	15 (-1)	0.06 (-0.96)	100 (1)	11.00	4.51	2.44	14.07	8.94
9	1000 (-1)	15 (-1)	3 (1)	0 (-1)	37.79	23.38	1.62	60.65	58.98
10	1400 (1)	50 (1)	2.6 (0.73)	100 (1)	39.79	17.22	2.31	49.40	44.67
11	1400 (1)	15 (-1)	3 (1)	100 (1)	19.45	13.61	1.43	28.62	30.85
12	1400 (1)	50 (1)	0 (-1)	0 (-1)	63.74	39.19	1.63	95.21	73.73
13	1200 (0)	15 (-1)	0 (-1)	33 (-0.34)	42.73	28.61	1.49	65.93	47.91
14	1400 (1)	18.5 (-0.8)	0 (-1)	100 (1)	34.99	14.39	2.43	42.79	28.53
15	1300 (0.5)	50 (1)	0.86 (-0.43)	67 (0.34)	47.51	20.00	2.38	59.68	46.83
16	1400 (1)	15 (-1)	3 (1)	100 (1)	22.04	15.41	1.43	32.42	33.90
17	1000 (-1)	50 (1)	3 (1)	100 (1)	13.84	2.31	6.00	14.36	10.11
18	1100 (-0.5)	31.63 (-0.05)	0 (-1)	0 (-1)	50.80	19.20	2.65	69.37	51.40
19	1000 (-1)	15 (-1)	0.06 (-0.96)	100 (1)	10.66	3.13	3.41	12.56	8.55
20	1200 (0)	38.63 (0.35)	1.22 (-0.19)	0 (-1)	54.37	35.22	1.54	85.89	71.41
21	1200 (0)	38.45 (0.34)	0 (-1)	67 (0.34)	42.74	14.51	2.95	51.29	36.50
22	1000 (-1)	50 (1)	1.53 (0.02)	33 (-0.34)	45.77	12.81	3.57	56.06	48.10
23	1200 (0)	50 (1)	3 (1)	0 (-1)	55.56	33.35	1.67	85.44	76.13
24	1400 (1)	33.22 (0.04)	3 (1)	33 (-0.34)	42.70	26.31	1.62	62.30	56.99
25	1000 (-1)	27.95 (-0.26)	3 (1)	67 (0.34)	21.00	6.85	3.06	25.73	33.03
26	1200 (0)	32.5 (0)	1.5 (0)	50 (0)	37.10	18.62	1.99	52.79	46.90
27	1200 (0)	32.5 (0)	1.5 (0)	50 (0)	36.10	16.65	2.168	51.34	44.25
28	1200 (0)	32.5 (0)	1.5 (0)	50 (0)	38.10	20.59	1.85	54.23	49.55
Additional design points									
1	1011	41.24	2.25	100	15.20	2.50	6.08	12.89	15.02
2	1001	23.78	2.83	67	17.52	4.80	3.65	22.89	28.01
3	1293	17.84	2.35	50	30.10	26.25	1.16	52.42	49.01
4	1116	48.88	1.31	33	47.50	19.58	2.43	64.76	51.02
5	1389	47.45	2.51	0	61.00	36.66	1.65	90.18	80.10

4.4.3 ANOVA tests

Multiple linear regression analysis was used to fit the response variables to the experimental data. The goodness of fit was evaluated by analysis of variance. The ANOVA tests showed that all the proposed models are statistically significant. Table 4.2 shows the results of ANOVA test for the response variables. Terms that were not statistically significant (p -value>0.1) were eliminated from the model without any negative effects on the model fit unless the model hierarchy could have been violated. Overall, the lack-of-fit F-values were not significant relative to the pure error in all the fits. Signal to noise ratios were significantly greater than 4 which indicate that the proposed models can be used

to navigate the design space. Predicted R-squared values were in reasonable agreement with adjusted R-squared with all adjusted R-squared greater than 0.95.

Figure 4.1 represents the normal probability and residuals plots for H₂ response variable. The normal probability plot demonstrates that the underlying assumption of analysis of variance with respect to the normal distribution of residuals is satisfied. Additionally, the random scatter pattern of data in residual plot and confinement of values of internally studentized residuals (between -3 and 3) validates the assumption of constant variance. The Box-Cox plots were also used to find the correct power transformation. Except the H₂/CO response which needed an inverse square root transformation, the rest of the responses did not require any further transformation. Similar results and patterns were observed for the rest of the response variables.

Table 4.3 represents the estimated coefficients for the response models in terms of both decoded and coded operating variables

Table 4.2 Analysis of Variance (ANOVA)

Source	H ₂			CO			H ₂ /CO			GE			X		
	SE	df	P	SE	df	P	SE	df	P	SE	df	P	SE	df	P
Model	5934.98	7	1e-4	3320.3	7	1e-4	0.45	8	1e-4	15665.5	9	1e-4	10747.0	8	1e-4
A-Temp	733.25	1	1e-4	883.5	1	1e-4	0.14	1	1e-4	2109.7	1	1e-4	1027.7	1	1e-4
B-H ₂ O	729.5	1	1e-4	3.9	1	0.2372	0.11	1	1e-4	515.7	1	1e-4	220.3	1	1e-4
C-O ₂	239.25	1	1e-4				0.013	1	0.0015	198.9	1	1e-4	160.4	1	2e-4
D-Coke	3164.3	1	1e-4	2292.6	1	1e-4	0.14	1	1e-4	9576.1	1	1e-4	6878.2	1	1e-4
AB	20.47	1	0.049							29.1	1	0.039	80.9	1	0.004
AC							0.011	1	0.002						
AD	302.82	1	1e-4	23.89	1	0.006				181.9	1	1e-4	127.2	1	7e-4
BC	40.14	1	0.008				4.4e-3	1	0.043	42.8	1	0.014			
BD													24.8	1	0.089
A ²				54.31	1	2e-4	0.018	1	4e-4	70.1	1	0.002	70.7	1	0.007
B ²				38.05	1	1.1e-3	0.021	1	2e-4	37.0	1	0.021			
D ²				17.6	1	0.017									
Residual	93.9	20		52.5	20		0.018	19		105.9	18		146.8	19	
Lack of Fit	77.6	13	0.108	39.8	13	0.246	0.012	12	0.484	76.4	11	0.258	118.7	12	0.118
Pure Error	16.3	7		12.6	7		6.4e-3	7		29.4	7		28.08	7	
R2	0.98			0.98			0.96			0.99			0.99		
Adj-R2	0.98			0.98			0.95			0.99			0.98		
Pre-R2	0.96			0.97			0.92			0.98			0.96		

df: degree of freedom, P: P-value for F-test, SE: sum of square

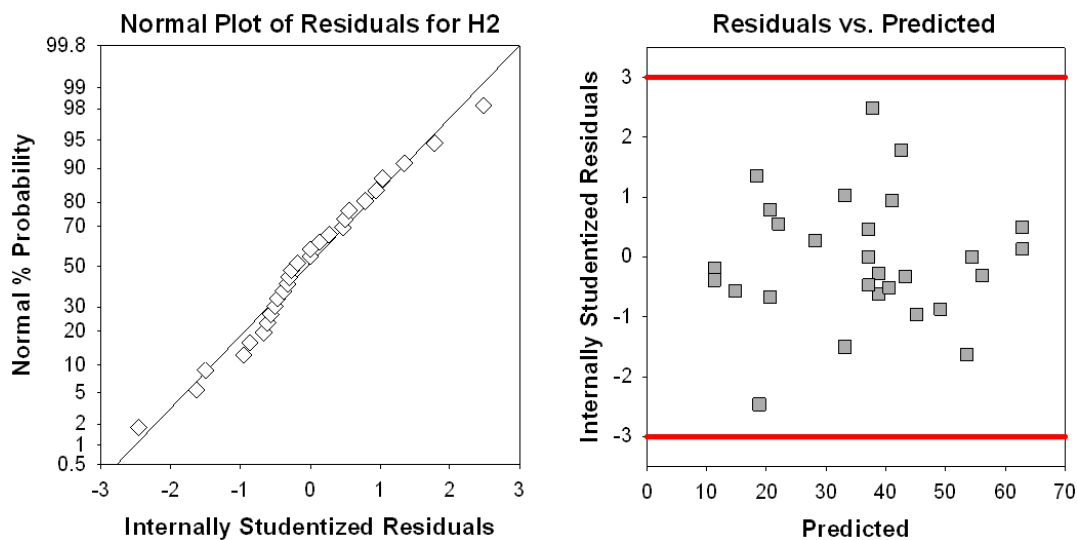


Figure 4.1 Normal probability and Residuals plot for H₂ response variable

Table 4.3 Matrix of coefficients estimated for the proposed response models as a function of decoded operating factors

Response	H ₂	CO	H ₂ +CO	$1/\sqrt{H_2/CO}$	GE	X
Intercept	50.84745	-137.443	36.98009	-1.53684	-84.25	-71.1545
A-Temp	-3.83E-03	0.26034	0.035747	4.11E-03	0.26165	0.20887
B-H ₂ O	-0.14325	-0.6906	-0.37483	-0.018108	-0.92663	-0.54656
C-O ₂	-4.7854	-	-5.54955	-0.072251	-4.70049	2.13038
D-Coke	-0.88058	-0.15061	-0.9294	-1.96E-03	-0.97697	-0.74683
AB	3.51E-04	-	4.79E-04	-	4.20E-04	7.00E-04
AC	-	-	-	9.54E-05	-	-
AD	4.95E-04	-1.34E-04	3.42E-04	-	3.87E-04	3.21E-04
BC	0.068706	-	0.095031	-7.44E-04	0.072824	-
BD	-	-	-	-	-	-1.65E-03
A ²	-	-9.11E-05	-	-1.59E-06	-9.99E-05	-8.66E-05
B ²	-	0.010195	-	2.28E-04	9.75E-03	-
D ²	-	8.37E-04	-	-	-	-
Models in terms of coded variables						
H ₂	37.1 + 6.46A + 6.66B - 3.83C - 14.35D + 1.23AB + 4.95AD + 1.8BC					
CO	18.62 + 7A - 0.49B - 11.37D - 1.34AD - 3.64A ² + 3.12B ² + 2.09D ²					
H ₂ + CO	56.74 + 13.68A + 5.99B - 3.69C - 25.94D + 1.68AB + 3.42AD + 2.49BC					
$1/\sqrt{H_2/CO}$	0.69 + 0.088A - 0.077B + 0.027C - 0.098D + 0.029AC - 0.02BC - 0.064A ² + 0.07B ²					
GE	53.4 + 11A + 5.62B - 3.5C - 25.61D + 1.47AB + 3.87AD + 1.91BC - 3.99A ² + 2.99B ²					
X	46.77 + 7.97A + 3.7B + 3.2C - 20.97D + 2.45AB + 3.21AD - 1.44BD - 3.46A ²					

A [=]°C, B, C [=] vol. %, D [=] wt. %

4.5 Results and discussions

In experimental design, graphical methods play an important role in data analysis and interpretation. In this work two common plot types were used. By using a simple transformation for all factors from original domain to new domain ranging from -1 to 1, one can plot effects of all factors on a response variable of interest in a single plot. This is called perturbation plot. Perturbation plots help to compare the effect of all factors in a single plot at a particular point in the design space. This makes the comparison of the factors much more effective than traditional “one-plot-per-factor”. A steep slope or curvature in a factor shows that the response is sensitive to that factor whereas a relatively flat line shows insensitivity to change in that factor. The second type of plots known as interaction graphs, allow identifying the existence of the interactions between experimental factors. The vital factors then can be used in plotting contour graphs.

4.5.1 Model validation

The proposed response variables were also validated using additional experimental points indicated in Table 4.1. These points were not part of the experimental design used to fit the models. In selecting the additional points, an attempt was made to cover the entire design space for robust evaluation of the response functions. Figure 4.2 shows the parity plot of predicted values versus experimental results for different response variables. Overall, a good correlation between actual and predicted values was found, in agreement with the results presented in Table 4.2. Figure 4.2 also revealed a close fit of additional experimental points to the predicted ones. The results confirm the appropriateness of the response functions to navigate the design space. This fact was already pointed out in section 4.4.3, by the mean of large values of signal to noise ratios. So, it can be concluded that the response functions adequately resolve the influence of operating variables and blending ratio on the dependent variables used in this work.

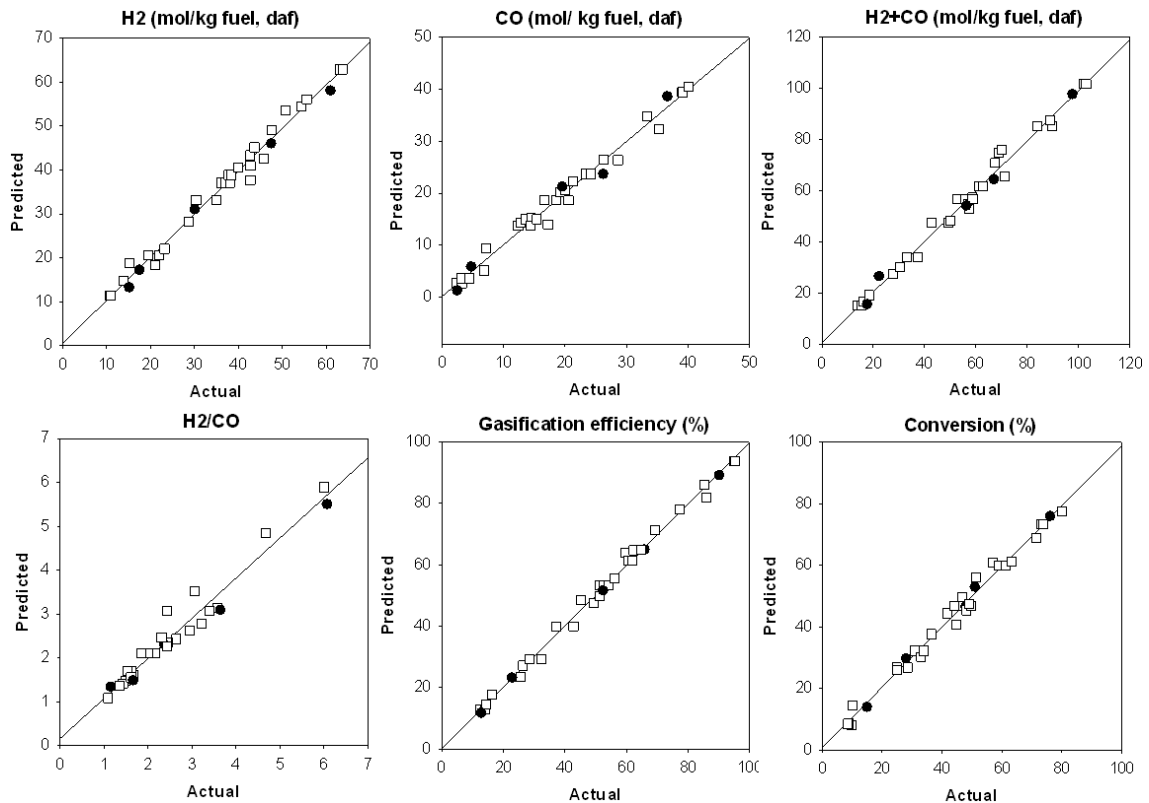


Figure 4.2 Predicated response values versus experimental values. (□) experimental design points used for fitting the models (●) Additional experimental points

4.5.2 H₂ production analysis

Figure 4.3 shows the effect of blending ratio of oil sand coke with coal on hydrogen production at the midpoints of the operating variables. The linear behavior demonstrates that there is no synergy between coke and coal on production of hydrogen under atmospheric pressures and high temperatures. However, these results differ from the findings at high pressure gasification reported by other authors [21] where the authors found a positive deviation from linear additive rule in co-gasification of fuels. However, the statistical significance of the reported data has not been discussed thoroughly. The slight deviations from linear additive behavior could be within the range of experimental errors. A through error propagation analysis is required for drawing such conclusions. The low solid volume fraction and short residence times

normally encountered in entrained flow gasifiers makes the interaction of coke particle with catalytic active sites of coal less probable. The catalytic effect was not even notable in high contact regimes of fixed and fluidized bed gasifiers using a direct blending of coke and coal [48]. Hernandez et al. [63] have also pointed out that as temperature rises the observed synergies will increasingly drop. It is worth mentioning that the highest temperature they studied was about 1100°C compared to 1400°C of this study. Synergies might only have happened due to the effect of pressure (the missing factor in this work), however, the mechanism is not known to the author.

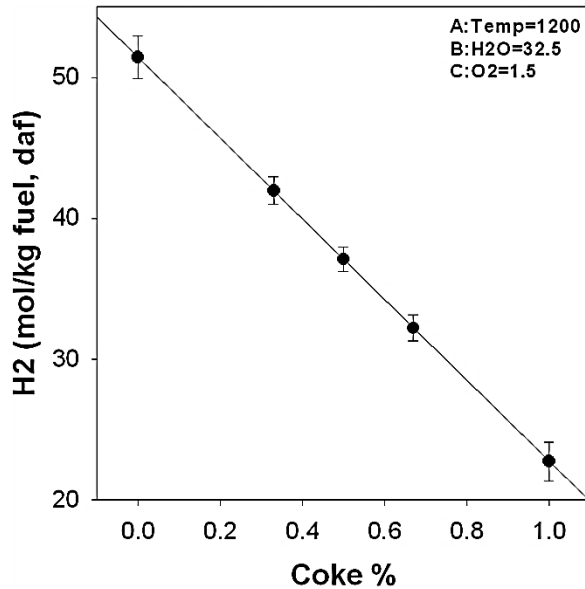


Figure 4.3 Effect of blending ratio on H₂ production

Figure 4.4 shows the perturbation plot for H₂ response variables at three different levels of coke ratio. The plots reveal that H₂ production depends on all four individual independent variables. Higher temperatures and steam concentrations result in an increase in hydrogen production whereas increasing coke ratio and oxygen decrease the H₂ concentration in flue gas. Effect of temperature and steam could be explained by the endothermic nature of steam gasification reaction ($C + H_2O \rightarrow H_2 + CO$) which is considered the main source of H₂ production in gasification process. On the other hand, oxygen depletes the

carbon sites necessary for steam gasification reaction. Figure 4.4 also reveals that the effectiveness of operating variables changes with the level of coke ratio.

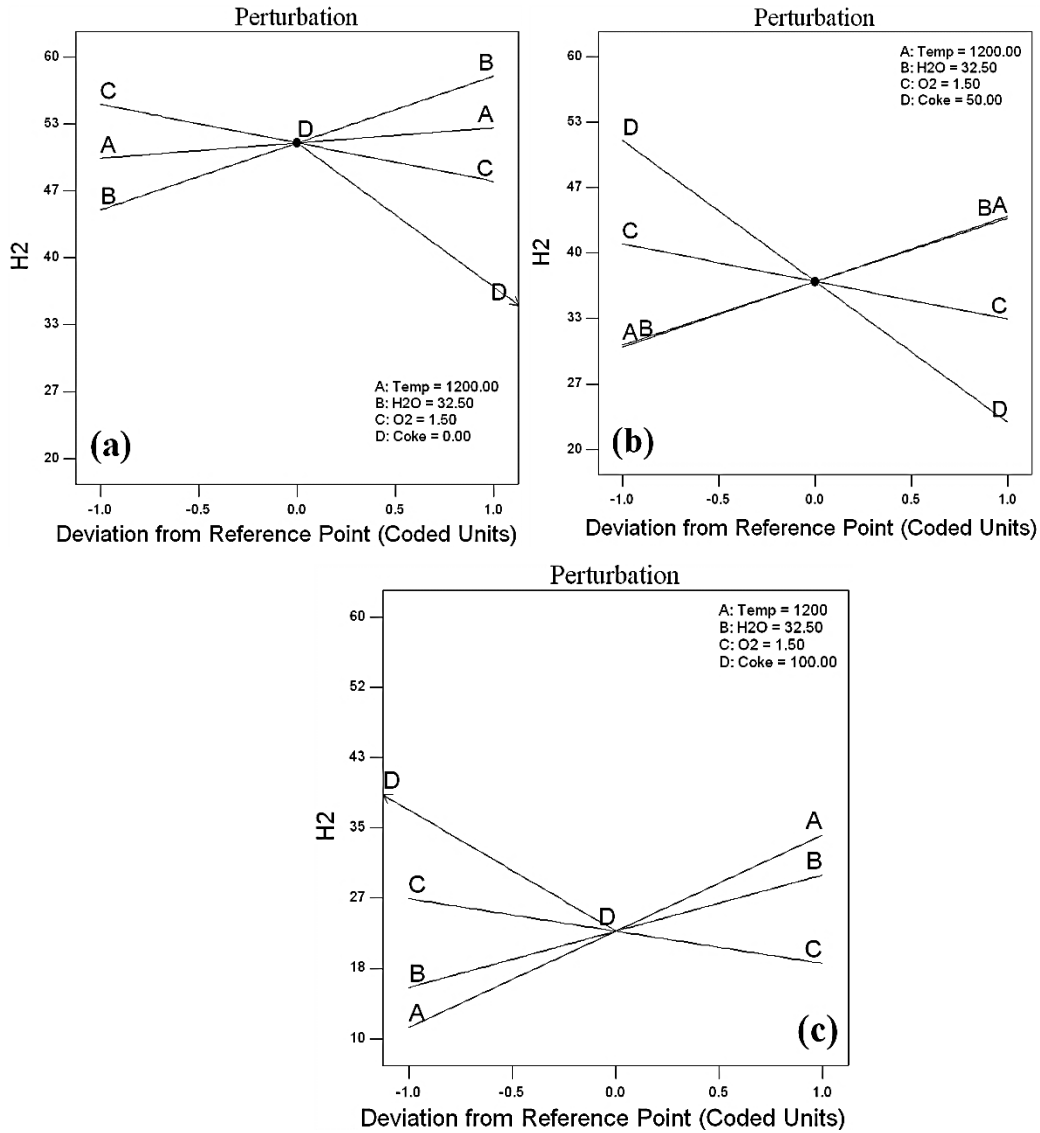


Figure 4.4 Perturbation plot representing the effects of experimental factors on H_2 production: (a) Genesee coal, (b) 50-50 wt. % blend of coal and coke, (c) pure coke

Figure 4.4(a) displays the perturbation plot of H_2 at the midpoint of all the operating variables ($T=1200^\circ\text{C}$, $H_2O=32.5$ vol. %, $O_2=1.5$ vol. %) for pure Genesee coal (coke%=0). In this case, steam and oxygen concentrations are more effective than temperature. H_2 production is almost insensitive to temperature in this case. At 50% coke ratio, temperature effect becomes almost as important as

the other two factors (Figure 4.4(b)). Finally, for the case of pure coke, temperature becomes the most effective factor (Figure 4.4(c)). This could be explained by the difference in reactivity of coal and coke which is manifested in higher activation energy of coke compared to coal. The higher the activation energy of an endothermic reaction is, the more sensitive it becomes to the temperature. Another important fact is the constant slope of oxygen profile for all levels of coke%. This shows that unlike the steam gasification reaction, the oxygen reaction is almost equally fast within the range of operating conditions in this study. So the effect of raising temperature is more pronounced in steam gasification rate rather than reaction with oxygen at temperatures higher than 1000°C. Overall, it can be observed that hydrogen production for a specific coke ratio is favored by an increase in temperature and steam concentration and a decrease in oxygen concentration.

In addition to the effect of individual factors, Table 4.3 shows that H₂ production also depends on the interaction between temperature-steam, temperature-coke ratio, and steam-oxygen. These interactions have been illustrated in Figure 4.5. Mutual interaction plots have been plotted by fixing the other variables at the midpoint values. The non-parallel segregated lines in the plots show that interactions are present. From the steam-oxygen interaction plot (Figure 4.5(c)) it is obvious that at higher concentrations of oxygen, the H₂ production is more sensitive to steam concentration. This could be explained by the fact that higher oxygen results in an elevated concentration of CO₂ which in turn could shift the water gas shift reaction ($\text{CO} + \text{H}_2\text{O} = \text{CO}_2 + \text{H}_2$) backward toward more CO production and a decrease in H₂ content of flue gas. So, higher amounts of steam are required to sustain the same amount of hydrogen. The produced CO₂ can further react with carbon ($\text{C} + \text{CO}_2 = 2\text{CO}$) to produce more CO which is in favor of hydrogen production. However, this reaction is much slower than steam gasification reaction. Figure 4.5(b) also shows the insensitivity of pure coal to temperature compared to coke as stated before using perturbation plots.

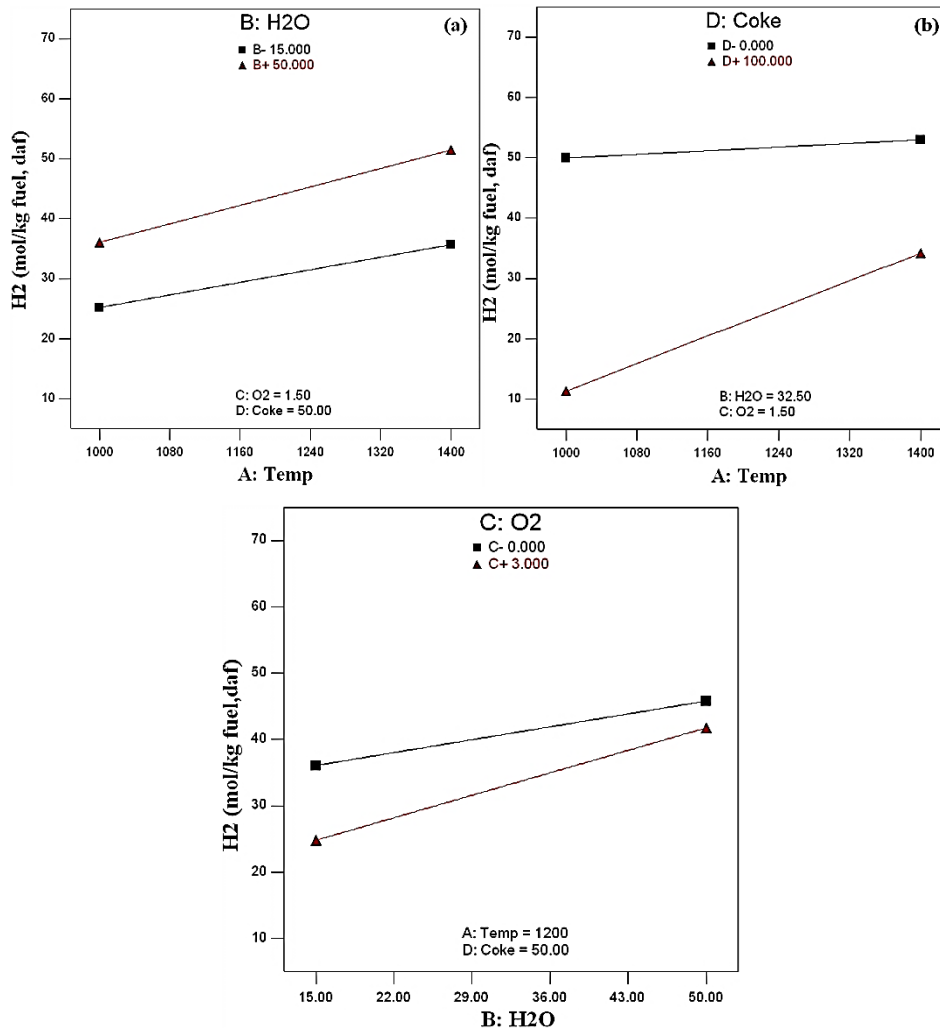


Figure 4.5 Interaction plots for hydrogen response variable: (a) steam-temperature interaction, (b) coke ratio-temperature interaction, (c) oxygen-steam interaction

Figure 4.6 represents the contour plot representing the combined effects of coke ratio and temperature on hydrogen production under 50 vol. % steam and oxygen free condition. The operating condition was chosen based on the effect of individual factors discussed earlier to obtain the maximum amount of hydrogen in flue gas. The curvatures of isolines reveal the effect of interaction between coke ratio and steam concentration. The plot shows that when gasification is carried out at higher coke ratio, a higher temperature is required to obtain the same amount of hydrogen production. However, the maximum hydrogen production attainable drops with increasing the coke ratio in the fuel.

Overall, the operating factors for H₂ production model can be sorted out in order of decreasing effectiveness as: coke ratio>steam>temperature > oxygen.

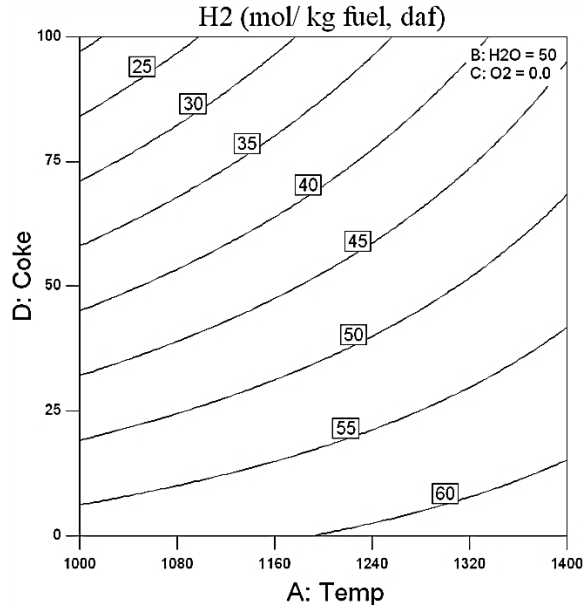


Figure 4.6 Contour plot representing the combined effect of Coke ratio and temperature on H₂ Production

4.5.3 CO production analysis

Similar to the case of hydrogen a linear additive behavior was observed for CO production which indicates the lack of any synergy between coal and coke in co-gasification process. This finding is in line with findings of other authors [63]. Figure 4.7 shows the perturbation plot for production of carbon monoxide. The plot reveals that CO production depends on Steam concentration, temperature, and coke ratio. The horizontal flat profile of oxygen indicates that CO production is not affected by oxygen concentration. This finding contradicts the results obtained by Fermoso et al. [144] at high pressures where they found that an increase in oxygen concentration reduces the CO production. They also reported that the reduction was much more noticeable at higher temperatures.

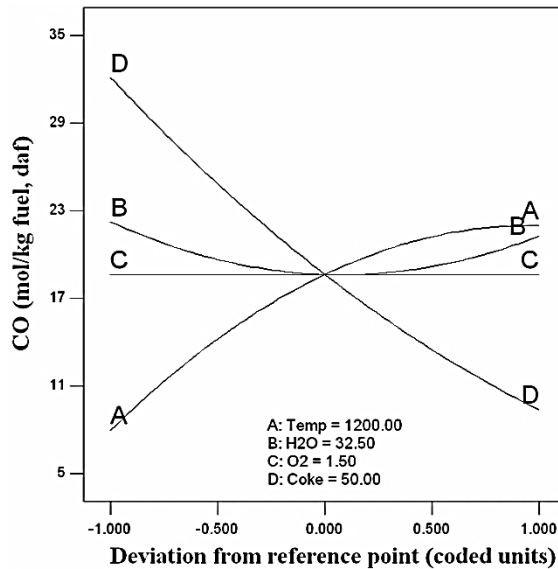


Figure 4.7 Perturbation plot representing the effects of experimental factors on CO production

However, the maximum temperature that was investigated in their work was 1000°C. At higher range of temperatures studied in the current work, increasing temperature increased the CO production but the production rate reached a plateau at higher temperatures. This trend has already been reported by other authors using thermodynamic equilibrium calculation [5]. The effect of steam concentration is however different. At lower concentrations, steam has a reducing effect on CO production, however as the concentration of steam is raised it creates a curvature in the response function (the squared term in Table 4.3) and creates a ridge system which passes through a minimum. Increasing steam favors the secondary steam gasification reaction ($C + 2H_2O \rightarrow CO_2 + 2H_2$) to the detriment of primary steam gasification reaction ($C + H_2O \rightarrow CO + H_2$). This initially results in an increase in CO_2 production and a reduction in CO production. However, the equilibrium constant of water gas shift reaction ($CO + H_2O = CO_2 + H_2$) becomes increasingly smaller at higher temperatures; in other words, the backward reaction rate grows faster than forward rate which in turn changes the distribution of gaseous product in favor of CO production. The higher concentrations of CO_2 and H_2 also shift the reaction further backward. However it is worth noting that, the variation of CO concentration in flue gas is a

weak function of steam concentration and in the order of the standard deviation associated with the prediction of an individual observation (SE Pred~1.94). Strictly speaking, at high temperatures and atmospheric pressures steam concentration has little effect on CO production rate. By far the most effective factor on CO production is coke ratio. An increase in coke ratio significantly drops the CO production. The response model shown in Table 4.3 also reveals an interaction between temperature and coke ratio. The higher the coke ratio the less sensitive CO production becomes to the variations of temperature. This fact has been illustrated in Figure 4.8. However, the interaction is considered to be weak. Overall, the operating factors for CO production model can be sorted out in order of decreasing effectiveness as: coke ratio > temperature > steam and with oxygen having a negligible effect.

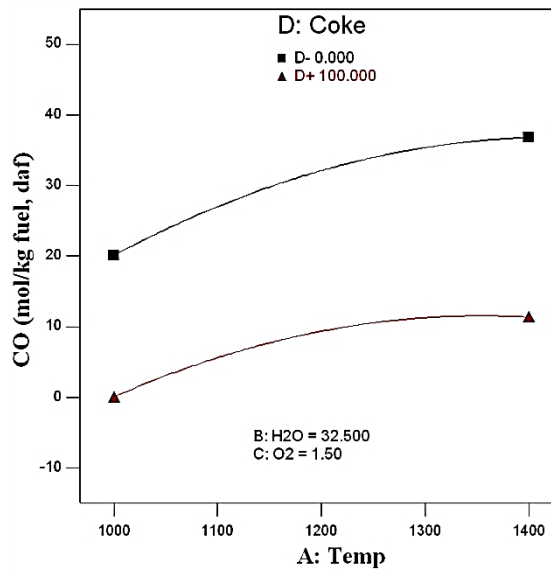


Figure 4.8 Interaction plot for carbon monoxide production (mol/kg fuel, daf)

Figure 4.9 shows the contour plot representing the combined effect of coke ratio and temperature on CO production at 15.0 and 1.5 vol. % of steam and oxygen concentrations respectively. The operating condition was chosen based on the effect of individual factors discussed earlier to obtain the maximum amount of carbon monoxide in flue gas. The curvature of isolines indicates the interaction

between the operating factors. As it can be seen in contour plot, isolines level off at high temperatures with low to medium range of the coke and any further increase in temperature will not change the CO production.

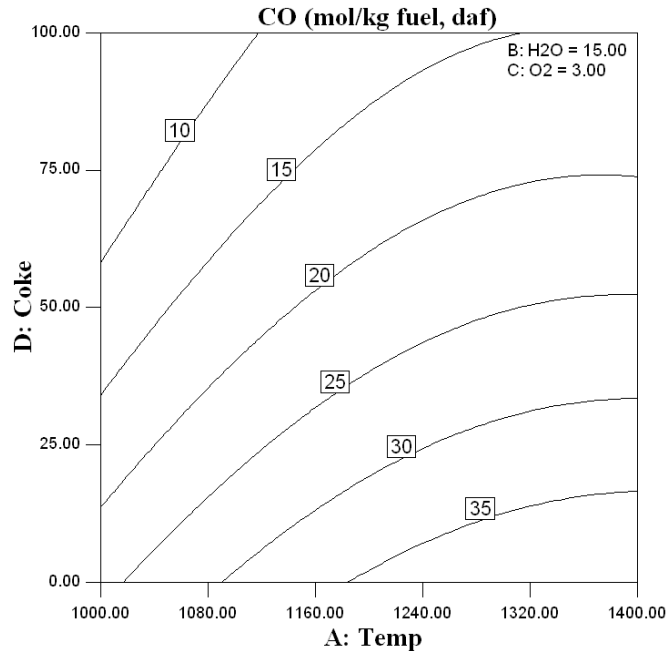


Figure 4.9 Contour plots representing the combined effect of Coke ratio and temperature on CO production

4.5.4 Syngas (CO+H₂) production analysis

Figure 4.10 shows the perturbation plot representing the effects of experimental factors on production of syngas. Syngas production is favored by an increase in temperature and steam concentration, a decrease in oxygen concentration and lower coke ratio. The operating factors for syngas production model can be sorted out in order of decreasing effectiveness as: coke ratio > temperature > steam > oxygen. Interaction between experimental factors has been clearly shown in Figure 4.11. Comparing the interactions plots for syngas (Figure 4.11) with those for hydrogen (Figure 4.5) one can easily notice that all the interactions have been weakened due to the counteraction of CO production. At high steam concentrations oxygen has little to no effect on syngas production,

also as the concentration of oxygen decreases the effectiveness of steam concentration on syngas production also diminishes (Figure 4.11(c)).

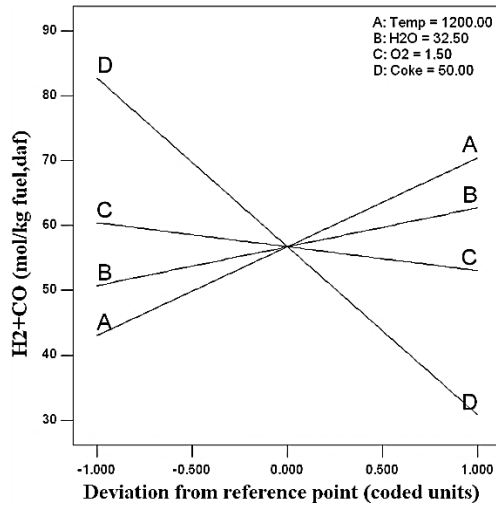


Figure 4.10 Perturbation plot representing the effects of experimental factors on syngas production

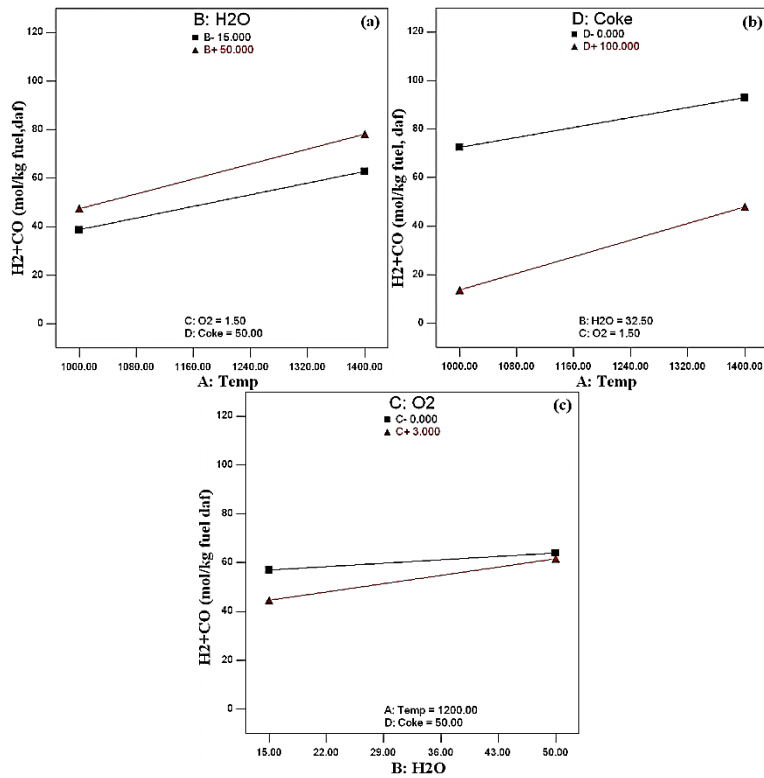


Figure 4.11 Interaction plots for hydrogen response variable: (a) steam-temperature interaction, (b) coke ratio-temperature interaction, (c) oxygen-steam interaction

Figure 4.12 shows the contour plot representing the combined effect of coke ratio and temperature on syngas production at 50.0 and 0.0 vol. % of steam and oxygen concentrations respectively. The operating condition was chosen to obtain the maximum amount of syngas in flue gas. The slight curvature of isolines due to the counteraction of CO indicates a weak interaction between the operating factors. Overall a high temperature and lower coke ratio are favored for maximum syngas production.

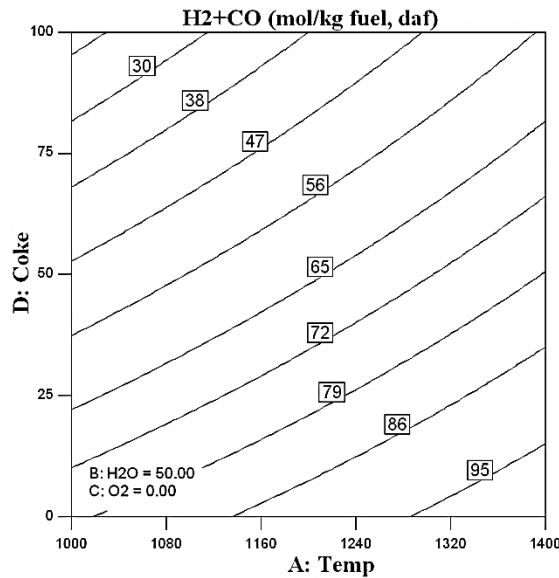


Figure 4.12 Contour plot representing the combined effect of Coke ratio and temperature on syngas production

4.5.5 H₂/CO ratio analysis

As mentioned earlier in section 4.4.3 the Box-Cox plot analysis indicated that a transformation in the form of “inverse-square” was needed for this ratio to fit the experiment results. The fitted model (Table 4.3) shows that H₂/CO ratio is a function of all four factors and temperature-oxygen and steam-oxygen interactions. The relevant perturbation plot of H₂/CO ratio is shown in Figure 4.13.

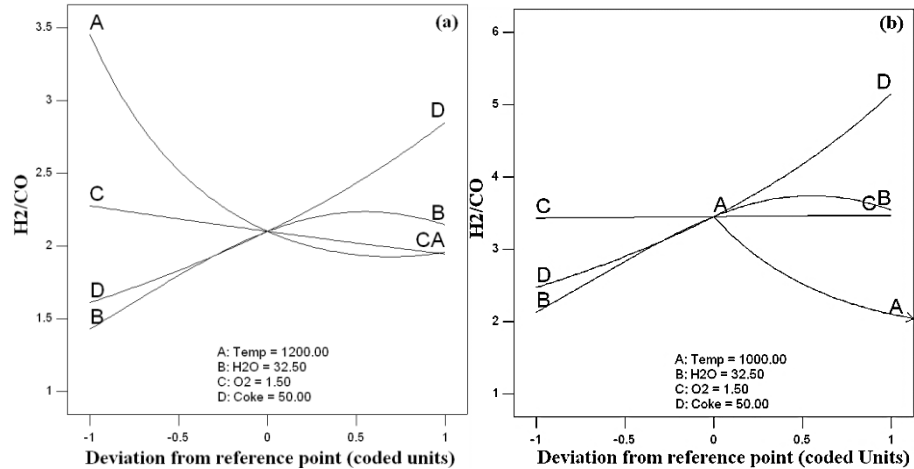


Figure 4.13 Perturbation plot representing the effects of experimental factors on H₂/CO ratio

Figure 4.13(a) reveals that the H₂/CO is favored by a decrease in temperature and oxygen, and an increase in Coke ratio and steam. This finding is in agreement with previous works [60, 144] except for the steam effect. The steam curve passes through a maximum close to the upper limit (~40 vol. %). This could be the fact that at higher steam concentrations the secondary steam gasification reaction is prevailed over primary one but as discussed earlier at the high temperatures, normally encountered in entrained flow gasifiers, the water shift reaction equilibrium constant becomes very small which results in production of CO to the detriment of H₂. Figure 4.13(b) shows the perturbation graph plotted at the lowest operating range of temperature. This plot clearly illustrates that at lower temperatures the effect of oxygen concentration diminishes. The effect of operating factors on H₂/CO ratio can be sorted out in order of decreasing effectiveness as: coke ratio > temperature > steam > oxygen. No positive deviation from linear additive rule was found in co-gasification of coal with oil sand coke in this case either.

Figure 4.14 also exhibits the variation of the interaction between temperature and oxygen at three levels of steam concentration. Plots disclose that an increase in steam concentration has a more notable effect on the response variable at higher concentrations of oxygen.

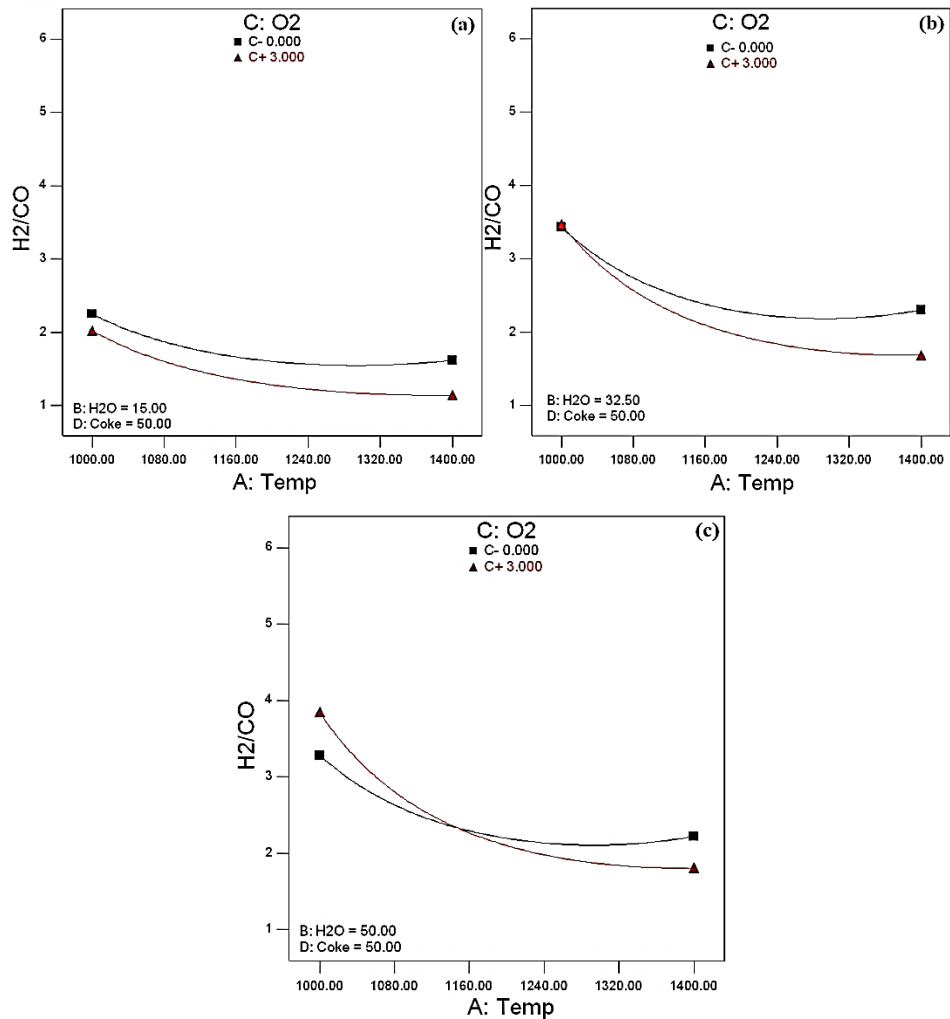


Figure 4.14 Temperature-oxygen interaction plots for H₂/CO ratio: (a) 15 vol. % steam, (b) 32.5 vol. % steam, (c) 50 vol. % steam

Figure 4.14(a-c) clearly explain this trend. At the highest steam concentration used in this study, the two curves cross each other at about 1150°C. So, at temperatures lower than this value, higher oxygen concentration is favored whereas at temperatures greater than 1150°C which is generally the case of entrained flow gasifiers, the lowest oxygen concentration is more suitable. More information can be found from the interaction plots shown in Figure 4.15. Figure 4.15(a) and (b) show the variation of the interaction between steam and oxygen for a blend of 50% coke at 1000°C and 1400°C, respectively. At 1400°C, it is clear that lower oxygen content is favored. However, as the temperature drops, this behavior changes and it becomes a function of steam concentration as

well (Figure 4.15(a)) where at high steam concentrations (>31 vol. %) higher oxygen content results in higher H₂/CO ratio. This fact, one more time shows the shift from primary to secondary steam gasification reaction at lower temperature.

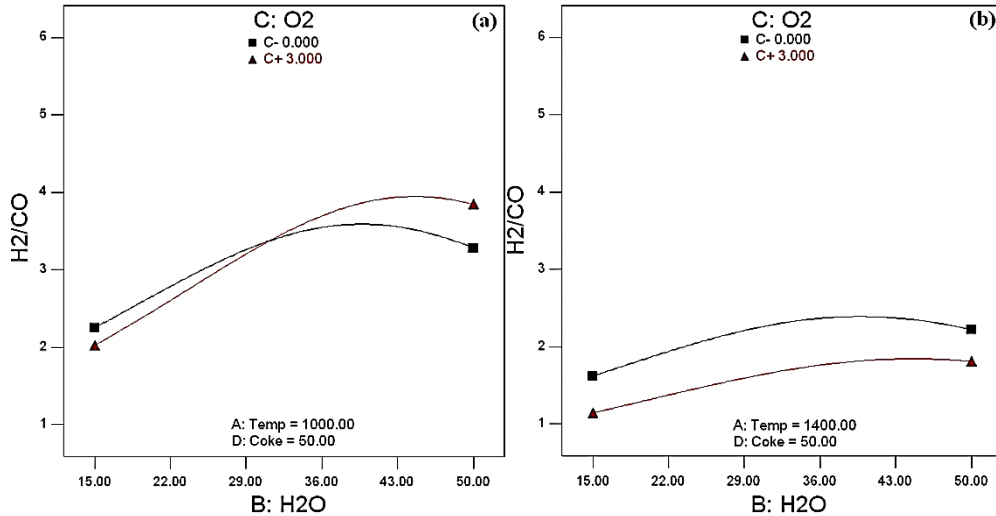


Figure 4.15 Steam-oxygen interaction plots for H₂/CO ratio: (a) 1000°C, (b) 1400°C

Figure 4.16 shows the contour plot representing the combined effect of coke ratio and temperature on H₂/CO ratio at 45.0 and 1.5 vol. % of steam and oxygen concentrations respectively. The operating condition was chosen to obtain the maximum amount of syngas in flue gas. The curvature of isolines particularly at high temperatures and low to medium coke ratios indicates a strong interaction between the operating factors. However, as the temperature drops and coke ratio increases, the isolines become increasingly linear which implies that interaction becomes less significant.

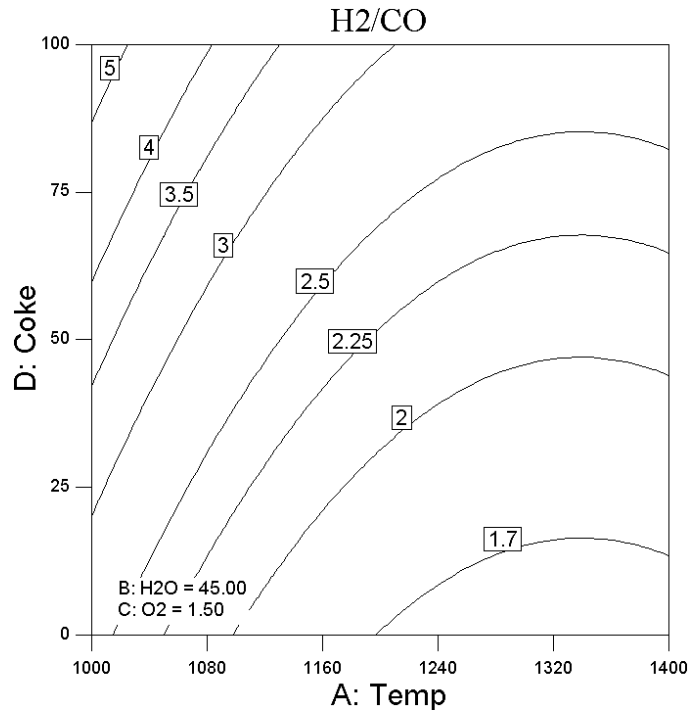


Figure 4.16 Contour plot representing the combined effect of Coke ratio and temperature on H₂/CO ratio

4.5.6 Gasification efficiency

A glance at Table 4.3 shows that gasification efficiency is a function of all four factors and the interactions between temperature-steam, temperature-coke ratio, and steam-oxygen. The interaction terms, temperature and steam concentration produce a certain level of curvature on the response surface. The perturbation plot in Figure 4.17 shows the effect of operating variables and coke ratio on response surface at the midpoints of all factors. From the plot it can be concluded that gasification efficiency is favored by an increase in temperature and steam concentration and a decrease in oxygen. These results agree with the previous studies available in literature [5, 144, 146]. Increasing temperature as explained in earlier sections favors H₂ and CO production which in turn results in higher values of gasification efficiency according to equation (1). Effect of steam concentration has been slightly moderated (compared to its increasing effect on

H₂ production) due to its reducing effect on CO production. Oxygen on the other hand, reduces the H₂ production which results in lower gasification efficiencies.

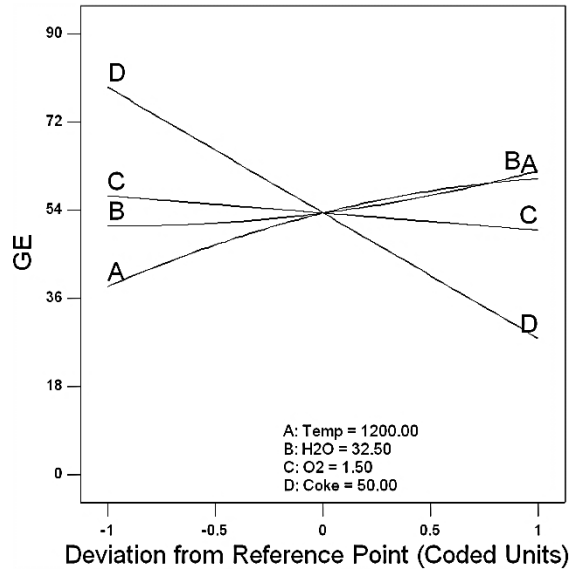


Figure 4.17 Perturbation plot representing the effects of experimental factors on gasification efficiency

Figure 4.18 also reveals a dearth of synergy in co-gasification of coke and coal. The results are different from the findings of other authors obtained at high pressures [21, 63, 147]. However, as mentioned earlier, other authors did not provide a detailed error analysis in their works. The relatively small positive deviations from linear additive behavior could be the results of experimental errors. Detailed error analysis and error propagation for gasification experiment calculations at high pressures are needed in order to properly investigate the role of pressure on the observed synergy differences between atmospheric and pressurized systems.

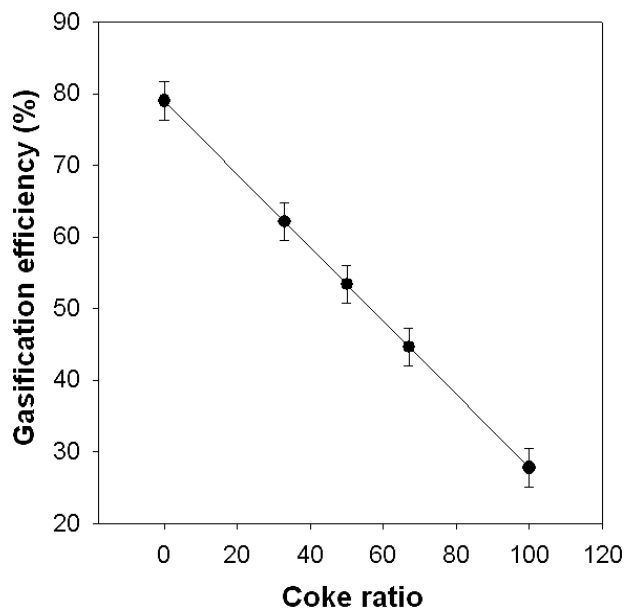


Figure 4.18 Effect of blending ratio on gasification efficiency at the midpoints of operating variables

Figure 4.19 shows the effect of interaction between factors on gasification efficiency. The non-parallel and non-overlapping curves show the existence of interaction between factors. Figure 4.19(a) reveals that at higher ranges of temperature, effect of steam concentration on gasification efficiency is more pronounced compared to lower ranges. Figure 4.19(b) also shows that the higher the steam concentration the smaller the effect of oxygen concentration becomes. Overall, the effect of operating factors on gasification efficiency can be sorted out in order of decreasing effectiveness as: coke ratio > temperature > steam > oxygen.

Figure 4.20 shows the contour plot representing the combined effect of coke ratio and temperature on gasification efficiency at 50.0 and 0.0 vol. % of steam and oxygen concentrations respectively. The operating condition was chosen to obtain the maximum amount of syngas in flue gas. The plot shows that gasification efficiency is favored by higher temperature and smaller coke ratio with coke-temperature interaction being more notable at higher temperatures and lower coke ratios.

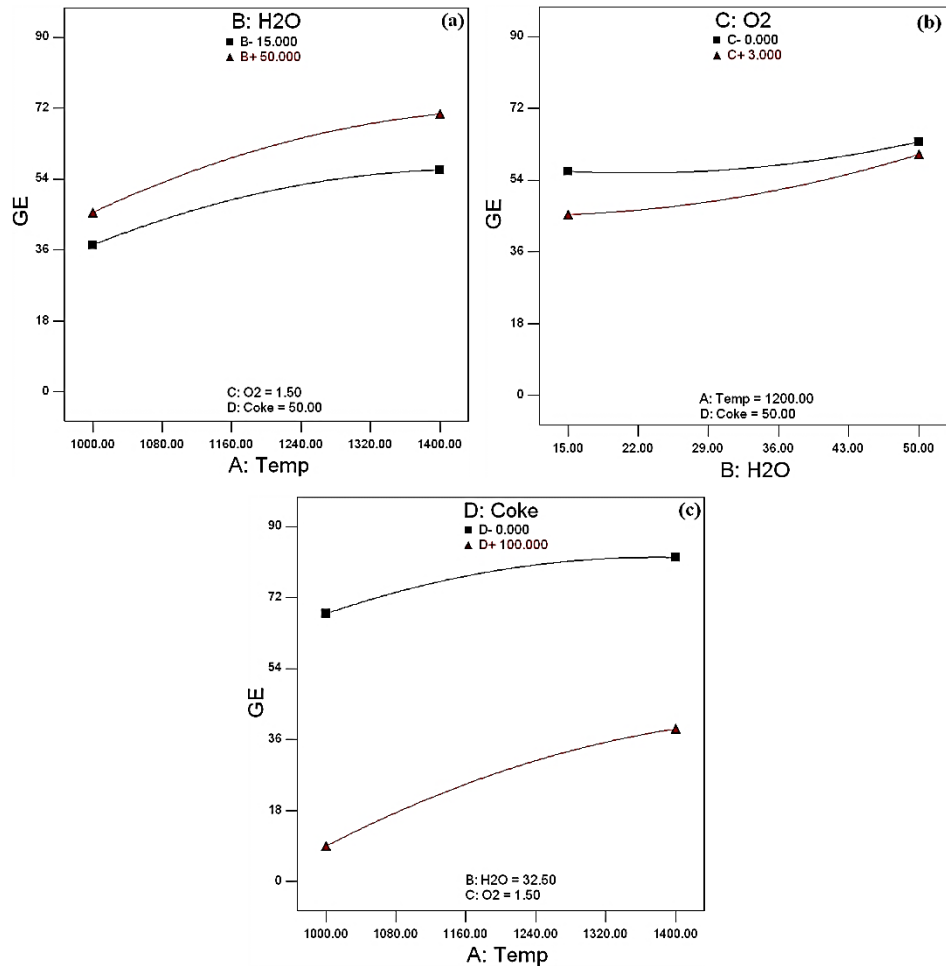


Figure 4.19 Interaction plots for gasification efficiency: (a) steam-temperature interaction, (b) oxygen-steam interaction, (c) coke ratio-temperature

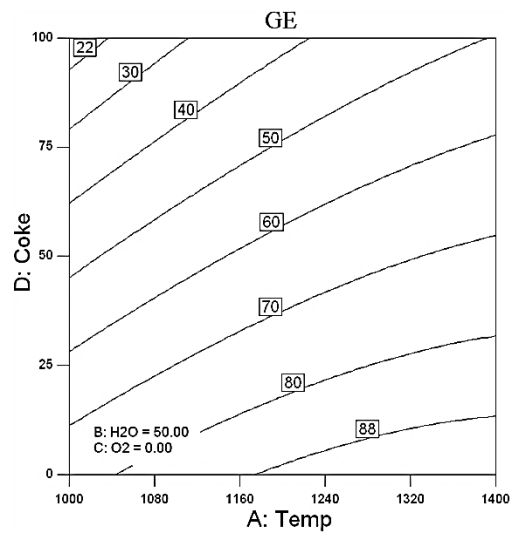


Figure 4.20 Contour plot representing the combined effect of Coke ratio and temperature on gasification efficiency

4.5.7 Conversion

The regression model of carbon conversion (Table 4.3) shows that conversion is affected by all four factors and the interactions between temperature-steam, temperature-coke ratio, and steam-coke ratio. In addition to the interactions, temperature creates a certain level of curvature in the response surface. In general, conversion is favored by an increase in temperature, oxygen and steam concentration. High temperatures and oxygen concentrations intensify the oxidation and cleavage of molecular bonds in coal [60]. The low reactivity of coke compared to coal results in a decrease in conversion as the coke ratio is increased in the blend. Figure 4.21(a) and (b) represent the perturbation plots for carbon conversion at minimum and maximum temperatures studied in this work, respectively, where the other factors are fixed at the midpoint values. It can be seen that at lower temperatures, oxygen concentration is more influential than steam on carbon conversion whereas at higher temperatures steam concentration effect is more pronounced. This is can be explained by the endothermic nature of steam gasification reactions where higher temperatures favor the endothermic reactions. Figure 4.21(c) and (d) show the effect of operating variables on pure coal and coke, respectively. The plots disclose that in case of pure coke, temperature is much more influential on conversion than steam and oxygen concentration, whereas for pure coal all the parameters have almost the same effect under the operating condition shown in figures. The order of influence of experimental factors is: coke ratio > temperature > steam > oxygen.

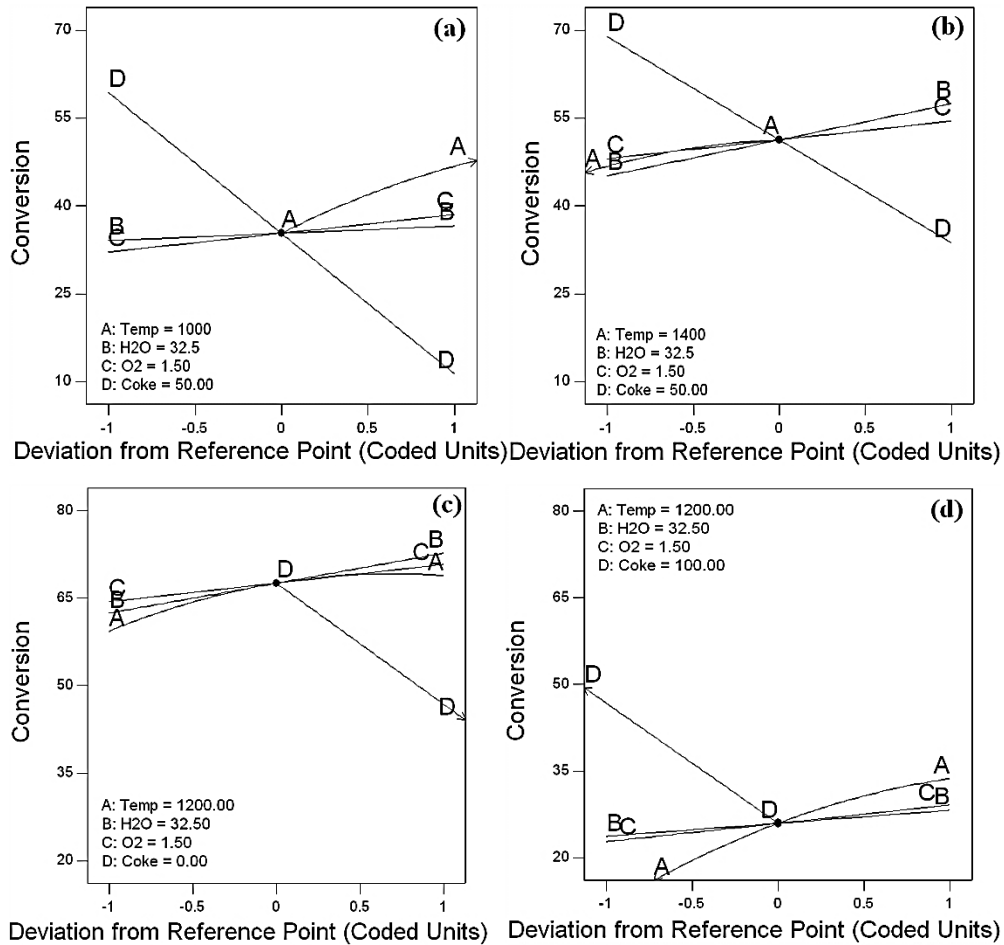


Figure 4.21 Perturbation plots representing the effects of experimental factors on carbon conversion: (a) 1000°C, (b) 1400°C, (c) pure coal, (d) pure coke

Figure 4.22 also shows that there is not any synergy between coke and coal under the conditions studies in this experiment. On other words, coke and coal burn separately inside the gasifier. This could be partially understood by low volume fraction and residence time of solid fuels in entrained flow gasifiers. The contour plot representing the combined effect of coke ratio and temperature on carbon conversion at 50.0 and 3.0 vol. % of steam and oxygen concentrations, respectively, is shown in Figure 4.23. The operating conditions correspond to the locus of maximum carbon conversion. The plot shows that carbon conversion is favored by higher temperature and smaller coke ratio with coke-temperature interaction being more notable at higher temperatures and lower coke ratios.

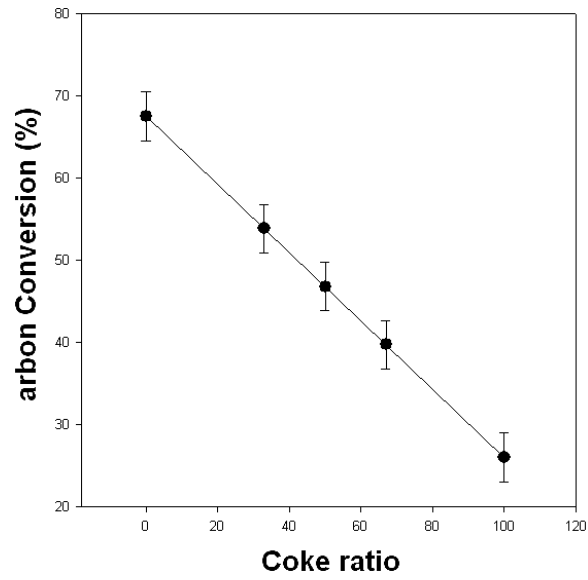


Figure 4.22 Effect of blending ratio on carbon conversion at the midpoints of operating variables

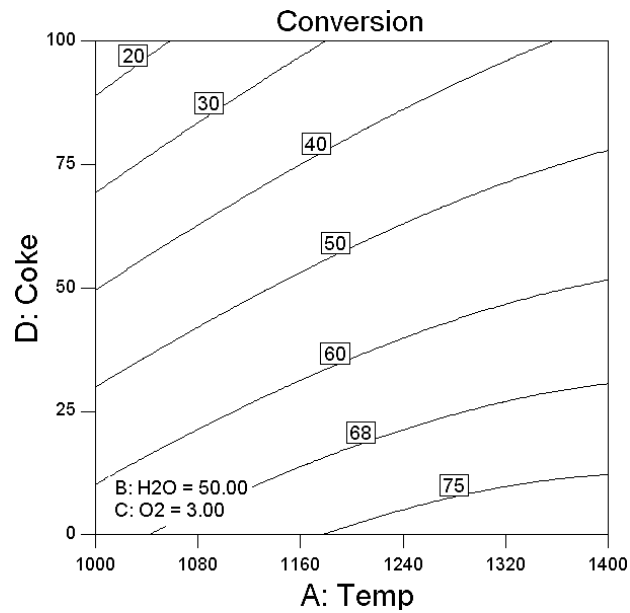


Figure 4.23 Contour plot representing the combined effect of Coke ratio and temperature on carbon conversion

4.5.8 Numerical optimization

The most attractive feature of response surface methodology is the fact that using mathematical and statistical methods one is able to quantify the relationship between vital factors and the response variable of interest which is otherwise impossible using traditional methodology. Having proved the statistical significance of the proposed response surface and suitability of the regression model to navigate the design space, one can easily use the correlations to optimize the response variables of interest. Optimization makes use of an objective function called desirability function which reflects the desirable range for each individual response. The desirable ranges are from zero to one (least to most desirable respectively). For multiple response factors the desirability function is a geometric mean of all responses [140, 143]. Given the empirical functions and the applicable constraints, any mathematical or statistical packages could be used to perform the constrained optimization. In this case numerical optimization reduces to a general constrained non-linear optimization algorithm. Design Expert uses Simplex (Nelder-Mead) multi-dimensional pattern search algorithm. More details can be found in APPENDIX C.

Within the context of gasification, carbon conversion is always desired to be maximized. The choice for other response variables depends on the downstream application. By far the most important response is hydrogen production for upgrading process in oil sands industry. Other constraints are introduced by the gasifier operability issues and environmental regulations. For instance, difficulties encountered with the Slag plugging the reactor and tapping system limit the solid loading of high ash content coals. Blending coal with coke can alleviate this problem. The environmental issues created by stockpiling oil sand coke and the need to reduce the environmental footprints of this by-product demand a cleaner and sustainable technology to use this material as feedstock. On the other hand, high sulfur content of this fuel drastically increases the downstream processing requirements. Blending with low sulfur fuels such as Albertan coal can mitigate the sulfur loading difficulties in the flue gas. So, a full

process and cost analysis should be considered to properly impose the optimization constraints.

In this study, a few scenarios were devised and checked with the experimental results to further explain the suitability of RSM in finding the optimum operating conditions. H₂ production was chosen as the main objective function to be maximized due to its importance in oil sands industry. Carbon conversion as mentioned earlier is always desired to be maximized. Blending ratio was fixed between 30-60 wt.%, a practical range taken from similar works in the literature [21, 148]. Optimization was performed using Design expert package. Four different design points obtained from the solutions of optimization were checked with the experimental results. Table 4.4 represents the results of optimization in comparison with the experimentally measured values for both hydrogen and conversion. There is a good agreement between predicted and measured values. A maximum hydrogen production of 55.75 (mol/kg fuel, daf) was obtained with a desirability value of 0.862. The minimum and maximum hydrogen production obtained within the design space used in this work were 10.6 and 63.7 (mol/kg fuel, daf), respectively. The maximum hydrogen production as expected was achieved by maximum temperature and steam concentration and minimum oxygen concentration levels studied in this work. Three extra points with decreasing desirability value were also selected as indicated in Table 4.4. As discussed earlier, an increase in oxygen and coke ratio reduces the hydrogen production even though a small increase in carbon conversion is gained.

Table 4.4 Optimization results for hydrogen response variable

<i>Temp</i> °C	<i>steam</i> vol. %	<i>oxygen</i> vol. %	<i>Coke ratio</i> wt. %	<i>Predicted</i>		<i>Experiment</i>		<i>Error</i>	
				H ₂ mol/kg fuel, daf	X mol/kg fuel, daf	H ₂ Mol/kg fuel, daf	X Mol/kg fuel, daf	H ₂	X
1400	50	0.01	30	57.2	61.9	55.8	59.9	2.6%	3.3%
1400	49.95	0.51	30	56.5	62.9	55.3	61.1	2.2%	3.0%
1400	50	0.08	43	54.7	57.2	53.3	55.2	2.7%	3.5%
1400	50	3	52	49.1	60.0	47.9	58.6	2.4%	2.5%

4.5.9 Synergy

As explained earlier, Furimsky and Palmer [48] using a fixed bed reactor found that a direct blending of cokes with lignite coal did not yield in any catalytic interaction. However, the addition of lignite ash to coke resulted in a noticeable increase in carbon conversion. This synergy was attributed to calcium and iron salts in lignite ash. In a similar attempt, a limited numbers of co-gasification experiments with blend of oil sand fluid coke and ash from Boundary Dam (BD) lignite coal were performed to investigate the catalytic effect of lignite ash on coke. Table 4.5 and Table 4.6 show the properties of BD coal and its ash.

Table 4.5 Proximate and ultimate analyses of Boundary Dam lignite coal

Sample	Proximate analysis (wt.%, AR)				Ultimate analysis (wt.% daf)				
	FC	VM	ash	M	C	H	N	S	O*
BD lignite coal	42.11	30.85	7.21	19.83	75.86	3.83	1.34	0.86	18.10

* by difference, FC: Fixed carbon, VM: volatile matter, M: moisture

Table 4.6 Major and minor composition and fusion temperature analyses of lignite ash

composition	Boundary Dam coal
SiO ₂	37.59
Al ₂ O ₃	16.61
Fe ₂ O ₃	5.54
TiO ₂	0.69
P ₂ O ₅	0.41
CaO	13.16
MgO	2.93
SO ₃	14.10
Na ₂ O	6.36
K ₂ O	0.28
BaO	0.4705
SrO	0.3561
V ₂ O ₅	<0.005
NiO	<0.005
MnO	0.0245
Cr ₂ O ₃	<0.005
Ash Fusion Temperature (°C) (reducing condition)	
Initial	1121
Softening	1152
Hemispherical	1163
Fluid	1188

A blend of 50% coke and 50% lignite ash was prepared with the same dry blending method and the results were compared to that of coke alone. Experiments were conducted at 1200°C, using 32.5 and 1.5 vol. % of steam and oxygen in N₂ carrier gas, respectively. Results did not show any sign of synergy in any of the response variables defined in this study. In fact, the small differences observed between response variables for pure coke and its blend with lignite ash were within the range of experimental errors. This could be predicted by low solid volume fraction and short residence times normally encountered in entrained flow gasifier which in turn makes the interaction of coke particle with catalytic active sites of ash less probable. Table 4.7 represents the experimental results for pure coke and a 50/50 blend of pure coke and lignite ash.

Table 4.7 Comparison of gasification performance between pure coke and 50/50 blend of pure coke and lignite ash

Sample	H ₂	H ₂ +CO	GE	X
Pure coke	22.7	30.8	27.8	25.9
Coke- ash (50/50)	23.2	31.7	28.1	26.7
Deviation from pure coke basis	2.2%	2.92%	1.08%	3.09%

However, it has to be highlighted that in this study we did not investigate the effect of pressure and micromechanical interaction between char and slag. Properly designed high pressure studies with adequate coverage of error analyses and propagation are also needed to be considered before drawing any conclusion about synergy. The issue of micromechanical interaction of Slag-char in entrained flow gasifiers, yet, has not been the subject of detailed experimental scrutiny. The main problem is that this phenomena has to be studied in at least pilot plants which sufficient solid loading rate which sustains the steady flow of slag on the gasifier wall. If not impossible, in fact it is very difficult to study this phenomenon in a lab scale reactor. The literature on this subject is indeed scarce. However, a recent modeling study [149] shows that permanent carbon entrapment

in the molten slag is not likely to occur under typical operational conditions of gasifiers, but it might occasionally occur due to an unfavorable combinations of small ash viscosities, large particle sizes, and large impact velocities. In this study the authors considered three possible regimes for char-slag interaction inside the gasifier (Figure 4.24). In regime E, char particles reaching the surface of the slag are permanently sink into the slag layer and will not react with gasifying agents. In regime S char particles reaching the wall stick to the slag layer's surface without being fully engulfed. Progress of char gasification and catalytic interaction is possible in this regime. It is important to notice that residence time significantly increases for trapped particles as slag layers move much slower than gases through the gasifier, which results in an increase in carbon conversion. Some commercial gasifiers use this principle to ensure that large carbon particles remain longer in the reactor by using some swirl in the top burner, as in Siemens gasifier, or by tangential firing as, for example, in the EAGLE gasifier [5]. And finally in regime SC, the entrapment of char does not take place due to the extensive coverage with 'unfused' carbon particles. Slag coverage by unfused carbon particles affects the micromechanical interaction by repulsion of an impinging char particle.

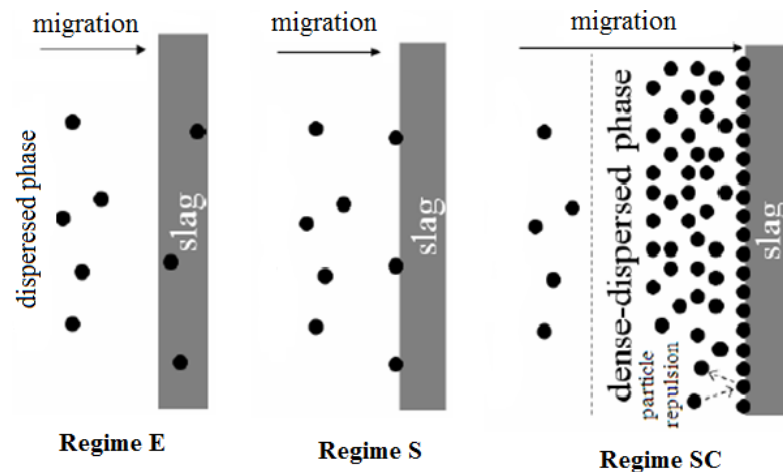


Figure 4.24 Regime of char-slag micromechanical interaction: E=entrapment; S= segregation, and SC= segregation and coverage [149]

However, this is just a pure mathematical modeling which needs to be further validated by credible experimental data which are currently missing in literature. Much more has to be done in this area to fully appreciate the underlying physics of char-slag interaction.

In order for synergistic effects to be thoroughly evaluated in co-gasification, studies must identify the effect of char-slag micromechanical interaction, effect of flow regime and fluid dynamics, and temperature profile. None of these can be studied in a lab scale setup. Having said these facts, it is worth noticing that the above mentioned shortcomings do not lessen the importance of lab scale studies. One needs to know the full potentiality of feedstocks before using it at larger scales. This work provides this information to the extent that has never been reported before.

4.6 Chapter findings and conclusions

A complete assessment of the effects of operating variables (temperature, steam and oxygen concentrations) and blending ratio of oil sand coke and coal on different response variables (H_2 , CO and syngas productions, H_2/CO ratio, carbon conversion and gasification efficiency) was achieved by means of response surface methodology at high temperatures in an atmospheric pressure entrained flow gasifier. All the response variables were successfully quantified as a function of operating factors and blending ratio. A detailed analysis of variances showed that models can be used to navigate the design space. For all the response variables studied in this work, different responses were obtained depending on the settings of at least two operating factors. These interactions are very difficult to be extracted with the classical design of experiment methodology if not impossible. Additional experiments were conducted to evaluate the robustness of regression models, all proved to be very successful.

Overall no synergy was found in co-gasification of oil sand coke and coal under the operating conditions studied in this work. A limited number of experiments were performed using a 50/50 blend of lignite ash and coke. Despite

the reported synergy in fixed bed reactors, no synergy was found in case of entrained flow gasifier.

Except H_2/CO ratio, raising temperature increased the amounts of all response variables. However, the maximum CO production attainable with increasing temperature is limited at high temperatures. An increase in oxygen concentration resulted to a reduction in H_2 and syngas productions, H_2/CO ratio and gasification efficiency and an increase in carbon conversion. CO production showed to be insensitive to oxygen concentration. An increase in steam concentration monotonously raised the H_2 and syngas productions, gasification efficiency and carbon conversion. As far as the production of CO is concerned, at higher temperatures studied in in this work, variation of CO in flue gas is a weak function of steam concentration. Effectiveness of steam in Hydrogen production was abated with increasing the coke ratio in the blend and it was shown that for higher range of coke ratio, temperature is more effective factor than steam in hydrogen production. Also, it was observed that effect of oxygen concentration on H_2 response remained the same for different levels of coke ratio. However, at higher concentrations of oxygen, the H_2 production was more sensitive to steam concentration. On the contrary to coke in case of H_2 production, pure coal was almost insensitive to temperature within the range of temperature used in this study. An increase in coke ratio drastically reduced the CO production. On the other hand, the higher the coke ratio is, the less sensitive CO production becomes to the variations of steam. It was found that H_2/CO ratio was favored by a drop in temperature and oxygen level and increase in coke ratio and steam concentration. The curve for steam however, passes through a maximum close to the 40 vol. %. Also, it was found that at lower temperatures, oxygen has little to no effect on H_2/CO ratio. The oxygen effect found to change with steam concentration though, with higher steam concentration, higher oxygen is required to sustain the same level of H_2/CO ratio. The results also revealed that at high temperatures effect of steam was more pronounced than low temperatures on gasification efficiency. Additionally, the higher steam concentration is, the smaller the effect of oxygen becomes.

Using the regression models, operating variables were tuned using a constrained non-linear optimization algorithm to find the location in design space which gives the maximum H₂ production. A maximum of 55.8(mol H₂/kg fuel, daf) was gained at 1400°C, 50% steam and 0.01% oxygen with a blend of 30% coke/ 70% coal. Given the excellent accuracy of RSM in quantitatively predicting the results, one can easily notice the unequivocal advantage of RSM in optimizing the gasifier operating conditions which is otherwise impossible using classical “one-factor-at-a-time” method. The latter often fails to produce firm and generalizable conclusions, either qualitatively or quantitatively, as far as the gasifier operation is concerned, due mainly to the relaxation of the interaction effects between operating variables.

CHAPTER 5³

Intrinsic reaction kinetics of fluid coke char with O₂, CO₂ and H₂O

5.1 Introduction

This chapter describes the intrinsic reaction kinetics study of Syncrude fluid coke samples and the experimental apparatus and techniques used to generate char samples and their O₂-, CO₂- and H₂O-reactivity measurements. A thermogravimetric analyzer was used to measure the reactivity. The data show that the reactivity measurements lie entirely within regime I conditions. The active surface area and total surface area measurements are also described along with their appropriateness for normalizing the specific reaction rates in order to derive the intrinsic rates.

5.2 Raw material

In this work, the Syncrude fluid coke supplied by Syncrude Co., studied for its reactivity to O₂, CO₂, and H₂O. The proximate and ultimate analyses of fluid coke were presented in previous chapter in section 3.2.1. The bulk sample

³ This work has been submitted for publication to Journal of Energy & Fuels.
Authors: Vejahati F. Gupta R.

were crushed using a jaw crusher and then pulverized and sieved to a particle cut-size of 53-75 μm using Retsch planetary ball mills and ASTM (D4749–87) wet sieving procedure, respectively.

5.3 Experimental procedure

The char samples were prepared under high temperature and high heating rates normally encountered in an industrial entrained flow reactors using the experimental setup described in section 3.1. For this work pyrolysis was conducted at 1400°C. Samples were dried for 2 hours at 105°C before pyrolysis experiment.

The furnace was heated up under air flow over night. After reaching the temperature set point, the air was replaced with a high purity N_2 (99.999%) and flow rate was set to 5 lit/min. The nitrogen concentration at the outlet of gasifier was analyzed with Micro-GC every 10 minutes till the concentration of nitrogen reached the purity level of gas cylinder. At this time the coke sample was fed into the reactor. Approximately 5 gr of char sample was collected. After pyrolysis the char sample was further ground to a particle size of 20-28 μm using Retsch planetary ball mills and ASTM (D4749–87) wet sieving procedure in order to eliminate the intraparticle mass diffusion limitations. The collected samples were sealed in bottles and stored in a fridge to avoid further oxidation.

5.3.1 Thermogravimetric analyzer

The char sample was gasified in a thermogravimetric analyzer (TGA) (TA instruments Q600), which consists of a horizontal balance beam which holds a sample pan with thermocouple directly in contact with the pan. A thin layer of Char sample (ca. 2 mg) was spread on an alumina pan and, dried at 110°C for 5 minutes in ultra-high purity nitrogen flow, and then heated to gasification temperature at the heating rate of 50°C/min. The final temperature was maintained for 5-10 minutes, then N_2 was switched to gasifying agent (O_2 , CO_2 , or H_2O) or their mixtures with N_2 and the weight loss was recorded with time.

Figure 5.1 shows the detail design of SDT Q600 thermogravimetric analyzer. The multiplicity of advantages in the design of Q600 compared to other hang down, up drift or down drift thermogravimetric analyzers makes it a superior apparatus for reactivity measurements:

- Dual beam balance provides superior TGA baseline compared to single beam designs.
- A combination of differential weight loss signal from dual horizontal balance mechanism and horizontal purge system make the weight measurements almost insensitive to buoyancy effect.
- Thermocouples are directly connected to sample pans, so for highly exothermic reaction like combustion reaction, more realistic temperature is recorded compared to the hang down designs where thermocouple is about 8-10 mm above the sample pan.
- Horizontal purge flow provides exceptional purge gas/sample interaction (no stale gas pockets).
- And finally the dual beam balance mechanism enables a high sensitivity of the order of 0.1 μg , which is an order magnitude higher than common hang down mechanisms (1 μg).

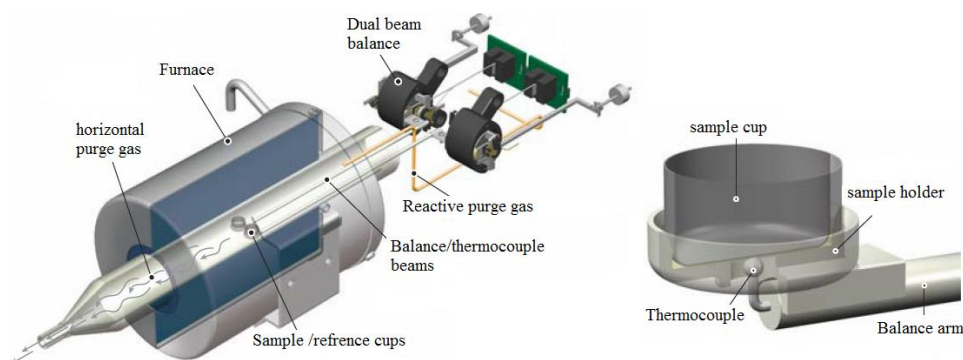


Figure 5.1 Schematic design of TA SDT Q600 thermogravimetric analyzer

The superiority of Q600 units was tested by running a similar experiment in another TGA unit from Thermofisher Scientific, Thermax400 using steam (10 kPa partial pressure) as gasifying agent and a sub-bituminous coal char samples.

The normal flow rates, beyond which no further improvement in TG curve could be observed, were determined separately for each unit and found to be 250 ml_n/min and 400 ml_n/min for Q600 and Thermax400, respectively. Figure 5.2 compares the performance of these units. Despite the higher normal flow rate of Thermax400 it is obvious that the up drift, hang down arrangement of Thermax400 still suffers from the stale gas pocket formation and less efficient purge configuration in comparison with Q600 unit.

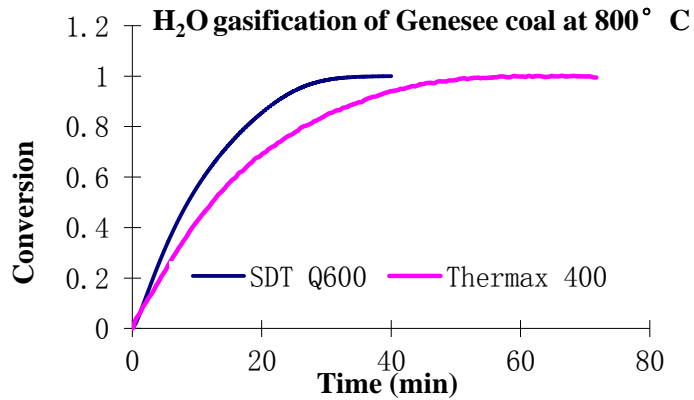


Figure 5.2 Performance comparison of SDT Q600 and Thermax 400 units

Figure 5.3 also shows the superiority of Q600 units in being less sensitive to buoyancy and in creating stable baseline by using dual beam mechanism compared with single beam mechanism in Thermax400. The data in Thermax400 needs an extensive smoothing in order to be used for reactivity analysis.

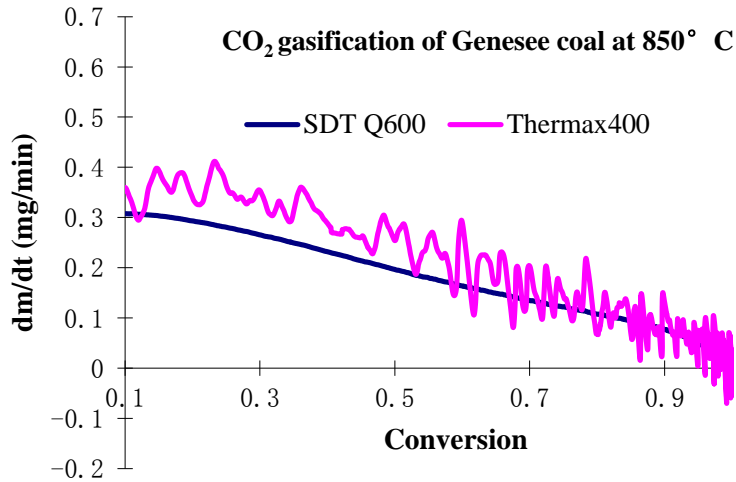


Figure 5.3 Rate of mass loss vs. conversion for two TGA units

In order to inject steam the design of TGA was modified by attaching a diffuser to the outlet of the reactive purge gas tubing inside the furnace. A high precision syringe pump was used to inject water through reactive purge tubing and into the diffuser where the furnace heat evaporates the water and generates steam. Steam then mixes with nitrogen in the furnace and reacts with the Char sample. Figure 5.4 shows the steam injection mechanism and diffuser configuration in TGA.



Figure 5.4 Diffuser configuration for steam injection in TGA

To further reduce the diffusion effects between the sample and bulk gas phase, as recommended by Ollero et al. [150], sample pans were polished from the original 4 mm to about 0.5 mm deep. The original and modified sample pans are shown in Figure 5.5.

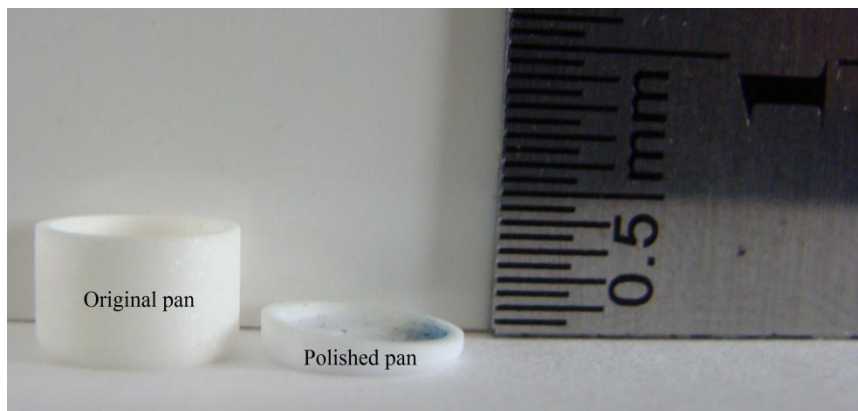


Figure 5.5 Original and modified sample pans

CO₂ and O₂ were directly introduced using the integrated high accuracy mass flow controllers and valve switching system of the SDT Q600 unit.

From a series of preliminary tests with varying total gas flow rate at highest temperature used in this study, a flow rate of 250ml_n/min was found enough for gasification to take place with very little effect of diffusion for all gasifying agents and also effect of particle size was examined for particle size ranges from 20-75 micron. A cut size of 20-28 micron was found enough to eliminate the effect of intraparticle diffusion.

5.3.2 Total surface area characterization

The total surface area (TSA) of original and partially converted char sample were determined by N₂ and CO₂ adsorption isotherms using a Quantachrome AutoSorb1 apparatus. The chars were partially converted with CO₂ in a horizontal tube furnace at 800°C and various times to generate char samples with various conversion levels. Four different levels of conversions were obtained for fluid coke in this study.

The significance of the differences between data obtained using these two techniques were discussed in chapter 2. NLDFT/GCMC has known to give the best results in characterization of microporous carbonaceous material compared to BET [27, 151]. A combination of NLDFT/GCMC and CO₂ and N₂ isotherms is believed to cover the whole range of pore sizes from ultra-microporosity to high mesoporosity [31, 32]. In this study we have adopted the same technique. N₂-BET and CO₂-Dubinin Radushkevich (DR) surface areas were also reported for the sake of comparison. More details about BET and NLDFT have been provided in APPENDIX B.

However, there are some uncertainties on the use of CO₂ as adsorbate gas in GCMC and DFT calculations. The first issue originates from the fact that CO₂ is by no mean a Lennard-Jones (LJ) fluid. However, it is possible to describe the vapor-liquid equilibrium of bulk CO₂ using an effective LJ potential [31, 152] by choosing LJ parameters and the hard spheres diameter from the best fit of the DFT equation of state to the experimental liquid-vapor phase diagram. Also, a very accurate description of two-phase bulk equilibrium have been reported by Ravikovitch et al. [31] using the three-centre model of Harris and Yung [153] in the GCMC simulations of CO₂ adsorption in combination with potential function of Steele which is widely used for modeling interactions of molecules with graphite. Vishnyakov et al. [152] were also able to predict the liquid and vapor densities with accuracy of 0.5% in a wide range of temperatures using one-centre GCMC model using the same potential function.

The second issue arises upon the fact that CO₂ adsorption is normally conducted at 273 K. Some people believe that CO₂ adsorption might not be necessarily a pure physisorption. There is a chance for chemisorption to be involved as well. For this reason, an adsorption-desorption experiment was conducted using AutoSorb1 on fluid coke char to check if the system is reversible or not. It took 72 hours to complete this analysis, particularly that desorption isotherm equilibration time is much longer than that of adsorption. Figure 5.6 clearly shows that adsorption–desorption isotherms close at low relative

pressures. This proves that system is reversible and only physisorption is involved.

Finally, the parameters for CO₂ interaction both for one-centre and three-centre model in GCMC and effective LJ parameters for NLDFT have been determined from the fit to the isotherm on Sterling graphite at 273 K and the fluid-fluid and solid-fluid parameters have been further verified by adsorption isotherms at CO₂ boiling temperature (195.5 K), at which the adsorbate forms a condensed monolayer. However, it is worth mentioning that there have been reports of polarization of the adsorbed Ar, CO₂ and nitrogen by the surface field, which reduces the fluid-fluid attraction [154]. However, Ravikovitch et al. [31] found that deviation are small and mainly occur at relative pressure greater than 0.1. So, they will not affect the microporosity measurements. To further prove the appropriateness of DFT/GCMC-CO₂ models for surface area assessments, Ravikovitch et al. [31] volumetrically measured the adsorption isotherms and calculated the pore size distribution of different materials such as low activated carbon Fibers and T3A carbon molecular sieve, Carbons of medium to high degree of activation using Ar, CO₂ and N₂ in combination with GCMC/NLDFT simulations. They observed that CO₂ isotherms are in good agreement with those obtained from N₂ and Ar, however, N₂ failed to fill the super-micropores (<1.5 nm). Ar also loses the accuracy for ultra-micropores smaller than 0.8 nm. So the best combination seems to be the measurement of ultra-micropores (0.35-1.5 nm) with CO₂ and larger pores with Ar or N₂.

However, it is worth noting that all the above mentioned models such as BET (which is an extension of Langmuir theory), GCMC and NLDFT suffer from the fact that all sites on the solid are assumed equivalent, and commonly graphite or pure carbon are used as base adsorbent in solid-fluid interaction.

Nonetheless, these methods have been standardized in pore size distribution and surface area measurements of carbonaceous material.

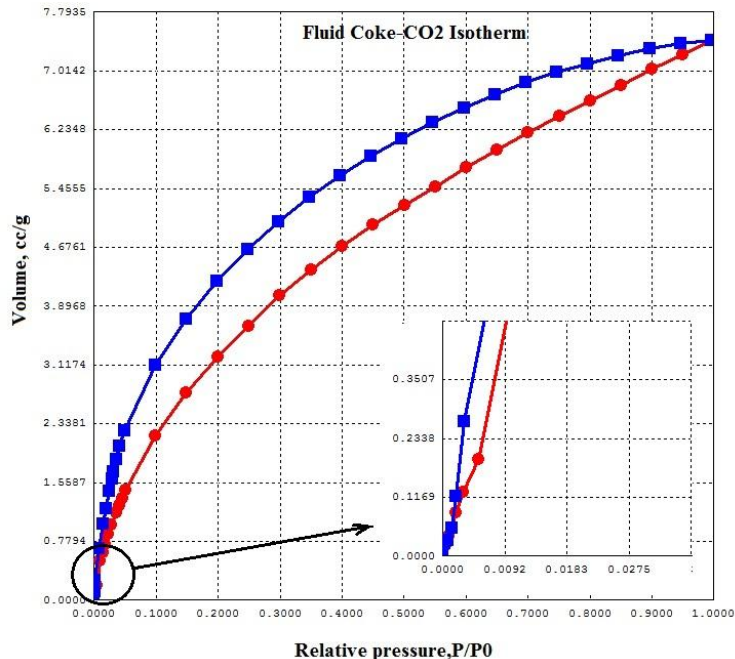


Figure 5.6 CO₂ isotherm for Fluid coke at 273 K

5.3.3 Active surface area characterization

The active surface area of samples was determined by thermogravimetric analysis. The thermogravimetric technique has already been used to investigate the oxygen chemisorption capacity of carbon materials [86, 155, 156].

The active site concentrations are commonly measured from the oxygen chemisorption capacity of the carbon surface. The principal steps in the experimental procedure are:

- (a) Outgassing the carbon surface to remove pre-adsorbed surface complexes;
- (b) Formation of chemisorbed surface complexes by exposure to oxygen, preferably at a temperature low enough to avoid gasification of the carbon;
- (c) Removal of chemisorbed oxygen as CO and CO₂ by heat-treatment of the carbon.

So the chemisorption capacity can be measured either at step (b) by gravimetric analysis or at step (c) by evolved gas analysis, such as Temperature Programmed Desorption (TPD) or Transient Kinetic (TK) studies [82, 83].

The easiest way of representing the chemisorption capacity of the char is as the amount of oxygen w [g of oxygen atoms/ (g of char)], either chemisorbed in step (b), or evolved as CO and CO₂ in step (c).

To calculate (C_t), the total active site concentration [sites/g char], from w an assumption about the stoichiometry, CO_ν , of the functional groups on the char surface is required. Usually it is assumed that $\nu = 1$ so that

$$(C_t) = wN_A/16.00 \quad (5.1)$$

Where N_A is Avogadro's number. This assumption is not necessarily valid. Some functional groups may contain more than one oxygen atom, e.g., carboxylates, C-O-O⁻, $\nu = 2$ in this case so assumption of $\nu = 1$ leads to an overestimation of (C_t). On the other hand, ethers, -C-O-C-, might bridge two active sites together so that $\nu = 0.5$. In this case assumption of $\nu = 1$ leads to underestimation of active sites. Nonetheless, the assumption of $\nu = 1$ has been widely used in literature in the absence of reliable quantitative analyses of functional groups by spectroscopic techniques. We have adopted the same assumption in the current work.

To further express active site concentration as an active surface area, ASA, requires an estimation about the cross sectional area, σ , of the active site. It is frequently assumed that $\sigma = 0.083 \text{ nm}^2$, which is the cross-sectional area of an edge carbon atom in the basal plane of graphite. With this assumption, the active surface area is calculated as:

$$ASA = \sigma(C_t) = (8.3 \times 10^{-20})(C_t) \quad (5.2)$$

Due to the fact that O₂ equilibrium chemisorption test is conducted at low temperature, about 383 K, on some carbons the oxygen uptake continues for a long time without reaching an equilibrium value. So, O₂ chemisorption rate is often conforms to a so-called, Elovich equation:

$$\frac{dw}{dt} = A \exp(-Bw) \quad (5.3)$$

This means that oxygen capacities reported by different authors may be arbitrary. Also, as discussed in section 2.7, stable complexes can form which remain on the surface of char up to 1300 K. These problems can be effectively solved by replacing O₂ with CO₂ chemisorption for measuring the active surface area due to the fact that measurements using CO₂ are conducted at higher temperatures where the formation of stable complexes are much less probable than the case of O₂. The CO₂ has been successfully used by Klose and Wolki [94] for developing the intrinsic rate of a biomass char gasification with CO₂.

In this work a temperature-switching method with CO₂ was employed. The pyrolyzed samples were degassed at 250°C under vacuum overnight to desorb any trapped molecules inside the pores. The degassed sample (~30 mg) was immediately transferred into an alumina pan and placed inside the TGA under the high purity N₂ gas flow. The sample then was heated up to 1323 K at a rate of 50K/min. This temperature is slightly higher than the maximum temperature that the stable oxygen surface oxides have been found on carbon materials. However, it is safely smaller than the heat treatment temperature (1673 K) in pyrolysis. So, the carbon structure reorganization (annealing) is assumed to be negligible. The temperature was fixed at the set point while the weight loss was monitored. The isothermal condition was kept till the weight loss change dropped below 0.01%/min. Then temperature was reduced to 850°C and kept at that temperature under N₂ gas flow for 5 minutes. Next, the gas was switched to CO₂ and reaction was allowed to proceed till a specific level of conversion was reached. At that point the temperature was rapidly cooled down (~100K/min) under the CO₂ gas flow. The choice of temperatures in gasification step was dictated by the reaction rate which has to be kept low enough to satisfy the assumption that reaction does not progress considerably during the cool down step following the gasification with CO₂. This will let to freeze the complexes on the surface. The cooling step was also conducted under a flow of CO₂ to further minimize desorption of surface complexes. The temperature was reduced to about 150°C and stabilized at that temperature. Then the gas was switched to N₂ and temperature was raised to 950°C with a rate of 5K/min and kept isothermal till the weight did not change

anymore ($<0.01\%/min$). At this point temperature was again reduced to 850°C and the same procedure repeated for different levels of conversion. Figure 5.7 represents a typical TGA experiment conducted to measure the ASA.

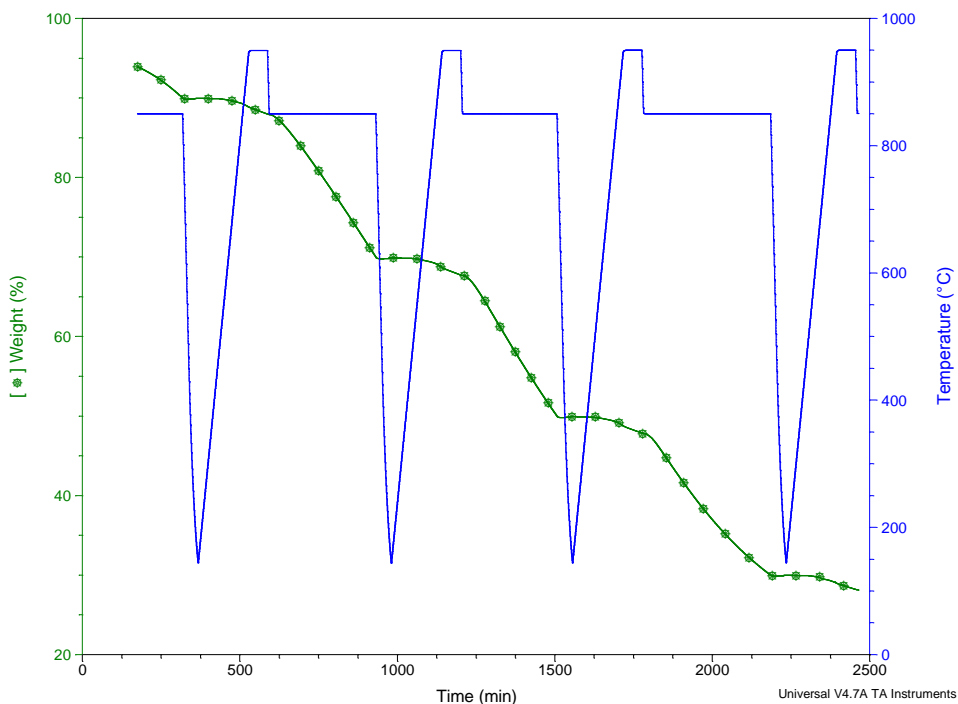


Figure 5.7 TG plot of fluid coke representing the ASA measurement

In order to further minimize the effect of buoyancy and accurately measure the weight of chemisorbed molecules using dual beam balance in Q600 TGA, the reference beam, which normally holds an empty pan, was also filled with the equal weight of sample char. This way, the movements of both beams were more or less the same and this further helped to minimize the weight difference signal which is used to correct the effect of buoyancy.

5.3.4 Treatment of TGA results

The char reactivity from TG curves at a given time was calculated as:

$$r(X) = -\frac{1}{m - m_f} \frac{d(m - m_f)}{dt} \quad (5.4)$$

The degree of conversion was obtained as:

$$X = \frac{m_0 - m}{m_0 - m_f} \quad (5.5)$$

Where m , m_0 , and m_f are the instantaneous, initial, and final weights of sample recorded by TGA, respectively. $r(X)$ is the specific rate of reaction (g/g.s)

Combination of above two equations gives:

$$r(X) = \frac{1}{1 - X} \frac{dX}{dt} \quad (5.6)$$

The specific rates were linked to intrinsic or surface related reaction rates by:

$$r_a = \frac{r(X)}{S(X)} = A \exp\left(-\frac{E}{RT}\right) P_i^n \quad (5.7)$$

Here $S(X)$ is the appropriate surface area (TSA or ASA), and r_a is the conversion independent intrinsic rate. For each reaction, the specific reaction rates were plotted against the specific surface area and the intrinsic rates were then determined from linear regression.

5.4 Char-O₂ reaction

The validity of TGA measurements for char-O₂ reaction has been discussed by Feng and Bhatia [106]. They highlighted that despite the fact the thermogravimetric analysis have been widely used in kinetic studies of carbon gasification, the weight change profiles are not always governed by intrinsic gasification activity due to the effect of chemisorption and its dynamics. They investigated the validity of steady state assumption (apparent pseudo-steady state concentration of oxygen complex) by normalizing the rate equations and

examining the terms in scaled equations. They found a region wherein the rate of weight change due to accumulation of surface complexes is negligible in comparison to the total rate of weight change, so the latter can be used to determine the intrinsic rate. Using this method they provided a plot of O₂ partial pressure versus temperature which gives the region where steady state assumption can be presumed. We already represented this plot in section 2.7.3. Using this criteria they showed that majority of works are falling outside the acceptable region.

However, Feng and Bhatia [106] did not take into consideration the effect of heat transfer in TGA experiments. The Char-O₂ is a highly exothermic reaction which releases considerable amount of energy where the underlying isothermal assumption might not hold. The heat transfer and mass balance for O₂ within a solid spherical particle under pseudo steady assumption (ref. Wen [157] has discussed the validity of Pseudo steady state assumption in detail) and first order reaction with respect to O₂ can be written as:

$$-\frac{1}{r^2} \frac{d\left(r^2 CD \frac{dX}{dr}\right)}{dr} - kC_{O_2} = 0 \quad (5.8)$$

$$-\frac{1}{r^2} \frac{d\left(r^2 \cdot k_c \cdot \frac{dT}{dr}\right)}{dr} + (-\Delta H)kC_{O_2} = 0 \quad (5.9)$$

Here r is radial dimension, X is mol fraction of O₂, D is diffusion coefficient (m²/s), C is total concentration (kmol/m³), k is rate constant (s⁻¹), T is temperature (K), k_c is the thermal conductivity (kJ/m.s.K).

Further simplifying the equations gives:

$$\frac{d\left(r^2 \frac{dX}{dr}\right)}{dr} - \frac{kr^2X}{D} = 0 \quad (5.10)$$

$$\frac{d\left(r^2 \frac{dT}{dr}\right)}{dr} - \frac{(-\Delta H)kCXr^2}{k_c} = 0 \quad (5.11)$$

Combining these equations and applying the boundary condition for zero fluxes at the centre of the particle results:

$$\frac{dT}{dr} + \frac{(-\Delta H)CD}{k_c} \frac{dX}{dr} = 0 \quad (5.12)$$

Further integration gives:

$$T + \frac{(-\Delta H)CD}{k_c} X = cte \quad (5.13)$$

Denoting the temperature and O₂ mole fraction at the surface of particle by $T = T_s$ and $X = X_s$ we can write:

$$T + \frac{(-\Delta H)CD}{k_c} X = T_s + \frac{(-\Delta H)CD}{k_c} X_s \quad (5.14)$$

$$(T - T_s) = \frac{(-\Delta H)CD}{k_c} (X_s - X) \quad (5.15)$$

The maximum value of the LHS term is obtained when $X = 0$. So:

$$(T - T_s)_{max} = \frac{(-\Delta H)CDX_s}{k_c} \quad or \quad (5.16)$$

$$\beta = \left(\frac{T - T_s}{T_s} \right)_{max} = \frac{(-\Delta H)CDX_s}{k_c T_s} \quad (5.17)$$

According to detailed calculations performed by Weisz and Hicks [158] and Bischoff [159] isothermal conditions may be assumed with good accuracy for $\beta < 0.03$.

The typical values of parameters for carbon were chosen from literature [160]:

$$k_c = 16.75 \times 10^{-4} \frac{kJ}{m} \cdot s \cdot K$$

$$D = 2 \times 10^{-4} \text{ m}^2/s$$

$$-\Delta H = 2.24 \times 10^5 \text{ kJ/kgmol}$$

For instance, at $T = 773.15K$ and 21% O₂ the value of $\beta = 0.11$ is obtained which is out of the acceptable range.

The surface temperature of particle can also be estimated through the convective and radiation heat transfer with gas and furnace wall. The heat transfer for a particle can be written as:

$$m_p C_p \frac{dT_p}{dt} = h A_p (T_i - T_p) - \frac{dm_p}{dt} \Delta H + A_p \varepsilon_p \sigma (T_i^4 - T_p^4) \quad (5.18)$$

With the pseudo steady state assumption one gets:

$$\frac{dm_p}{dt} \Delta H = hA_p(T_i - T_p) + A_p \varepsilon_p \sigma (T_i^4 - T_p^4) \quad (5.19)$$

Where m_p is particle mass, h is convective heat transfer coefficient (w/m^2k), T_i and T_p are gas and particle temperatures, A_p is the external surface area of particle, ε_p is particle emissivity, and σ is Boltzmann constant.

At low temperatures that normally Char-O₂ reactivity is determined (<500°C) the radiation can be ignored in comparison to convection heat transfer, so the equation can be further simplified as:

$$m_0 \frac{dX_c}{dt} \Delta H = hA_p(T_p - T_i) \quad (5.20)$$

Here, X_c is conversion and m_0 is initial mass of particle. In terms of temperature gradient:

$$(T_p - T_i) = \frac{m_0 \Delta H}{hA_p} \frac{dX_c}{dt} \quad (5.21)$$

The maximum temperature gradient occurs when conversion rate is at its maximum value:

$$(T_p - T_i)_{max} = \frac{m_0 \Delta H}{hA_p} \left(\frac{dX_c}{dt} \right)_{max} \quad (5.22)$$

Considering that the maximum conversion rate at low temperatures range is about 10^{-3} (1/s) using a typical values for heat transfer coefficient and particle sizes of 100 micron calculated under typical TGA operating conditions of this study, the maximum temperature deviation of 0.5 K was found. It is clear that the released heat of reaction has more effect on intraparticle temperature gradient.

In this work we have adopted similar criterion of $\beta < 0.03$ to satisfy the isothermal particle assumption. However, it is worth noting that that the estimated intraparticle temperature gradient is the worst case and has not taken into consideration the effect of endothermic char-CO₂ reaction which can absorb a portion of released heat. Combining this criteria with the chemisorption criteria of Feng and Bhatia [106], the maximum temperature and O₂ mole percentage for Char-O₂ reactivity measurements in TGA were found to be 550°C and 4%, respectively.

In order to more accurately measure the temperature, the ceramic pans (Figure 5.5) were replaced with Platinum pans with similar dimensions of the modified ceramic pan. The interesting design feature of Q600 unit is that if the temperature difference between thermocouple beams which are directly in touch with sample pan grows more than 100°C, the TGA will automatically stops the run and prompts a system error (i.e. temperature out of range warning).

Figure 5.8 shows the Arrhenius plot char-O₂ reaction at 3% O₂ and X=50%. The linear trend of points confirms that we are in regime I or chemical reaction rate controlled regime (the effect of diffusion was already eliminated, section 5.3.1).

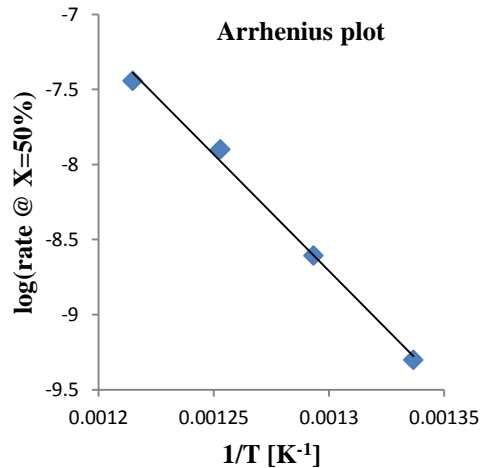


Figure 5.8 Arrhenius plot for char-O₂ reaction at 3% O₂ and 50% carbon conversion level in the range of 475°C-550°C

The activation energy was determined using isothermal TGA analysis at 475°C, 500°C, 525°C, and 550°C and 3% O₂. The rate exponent was also determined using a series of isothermal runs at 500°C and oxygen mole percentages of 1%, 2%, 3%, and 4%.

Figure 5.9 represents the temporal variation of carbon conversion measured by TGA at four different temperatures and a fixed O₂ partial pressure of 0.03 atm. The reaction rates were calculated from the slope of

conversion profiles at different levels of conversion between 0.1-0.9 for all 4 temperatures. The activation energy of char-O₂ reaction was calculated from the rate data by non-linear regression analysis using curve fitting toolbox in MATLAB. The activation energy was found relatively constant over the whole range of conversion. The average value of activation energy was determined as 134kJ/mol. Figure 5.10 show the variation of activation energy with conversion.

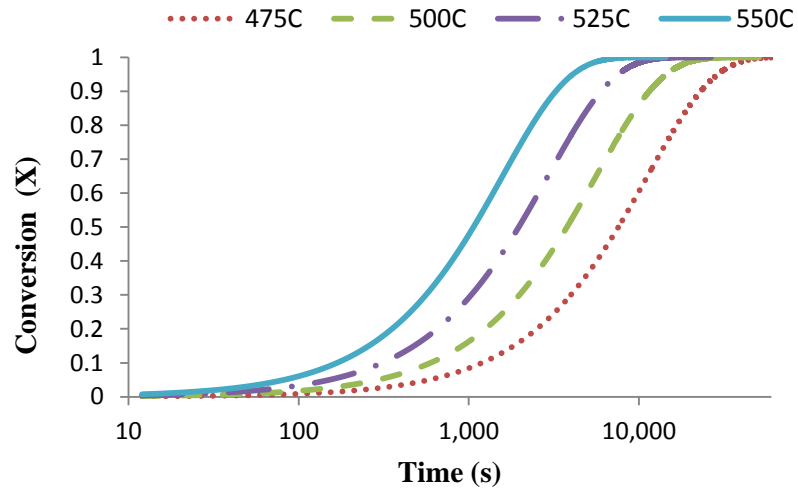


Figure 5.9 The temporal variation of carbon conversion as a function of temperature at 3% O₂

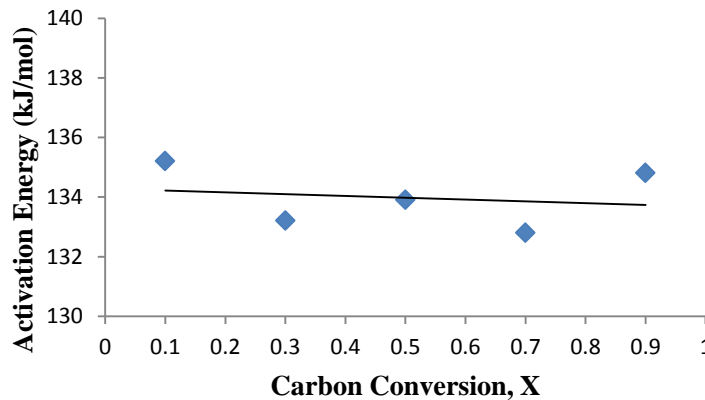


Figure 5.10 Variation of activation energy with conversion

Figure 5.11 represents the temporal variation of carbon conversion at 500°C measured by TGA for four different levels of O₂ partial pressure. Using a similar procedure the average rate exponent of reaction was found as $n = 0.87$.

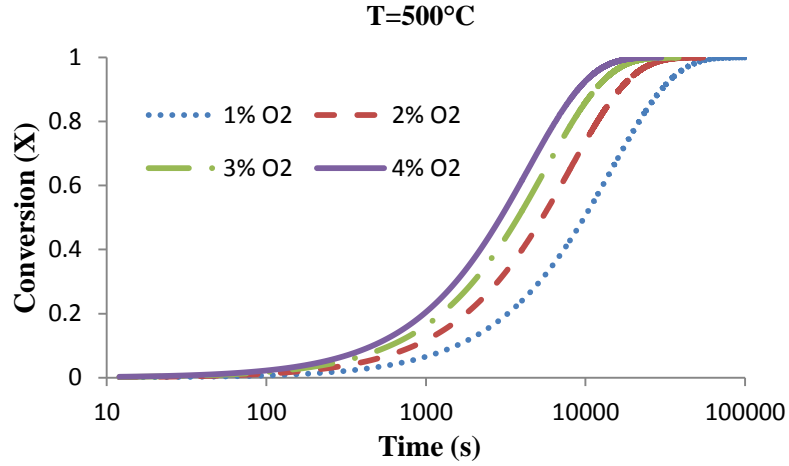


Figure 5.11 The temporal variation of carbon conversion at 500°C

In order to determining the intrinsic reaction rate, the reaction rates calculated at different levels of conversion for a fixed temperature and partial pressure were divided by specific surface area:

$$\frac{r(X)}{S(X)} = r_a = A \exp\left(-\frac{E}{RT}\right) P_{O_2}^n \quad (5.23)$$

Rearranging gives:

$$r(X) = r_a \cdot S(X) \quad (5.24)$$

So the objective here is to find the specific surface area which gives the best reduction in the variability of $r(X)$ (highest R^2) in the equation by using the regressor variable $S(X)$.

The frequency factor can be calculated from the slop of the line knowing the activation energy and reaction rate exponent. Four different specific surface areas were examined in this respect: N₂-BET surface area $S_{BET}(X)$, NLDFT/GCMC surface areas measured by a combination of N₂ and CO₂ adsorbates, $S_{NLDFT-GCMC}(X)$, Dubinin Radushkevich (DR) surface area using CO₂

adsorbate gas, $S_{DR}(X)$ and Active surface area measured by chemisorption of CO_2 , $S_{ASA}(X)$.

As mentioned earlier in this chapter, coke chars were gasified in carbon dioxide in a horizontal tube furnace for various times to generate chars with different conversion levels. The tube was stabilized and held at 800°C for 1hr under high purity N_2 to purge the oxygen. Overall four conversion levels were prepared for this study: 5%, 14%, 39%, and 76%.

The N_2 -BET of was determined for original and converted chars using Autosorb1 pore size analyzer within the relative pressure of 0.05-0.35 at 78K. The NLDFT/GCMC surface area was determined by a combination of N_2 adsorption for pore sizes down to 14\AA and CO_2 adsorption for pore size less than 14\AA at low relative pressures of 10^{-6} -1 and 10^{-5} - 10^{-2} , respectively. The DR surface area was determined using CO_2 at relative pressures less than 0.01. The ASA surface area measurement procedure was already discussed in section 5.3.3.

Figure 5.12 represents the pore size distribution of fluid coke char prepared at 1400°C . It is clear from the stacked column plot that N_2 can hardly diffuse into pores smaller than 14\AA and that fluid coke is mainly an ultra-microporous material with majority of pore surface area distributed between 6\AA to 14\AA . This could be the reason that previous works (e.g. [18]) using N_2 adsorption and mercury porosimetry have concluded that fluid coke is a non-porous solid. None of these techniques has the capability to measure the ultra-microporosity in fluid coke. It is important to notice that at high temperatures, these ultra-micropores are easily accessible to gasifying agents [27].

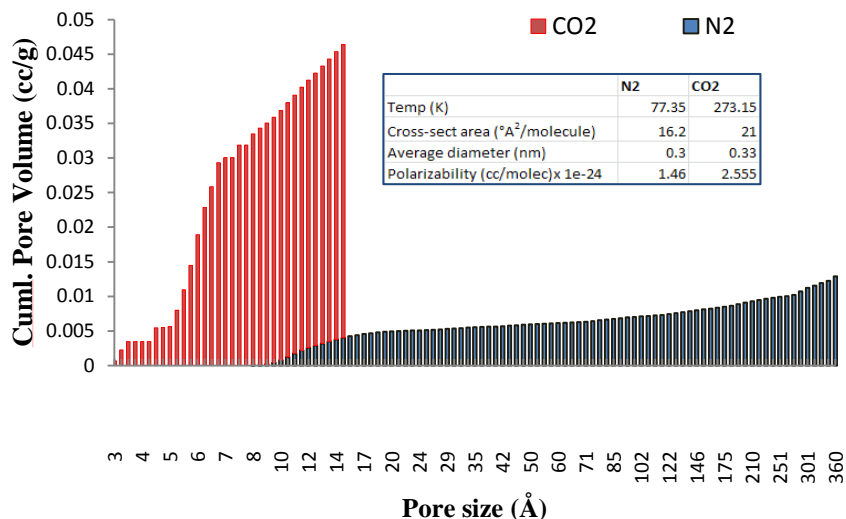


Figure 5.12 Porosity distribution in fluid coke char at X=0%

Table 5.1 and Table 5.2 show the variation of total surface area and active surface area with conversion, respectively. It can be seen that $S_{BET}(X)$ underestimate the pore development in char compare to other techniques. The fact that BET surface area is even less than measured ASA shows that a portion of ultra-micropores are also taking part in reaction which are not detectable by N_2 adsorption. However, it is worth mentioning that active surface area values are much closer to that of BET than the other two techniques.

Table 5.1 Variation of total Surface area with conversion for fluid coke char

Conversion (X)	Surface area (m ² /g)		
	$S_{DR}(X)$	$S_{NLDFT-GCMC}(X)$	$S_{BET}(X)$
0%	156	109	15
5%	190	141	25
14%	264	189	42
39%	320	232	61
76%	301	241	83

Table 5.2 Variation of active surface area with conversion for fluid coke char

Conversion	4.4%	26.7%	48.8%	71.1%
ASA (m ² /g)	38	54	72	96

To determine which specific surface area is more appropriate to be used for derivation of intrinsic reaction rate of chars, the reaction rates at different

conversion levels (the same levels used in Table 5.1 and Table 5.2) were determined from the TG profiles at 500°C and 0.03atm partial pressure of O₂. Then these rates were plotted against the corresponding surface areas. Figure 5.13 represents such a plot. From the figure it is obvious that the specific rate normalized with ASA gives the best results. However, none of the specific surface areas result in an acceptable range of R². Two reasons may cause this effect. First, the char preparation temperature for TSA and ASA measurements are different from the temperature the reactivity has been measured. Different temperature could result in different porosity development in char. Second, char preparation and ASA measurements were conducted in CO₂ atmosphere. Surface area development might be different in O₂ atmosphere used for rate measurement. Perhaps using TPD or TK experiments in combination with O₂ could give better results in this respect.

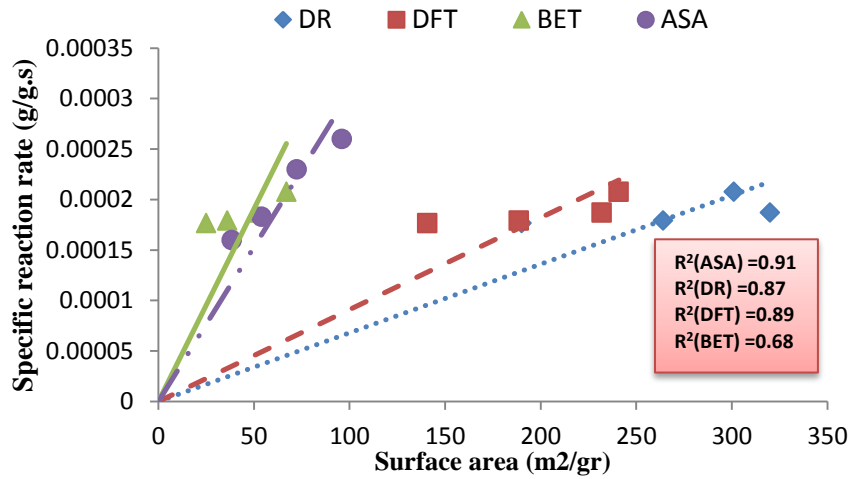


Figure 5.13 Specific rate as a function of different measures of surface area at 500°C and 3% O₂

However, using ASA as normalizing factor one could get a fair estimate of intrinsic rate. Doing so, the intrinsic reaction rate for char-O₂ reaction was determined from the slope of the corresponding line as:

$$r_a = 7.2 \times 10^4 \exp\left(-\frac{134000}{RT}\right) P_{O_2}^{0.87} \quad (5.25)$$

Where r_a is intrinsic rate expressed in $[g/m^2 \cdot s]$ and P_{O_2} is the partial pressure of oxygen in $[atm]$, R is universal gas constant in $[J/mol \cdot K]$, and T is temperature in $[K]$.

Similar results were obtained at different temperatures studied in this work. Figure 5.14 represents the plot of specific rate against active surface area at 4 different temperatures.

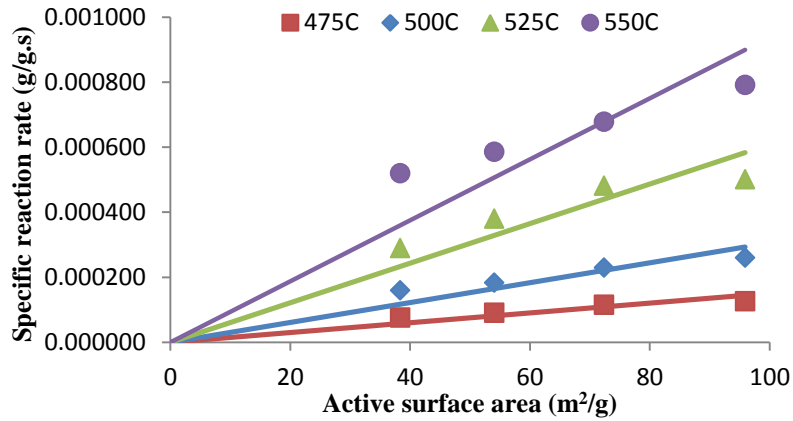


Figure 5.14 Specific rate as a function of different temperatures

5.5 Char-CO₂ reaction

The validity of TGA measurements for char-CO₂ reaction was also investigated by Feng and Bhatia [106] in a similar way. Unlike the char-O₂ reaction, they did not find any limitation on partial pressure of CO₂ as long as initial active surface area of carbon is less than 312 m²/g which is the case for fluid coke chars. No limitation regarding the heat transfer exists for a slow endothermic char-CO₂ reaction.

The activation energy was determined using isothermal TGA analysis at 950°C, 975°C, 1000°C, and 1025°C under pure CO₂ flow. The rate exponent was also determined using a series of isothermal runs at 1025°C and CO₂ partial pressures of 0.25, 0.50, 0.75, and 1.00 atm.

Figure 5.15 represents the Arrhenius plot of char-CO₂ reaction in the range of 950°C-1025°C for pure CO₂ at 50% carbon conversion level. The linear trend of points confirms that we are in regime I or chemical reaction rate controlled regime (the effect of diffusion was already eliminated, section 5.3.1). At temperatures above 1050°C, char-CO₂ reaction found to be affected by diffusion.

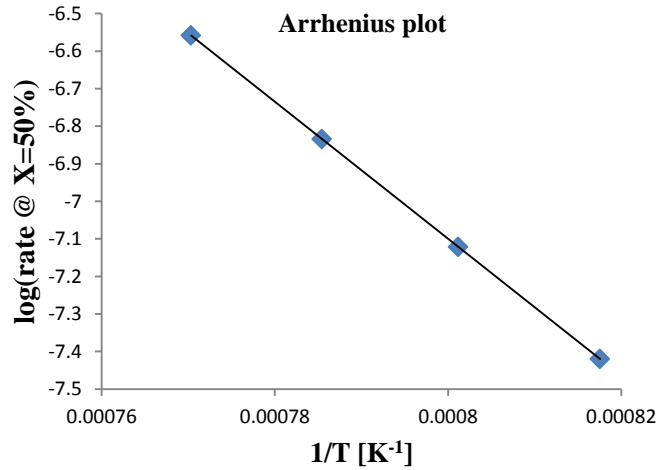


Figure 5.15 Arrhenius plot for char-CO₂ reaction at 100% CO₂ and 50% carbon conversion level in range of 950°C-1025°C

Figure 5.16 represents the temporal variation of carbon conversion measured by TGA at four different temperatures and 100% CO₂. The reaction rates were calculated from the slope of conversion profiles at different levels of conversion between 0.1-0.9 for all 4 temperatures. The activation energy of char-CO₂ reaction was calculated from the rate data by non-linear regression analysis using curve fitting toolbox in MATLAB. The activation energy was found relatively constant, similar to char-O₂ reaction, over the whole range of conversion. The average value of activation energy was determined as 151660 J/mol.

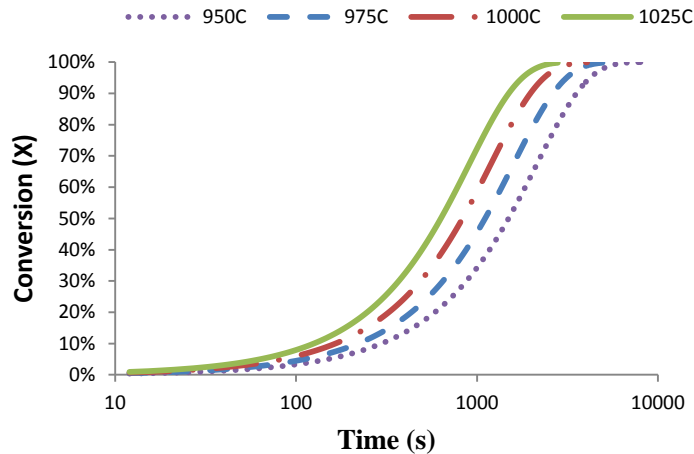


Figure 5.16 The temporal variation of carbon conversion as a function of temperature at 100% CO₂

The reaction rate exponent was measured using different partial pressure of CO₂ (0.25, 0.5, 0.75, and 1.00atm) at 1025°C and carbon conversion levels of 0.1, 0.3, 0.5, 0.7, and 0.9. The rates were determined from the slope of weight change profile. Using a non-linear regression, the average rate exponent of reaction was found as $n = 0.52$.

The BET specific surface area was determined by a similar procedure used for char-O₂ reaction. Figure 5.17 represents the plot of specific rate versus surface area for char-CO₂ reaction. It is clear from the plot that, similar to char-O₂ reaction, here again $S_{ASA}(X)$ gives the best linear fit with highest R^2 value, with the goodness of fit improved drastically compared to combustion reaction. Interestingly, $S_{BET}(X)$ also gives an equally good fit for char-CO₂ reaction, in contrast to char-O₂ reaction. The more important point to notice is that $S_{DR}(X)$ and $S_{GCMC-NLDFT}(X)$ still are not suitable for normalization of the specific reaction rates.

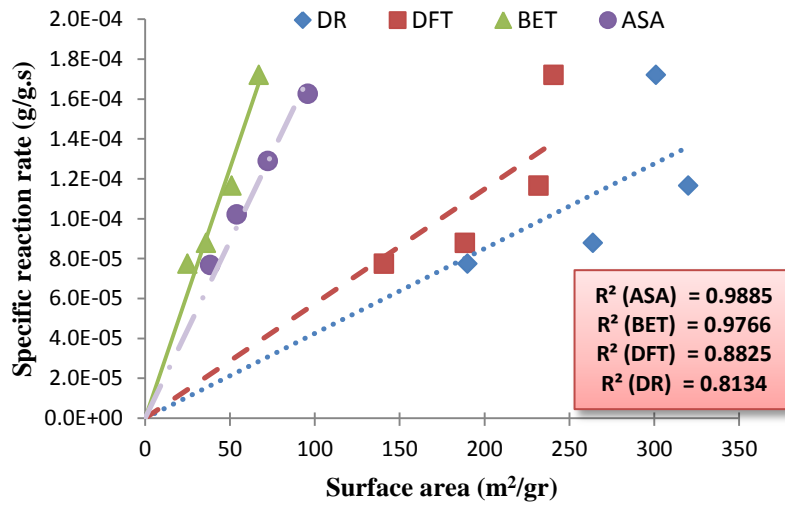


Figure 5.17 Specific rate as a function of different measures of surface area at 1025°C and 100% CO₂

Using ASA as the best normalizing factor for char-CO₂ reaction, the intrinsic reaction rate was calculated from the slope of the corresponding line as:

$$r_a = 24.41 \exp\left(-\frac{151660}{RT}\right) P_{CO_2}^{0.52} \quad (5.26)$$

Where r_a is intrinsic rate expressed in $[g/m^2 \cdot s]$ and P_{CO_2} is the partial pressure of CO₂ in $[atm]$, R is universal gas constant in $[J/mol \cdot K]$, and T is temperature in $[K]$.

Similar results were obtained at different temperatures studied in this work. Figure 5.18 represents the plot of specific rate against active surface area at 3 different temperatures.

Overall, the intrinsic rate for char-CO₂ reaction was measured with greater certainty compared to char-O₂ reaction. In case of char-CO₂ reaction, normalizing the specific rate by ASA pretty much explained all the variability of the rate over the whole range of carbon conversion. This higher certainty could be partially related to the fact that both the gasifying agent in TGA reaction rate measurements and ASA measurements were the same. Also, the temperatures which used to determine the reaction rates are much closer to that of ASA measurements.

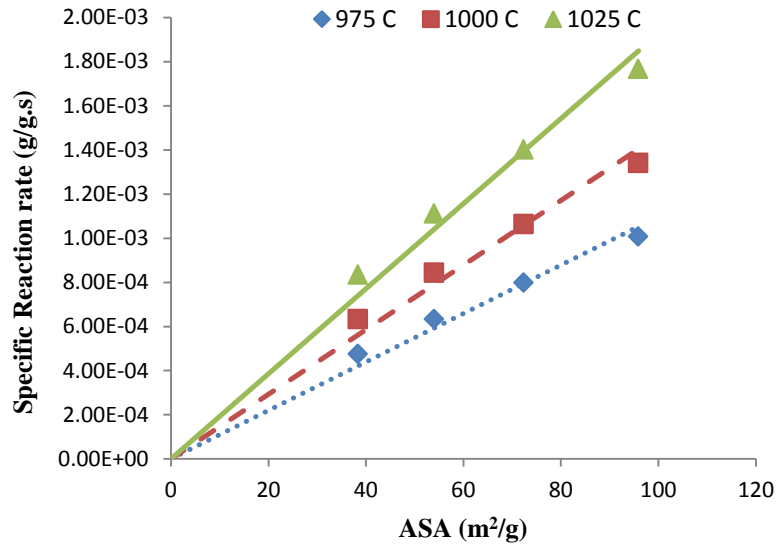


Figure 5.18 Specific rate as a function of different temperatures

5.6 Char-H₂O reaction

For char-H₂O reaction, the activation energy was determined using isothermal TGA analysis at 900°C, 925°C, 950°C, and 975°C and 50% H₂O. The rate exponent was also determined using a series of isothermal runs at 950°C and H₂O partial pressures of 0.20, 0.30, 0.40, and 0.50 atm.

Figure 5.19 represents the Arrhenius plot of char-H₂O reaction in the range of 900°C-975°C using 50% H₂O at 50% carbon conversion level. The linear trend of points confirms that we are in regime I or chemical reaction rate controlled regime (the effect of diffusion was already eliminated, section 5.3.1). At temperatures above 1000°C, char-H₂O reaction found to be affected by diffusion.

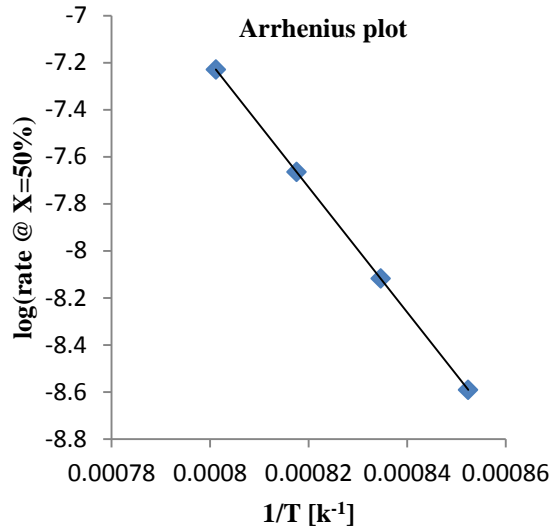


Figure 5.19 Arrhenius plot for char-H₂O reaction at 50% H₂O and 50% carbon conversion level in the range of 900°C-975°C

Figure 5.20 represents the temporal variation of carbon conversion measured by TGA at four different temperatures and 50% H₂O. The reaction rates were calculated from the slope of conversion profiles at different levels of conversion between 0.1-0.9 for all 4 temperatures. The activation energy of char-H₂O reaction was calculated from the rate data by non-linear regression analysis using curve fitting toolbox in MATLAB. The activation energy was found relatively constant, similar to char-O₂ and char-CO₂ reaction, over the whole range of conversion. The average value of activation energy was determined as 221000 J/mol.

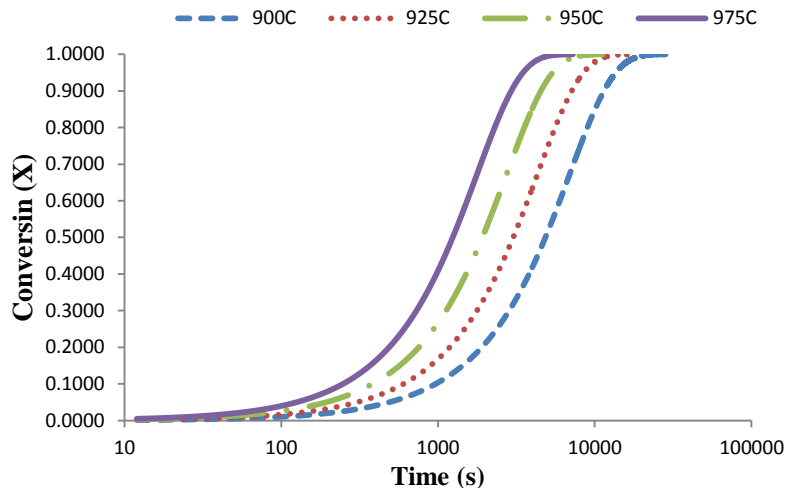


Figure 5.20 The temporal variation of carbon conversion as a function of temperature at 50% H₂O

The reaction rate exponent was measured using different partial pressure of H₂O (0.20, 0.30, 0.40, and 0.50 atm) at 975°C and carbon conversion levels of 0.1, 0.3, 0.5, 0.7, and 0.9. The rates were determined from the slope of weight change profile. Using a non-linear regression, the average rate exponent of reaction was found as $n \cong 1.0$.

Similar to other reactions, the bet's specific surface area was determined by fitting specific rates to surface area. Figure 5.21 represents the plot of specific rate versus surface area for char-H₂O reaction. It is clear from the plot that $S_{ASA}(X)$ gives the best linear fit with highest R^2 value, with the goodness of fit slightly less than char-CO₂ reaction. $S_{BET}(X)$ also gives an equally good fit for char-H₂O reaction. Both $S_{ASA}(X)$ and $S_{BET}(X)$ can be used to normalize the specific rate, with $S_{ASA}(X)$ being superior. Here again $S_{DR}(X)$ and $S_{GCMC-NLDFT}(X)$ did not find to be suitable for normalization of the specific reaction rates.

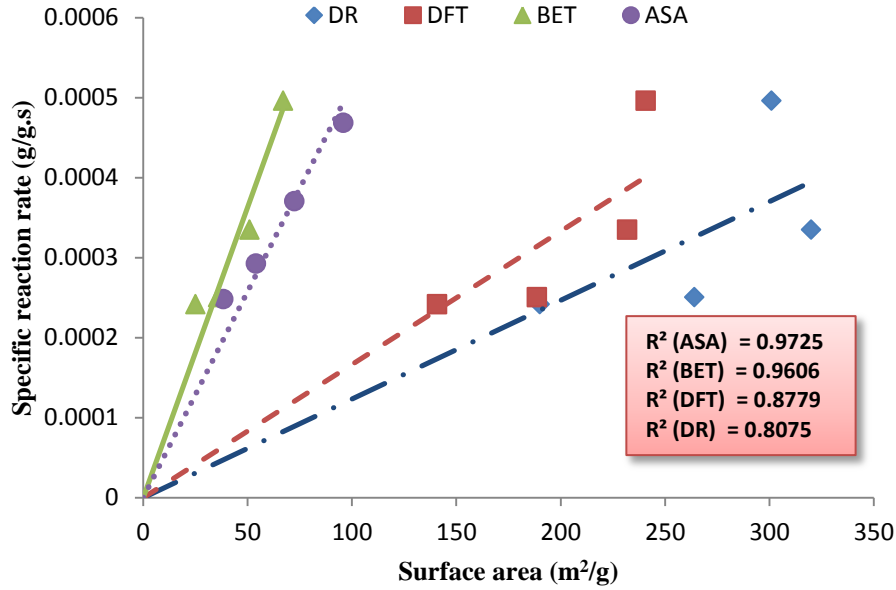


Figure 5.21 Specific rate as a function of different measures of surface area at 950°C and 40% H₂O

Using ASA as the best normalizing factor for char-H₂O reaction, the intrinsic reaction rate was calculated as:

$$r_a = 35364 \exp\left(-\frac{221000}{RT}\right) P_{H_2O} \quad (5.27)$$

Where r_a is intrinsic rate expressed in $[g/m^2 \cdot s]$ and P_{H_2O} is the partial pressure of steam in $[atm]$, R is universal gas constant in $[J/mol \cdot K]$, and T is temperature in $[K]$.

Similar results were obtained at different temperatures studied in this work.

Overall, the intrinsic rate for char-H₂O reaction was measured with greater certainty compared to char-O₂ reaction. However, the goodness of fits was slightly downgraded compared to char-CO₂ reaction.

Using the intrinsic rate functions and the relationship between specific and intrinsic reaction rates, a correlation for variation of active surface area as a function of conversion in the range of 5% to 85% carbon conversion was developed. The initial ASA of char was determined by extrapolation to zero conversion:

$$S_{ASA}(X) = 280.1X^3 - 350.97X^2 + 201.41X + 25.2 \quad (5.28)$$

This relation was used for CFD simulation of fluid coke gasification.

5.7 Chapter findings and conclusions

The intrinsic rates for Char-O₂, char-CO₂, and char-H₂O gasification reactions were developed for fluid coke. A through discussion was provided on the validity of thermogravimetric determination of char gasification kinetics with oxygen. For char-O₂ reaction, the application of thermogravimetric analyses for reaction rate determination for fluid coke was found limited to a maximum temperature of 550°C and 0.04atm partial pressure of oxygen. No limitations were found for char-CO₂ and char-H₂O endothermic reactions.

A detail discussion was also provided on the comparison of different designs of thermogravimetric analyzers. The modification of TA SDT-Q600 analyzer for steam injection and its sample pan was presented as well.

Four different specific surface area measurement techniques were used to normalize the specific reaction rate calculated from the weight loss profiles of TGA: N₂-BET surface area (macro- & meso-porosity), two microporosity measurement techniques based on GCMC-NLDFT and DR models, and finally active surface measured by CO₂ chemisorption at different levels of conversion. The specific reaction rates, calculated at different levels of conversion for a fixed temperature and partial pressure, were divided by specific surface area:

$$r(X) = r_a \cdot S(X)$$

The objective was to find the specific surface area which gives the best reduction in the variability of $r(X)$ (highest R^2) in the above equation by using the regressor variable $S(X)$.

Overall ASA was found to be the best regressor for deriving the intrinsic rates. Despite the fact that the variability of $r(X)$ was successfully reduced using ASA for char-CO₂ and char-H₂O reactions, the certainty in char-O₂ reaction was not as satisfactory as those of char-CO₂ and char-H₂O reactions. Nonetheless, a

fair estimate of intrinsic rate could still be developed using ASA. The reason could be linked to the different temperature at which the ASA and rates in TGA were measured.

Surface areas based on N₂-BET technique were also proven to be a better regressor for normalizing the specific rates compared to the ones based on GCMC-NLDFT and DR models.

CHAPTER 6⁴

CFD simulation of entrained flow gasifier

6.1 Introduction

The gasification process is one of the key technologies to any IGCC system, which is influenced by feedstock type and operating conditions. The importance of Alberta's oil sand coke was already discussed in section 1.4.1. It is of prime importance that the behavior of oil sand cokes is fully understood in order to assist industry section in their adoption of the new technologies. According to DOE/NETL gasification database [161] nearly all the planned gasifiers will be of the entrained flow family. Computer-based modeling is one of the methods whereby improved gasifier design can be analyzed and compared. Computational fluid dynamics has gained a significant acceptance in order to model and improve the dynamic processes occurring inside the gasifier using a minimum set of assumptions. Despite the profusion of works devoted to computational fluid dynamic simulation of gasification process, few have dealt

⁴ This work will be submitted for publication to The Canadian Journal of Chemical Engineering

with the modeling of the entrained flow gasifiers, leaving the majority of works focused on fluidized bed reactors. Also, of those studies dedicated to the modeling of entrained flow gasifiers, neither has focused on the use of intrinsic reaction rates nor has tried to model the gasification of fuel blends. Also, majority of the studies are lacking a proper solid fuel mass and energy conservation.

In this chapter, the CFD simulation of the entrained flow gasification process covering the underlying phenomenological aspects of reactor including the development of a new calculator scheme for Discrete Particle Modeling (DPM) option of ANSYS Fluent software (Eulerian-Lagrangian method) will be presented. The model includes the elemental mass and energy conservation in the solid fuels, multiple User Defined Functions (UDF) for modeling devolatilization, and char gasification/combustion using intrinsic reaction rates. The model is built upon the assumption that slag-char micromechanical interactions are negligible.

6.2 Numerical models

The presented 3D model in this work was added to the commercial ANSYS Fluent code via a series of User Defined Functions (UDF). Particle interaction with continuous phase was modeled using Discrete Particle Modeling (DPM) techniques available in Fluent. The reaction scheme were developed using the intrinsic rates developed for fluid coke in previous chapter.

For modeling entrained flow gasification, Fluent solves the time-averaged steady state Navier-Stokes equation in combination with the mass and energy conservation equations. The reaction scheme developed in this study consists of three processes: pyrolysis, char gasification and gas phase reactions.

6.2.1 Drying and devolatilization

During particle drying, all the moisture is assumed to leave the particle upon heating. This will happen almost instantaneously so no drying rate was calculated for drying. The moisture content of coke in Fluent is represented as

droplet which vaporizes as soon as the particle temperature exceeds the boiling point of water (in this case 373K). In case of high heating rates of the order of 40,000-60,000K/min, the whole moisture can be assumed to be in the gas phase instantaneously.

At high temperatures in entrained flow gasifier, the pyrolysis process completes in fraction of milliseconds. The devolatilization rate in this study was modeled using a single kinetic rate model:

$$-\frac{dm_p}{dt} = A \exp\left(-\frac{E}{RT}\right)[m_p - (1 - f_{v0})(1 - f_{w0})m_{p0}] \quad (6.1)$$

m_p = Particle mass [kg]

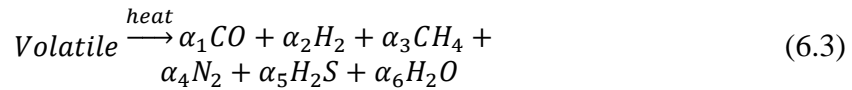
m_{p0} = Initial particle mass [kg]

f_{v0} = Mass fraction of volatile initially present in the particle

$A = 4.92 \times 10^5 [S^{-1}]$ & $E = 7.4 \times 10^7 [J/kgmol]$

f_{w0} = mass fraction of water in coke

Devolatilization process produces char, and gaseous species:



In Fluent char only consists of carbon and ash. The rest of elements are normally present in the gas phase as volatiles. So, the mass fractions of the most important volatile products from coke devolatilization were calculated according to Table 6.1:

Table 6.1 Yield of volatile gases

Yield (kg/kg gas mixture)	correlation
$X_{c,VM}$	$\frac{X_{C,coke} - FC_{daf}}{VM_{daf}}$
$X_{H,VM}$	$X_{H,coke}/VM_{daf}$
$X_{N,VM}$	$X_{N,coke}/VM_{daf}$
$X_{S,VM}$	$X_{S,coke}/VM_{daf}$
$X_{O,VM}$	$X_{O,coke}/VM_{daf}$

$X_{i,VM}$ and $X_{i,coke}$: mass fraction in volatile and coke, daf

VM_{daf} & FC_{daf} : volatile and fixed carbon in proximate analysis, daf

All ash is assumed to remain in the char. Given this information the chemical formula of the volatile was calculated in the form of $C_mH_nN_xS_yO_z$ using an elemental mass balance.

6.2.1.1 Fuel Energy Conservation

In Fluent a solid particle phase is simulated by breaking it down into volatile, char and moisture. Volatile thermally cracks to a variety of light gases. Moisture in coke is simulated by a separate liquid droplet, so-called, wet combustion model in Fluent. The remaining char contains the combustible fraction and ash. In this study all the volatile were calculated according to Table 6.1. A mass balance using proximate and ultimate analysis and volatile yield gives the chemical formula of the volatile ($C_mH_nN_xS_yO_z$).

In all these steps it is very important to make sure that the energy content of coke particle on a dry basis is conserved. This is done by properly calculating the formation enthalpy of volatile as follows:

$$h_{f,VM} = m \cdot h_{f,CO_2} + \frac{n}{2} \cdot h_{f,H_2O} + z \cdot h_{f,SO_2} + \frac{LHV_{coke,daf} - LHV_{char,daf}}{VM_{daf}} \cdot MW_{volatile} \quad (6.4)$$

$h_{f,VM}$ = Formation enthalpy of volatile [J/kmol]

$h_{f,i}$ = Formation enthalpy of CO₂, H₂O and SO₂ [J/kmol]

$LHV_{coke,daf}$ = Low heating value of coke on dry ash free basis [J/kg]

$LHV_{char,daf}$ = Low heating value of char on dry ash free basis [J/kg]

$MW_{volatile}$ = molecular weight of volatile [kg/kmol]

VM_{daf} = volatile mass fraction in proximate analysis on dry ash free basis

Where the low heating values on dry-ash-free basis is derived from the input of fuel high heating value on as-received basis. In this work the high heating value was calculated from the work of Channiwala and Parikh [162]:

$$HHV \left[\frac{MJ}{kg} \right] = 0.3491X_{C,db} + 1.1783X_{H,db} + 0.1005X_{S,db} - 0.1304X_{O,db} - 0.015X_{N,db} - 0.0211X_{ash,db} \quad (6.5)$$

$X_{i,db}$ = mass fraction of carbon, hydrogen, sulfur, oxygen, nitrogen and ash on a dry basis.

$$LHV_{coke,daf} = \frac{LHV_{coke,AR}}{1 - X_{ash,AR} - X_{M,AR}} \quad (6.6)$$

And

$$LHV_{coke,AR} = HHV_{coke,AR} - \left(X_{M,AR} + \frac{X_{H,AR} \cdot MW_{H_2O}}{2 MW_H} \right) \cdot \lambda_{H_2O} \quad (6.7)$$

With

$$X_{H,AR} = X_{H,daf} (1 - X_{ash,AR} - X_{M,AR}) \quad (6.8)$$

$X_{ash,AR}$ = mass fraction of ash in proximate analysis on as-received basis

$X_{M,AR}$ = mass fraction of moisture in proximate analysis on as-received basis

$LHV_{coke,AR}$ = Low heating value of coke on as-received basis [J/kg]

$HHV_{coke,AR}$ = High heating value of coke on as-received basis [J/kg]

$X_{H,AR}$ = mass fraction of hydrogen in ultimate analysis on as-received basis

$X_{H,daf}$ = mass fraction of hydrogen in ultimate analysis on dry ash free basis

MW = molecular weight [kg/kmol]

λ_{H_2O} = Latent heat of water: 2395780[J/kg]

The devolatilization and formation enthalpy of volatile matter were included as a scheme into the ANSYS Fluent.

6.2.2 Liquid droplets

As mentioned earlier, the moisture content of fuel particle is represented as liquid droplet in Fluent. So the evaporation rate of liquid droplet and its mass

and heat transfer are calculated under the particle evaporating law in fluent. Evaporation occurs at two steps depending on the particle temperature: (1) when temperature is higher than saturation temperature, depending on the water vapor concentration (2) when temperature is above boiling point of water. The rate of evaporation below boiling point is obtained by:

$$\frac{dm_p}{dt} = \pi d_p^2 k_g (C_s - C_\infty) \quad (6.9)$$

Here k_g is the mass transfer coefficient. C_s and C_∞ are concentration of the vapor at particle surface and bulk, respectively. The value of k_g is calculated from Ranz-Marshall equation [101]:

$$sh = \frac{k_g d_p}{D} = 2 + 0.6Re^{0.5} Sc^{0.33} \quad (6.10)$$

At boiling point, the evaporation rate is governed by

$$\frac{dm_p}{dt} = \pi d_p k_c (2 + 0.46Re^{0.5}) \ln \left(1 + \frac{c_p (T_\infty - T_p)}{h_{fg}} \right) / c_p \quad (6.11)$$

Here k_c is conductivity of the gas, h_{fg} is the droplet latent heat and c_p is the specific heat of bulk flow.

The droplet temperature can also be calculated using the following equation:

$$m_p c_p \frac{dT}{dt} = A_p h (T_\infty - T_p) + \frac{dm_p}{dt} h_{fg} + \varepsilon_p A_p \sigma (\theta_R^4 - T_p^4) \quad (6.12)$$

θ_R is the radiation temperature. The convective heat transfer, h , is calculated as:

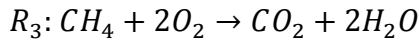
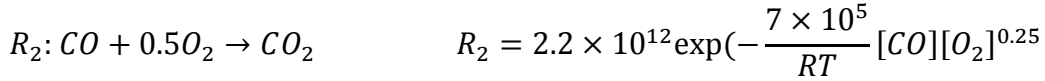
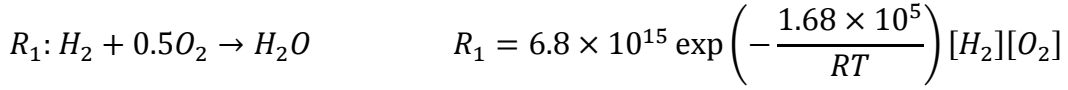
$$Nu = \frac{h d_p}{k_c} = 2.0 + 0.6Re^{0.5} Pr^{0.5} \quad (6.13)$$

Here Nu is the Nusselt number, and Pr is the Prandtl number.

6.2.3 Volatile oxidation

The volatile matter is composed of CO, H₂, H₂S, N₂, and CH₄. Among these gases, CO, H₂, and CH₄ are combustible gases. So after the pyrolysis, these

combustible gases will react with oxygen fed into the gasifier as shown in the following reactions:

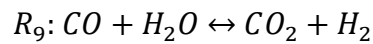
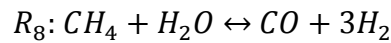
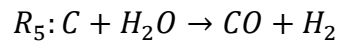
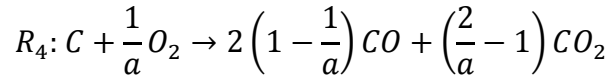


$$R_3 = 2.119 \times 10^{11} \exp\left(-\frac{2.027 \times 10^5}{RT}\right) [CH_4]^{0.2}[O_2]^{1.3}$$

Here R_i are reaction rates expressed in units of [kmol/m³/s] and R is universal gas constant in units of [J/mol/K]. The reaction rates for (R_2 - R_4) were adopted from Westbrook [163] and Jones [164].

6.2.4 Gasification reactions

After the volatile combustion process, the char from pyrolysis is further gasified by the reaction with gases in the gas phase. This process may include reactions (R_1 - R_3) above, as well as following reactions:



In reaction (R_4), a is a coefficient which depends on the diameter of the particle (d_p) and can be calculated by the relations in Table 6.2. For a given temperature, a is constant at $d_p < 0.005$ and $d_p > 0.1$ cm. At $0.005 < d_p < 0.1$ cm, a decreases with the increase in d_p . For a given d_p , a shows a slight change with the temperature at $d_p \leq 0.1$ cm. At $d_p > 0.1$ cm, a is independent of temperature and has the value of 1.0.

Table 6.2 Expressions of a for different size of fuel particle[145]

d_p (cm)	a	comment
<0.005	$2Z + 2/Z + 2$	$Z = \frac{[CO]}{[CO_2]}$ $= 2500 \exp(-\frac{6249}{T_p})$
0.005-0.1	$\frac{(2Z + 2) - Z(d_p - 0.005)/0.095}{Z + 2}$	
>0.1	1.0	

The reaction kinetics developed in previous chapter was used for R_4 - R_6 . The rates for R_7 - R_9 were adopted from the work of Wen [145]. Table 6.3 represents the kinetics of the reactions.

Table 6.3 Kinetics of reaction R_4 - R_9

Rxn	rate	Comment	unit
R_4	$7.2 \times 10^4 \exp\left(-\frac{134000}{RT}\right) P_{O_2}^{0.87}$	-	g/m ² /s
R_5	$35364 \exp\left(-\frac{221000}{RT}\right) P_{H_2O}$	-	g/m ² /s
R_6	$24.41 \exp\left(-\frac{151660}{RT}\right) P_{CO_2}^{0.52}$	-	g/m ² /s
R_7	$0.12 \exp\left(-\frac{17921}{T}\right) \left(P_{H_2} - \sqrt{\frac{P_{CH_4}}{K_{eq}}}\right)$	$K_{eq} = \frac{0.175}{34173} \exp\left(\frac{18400}{1.8T}\right)$	g/cm ² /s
R_8	$312 \exp\left(-\frac{30000}{1.987T}\right) \left(C_{CH_4} - \frac{C_{CO} C_{H_2}^3}{K_{eq} C_{H_2O}}\right)$	$K_{eq} = \exp\left(33.14 - \frac{25014.05}{T}\right)$	mol/m ³ /s
R_9	$2.77 \times 10^5 (x_{CO} - x_{CO}^*) \cdot \exp\left(-\frac{27760}{1.987T}\right) P_t^{0.5 - \frac{P_t}{250}} \exp(-8.91 + \frac{5553}{T})$	$x_{CO} = \frac{P_{CO}}{P_t}$ $x_{CO}^* = \frac{1}{P_t} \frac{P_{CO_2} P_{H_2}}{K_{eq} P_{H_2O}}$ $K_{eq} = \exp\left(-3.6893 + \frac{7234}{1.8T}\right)$	mol/m ³ /s

6.2.4.1 Particle reactions

Conversion level and gas composition in gasification is controlled by heterogeneous reaction rates due to their relative slowness compared with the combustion reactions. For the present modeling purposes, an empirical nth order

rate equation with an effectiveness factor is used to represent the overall reaction rates in these different regimes by using an appropriate effectiveness factor. The solid particle reaction rates in Fluent have to be in units of [kg/s].

The general reaction rates model representing all three regimes mentioned above is normally expressed as:

$$\widehat{R}_{p,j} = (\eta A_i + A_e) \widehat{k} P_{s,j}^m \quad [\text{g/g s}^{-1}] \quad (6.14)$$

Where A_i is the specific internal surface area which is a function of conversion (m^2/gr). In this study, the correlation of ASA as a function of conversion estimated in chapter 5 was used:

$$A_i = 280.1X^3 - 350.97X^2 + 201.41X + 25.2 \quad (6.15)$$

A_e is the external surface area of particle. From the A_i correlation it is clear that $A_i \gg A_e$. So, the reaction rate simplifies as:

$$\widehat{R}_{p,j} = \eta A_i \widehat{k} P_{s,j}^m \quad [\text{g/g s}^{-1}] \quad (6.16)$$

η is the effectiveness factor defined as: [77, 165]

$$\eta = \frac{3}{\phi} \left(\frac{1}{\tanh \phi} - \frac{1}{\phi} \right) \quad (6.17)$$

Here ϕ is dimensionless Thiele modulus [166] which is defined as:

$$\phi = \frac{d_p}{6} \left(\frac{(m+1) \widehat{k} \rho_a \nu_g A_g R T_g P_s^{m-1}}{2 M_c D_e} \right) \quad (6.18)$$

d_p = diameter of char particle [m]

m = reaction order []

\widehat{k} = intrinsic rate constant on area basis [$\text{kg} \cdot \text{m}^{-2} \cdot \text{S}^{-1} \cdot \text{atm}^{-m}$]

ρ_a = apparent density [$\text{kg} \cdot \text{m}^{-3}$]

ν_g = stoichiometric coefficient (gas moles /Carbon moles) []

A_g = specific internal surface area [$\text{m}^2 \cdot \text{g}^{-1}$]

P_s = partial pressure of gaseous reactant at the surface of particle [atm]

R = universal gas constant [$\text{atm} \cdot \text{m}^3 \cdot \text{kmol}^{-1} \cdot \text{k}^{-1}$]

T_g = gas temperature [K]

D_e = effective diffusivity [$\text{m}^2 \cdot \text{s}^{-1}$]

M_c = molecular weight of carbon [kg/kmol]

The reaction rate can be further expressed in terms of particle external surface area as:

$$R_{P,j} = \frac{\rho_a d_p}{6} \eta A_i \hat{k}_{P,s,j}^m \quad [\text{g}/\text{m}_{P,\text{ext}}^2 \text{ s}^{-1}] \quad (6.19)$$

Properties of solid particle were calculated according to Table 6.4. Variation of particle density with carbon conversion was taken into account using the density evolution parameter β .

Table 6.4 Solid phase properties

Expression	Ref
$\frac{1}{\rho_{P_0}} = \frac{X_{char,daf}}{\rho_{char,daf}} + \frac{X_{ash}}{\rho_{ash}}$	[166, 167]
$\rho_P = \rho_{P,0} \left(\frac{m_P}{m_{P,0}} \right)^{\frac{\beta}{3+\beta}}$ $\beta = \eta d_P A_i / 2V_P$	
$d_P = d_{P,0} \left(\frac{\rho_P}{\rho_{P,0}} \right)^{-\frac{1}{3}} \left(\frac{m_P}{m_{P,0}} \right)^{\frac{1}{3}}$	
$m_P = \rho_P V_P, \quad \varepsilon = \varepsilon_0 + (1 - \varepsilon_0)X \quad V_P = \pi d_P^3 / 6$	

X_i = mass fraction of char and ash, V_P = particle volume [m^3], ε = porosity

D_e is the coefficient of diffusion of reactants through the pores of the particle. Its definition combines the effect of both molecular and Knudsen diffusion [168]:

$$D_e = \frac{\varepsilon}{2} \left(\frac{1}{D_i} + \frac{1}{D_k} \right) \quad (6.20)$$

$$D_k = 2 \times 10^6 \frac{\bar{r}_{pore}}{3} \sqrt{\frac{8RT_g}{\pi MW_i}} \quad (6.21)$$

r_{pore} = average pore radius [μm]

MW_i = molecular weight of component i

The average pore radius was adopted from Haynes [169] defined based on the correlation as:

$$\bar{r}_{pore}(X) = \frac{2\varepsilon}{\rho_p A_i(X)} = \frac{2[\varepsilon_0 + (1 - \varepsilon_0)X]}{\rho_p A_i(X)} \quad (6.22)$$

The partial pressure of reactant at the particle surface, $P_{s,j}$, in particle reaction rate, $R_{P,j}$, is unknown, but it can be estimated using the bulk diffusion rate as:

$$\frac{k_g}{RT_g}(P_g - P_s) = R_{P,j}v_g/M_C \quad (6.23)$$

k_g = mass transfer coefficient between fluid and particle [m/s]

P_g = partial pressure of gaseous reactant in bulk of gas [atm]

k_g can be calculated from Frössling [170] equation as:

$$\frac{k_g d_p}{D} = 2 + (Sc)^{\frac{1}{3}}(Re)^{\frac{1}{2}} = 2 + 0.6 \left(\frac{\mu_g}{\rho_g D} \right)^{\frac{1}{3}} \left(\frac{d_p |u_g - u_p| \rho_g}{\mu_g} \right)^{1/2} \quad (6.24)$$

μ_g = gas viscosity [Pa.s]

ρ_g = gas density [kg/m³]

D = molecular diffusivity [m²/s]

u_g = gas velocity [m/s]

u_p = particle velocity [m/s]

Sc = Schmidt number []

Re = Reynolds number []

In entrained flow gasification, relative velocities between gas and particle are usually sufficiently small. In this case the second term in Frössling equation can be ignored and the equation simplifies as:

$$\frac{k_g d_p}{D} = 2 \quad (6.25)$$

Replacing k_g from this equation results:

$$P_{s,j} = P_{g,j} - \frac{R_{P,j}}{K_d} \quad (6.26)$$

Where

$$K_d = \frac{2M_c D}{\nu_g d_p R T_g} = \frac{24}{\nu_g d_p R T_g} D = \frac{24}{\nu_g d_p R T_g} D_0 \left(\frac{T_m}{T_0} \right)^{1.75} \quad (6.27)$$

T_0 = reference temperature [K]

$$T_m = \frac{T_p + T_g}{2} \text{ [K]}$$

T_p = particle temperature [K]

T_g = gas temperature [K]

D_0 = molecular diffusivity at reference temperature [m^2/s]

Plugging $P_{s,j}$ into the rate equation gives:

$$R_{P,j} = \frac{\rho_a d_p}{6} (\eta A_i) \hat{k} \left(P_{g,j} - \frac{R_{P,j}}{K_d} \right)^m \quad (6.28)$$

It is clear that an iterative procedure is needed to determine $R_{P,j}$. Fluent uses Brent's method [171] for solving this problem.

The particle reaction rate in fluent is expressed in units of [kg/s]. So the rate is multiplied by external surface area to give:

$$\bar{R}_{P,j} = \frac{\pi d_p^2}{1000} R_{P,j} \quad \left[\frac{\text{kg}}{\text{s}} \right] \quad (6.29)$$

6.2.5 Gas phase reactions

Global reactions were used to describe the gas phase reactions mentioned earlier. The Finite-Rate/Eddy-Dissipation model in fluent was used to calculate the reaction rate:

Eddy-dissipation model takes into account the turbulent mixing of the gases. It assumes that the chemical reaction is faster than the time scale of the turbulence eddies. Thus, the reaction rate is determined by the turbulence mixing of the species. The reaction is assumed to occur instantaneously when the reactants meet.

In Finite-Rate/Eddy-Dissipation model, the net rate of production or destruction of a species is given by the smaller of the expressions below:

$$R_{i,r} = v'_{i,r} \cdot MW_i \cdot A \cdot \rho \cdot \frac{\varepsilon}{k} \min\left(\frac{Y_R}{v'_{R,r} \cdot MW_R}\right) \quad (6.30)$$

$$R_{i,r} = v'_{i,r} \cdot MW_i \cdot AB \cdot \rho \cdot \frac{\varepsilon}{k} \frac{\sum Y_p}{\sum v''_{j,r} MW_j} \quad (6.31)$$

$$R_{i,r} = A_i \exp\left(-\frac{E_i}{RT}\right) [X]^a [Y]^b \quad (6.32)$$

Where

Y_p = the mass fraction of any product species, p

Y_R = the mass fraction of a particular reactant, R

A = an empirical constant equal to 4.0

B = and empirical constant equal to 0.5

$\frac{\varepsilon}{k}$ = Inverse of large-eddy mixing time scale

v' & v'' = reactant and product stoichiometric ratio

ρ = density [kg/m³]

Due to their complexities, sub-models to determine the reaction rates for heterogeneous char reactions, water-gas shift and methane steam reforming reactions were separately developed and exported to Fluent as user-defined functions (UDFs). In order to incorporate the realistic particle diameter and particle density changes in fluent, the default DPM laws in Fluent had to be recoded and replaced with a custom DPM law developed using the available macros features in package.

6.2.6 Continuous phase equations

The gas phase was assumed incompressible. The governing mass, momentum equations are:

$$\frac{\partial}{\partial x_i} (\rho u_i) = S_p \quad (6.33)$$

$$\frac{\partial}{\partial x_i}(\rho u_i u_j) = \rho g - \frac{\partial P}{\partial x_i} + \frac{\partial}{\partial x_j} \mu \left[\frac{\partial u_j}{\partial x_i} + \frac{\partial u_i}{\partial x_j} \right] - \frac{\partial}{\partial x_j} (\overline{\rho u'_i u'_j}) + S_u \quad (6.34)$$

Where terms S_p and S_u are the source terms due to the presence of particles, P is the pressure and μ is the viscosity. u_i is the average velocity and u'_i is the velocity fluctuation. The Reynolds stress is expressed by the hypothesis of Boussinesq [172].

$$-\overline{\rho u'_i u'_j} = -\frac{2}{3} \rho k \delta_{ij} + \mu_e \left(\frac{\partial u_j}{\partial x_i} + \frac{\partial u_i}{\partial x_j} \right) \quad (6.35)$$

A standard $k - \varepsilon$ turbulent model [172] was utilized to solve turbulence. The turbulence kinematic viscosity (μ_e/ρ) is given by:

$$v_e = C_\mu k^2 / \varepsilon \quad (6.36)$$

The transport equations for k and ε are:

$$\frac{\partial}{\partial x_i}(\rho u_i k) = P_k + \frac{\partial}{\partial x_i} \left(\frac{\mu_e}{\sigma_k} \frac{\partial k}{\partial x_i} \right) - \rho \varepsilon \quad (6.37)$$

$$\frac{\partial}{\partial x_i}(\rho u_i \varepsilon) = \frac{\partial}{\partial x_i} \left(\frac{\mu_e}{\sigma_\varepsilon} \frac{\partial \varepsilon}{\partial x_i} \right) - \frac{\varepsilon}{k} (C_{\varepsilon 1} P_k - C_{\varepsilon 2} \varepsilon) \quad (6.38)$$

Where the production term P_k is defined by:

$$P_k = \frac{1}{2} v_e \left(\frac{\partial u_j}{\partial x_i} + \frac{\partial u_i}{\partial x_j} \right)^2 \quad (6.39)$$

The turbulent model constants were adopted from Launder et al. [173] work:

$$C_\mu = 0.09, C_{\varepsilon 1} = 1.44, C_{\varepsilon 2} = 1.92, \sigma_k = 1.0, \sigma_\varepsilon = 1.3$$

The turbulence models are valid for the turbulent core flows, i.e. the flow in the regions somewhat far from walls. The flow very near the walls is affected by the presence of the walls. Viscous damping reduces the tangential velocity fluctuations and the kinematic blocking reduces the normal fluctuations. So, in near wall region a wall function, was employed to connect the viscosity-affected region between the wall and the fully-turbulent region. The wall functions consist of laws-of-the-wall for mean velocity and temperature (or other scalars) and

formulas for near-wall turbulent quantities. In this study the standard wall function in Fluent was employed. The momentum is expressed as:

$$U^+ = \frac{1}{\kappa} \ln(Ey^+) \quad (6.40)$$

Where

$$U^+ = \frac{U'_P C_\mu^{1/4} k^{1/2}}{\tau_\omega / \rho} \quad (6.41)$$

$$y^+ = \frac{\rho C_\mu^{1/4} k^{1/2} y_P}{\mu} \quad (6.42)$$

κ = von Karman constant (=0.42)

E = empirical constant (=9.793)

U'_P = mean velocity of fluid at point P

k = turbulence kinetic energy at point P

y_P = distance from point P to wall

The wall function for the temperature is given as:

$$T^+ = \frac{(T_W - T_P) \rho c_p C_\mu^{1/4} k^{1/2}}{\dot{q}} = \begin{cases} Pr \cdot y^+, & y^+ < y_T^+ \\ Pr_t \left[\frac{1}{\kappa} \ln(Ey^+) + P' \right], & y^+ > y_T^+ \end{cases} \quad (6.43)$$

Where

$$P' = 9.24 \left[\left(\frac{Pr}{Pr_t} \right)^{3/4} - 1 \right] \left[1 + 0.28 \exp\left(-\frac{0.007}{Pr_t}\right) \right] \quad (6.44)$$

c_p = specific heat of fluid

\dot{q} = wall heat flux

T_P = temperature at cell adjacent to the wall

T_W = temperature at the wall

Pr = molecular Prandtl number

Pr_t = turbulent Prandtl number (0.85 at the wall)

y_T^+ = non-dimensional thermal sub-layer thickness

The species transport is modeled similar to heat transfer:

$$T^+ = \frac{(Y_{iW} - Y_i)\rho c_p C_\mu^{1/4} k^{1/2}}{J_{iW}} = \begin{cases} Sc \cdot y^+, & y^+ < y_c^+ \\ Sc_t \left[\frac{1}{\kappa} \ln(Ey^+) + P_c' \right], & y^+ > y_c^+ \end{cases} \quad (6.45)$$

Where Y_i is the local mass fraction of species I, Sc and Sc_t are the molecular and turbulence Schmidt numbers, respectively. J_{iW} is diffusion flux at wall. P_c' and y_c^+ are analogous to heat transfer.

In the k- ϵ model, the k equation is solved in the whole domain, including the wall adjacent cells. The boundary condition for k imposed at the wall is

$$\frac{\partial k}{\partial n} = 0 \quad (6.46)$$

Where n is the coordinate perpendicular to the wall.

The governing equations of energy and chemical species mass fraction equation are:

$$\frac{\partial}{\partial x_i} (\overline{\rho u_i h}) = \frac{\partial}{\partial x_i} \left(\lambda \frac{\partial T}{\partial x_i} \right) + S_{ph} \quad (6.47)$$

$$\frac{\partial}{\partial x_i} (\overline{\rho u_i y_i}) = \frac{\partial}{\partial x_i} (\rho D Y_i) + S_{pY_i} + R_{fY_i} \quad (6.48)$$

where λ and D are the thermal conductivity of diffusion coefficient, respectively. S_{ph} and S_{pY_i} are the source terms of the particle transport, and R_{fY_i} is the source term of the chemical reactions. The Reynolds flux in above equations is given by:

$$-\overline{\rho u'_i \phi} = \frac{\partial}{\partial x_i} \left(\frac{\mu_e}{\sigma_t} \frac{\partial \phi}{\partial x_j} \right) \quad (6.49)$$

The turbulent Prandtl number σ_t was set to 0.9.

6.2.7 Radiation model

The P-1 model was used to calculate the flux of the radiation at the inside walls of the gasifier. The emissivity of the inner wall and particle were set to 0.9 and 0.35, respectively. The directional emissivity of gas obtained by the correction of the coexistence of carbon dioxide with steam on Leckner's diagram

[174]. The scattering coefficient due to the existence of particles was set to 0.77 recommended by Watanabe and Otaka [125].

The heat sources or sinks due to radiation is calculated as:

$$-\nabla \cdot \mathbf{q}_r = aG - 4a\sigma T^4 \quad (6.50)$$

Where

$$q_r = -\frac{1}{3(a + \sigma_s) - C\sigma_s} \nabla G \quad (6.51)$$

Here q_r is the radiation heat flux, a is the absorption coefficient, σ_s is the scattering coefficient, G is the incident radiation, C is the linear-anisotropic phase function coefficient, and σ is the Stefan-Boltzmann constant.

Effect of particles in radiation model in Fluent is modeled by:

$$-\nabla \cdot \mathbf{q}_r = -4\pi \left(\frac{a\sigma T^4}{\pi} + \varepsilon_p \right) + (a + a_p)G \quad (6.52)$$

Where ε_p and a_p are the emissivity and absorption of the particles, respectively.

The flux of radiation at walls caused by incident radiation of G_W is defined by:

$$q_{r,W} = -\frac{4\pi\varepsilon_W \frac{\sigma T^4}{\pi} - (1 - \rho_W)G_W}{2(1 + \rho_W)} \quad (6.53)$$

Where ε_W is the emissivity and is defined as:

$$\varepsilon_W = 1 - \rho_W \quad (6.54)$$

ρ_W is the wall reflectivity.

6.2.8 Particle transport equations

The fuel particle was modeled in Lagrangian coordinate where particles were assumed to consist of a mixture of volatile matter, carbon and ash, and represented as a homogeneous, spherical shape with the Rosin-Rammler particle size distribution. The transfer of momentum, heat, and mass between gas phase and particle phase are modeled, in addition to transportation of the particles.

The governing equation of the particle trajectory is:

$$m_p \frac{dU_p}{dt} = \sum F_i \quad (6.55)$$

Where m_p the particle is mass, U_p is the particle velocity. $\sum F_i$ represents the sum of all momentum exchange mechanisms between solid particles and fluid phase.

Studies conducted on the dynamics of a single particle in a fluid have proved several mechanisms of momentum transfer between solid particles and fluid [175]:

6.2.8.1 Drag force

At low Reynolds number, the inertial terms in the Navier-Stokes equations may be neglected. The resulting drag force on a sphere is given by:

$$F_D = 6\pi r_p \mu u_r \quad (6.56)$$

where μ is the viscosity of the fluid, r_p is the radius of particle, and u_r is relative velocity between gas and particle. This equation is known as Stokes' law for the resistance of a moving sphere.

Forces exerted on bodies moving through a fluid are generally expressed in terms of a dimensionless drag coefficient, C_D , defined through the relation:

$$C_D = \frac{F_D}{1/2 \rho u_r^2 \pi r_p^2} \quad (6.57)$$

With this definition drag equation is represented as:

$$C_D = \frac{24}{Re} \quad (6.58)$$

$$Re = \frac{2r_p u_r \rho}{\mu} \quad (6.59)$$

This drag coefficient is generally an acceptable approximation up to $Re = 0.2$. This equation was further modified including the inertial terms of the Navier-Stokes equations for the flow field far from the body [176]:

$$C_D = \frac{24}{Re} \left(1 + \frac{3}{16} Re\right) \quad (6.60)$$

and is applicable for values of Reynolds number up to about 2. The drag coefficients for higher Reynolds numbers are summarized by Ranade [177].

In this study the following drag force was used as [172]:

$$C_D = \begin{cases} 0.424 & Re > 1000 \\ \frac{24}{Re} \left(1 + \frac{1}{6} Re^{\frac{2}{3}} \right) & Re \leq 1000 \end{cases} \quad (6.61)$$

6.2.8.2 Lift force

It is observed that spheres in laminar Poiseuille flow through a pipe (at low Re) accumulate in an annulus some distance from the tube axis. Following the initial observations, a number of investigators verify this ‘tubular pinch’ effect and attempt to explain the lateral (or lift) force acting on the spheres (Denton et al., [178]). Though some authors attempt to explain the radial migrations in terms of particle spin (i.e., Magnus forces), spheres prevented from spinning also reached equilibrium positions between wall and centerline ([178]). Bretherton [179] shows that based on creeping flow equations; there is no lateral force on a single rigid spherical particle in a unidirectional flow. Saffman [180] deduced that, since experimental results contradict this conclusion, inertial effects must be involved. Saffman obtains a result for ‘slip-shear’ lift on a particle at low Reynolds number analogous to a result derived earlier for ‘spin’ lift by Rubinow and Keller [181]. Saffman included the particle spin in his analysis and showed that, under circumstances in which his results and Rubinow and Keller’s results strictly apply, the “shear” lift dominates the “spin” lift.

6.2.8.2.1 Slip-shear lift force

Saffman [180] used an expansion valid for small values of the reciprocal viscosity to calculate the lift force on a small sphere in a slow unbounded simple shear flow. His result is given by:

$$F_L = 6.46\mu^{0.5}\rho^{0.5}r_p^2k^{0.5}u_r \quad (6.62)$$

Where k'' is the velocity gradient in simple shear. Even though Saffman has retained the inertial terms of the Navier-Stokes equations in his analysis, the flow is not inertially dominated. Saffman's analysis of lift force includes the following implicit assumptions: the flow is uniform and parallel, the slip velocity is parallel to the plane of fluid shear, the shear or velocity gradients of the fluid are linear, and the particle spin vector lies in the plane of fluid shear but is normal to the slip vector. The lift force Saffman derived is normal to the slip vector and the spin vector of the particle. If the particle lags the fluid, the lift will move the particle towards the faster adjacent fluid and vice versa if the particle leads the fluid.

6.2.8.2.1 Magnus force

Consider a spinning body traveling through a fluid such that its axis of rotation does not coincide with its direction of translation (i.e., its path or trajectory). The body will experience a lift force in a direction perpendicular to the plane defined by its axis of rotation and its trajectory. The magnitude of this force, known as the Magnus force, depends upon spin rate, velocity, and shape of the body. The so-called 'Magnus effect,' in which the force just described causes a deflection perpendicular to the flight path, was first investigated in relation to deflection of projectiles (such as tennis balls or baseballs). Although named after Magnus, who studied the lift caused by rotation of a cylinder, the effect of spin on the flight of tennis balls was first noted by Newton in the 1600s.

A relatively large amount of work has been done concerning the Magnus force acting on spinning objects of large size [182]. The theoretical analyses for these situations, however, are based on inviscid flow and are, therefore, inappropriate for predicting lift on small particles at low Reynolds numbers where viscous effects are expected to dominate. Generally, lift coefficients are measured empirically, though experimental work has also been primarily concerned with large objects at high Reynolds numbers. Tsuji et al. [183] performed experiments on small spheres (5 mm dia.) at Reynolds numbers as low as 550. These are

apparently the smallest particles and lowest Reynolds numbers for which experimental data exists.

Rubinow and Keller [181] obtained an analytic expression for the lift force on a small spinning sphere. They used an expansion valid for small values of the particle Reynolds number to calculate the transverse force on the sphere. For a sphere of radius r_p , spinning with angular velocity Ω and moving through an unbounded stationary fluid with velocity u , they obtain a lift force of:

$$F_L = \pi \rho r_p^3 \Omega u \quad (6.63)$$

6.2.8.3 Virtual mass

When a particle is accelerating with respect to a fluid, an added mass force that is not present under steady conditions must be included in the force balance on the particle. A good qualitative explanation is given by Birkhoff [184]:

“... let a light paddle be dipped into still water and then suddenly given a rapid acceleration broadside. It is a matter of common experience that the apparent inertia (i.e., resistance to acceleration) of the paddle is greatly increased by the water around it. This increased inertia is what is called the "virtual mass" of the paddle, the difference between the real mass and the virtual mass being called the 'induced mass' or 'added mass.'”

The virtual mass is a means of quantifying the force required to displace the fluid surrounding the accelerating body. One can write Newton's Second Law for a solid spherical body of diameter d_p and density ρ_p accelerating through a liquid of density ρ , as (Lahey, [185]):

$$F_{VM} = (m_p + m_{VM})a_{VM} = \frac{4\pi}{3} r_p^3 (\rho_p + 0.5\rho) a_{VM} \quad (6.64)$$

The added mass, m_{VM} , accounts for having to accelerate the surrounding fluid and is equal to one-half the mass of the displaced fluid for a perfect sphere. a_{VM} is acceleration.

6.2.8.4 Basset force

A particle accelerating through a fluid medium will experience virtual mass and Basset forces. One may think of virtual mass forces as resulting from the potential flow field created by the accelerating particle. Likewise, the Basset force may be considered a result of the viscous flow field created by the particles' motion. Viscous phenomena, such as boundary layer growth, are described by diffusion equations, and thus, the flow field at time t is a function of the entire history of the particle motion. For laminar flow around a sphere, Basset [175] obtained the result:

$$F_H = -6\rho r_p^2 \sqrt{\pi\rho\mu} \int_{t_0}^t \sqrt{(t-t')} \frac{d}{dt}(u_r) dt' \quad (6.65)$$

6.2.8.5 Faxen force

Stokes' expression for drag is derived for a single sphere translating at low Reynolds number in a stationary fluid. The drag force on a sphere translating through a fluid that is moving and has velocity gradients will generally have a different value. For steady Stokes flow, the correction for this condition is given by the Faxen relations [186], so that the drag force on a sphere is:

$$F_F = 6\pi r_p \mu u_r + \mu \pi r_p^3 \nabla^2 u_r \quad (6.66)$$

6.2.8.6 Buoyancy

The buoyancy force originated from density difference is defined as:

$$F_B = \frac{1}{6} \pi d_p^3 (\rho_P - \rho) g \quad (6.67)$$

6.2.8.7 Pressure gradient

An object of finite size immersed in a viscous fluid with a pressure gradient will experience a force due to that pressure gradient. This force arises from the fact that the pressure on the 'upstream' side of the object will be greater than that on the 'down-stream' side. A force balance on a sphere in a fluid with a pressure gradient yields the relation:

$$F_P = -\frac{\pi d_p^3}{6} \nabla P \quad (6.68)$$

6.2.8.8 Temperature gradient

When a small particle or a liquid drop is suspended or inserted in a gas or a liquid that is not in thermal equilibrium (i.e., a temperature gradient exists), then the particle moves in the direction of decreasing temperature (if there are no other outside forces acting on the particle). This phenomenon is studied by Phillips [187], and Talbot et al. [188], among others.

6.2.9 Stochastic tracking of particles

In the real flow, the instantaneous velocity fluctuation would make the droplet dance around. However, the instantaneous velocity is not calculated in the current approach as the time averaged Navier-Stokes equations are solved for continuum. One way to simulate the effect of instantaneous turbulence on droplets dispersion is to use the stochastic tracking scheme.

In this approach the particle trajectories are calculated by using instantaneous flow velocity rather than the average one. The fluctuations in velocity are given as:

$$u' = \xi (\overline{u'^2})^{0.5} = \xi \left(\frac{2k}{3} \right)^{0.5} \quad (6.69)$$

ξ is an normally distributed random number. This velocity is applied over the characteristic lifetime of the eddy defined as:

$$\tau_e = 2T_L = 2\left(\frac{0.3k}{\varepsilon}\right) \quad (6.70)$$

After this period, the instantaneous velocity is updated by a new random number until the full trajectory is obtained.

6.3 Computational schemes

Mathematical models of flow processes are non-linear, coupled partial differential equations. Analytical solutions are possible only for some simple cases. For most flow processes of interest to a reactor engineer, the governing equations need to be solved numerically.

In general, numerical solution of the governing transport equation replaces the exact solution of partial differential equations by discrete information available at a finite number of locations (grid points). For a given differential equation, there can be several different ways to derive the discretized equations (finite difference, finite volume, and finite element). Finite volume is the most widely used method by engineers due to the clear relationship between the numerical algorithm and the underlying physical conservation principles.

FLUENT uses a control-volume-based technique to convert a general scalar transport equation to an algebraic equation that can be solved numerically. This control volume technique consists of integrating the transport equation about each control volume, yielding a discrete equation that expresses the conservation law on a control-volume basis. Discretization of the governing equations can be illustrated most easily by considering the unsteady conservation equation for transport of a scalar quantity φ . This is demonstrated by the following equation, written in integral form for an arbitrary control volume V as follows:

$$\int_V \frac{\partial \rho \varphi}{\partial t} dV + \oint \rho \varphi \vec{U} \cdot dA = \oint \Gamma_\varphi \nabla \varphi \cdot dA + \int_V S_\varphi dV \quad (6.71)$$

Where ρ is density, \vec{U} is velocity vector, A is surface area, Γ_φ is diffusion coefficient, and S_φ is source of φ per unit volume.

This equation is applied to each control volume, or cell, in the computational domain. Discretization of the above equation on a given cell yields:

$$\frac{\partial \rho \varphi}{\partial t} V + \sum_f^{N_{faces}} \rho_f U_f \varphi_f \cdot A_f = \sum_f^{N_{faces}} \Gamma_{\varphi_f} \nabla \varphi_f \cdot A_f + S_\varphi V \quad (6.72)$$

Where N_{faces} is the number of faces enclosing the cell, φ_f is the value of φ convected through face f , and $\rho_f U_f \cdot A_f$ is mass flux through the face.

The above discretized scalar transport equation contains the unknown scalar variable φ at the cell center as well as the unknown values in surrounding neighbor cells. A linearized form of this equation can be written as [189]:

$$a_p \varphi = \sum a_{nb} \varphi_{nb} + b \quad (6.73)$$

Where the subscript nb refers to neighbor cells, b is introduced from linearized form of source term, and a_p and a_{nb} are the linearized coefficients for φ and φ_{nb} , respectively. The number of neighbors for each cell will typically equal the number of faces enclosing the cell. Similar equations can be written for each cell in the grid. This results in a set of algebraic equations with a sparse coefficient matrix. For scalar equations, FLUENT solves this linear system using a point implicit (Gauss-Seidel) linear equation solver.

By default, FLUENT stores discrete values of the scalar φ at the cell centers. However, face values φ_f are required for the convection terms in and must be interpolated from the cell center values. This is accomplished using an upwind scheme. Up-winding means that the face value is derived from quantities in the cell upstream, or ‘upwind,’ relative to the direction of the normal velocity. FLUENT allows you to choose from several upwind schemes: first-order upwind, second-order upwind, power law, and QUICK. The diffusion terms in discretized equation are central-differenced and are always second-order accurate. The first order upwind scheme converges much faster than second order. In this study the initial convergence was obtained by a first order upwind scheme, and then the

converged solution was used as the initial condition for a more accurate second order upwind scheme.

In first-order upwind, the face value φ_f is set equal to the cell-center value of φ_f in the upstream cell. Higher-order accuracy is achieved in second order upwind scheme at cell faces through a Taylor series expansion of the cell-centered solution about the cell centroid. Thus the face value φ_f is computed using the following expression:

$$\varphi_f = \varphi + \nabla\varphi \cdot \vec{r} \quad (6.74)$$

Where φ and $\nabla\varphi$ are the cell-centered value and its gradient in the upstream cell, and \vec{r} is the displacement vector from the upstream cell centroid to the face centroid. This formulation requires the determination of the gradient $\nabla\varphi$ in each cell. The Green-Gauss theorem is used to compute the gradient of the scalar φ at the cell center, the following discrete form is written as:

$$\nabla\varphi_{centre} = \frac{1}{V} \sum_f \bar{\varphi}_f A_f \quad (6.75)$$

By default, the face value, φ_f , is taken from the arithmetic average of the values at the neighboring cell centers, viz.,

$$\bar{\varphi}_f = \frac{\varphi_{f,cell1} + \varphi_{f,cell2}}{2} \quad (6.76)$$

The discretization scheme described for scalar transport equation is also used to discretize the momentum equations. For example, the x-momentum equation can be obtained by setting $\varphi = u$:

$$a_p u = \sum_{nb} a_{nb} u_{nb} + \sum p_f A \cdot \hat{i} + s \quad (6.77)$$

If the pressure field and face mass fluxes are known, this equation can be solved in the manner outlined for scalar quantity, and a velocity field is obtained. However, the pressure field and face mass fluxes are not known a priori and must be obtained as a part of the solution. FLUENT uses a co-located scheme, whereby pressure and velocity are both stored at cell centers. However, the discretized momentum equation requires the value of the pressure at the face between cells c_0 and c_1 . Therefore, an interpolation scheme is required to compute the face values of pressure from the cell values.

The default scheme in FLUENT interpolates the pressure values at the faces using momentum equation coefficients:

$$P_f = \frac{\frac{P_{c_0}}{a_{p,c_0}} + \frac{P_{c_1}}{a_{p,c_1}}}{\frac{1}{a_{p,c_0}} + \frac{1}{a_{p,c_1}}} \quad (6.78)$$

The discretized form of continuity equation for steady state is as follows:

$$\sum_f J_f A_f = 0 \quad (6.79)$$

Where J_f is the mass flux through face f .

The momentum and continuity equations are solved sequentially. In this sequential procedure, the continuity equation is used as an equation for pressure. However, pressure does not appear explicitly in discretized equation for incompressible flows, since density is not directly related to pressure. The SIMPLE (Semi-Implicit Method for Pressure-Linked Equations) family of algorithms [189] is used for introducing pressure into the continuity equation. In order to proceed further, it is necessary to relate the face values of velocity, U_n , to the stored values of velocity at the cell centers. The face value of velocity is not averaged linearly; instead, momentum-weighted averaging, using weighting factors based on the a_p coefficient from equation is performed. Using this procedure, the face flux, J_f , may be written as

$$\begin{aligned} J_f &= \rho_f \frac{a_{p,c_0} U_{n,c_0} + a_{p,c_1} U_{n,c_1}}{a_{p,c_0} + a_{p,c_1}} + d_f \left((p_{c_0} + (\nabla p)_{c_0} \cdot \vec{r}_0) - (p_{c_1} + (\nabla p)_{c_1} \cdot \vec{r}_1) \right) \\ &= \hat{J}_f + d_f (p_{c_0} - p_{c_1}) \end{aligned} \quad (6.80)$$

Where p_{c_0} , p_{c_1} and U_{n,c_0} , U_{n,c_1} are the pressures and normal velocities, respectively, within the two cells on either side of the face, and \hat{J}_f contains the influence of velocities in these cells. The term d_f is a function of \bar{a}_p the average of the momentum equation coefficients for the cells on either side of face f .

The SIMPLE algorithm uses a relationship between velocity and pressure corrections to enforce mass conservation and to obtain the pressure field. If the

momentum equation is solved with a guessed pressure field p^* , the resulting face flux, J_f^* :

$$J_f^* = \hat{J}_f^* + d_f (p_{c_0}^* - p_{c_1}^*) \quad (6.81)$$

does not satisfy the continuity equation. Consequently, a correction J_f' is added to the face flux J_f^* so that the corrected face flux,

$$J_f = J_f^* + J_f' \quad (6.82)$$

satisfies the continuity equation. The SIMPLE algorithm postulates that J_f' can be written as

$$J_f' = d_f (p'_{c_0} - p'_{c_1}) \quad (6.83)$$

Where p' is the cell pressure correction.

The SIMPLE algorithm substitutes the flux correction equations into the discrete continuity equation to obtain a discrete equation for the pressure correction p' in the cell:

$$a_p p' = \sum_{nb} a_{nb} p'_{nb} + b \quad (6.84)$$

Where the source term b is the net flow rate into the cell:

$$b = \sum_f J_f^* A_f \quad (6.85)$$

The pressure-correction equation may be solved using the different algebraic methods. Once a solution is obtained, the cell pressure and the face flux are corrected using

$$p = p^* + \eta p' \quad (6.86)$$

$$J_f = J_f^* + d_f (p'_{c_0} - p'_{c_1}) \quad (6.87)$$

Here, η is the under-relaxation factor for pressure. The corrected face flux, J_f , satisfies the discrete continuity equation identically during each iteration.

For transient simulations, the governing equations must be discretized in both space and time. The spatial discretization for the time-dependent equations is identical to the steady-state case. Temporal discretization involves the integration of every term in the differential equations over a time step Δt . The integration of the transient terms is straightforward, as shown below.

A generic expression for the time evolution of a variable φ is given by:

$$\frac{\partial \varphi}{\partial t} = F(\varphi) \quad (6.88)$$

The function $F(\varphi)$ incorporates any spatial discretization. If the time derivative is discretized using backward differences, the first-order accurate temporal discretization is given by:

$$\frac{3\varphi^{n+1} - 4\varphi^n + \varphi^{n-1}}{2\Delta t} = F(\varphi) \quad (6.89)$$

Where $n+1$ is the next time level, $t + \Delta t$, and so on. Depending on the way one evaluates $F(\varphi)$ at either future time step or current time step the method is called implicit or explicit, respectively.

In this study, the geometry creation and mesh generation was performed in ANSYS Design-Modeler/Workbench mesh generator software. Upon generation, the mesh was imported in the commercial CFD code ANSYS Fluent (v.13.0 sp2) where appropriate models and boundary conditions were applied.

A segregated solver was employed to solve the governing equations. In segregated solution technique, the governing equations of continuity, momentum, energy and species transport are solved sequentially. A second order Up-wind scheme was used for spatial discretization. The SIMPLE algorithm was used for pressure-velocity coupling. Converged solution were obtained where residuals were less than 10^{-3} for mass, less than 10^{-5} for species and energy, and less than 10^{-4} for momentum and turbulence parameters.

6.4 Results and discussions

The presented 3D model in this work was added to the commercial ANSYS Fluent code. The developed UDFs and schemes were verified and validated by simulating the fluid coke gasification process in the atmospheric entrained flow gasifier setup described earlier in chapter 3 for different operating conditions.

6.4.1 Atmospheric pressure entrained flow gasifier

The 3D model of atmospheric pressure entrained flow gasifier was added to the commercial ANSYS Fluent code. The experimental setup was described earlier in section 3.1. The geometry was created in ANSYS Design Modeler and mesh was created using ANSYS meshing application using automatic patch conforming/sweeping algorithm. The geometry was meshed with a total number of 49615 tetrahedral elements, consisting of 10602 computational nodes. Table 6.5 represents the generated mesh quality.

Table 6.5 Generated mesh quality

Mesh property	Min.	Max.
Face Angle	19.54	123.09
Edge Length Ratio	1.02	2.96
Element Volume Ratio	1.02	4.21

Figure 6.1 represents the computational domain and mesh quality annotated with the relevant boundary conditions.

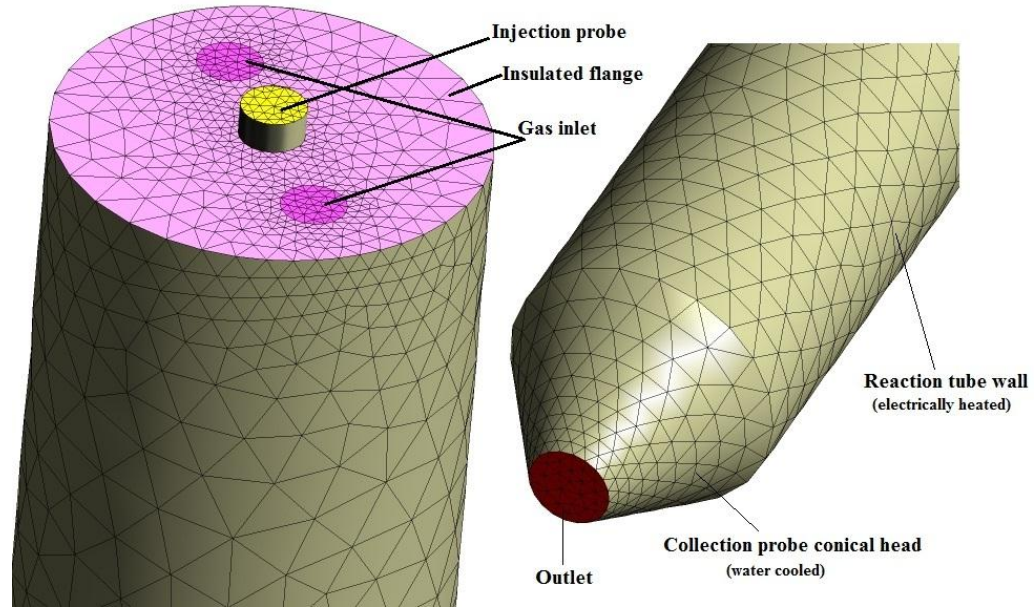


Figure 6.1 Schematic of computational domain

The boundary physics for the computational physics are summarized as follows:

- Velocity inlet boundary for gas inlet and injection probe ports.
- Pressure outlet boundary for outlet port
- Wall boundary with zero heat flux for insulated flange
- Wall boundary with 100 w/m^2 heat flux for collection probe conical head (approximated from Dittus-Boelter correlation)
- Wall boundary with fixed wall temperature for reaction tube wall

The internal diameter of the reactor tube is 6.55 cm and the total heated length is 153 cm. The outlet port has a diameter of 1.5 cm and those of injection probe and gas inlet are 1 cm. The fuel particles are injected at room temperature into the reactor along with some inert gas (N_2) through the central nozzle while preheated and diluted steam and oxygen are injected through the two off-center nozzles of the top flange. For simplicity of simulation the preheated section of tube was modeled by fixing the temperature at the top 10 cm of the computational domain at the reaction tube temperature. The temperature of gases entering the

reaction tube (steam, O₂ and N₂) was set to the outlet temperature of steam generator at 400°C.

6.4.1.1 Model results

The model results were validated with experiment results described in chapter 4. In this work 3 different operating conditions were chosen for gasification of fluid coke. Table 6.6 shows the operating conditions used for validating the simulation results.

Table 6.6 Gasification operating conditions

Run#	Temp (°C)	H2O	O2	Kg/s		
		Vol. %		N ₂	O ₂	H ₂ O
1	1200	31	1.5	6.22E-05	3.33E-06	3.73E-05
2	1400	15	3	7.15E-05	5.54E-06	1.58E-05
3	1400	50	2.5	1.57E-05	4.79E-06	5.25E-05

The fluid coke loading of 72.72 g/h equivalent to 60 gr/hr of carbon was used in all simulation runs.

Figure 6.2 shows coke particle trajectories, colored by particle temperature, particle burn out, particle residence time, and particle Y-velocity, reflecting a typical gasification run for fluid coke at 1400°C in an atmosphere of 50 vol% and 2.5 vol% steam and oxygen, respectively (Run# 3). Coke particles enter the reactor and they are quickly heated and devolatilized. The coke particles rapidly form char, partially combust, and the remainder is consumed by the relatively slow gasification reactions.

At the entrance of the reactor, the particle velocity increases due to the temperature increase of the inert carrier as it mixes with preheated gas and also the volatile gas evolution. When the gas mixture flow develops well inside the reactor tube, the coke particles are entrained with the gas mixture and the particle

velocity reduces to the gas mixture velocities along the remaining length of the reactor. The effect of gas expansion on particle trajectory can also be noted at the upper section of tube adjacent to the inlet boundaries. The plot shows that the particle temperature rapidly rises to the operating temperature (furnace wall temperature) within the top 20 cm of the reaction tube.

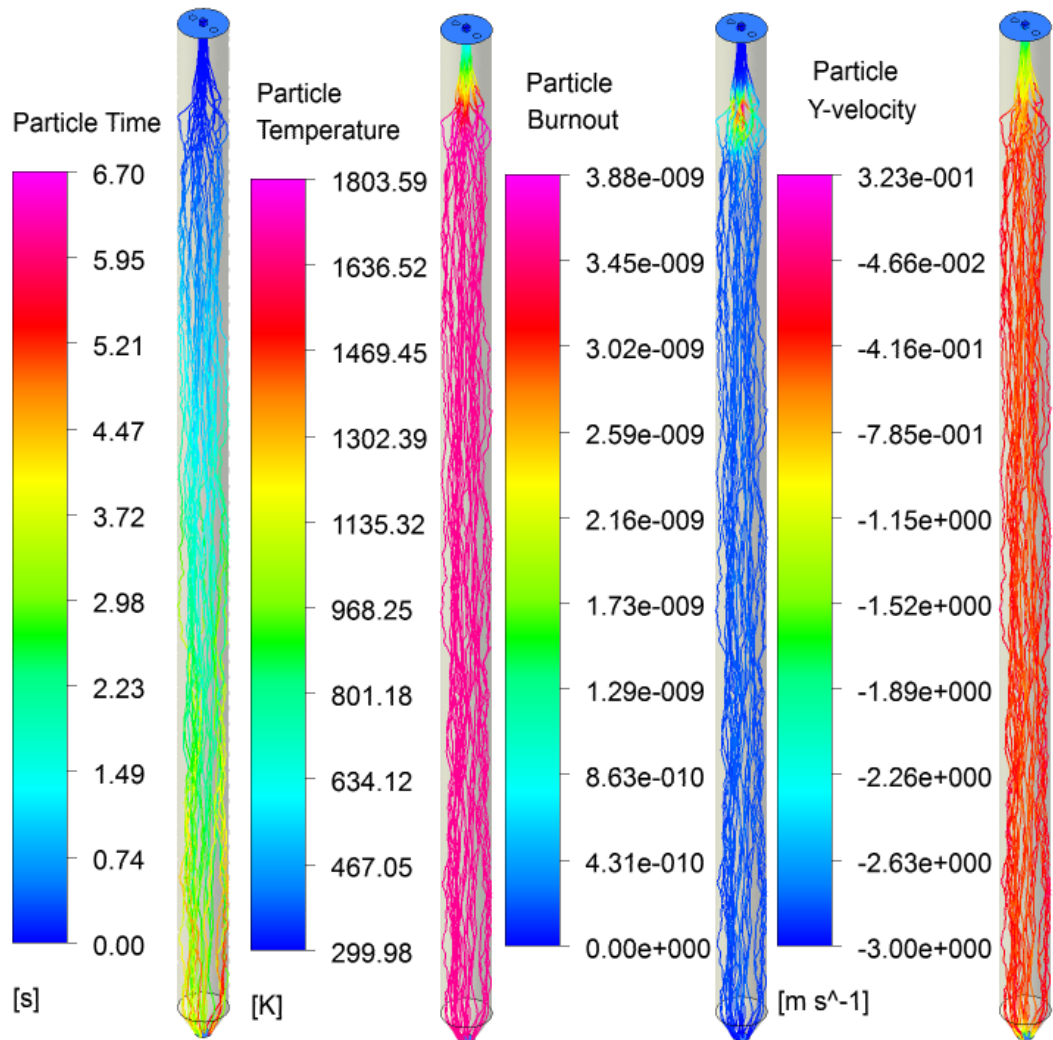


Figure 6.2 Coke particle trajectories at 1400°C (Run# 3)

Table 6.7 represents the typical particle tracking history for 580 particles injected into the gasifier. Particle residence time is well fluctuating around the average of 3.9 sec with and standard deviations of 0.73 sec. Due to the particle size distribution, residence times as small as 2.58 sec and as high as 7.05 sec can

be detected in the modeling. So, the assumption of fixed residence time used by some authors such as Kajitani and Zhang [64] and Kajitani and Suzuki [126] in order to develop the kinetic rates of coal particles using an entrained flow gasifier does not hold anymore. It is worth noticing that the table also shows that about 35% of heat change for particles is in the form of sensible heat required to heat the particle to the operating temperature and the rest is in the form of the heat of reaction. Considering that dried particles were injected into the gasifier and also considering that volatile fraction is very low in fluid coke, the latent heat is negligible. The table also shows a total of 43.03% carbon conversion of the fluid coke for run# 3. This is in excellent agreement with the 44.67% conversion experimentally measured based on the gas analysis in AEEG.

Table 6.7 Particle tracking history (Run# 3)

Fate	Number	Elapsed Time (s)		Avg	Std Dev	
		Min	Max			
Escaped - Zone 8	580	2.581e+00	7.051e+00	3.934e+00	7.371e-01	
(*)- Mass Transfer Summary -(*)						
Fate	Mass Flow (kg/s)					
	Initial	Final	Change			
Escaped - Zone 8	2.018e-05	1.127e-05	-8.906e-06			
(*)- Energy Transfer Summary -(*)						
Fate	Change of Heat (w)			Total		
	Sensible	Latent	Reaction			
Escaped - Zone 8	2.570e+01	4.497e-04	4.578e+01	7.148e+01		
(*)- Combusting Particles -(*)						
Fate	Volatile Content (kg/s)			Char Content (kg/s)		
	Initial	Final	%Conv	Initial	Final	%Conv
Escaped - Zone 8	1.350e-06	0.000e+00	100.00	1.756e-05	1.000e-05	43.04
(*) - Multiple Surface Reactions -(*)						
Fate	Species Names	Species Content (kg/s)				
		Initial	Final	%Conv		
Escaped - Zone 8	c<s>	1.756e-05	1.000e-05	43.03		

Figure 6.3 represents the contour plots of a typical simulation run (Run# 3). The temperature contour plot shows that temperature of gas phase quickly

rises to the furnace temperature. Overall, the cooling effect of gases at the inlet is not significant.

The contour plot of volatile matter mass fraction also shows that devolatilization completes as soon as temperature exceeds about 1400K within the top 15 cm of the furnace. Volatiles are released while coal particles are mainly entrained by the carrier gas before this inert gas fully mixes with the inlet gas mixture. Therefore volatile gases are mainly released and consumed at the centre of the reactor.

Following the devolatilization, the produced char reacts with gasifying agents along the length of reaction tube. The initial faster char consumption depicted by contour plot of particle burnout is due to the char-O₂ reaction. However, oxygen quickly depletes within about 10 cm of tube length following the devolatilization zone. After that the slower char-H₂O, char-H₂ and char-CO₂ proceed along the rest of the furnace length.

The particle mass concentration contour also shows the radial distribution of particles. The laminar velocity profile pushes the particles from high velocity high pressure gradient centre line to the low velocity, low pressure gradient region close to the furnace wall. So, it can be seen that after an initial entrance length of about 30cm the particles are spread all over the reaction tube diameter.

The contour plot of the heat of reactions also shows a small region of exothermic release of heat due to the char-O₂ and exothermic gas phase reactions while the majority of the length of the reaction tube is shown to act as a heat sink due to the endothermic nature of char gasification reactions. The endothermic entrance region of devolatilization also is shown just before the incipient of exothermic reactions as well.

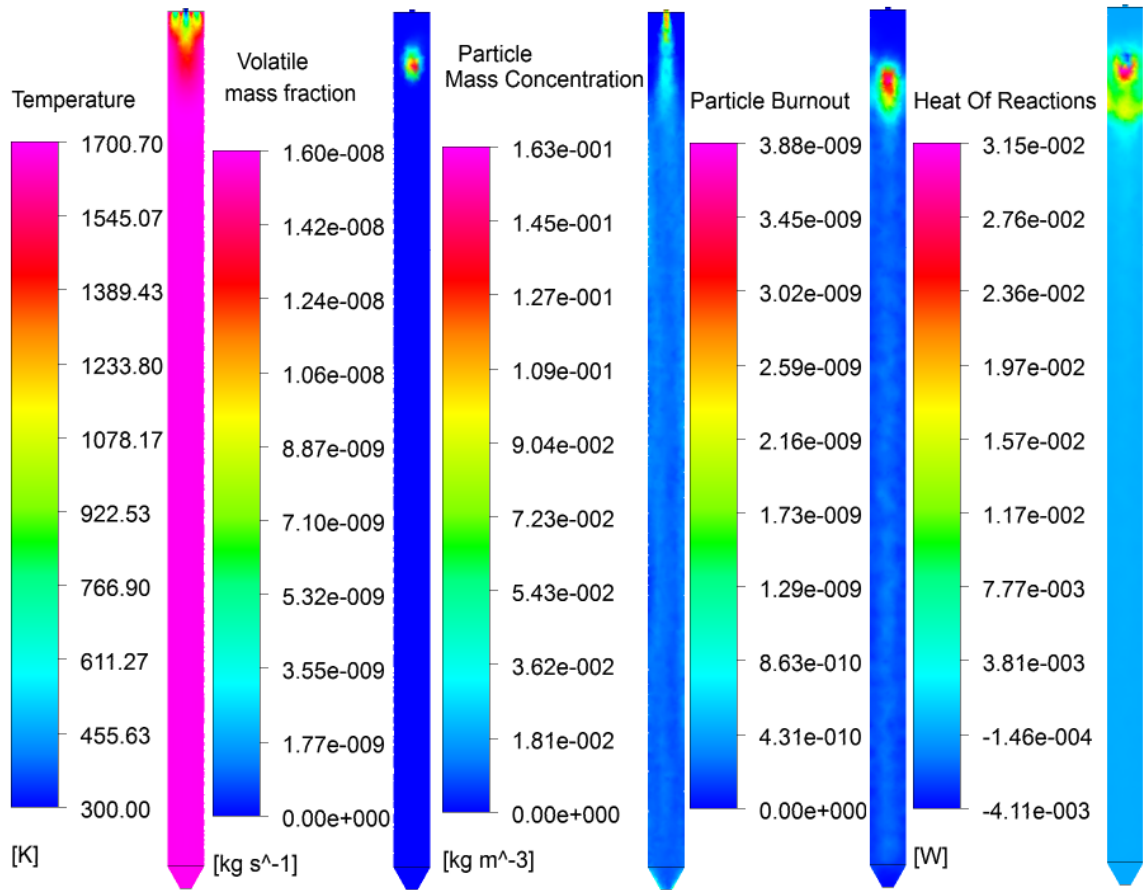


Figure 6.3 Contour plot of several parameters (Run#3)

Figure 6.4 shows the simulated axial and radial distributions of gaseous species mass fraction which represents a typical entrained flow reactor experimental run (Run#3) using the reference fluid coke sample. In the first 15 cm of the reactor, oxygen is available in the peripheral annulus of the flow before it diffuses and mixes with inert gas. As oxygen moves further into the gasifier, more and more is consumed by volatile and char combustion and eventually no O_2 remains in the rest of the reactor length.

During the initial combustion stage where O_2 is present (top 15 cm of reactor), although the gasification reactions occur, any hydrogen or carbon monoxide produced is immediately consumed in the gas phase so that very small amount of CO and H_2 are observed within the char combustion zone. Only when the oxygen mass fraction falls to zero H_2 appear in the bulk gas. The mass

fractions of all the gaseous species then increases monotonically all the way to the outlet of reactor.

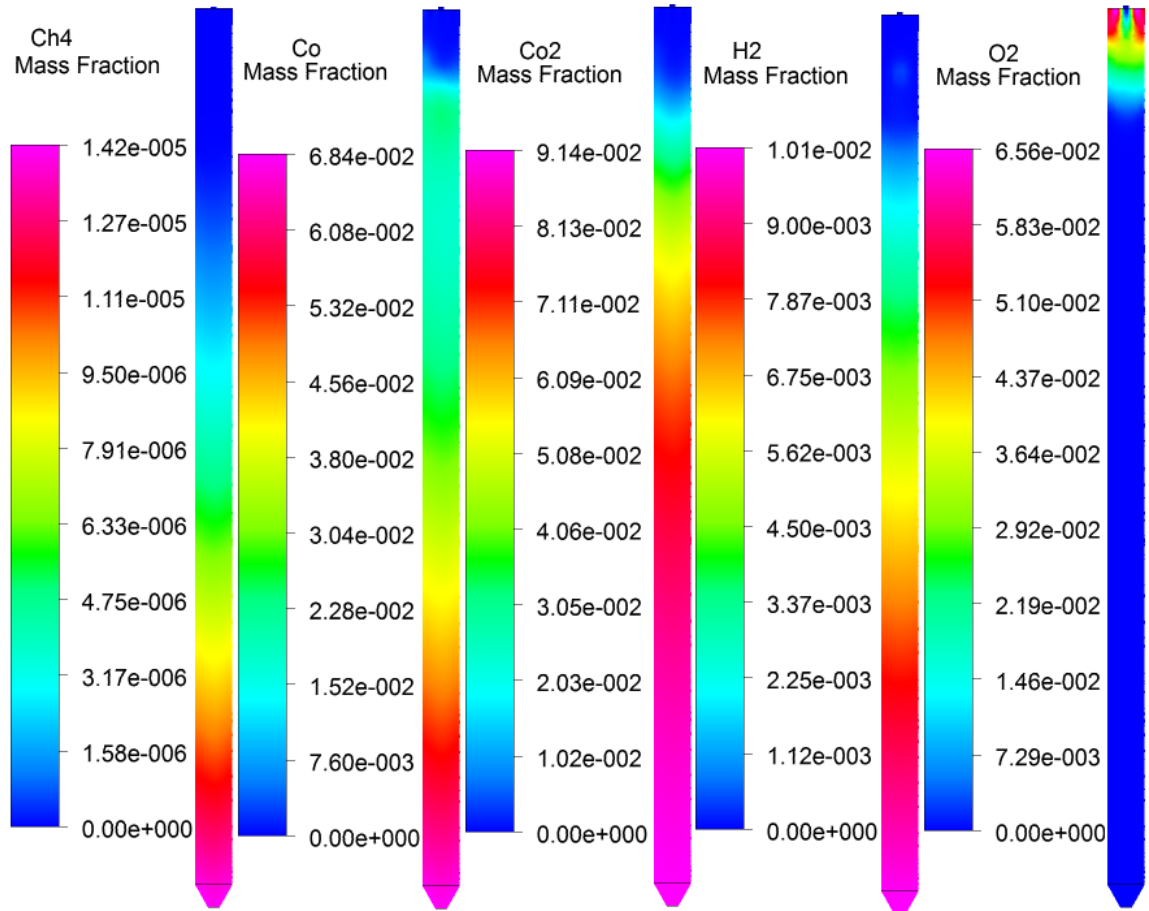


Figure 6.4 Contour plot of gas composition in mass fraction (Run#3)

The comparison of reaction rates shown in Figure 6.5 shed more light into the radial and axial distribution of gaseous species as well. The CO and H₂ combustion rates as stated before are starting as soon as the devolatilization starts. This means that gasification reactions take place in parallel to devolatilization however to a lesser extent. A closer look at plots reveals that water gas shift and steam methane reforming reactions play an important role in distribution of species in the reactor.

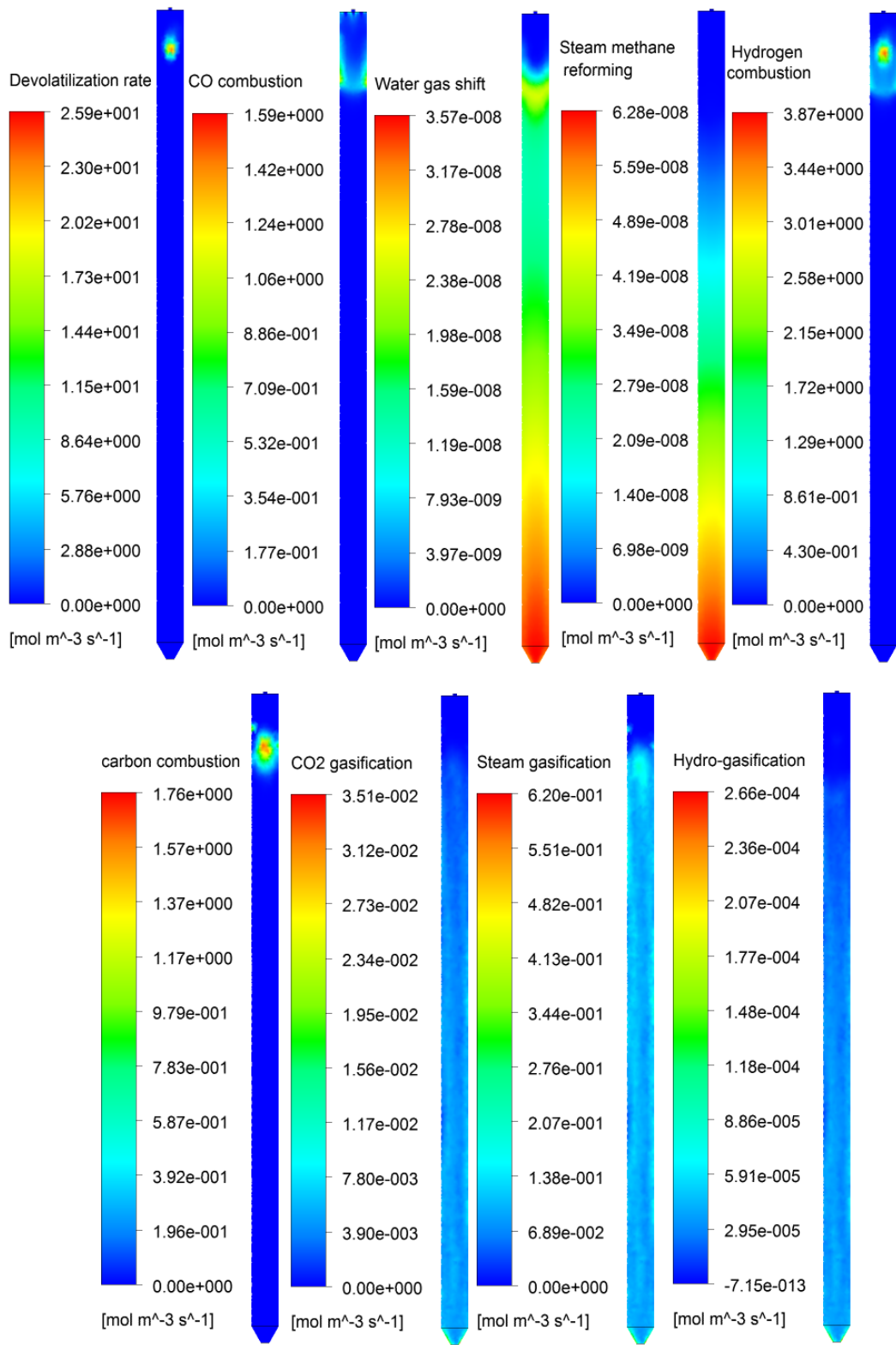


Figure 6.5 Contour plot of homogenous and heterogeneous gasification reactions (Run#3)

Figure 6.5 also shows that the rate of hydro-gasification reaction is much smaller than the other three gasification reaction. Considering that the orders of magnitude of water gas shift and steam methane reforming reactions are almost the same, and further the fact that the extent to which the hydro-gasification reaction proceeds is at least three orders of magnitude smaller than Char-CO₂ and char-H₂O reactions, one may conclude that the water gas shift reaction is much more important than steam methane reforming reaction in final distribution of gaseous species at the outlet of gasifier.

Table 6.8 represents the comparison of simulation results with experiment data on carbon conversion and mole fractions of major compositions in flue gas for all three simulation runs. It is seen that all the conversions and gaseous species concentrations are in fair agreement except methane. This could be due to the fact that in this study we did not develop the kinetic rate for char-H₂ reaction and we arbitrarily adopted the rate model from literature. The char-H₂ rate selected in this study is based on the unreacted shrinking core model developed by Wen [157]. This by itself shows the importance of developing reaction rates specific to the fuel rather than using the generic rates reported in the literature for a wide range of fuels which might show completely different surface structure development and reactivity under the gasification environment. Nonetheless, the concentration of methane in the flue gas is negligible in comparison to other gaseous species as was earlier discussed in terms of smaller char-H₂ reaction rate compared to the other char reactions. So, as far as the quality of flue gas in terms of energy content is concerned the methane concentration plays a minor role in distribution of gaseous species in flue gas.

The results in Table 6.8 could be further improved by taking into consideration that reaction in zone II does not permit as effective opening up of microporosity, mesoporosity and macroporosity as reaction under zone I conditions. This findings has been discussed in details by Aarna and Suuberg [190]. In this study, the surface area development as a function of carbon conversion was studied under the zone I reaction conditions. Perhaps the better alternative is to prepare chars at different levels of conversion under the zone II

conditions using the entrained flow setup equipped with water and gas cooled collection probe which makes it possible to freeze the surface complexes by rapidly cooling down the char and flue gas to temperatures that no reaction takes place followed by degasing under vacuum and using TGA or TPD/TK to measure the active surface area.

Table 6.8 Comparison of gas composition between experiment and simulation

Run #	factors	Simulation	Experiment	Error
1	Conversion (%)	22.87	24.94	8.29%
	H2	7.52	8.41	10.58%
	CH4	0.0031	0.0046	32.61%
	CO	3.05	2.61	16.85%
	CO2	4.16	3.89	6.94%
2	Conversion (%)	28.95	30.85	6.16%
	H2	5.94	6.61	10.14%
	CH4	0.0019	0.0024	20.83%
	CO	5.01	4.62	8.44%
	CO2	3.20	2.92	9.59%
3	Conversion (%)	43.03	44.67	5.17%
	H2	17.74	18.93	6.28%
	CH4	0.00082	0.001	20%
	CO	8.4	7.8	7.69%
	CO2	7.2	6.7	7.46%

6.5 Chapter findings and conclusions

A lab scale atmospheric pressure entrained flow gasifier was successfully simulated using the underlying physics and intrinsic reaction rates developed in this study. Overall 10 reactions (4 heterogeneous and 6 homogeneous reactions) were adopted in this study. The energy content of coke particle on a dry basis was conserved by properly calculating the formation enthalpy of volatile matter a crucial fact which is often missing from literature. The char-H₂ reaction rate model was adopted from literature in this study. Due to the complexities in the reaction rate models, all the intrinsic heterogeneous reactions and water gas shift and steam methane reforming reaction rate models were implemented into the ANSYS FLUENT commercial CFD code using the user defined function (UDF)

capability of the software. The results were compared to the experiment data for carbon conversion, H_2 , CH_4 , CO and CO_2 concentrations at the outlet. In general, a fair agreement between simulation and experiment results were found except the case of CH_4 with less satisfactory results. This could have been caused by the fact that, unlike all the other heterogeneous reactions char- H_2 was not directly developed for fluid coke in this work. The rate was arbitrarily chosen from the literature based on the unreacted shrinking core model. However, the low char- H_2 reaction rate and accordingly small mass fraction of methane in flue gas had negligible effect on axial and radial distribution of gaseous species in the reactor.

In developing the intrinsic rate models in this work, the char surface area development as a function of carbon conversion was determined under the reaction zone I. The simulation results are anticipated to be further improved by taking into consideration that char surface area developments are reportedly different under reaction zone II and I for coal samples. This needs to be further investigated for coke particles under reaction zone II.

The stochastic particle tracking feature of ANSYS FLUENT CFD code based on the discrete random walk model resulted in a relatively wide range of particle residence time in the gasifier. So, any assumptions of equal gas phase and particle residence times which have been used to develop the reaction rates at high temperatures such as the works of Kajitani et al. [64, 126] could significantly underestimate or overestimate the reaction rates. The importance of this issue is more pronounced considering that in this study we have used a very narrow range of particle sizes (53-75 μm) combined with a wet sieving procedure which results in much greater particle size certainty than dry sieved methodology. In conclusion, one could expect a wide range of uncertainty in reaction rates developed based on the parity of gas phase and solid phase residence times.

CHAPTER 7

Conclusions and Recommendations

7.1 Conclusions

The effect of blending woody biomass material with fluid coke and coal on the co-pyrolysis process was investigated in an atmospheric pressure entrained flow gasifier. The morphological study using SEM showed a particle size decrease and shape change from needle to spherical shape as the pyrolysis temperature was increased which was mainly linked to the biomass material. Further investigation revealed that, as the pyrolysis temperature was increased beyond 1250°C, agglomeration seemed to start occurring. The reason for the agglomeration could be due to the low ash fusion temperature of biomass which is related to the melting of alkali silicates in biomass. The molten layer on the surface enables coal and coke particles to attach themselves to sawdust particles, leading to the particle agglomeration at higher temperatures. The shrinking and

agglomeration phenomena were also verified by the particle size distribution analysis.

It was further observed that reactivity of pyrolyzed blended and pure fuels decreased with increasing the temperature. This is due the reorganization of carbon crystallite in carbonaceous fuels.

A series of tests were conducted on blends of sub-bituminous coal and fluid coke. No agglomeration was found in SEM analysis even at highest temperature studies in this work.

From the surface area analysis, it can be pointed out that, even though the surface area of both pure and biomass blended chars increase with increasing pyrolytic temperature, the increase in blended chars is much more pronounced when compared to that of the corresponding pure chars. This might be due to the strong physical or chemical agglomeration that occurs at high pyrolytic temperatures between biomass and other fuel.

Despite the fact that fluid coke originally looked mostly as non-porous particles, pyrolysis at high temperatures showed a significant surface area development corroborated with scanning electron microscopy.

A complete assessment of the effects of operating variables (temperature, steam and oxygen concentrations) and blending ratio of oil sand coke and coal on different response variables (H_2 , CO and syngas productions, H_2/CO ratio, carbon conversion and gasification efficiency) was achieved by means of response surface methodology at high temperatures in an atmospheric pressure entrained flow gasifier. All the response variables were successfully quantified as a function of operating factors and blending ratio. A detailed analysis of variances showed that models can be used to navigate the design space. For all the response variables studied in this work, different responses were obtained depending on the settings of at least two operating factors. These interactions are very difficult to be extracted with the classical design of experiment methodology if not impossible. Additional experiments were conducted to evaluate the robustness of regression models, all proved to be very successful.

Overall no synergy was found in co-gasification of oil sand coke and coal under the operating conditions studied in this work. A limited number of experiments were performed using a 50/50 blend of lignite ash and coke. Despite the reported synergy in fixed bed reactors, no synergy was found in case of entrained flow gasifier.

Except H_2/CO ratio, raising temperature increased the amounts of all response variables. However, the maximum CO production attainable with increasing temperature is limited at high temperatures. An increase in oxygen concentration resulted to a reduction in H_2 and syngas productions, H_2/CO ratio and gasification efficiency and an increase in carbon conversion. CO production showed to be insensitive to oxygen concentration. An increase in steam concentration monotonously raised the H_2 and syngas productions, gasification efficiency and carbon conversion. As far as the production of CO is concerned, at higher temperatures studied in in this work, variation of CO in flue gas is a weak function of steam concentration. Effectiveness of steam in Hydrogen production was abated with increasing the coke ratio in the blend and it was shown that for higher range of coke ratio, temperature is more effective factor than steam in hydrogen production. Also, it was observed that effect of oxygen concentration on H_2 response remained the same for different levels of coke ratio. However, at higher concentrations of oxygen, the H_2 production was more sensitive to steam concentration. On the contrary to coke in case of H_2 production, pure coal was almost insensitive to temperature within the range of temperature used in this study. An increase in coke ratio drastically reduced the CO production. On the other hand, the higher the coke ratio is, the less sensitive CO production becomes to the variations of steam. It was found that H_2/CO ratio was favored by a drop in temperature and oxygen level and increase in coke ratio and steam concentration. The curve for steam however, passes through a maximum close to the 40 vol. %. Also, it was found that at lower temperatures, oxygen has little to no effect on H_2/CO ratio. The oxygen effect found to change with steam concentration though, with higher steam concentration, higher oxygen is required to sustain the same level of H_2/CO ratio. The results also revealed that at high temperatures effect of

steam was more pronounced than low temperatures on gasification efficiency. Additionally, the higher steam concentration is, the smaller the effect of oxygen becomes.

Using the regression models, operating variables were tuned using a constrained non-linear optimization algorithm to find the location in design space which gives the maximum H₂ production. A maximum of 55.8(mol H₂/kg fuel, daf) was gained at 1400°C, 50% steam and 0.01% oxygen with a blend of 30% coke/ 70% coal. Given the excellent accuracy of RSM in quantitatively predicting the results, one can easily notice the unequivocal advantage of RSM in optimizing the gasifier operating conditions which is otherwise impossible using classical “one-factor-at-a-time” method. The latter often fails to produce firm and generalizable conclusions, either qualitatively or quantitatively, as far as the gasifier operation is concerned, due mainly to the relaxation of the interaction effects between operating variables.

The intrinsic rates for Char-O₂, char-CO₂, and char-H₂O gasification reactions were developed for fluid coke. A through discussion was provided on the validity of thermogravimetric determination of char gasification kinetics with oxygen. For char-O₂ reaction, the application of thermogravimetric analyses for reaction rate determination for fluid coke was found limited to a maximum temperature of 550°C and 0.04atm partial pressure of oxygen. No limitations were found for char-CO₂ and char-H₂O endothermic reactions in terms of partial pressure of gasifying agents.

A detail discussion was also provided on the comparison of different designs of thermogravimetric analyzers. The modification of TA SDT-Q600 analyzer for steam injection and its sample pan was presented as well.

Four different specific surface area measurement techniques were used to normalize the specific reaction rate calculated from the weight loss profiles of TGA: N₂-BET surface area (macro- & meso-porosity), two microporosity measurement techniques based on GCMC-NLDFT and DR models, and finally active surface area measured by CO₂ chemisorption at different levels of

conversion. The specific reaction rates, calculated at different levels of conversion for a fixed temperature and partial pressure, were divided by specific surface area:

$$r(X) = r_a \cdot S(X)$$

Overall ASA was found to be the best regressor for deriving the intrinsic rates. Despite the fact that the variability of $r(X)$ was successfully reduced using ASA for char-CO₂ and char-H₂O reactions, the certainty in char-O₂ reaction was not as satisfactory as those of char-CO₂ and char-H₂O reactions. Nonetheless, a fair estimate of intrinsic rate could still be developed using ASA. The reason could be linked to the different temperatures at which the ASA and rates in TGA were measured.

Surface areas based on N₂-BET technique were also proven to be a better regressor for normalizing the specific rates compared to the ones based on GCMC-NLDFT and DR models.

The atmospheric pressure entrained flow gasifier was further successfully simulated using the underlying physics and intrinsic reaction rates developed in this study. The intrinsic rates developed in this study were successfully implemented into the ANSYS Fluent CFD code. The energy content of coke particle on a dry basis was conserved by properly calculating the formation enthalpy of volatile matter a crucial fact which is normally missing from literature. The results were compared to the experiment data for carbon conversion, H₂, CH₄, CO and CO₂ concentrations at the outlet of gasifier. In general, a fair agreement between simulation and experiment results were found except for the case of CH₄. This could have been caused by the fact that, unlike all the other heterogeneous reactions char-H₂ was not directly developed for fluid coke in this work. However, the low char-H₂ reaction rate and accordingly small mass fraction of methane in flue gas had negligible effect on axial and radial distribution of gaseous species in the reactor. The stochastic particle tracking feature of ANSYS FLUENT CFD code based on the discrete random walk model resulted in a relatively wide range of particle residence time in the gasifier. So, any assumptions of equal gas phase and particle residence time which has been

used to develop the reaction rates at high temperatures could significantly underestimate or overestimate the reaction rates.

7.2 Recommendations for future work

The following recommendations for the extension of this research project are made based on the present study:

1. The co-pyrolysis of fuels was investigated at atmospheric pressure in this study. However, most of the commercial scale entrained flow gasifiers are operated at high pressures. Despite the fact that pure fuels have been extensively investigated for their pyrolysis behavior at high temperatures and high pressures, less is done on the co-pyrolysis of blended flues at high pressures and temperatures. Behavior of blended fuels with respect to the pore structural developments, morphology, particle size distribution and reactivity of produced chars need to be investigated at high pressures.
2. RSM was successfully employed in co-gasification studies in this work. Combined effects of concentration of gasifying agents and temperature were investigated using this technique. Effect of pressure, however, was not considered in this study. Similar work needs to be extended to cover the effect of pressure as an extra factor in RSM technique as well.
3. Despite the importance of micromechanical interaction between char-slag in slagging entrained flow gasifier, most of the available studies are at best a qualitative representation of the system. It is of great importance to devise a system which enables us to quantify this effect in terms of operating variables, particle and slag properties.
4. It is also important that different blending techniques and their effects on gasification performance to be considered as well.

5. In kinetics studies and char surface area characterization at different levels of carbon conversion, a low heating rate horizontal tube furnace was used. The more realistic data will be obtained by producing chars under high heating rates of entrained flow gasifier. A comparative study in this field can help shed more light to the gasification intrinsic rate developments.
6. In the current work, the active surface area was measured using a thermogravimetric technique at low heating rates. The design of the entrained flow gasifier used in this study can be effectively used to prepare chars with different levels of conversion by immediately freezing the surface complexes in water- and gas-cooled collection probe. These chars can be further degassed under vacuum and studied for the number of active sites using a similar technique used in this study or TPD/TK techniques. The ASA determined in this way would be a more representative of the real case in entrained flow gasifiers.
7. It is also crucial to take into account the effect of pressure on ASA development. This makes the developed intrinsic rates more appropriate to be used in designing and modeling high pressure commercial entrained flow gasifiers.

References

1. EIA-Annual Energy Outlook 2010, <http://www.eia.gov/forecasts/aeo/er/>.
2. Anthony, B. and D. Granatstein. *Gasification fundamentals: the latest developments and the future outlook*. in *Gasification Conference*. Calgary Telus convention centre.
3. Cicconardi, S.P., A. Perna, and G. Spazzafumo, *Combined power and hydrogen production from coal. Part B: Comparison between the IGHP and CPH systems*. International Journal of Hydrogen Energy, 2008. **33**(16): p. 4397-4404.
4. Cicconardi, S.P., et al., *CPH systems for cogeneration of power and hydrogen from coal*. International Journal of Hydrogen Energy, 2006. **31**(6): p. 693-700.
5. Higman, C. and M. van der Burgt, *Gasification*. Vol. 2nd. 2008, Amsterdam; Boston: Gulf Professional Pub./Elsevier Science. 435.
6. Harris, D., D. Roberts, and D. Henderson, *Gasification behaviour of Australian coals*. 2003, Australia: Pullenvale, Qld. : QCAT Technology Transfer Centre. 75.
7. Collot, A.-G. and I.E.A.C.R.C.C. Centre, *Matching gasifiers to coals*. IEA Coal Research ; CCC/65; IEA Coal Research ; CCC/65. 2002, London: IEA Clean Coal Centre. 64.
8. Kinaev, N., *A review of mineral matter in coal gasification*, in *Cooperative Research Centre for Coal in Sustainable Development*. 2006, QCAT Technology Transfer Centre: Australia.
9. Duke du, P., *Coal Gasification*. gasification symposium calgary, 2011.
10. Ordorica-Garcia, G., et al., *Technoeconomic evaluation of IGCC power plants for CO2 avoidance*. Energy Conversion and Management, 2006. **47**(15-16): p. 2250-2259.
11. Consultancy, J., *Alternative Fuels Study, Technology Review Prepared for Alberta Innovates Energy and Environment solutions*. 2008.
12. Ian, D., *Shale gas: Energy and Environment Issues*. Golf Coast Carbon Centre, Bureau of Economic Geology, 2009(Journal Article).
13. *Energy Resources Conservation Board 2010*
<http://www.ercb.ca/portal/server.pt?>

14. National Energy Board. *Canada's Energy Future. Reference Case and Scenarios to 2030*. National Energy Board Publications Office, 2007(Journal Article).
15. Plessis, D. *Gasification and CO2 capture technologies in IGCC and upgrading application (AERI)*. in *Gasification Conference, Calgary, Canada, 2010*.
16. Chmielniak, T. and M. Sciazko, *Co-gasification of biomass and coal for methanol synthesis*. *Applied Energy*, 2003. **74**(3-4): p. 393-403.
17. Government of, Alberta, *Alberta's Oil Sands: Opportunity, Balance*. 2008. <http://alberta.ca/>
18. Nguyen, Q.T., *Kinetics of gasification and sulphur capture of oil sand cokes*. 1988, The University of British Columbia (Canada): Canada.
19. Takamura, K., *Microscopic structure of Athabasca oil sand*. *Can J Chem Eng*, 1982. **V 60**(N 4): p. 538-545.
20. Furimsky, E., *Gasification of oil sand coke: Review*. *Fuel Processing Technology*, 1998. **56**(3): p. 263-290.
21. Cousins, A., et al., *Entrained-flow gasifier fuel blending studies at pilot scale*. *Canadian Journal of Chemical Engineering*, 2008. **86**(3): p. 335-346.
22. Jack, T.R., E.A. Sullivan, and J.E. Zajic, *Comparison of the structure and composition of cokes from the thermal cracking of Athabasca Oil Sands bitumen*. *Fuel*, 1979. **58**(8): p. 585-588.
23. Har, S.H.H., *Characterization of Oil Sands Fluid Coke*. 1981.
24. E.S. Hall, E.L.T. *Physical Parameters that Control the Rates and Extents of Hydro Desulphurization of Oil Sand Cokes*.
25. Fairbridge, C., S.H. Ng, and A.D. Palmer, *Fractal analysis of gas adsorption on Syncrude coke*. *Fuel*, 1986. **65**(12): p. 1759-1762.
26. Hall, E.S., et al., *Upgrading of Delayed and Fluid cokes from oil sand by desulfurization*. *Canadian Journal of Chemical Engineering*, 1982. **60**(3): p. 418-424.
27. Feng, B. and S.K. Bhatia, *Variation of the pore structure of coal chars during gasification*. *Carbon*, 2003. **41**(3): p. 507-523.

28. Su, J.L. and D.D. Perlmutter, *Effect of pore structure on char oxidation kinetics*. AIChE Journal, 1985. **31**(6): p. 973-981.
29. Tseng, H.P. and T.F. Edgar, *Identification of the combustion behaviour of lignite char between 350 and 900 °C*. Fuel, 1984. **63**(3): p. 385-393.
30. Nandi, S.P. and P.L. Walker Jr, *Adsorption of dyes from aqueous solution by coals, chars, and active carbons*. Fuel, 1971. **50**(4): p. 345-366.
31. Ravikovitch, P.I., et al., *Unified approach to pore size characterization of microporous carbonaceous materials from N₂, Ar, and CO₂ adsorption isotherms*. Langmuir, 2000. **16**(5): p. 2311-2320.
32. Jagiello, J. and M. Thommes, *Comparison of DFT characterization methods based on N₂, Ar, CO₂, and H₂ adsorption applied to carbons with various pore size distributions*. Carbon, 2004. **42**(7): p. 1225-1229.
33. Edward, F., *Characterization of cokes from fluid/flexi-coking of heavy feeds*. Fuel Processing Technology, 2000. **67**(3): p. 205-230.
34. Alpern, B., et al., *Coal : classification, coalification, mineralogy, trace-element chemistry, and oil and gas potential*. 1989, Amsterdam, The Netherlands: Elsevier. 678.
35. Huggins, F., et al., *Nondestructive determination of trace element speciation in coal and coal ash by XAFS spectroscopy*. Energy & Fuels, 1993. **7**(4): p. 482-489.
36. Huggins, F.E., F. Goodarzi, and C.J. Lafferty, *Mode of Occurrence of Arsenic in Subbituminous Coals*. Energy & Fuels, 1996. **10**(4): p. 1001-1004.
37. Huggins, F.E., et al., *Mode of occurrence of chromium in four US coals*. Fuel Processing Technology, 2000. **63**(2-3): p. 79-92.
38. Godbeer, W.G., D.J. Swaine, and F. Goodarzi, *Fluorine in Canadian coals*. Fuel, 1994. **73**(8): p. 1291-1293.
39. Goodarzi, F., *Elemental concentrations in Canadian coals : 2. Byron creek collieries, British Columbia*. Fuel, 1987. **66**(2): p. 250-254.
40. Goodarzi, F., A.E. Foscolos, and A.R. Cameron, *Mineral matter and elemental concentrations in selected western canadian coals*. Fuel, 1985. **64**(11): p. 1599-1605.

41. Goodarzi, F. and N.N. Goodarzi, *Mercury in Western Canadian subbituminous coal—a weighted average study to evaluate potential mercury reduction by selective mining*. International Journal of Coal Geology, 2004. **58**(4): p. 251-259.
42. Landheer, F., et al., *Trace elements in Canadian coals*. Economic and technical review report / Canada. Environmental Protection Service ; EPS 3-AP-82-6; Economic and technical review report (Canada. Environmental Protection Service) ; EPS 3-AP-82-6. 1982, Ottawa: Air Pollution Control Directorate, Environmental Protection Service. 41.
43. Kronberg, B.I., et al., *Distributions of trace elements in Western Canadian coal ashes*. Fuel, 1981. **60**(1): p. 59-63.
44. Johnson, J.L., *Kinetics of coal gasification : a compilation of research*. 1979, New York: Wiley. 324.
45. Kristiansen, A., et al., *Understanding coal gasification*. Report (IEA Coal Research) ; IEACR/86. 1996, London, England: IEA Coal Research. 69.
46. Prabir, B., *Biomass Gasification and Pyrolysis: Practical Design and Theory*. Vol. 1st. 2010: Academic Press. 376.
47. Scott, D.H. and A.M. Carpenter, *Advanced power systems and coal quality*. 1996: London.
48. Furimsky, E. and A. Palmer, *Catalytic effect of lignite ash on steam gasification of oil sand coke*. Applied Catalysis, 1986. **23**(2): p. 355-365.
49. Furimsky, E., *Gasification reactivities of cokes derived from athabasca bitumen*. Fuel Processing Technology, 1985. **11**(2): p. 167-182.
50. Watkinson, A.P., G. Cheng, and D.P.C. Fung, *Gasification of oil sand coke*. Fuel, 1989. **68**(1): p. 4-10.
51. Nguyen, Q.T. and A.P. Watkinson, *Gasification kinetics of oil sand coke*. Can. J. Chem. Eng., 1990. **68**(Journal Article): p. 814.
52. Karimi, A. and M.R. Gray, *Effectiveness and mobility of catalysts for gasification of bitumen coke*. Fuel, 2011. **90**(1): p. 120-125.
53. Collot, A.G., et al., *Co-pyrolysis and co-gasification of coal and biomass in bench-scale fixed-bed and fluidized bed reactors*. Fuel, 1999. **78**(6): p. 667-679.

54. Sjöström, K., et al., *Promoted reactivity of char in co-gasification of biomass and coal: Synergies in the thermochemical process*. Fuel, 1999. **78**(10): p. 1189-1194.
55. Pinto, F., et al., *Effect of experimental conditions on co-gasification of coal, biomass and plastics wastes with air/steam mixtures in a fluidized bed system*. Fuel, 2003. **82**(15-17): p. 1967-1976.
56. Vuthaluru, H.B., *Thermal behaviour of coal/biomass blends during co-pyrolysis*. Fuel Processing Technology, 2004. **85**(2-3): p. 141-155.
57. Kumabe, K., et al., *Co-gasification of woody biomass and coal with air and steam*. Fuel, 2007. **86**(5-6): p. 684-689.
58. Zhang, L., et al., *Co-pyrolysis of biomass and coal in a free fall reactor*. Fuel, 2007. **86**(3): p. 353-359.
59. Zhu, W., W. Song, and W. Lin, *Catalytic gasification of char from co-pyrolysis of coal and biomass*. Fuel Processing Technology, 2008. **89**(9): p. 890-896.
60. Feroso, J., et al., *High-pressure co-gasification of coal with biomass and petroleum coke*. Fuel Processing Technology, 2009. **90**(7-8): p. 926-932.
61. Lu, X.A. and W.P. Yan, *Influence of blending ratios on fluidized bed co-gasification of biomass and coal*. Dongli Gongcheng/Power Engineering, 2009. **29**(10): p. 977-983.
62. Wang, L., et al., *Experiment of hydrogen production from co-gasification of biomass and coal*. Jiangsu Daxue Xuebao (Ziran Kexue Ban) / Journal of Jiangsu University (Natural Science Edition), 2009. **30**(5): p. 496-500.
63. Hernández, J.J., G. Aranda-Almansa, and C. Serrano, *Co-gasification of biomass wastes and coal-coke blends in an entrained flow gasifier: An experimental study*. Energy and Fuels, 2010. **24**(4): p. 2479-2488.
64. Kajitani, S., et al., *Co-gasification reactivity of coal and woody biomass in high-temperature gasification*. Energy and Fuels, 2010. **24**(1): p. 145-151.
65. Li, K., R. Zhang, and J. Bi, *Experimental study on syngas production by co-gasification of coal and biomass in a fluidized bed*. International Journal of Hydrogen Energy, 2010. **35**(7): p. 2722-2726.
66. Aigner, I., C. Pfeifer, and H. Hofbauer, *Co-gasification of coal and wood in a dual fluidized bed gasifier*. Fuel, 2011. **90**(7): p. 2404-2412.

67. Howaniec, N., et al., *Steam co-gasification of coal and biomass derived chars with synergy effect as an innovative way of hydrogen-rich gas production*. International Journal of Hydrogen Energy, 2011(Journal Article).
68. Liu, X., et al., *Experimental study on co-gasification of coal liquefaction residue and petroleum coke*. Energy and Fuels, 2011. **25**(8): p. 3377-3381.
69. Shen, C.H., et al., *Co-gasification performance of coal and petroleum coke blends in a pilot-scale pressurized entrained-flow gasifier*. International Journal of Energy Research, 2011(Journal Article).
70. Xu, G.Y. and G.G. Sun, *Study on characteristics of co-gasification of biomass and petroleum coke*. Ranliao Huaxue Xuebao/Journal of Fuel Chemistry and Technology, 2011. **39**(6): p. 438-442.
71. Zhan, X., et al., *Influence of blending methods on the co-gasification reactivity of petroleum coke and lignite*. Energy Conversion and Management, 2011. **52**(4): p. 1810-1814.
72. Karimi, A., N. Semagina, and M.R. Gray, *Kinetics of catalytic steam gasification of bitumen coke*. Fuel, 2011. **90**(3): p. 1285-1291.
73. Gavalas, G.R., *A random capillary model with application to char gasification at chemically controlled rates*. AIChE J., 1980. **26**(Journal Article): p. 557-584.
74. Bhatia, S.K. and D.D. Perlmutter, *A random model for fluid-solid reactions: I diffusion and transport effects*. AIChE J., 1981. **27**(Journal Article): p. 247-254.
75. Kasaoka, S., Y. Sakata, and C. Tong, *Kinetic evaluation of the reactivity of various coal chars for gasification with carbon dioxide in comparison with steam*. Int. Chem. Eng., 1985. **25**(Journal Article): p. 160-175.
76. Carbon, N.A.S.I.o., et al., *Carbon and coal gasification : science and technology*. NATO ASI series. Series E, Applied sciences. no. 105. 1986, Dordrecht, Boston; Hingham, MA: Martinus Nijhoff; Distributors for the U.S. and Canada, Kluwer Academic Publishers. 655.
77. Laurendeau, N.M., *Heterogeneous kinetics of coal char gasification and combustion*. Progress in Energy and Combustion Science, 1978. **4**(4): p. 221-270.
78. Philip L, W., Jr., *Structure of coals and their conversion to gaseous fuels*. Fuel, 1981. **60**(9): p. 801-802.

79. Thiele, E.W., *Relation between Catalytic Activity and Size of Particle*. Industrial & Engineering Chemistry, 1939. **31**(7): p. 916-920.
80. Ian W, S., *The intrinsic reactivity of carbons to oxygen*. Fuel, 1978. **57**(7): p. 409-414.
81. Roberts, D.G., *Intrinsic reaction kinetics of coal chars with oxygen, carbon dioxide and steam at elevated pressures, PhD thesis*. 2000. p. 299 leaves.
82. Lahaye, J.E.P., *Fundamental issues in control of carbon gasification reactivity*. NATO ASI series. Series E, Applied sciences. 1991, Dordrecht: Boston. xii, 622 p.
83. Laine, N.R., F.J. Vastola, and P.L. Walker, *The importance of active surface area in the carbon-oxygen reaction*^{1,2}. The Journal of Physical Chemistry, 1963. **67**(10): p. 2030-2034.
84. Mahajan, O.P., R. Yarzab, and P.L. Walker Jr, *Unification of coal-char gasification reaction mechanisms*. Fuel, 1978. **57**(10): p. 643-646.
85. Taylor, H.S., *Fourth Report of the Committee on Contact Catalysis*. The Journal of Physical Chemistry, 1925. **30**(2): p. 145-171.
86. Radovic, L., *Chemisorption, reaction and desorption studies of coal chars in steam, oxygen and carbon dioxide : final report (January 1986-December 1989)*. GRI-90/0071; Report No: GRI-90/0071. 1990, Chicago, Ill.: Gas Research Institute. xii, 212 p.
87. Tong, S.B., P. Pareja, and M.H. Back, *Correlation of the reactivity, the active surface area and the total surface area of thin films of pyrolytic carbon*. Carbon, 1982. **20**(3): p. 191-194.
88. Jenkins, R.G. and A. Piotrowski. *Role of carbon active sites in the oxidation of coal chars*. 1987.
89. Kelemen, S.R. and H. Freund, *O₂ oxidation studies of the edge surface of graphite*. Carbon, 1985. **23**(6): p. 619-625.
90. Kelemen, S.R. and H. Freund, *A comparison of O₂ and CO₂ oxidation of glassy carbon surfaces*. Carbon, 1985. **23**(6): p. 723-729.
91. Marchon, B., et al., *TPD and XPS studies of O₂, CO₂, and H₂O adsorption on clean polycrystalline graphite*. Carbon, 1988. **26**(4): p. 507-514.

92. Radović, L.R., P.L. Walker Jr, and R.G. Jenkins, *Importance of carbon active sites in the gasification of coal chars*. Fuel, 1983. **62**(7): p. 849-856.
93. Suuberg, E.M., J.M. Calo, and M. Wojtowicz. *Oxygen chemisorption as as tool for characterizing 'Young' chars*. 1986.
94. Klose, W. and M. Wölki, *On the intrinsic reaction rate of biomass char gasification with carbon dioxide and steam*. Fuel, 2005. **84**(7-8): p. 885-892.
95. Elliott, M.A., *Chemistry of coal utilization : second supplementary volume*. 1981, New York: Wiley. xxi, 2374 p.
96. Jenkins, R.G., S.P. Nandi, and P.L. Walker Jr, *Reactivity of heat-treated coals in air at 500 °C*. Fuel, 1973. **52**(4): p. 288-293.
97. Gale, T.K., C.H. Bartholomew, and T.H. Fletcher, *Effects of pyrolysis heating rate on intrinsic reactivities of coal chars*. Energy and Fuels, 1996. **10**(3): p. 766-775.
98. van Heek, K.H. and H.J. Mühlen, *Effect of coal and char properties on gasification*. Fuel Processing Technology, 1987. **15**(C): p. 113-133.
99. Smith, I.W., *The intrinsic reactivity of carbons to oxygen*. Fuel, 1978. **57**(7): p. 409-414.
100. Smith, I.W., *The combustion rates of coal chars: A review*. Symposium (International) on Combustion, 1982. **19**(1): p. 1045-1065.
101. Bird, R.B. and E.N. Lightfoot, *Transport phenomena*. 2007, J. Wiley.
102. Smith, I.W. and R.J. Tyler, *Internal burning of pulverized semi-anthracite: the relation between particle structure and reactivity*. Fuel, 1972. **51**(4): p. 312-321.
103. Harris, D.J. and I.W. Smith, *Intrinsic reactivity of petroleum coke and brown coal char to carbon dioxide, steam and oxygen*. Symposium (International) on Combustion, 1991. **23**(1): p. 1185-1190.
104. Dutta, S. and C.Y. Wen, *Reactivity of Coal and Char. 2. In Oxygen-Nitrogen Atmosphere*. Industrial & Engineering Chemistry Process Design and Development, 1977. **16**(1): p. 31-37.
105. Young, B.C. and I.W. Smith, *The kinetics of combustion of petroleum coke particles at 1000 to 1800 K: The reaction order*. Symposium (International) on Combustion, 1981. **18**(1): p. 1249-1255.

106. Feng, B. and S.K. Bhatia, *On the validity of thermogravimetric determination of carbon gasification kinetics*. Chemical Engineering Science, 2002. **57**(15): p. 2907-2920.
107. Lin, S.Y., M. Hirato, and M. Horio, *The characteristics of coal char gasification at around ash melting temperature*. Energy & Fuels, 1994. **8**(3): p. 598-606.
108. Matsui, I., D. Kunii, and T. Furusawa, *Study of char gasification by carbon dioxide. 1. Kinetic study by thermogravimetric analysis*. Industrial and Engineering Chemistry Research, 1987. **26**(1): p. 91-95.
109. Dutta, S., C.Y. Wen, and R.J. Belt, *Reactivity of coal and char. 1. In carbon dioxide atmosphere*. Industrial & Engineering Chemistry Process Design and Development, 1977. **16**(1): p. 20-30.
110. Hampartsoumian, E., et al., *The Reactivity of Coal Chars Gasified in a Carbon Dioxide Environment*. Combustion Science and Technology, 1993. **92**(1-3): p. 105-121.
111. Harris, D.J., Kelly, M. D., *Intrinsic Reactivity of Both a Raw and a Cleaned Hunter Valley Coal*. In: A Tomita (Ed.) Development of Advanced Power Generation System by Using Clean Coal. Final Report of International Joint Research Project, Supported by NEDO, Japan., 1996: p. 172-189.
112. Walker, P.L.R.F.A.L.G., *Gas reactions of carbon*. 1958, University Park, Penn.: Mineral Industries Experiment Station, College of Mineral Industries, Pennsylvania State University. ii, 115, [34] leaves.
113. Mühlen, H.J., K.H. van Heek, and H. Jüntgen, *Kinetic studies of steam gasification of char in the presence of H₂, CO₂ and CO*. Fuel, 1985. **64**(7): p. 944-949.
114. Blied, A., *Mathematical modeling of a cocurrent fixed bed coal gasifier*. 1984, Dissertation: Enschede, Techn. Hogesch., Diss., 1984.
115. Huang, Z., et al., *Kinetic studies of char gasification by steam and CO₂ in the presence of H₂ and CO*. Fuel Processing Technology, 2010. **91**(8): p. 843-847.
116. Rabbitts, M.C., et al., *Modeling of residence time distribution in an entrained flow coal gasification reactor*. CHEMSA, 1983. **9**(11): p. 220-223.

117. Benyon, P.J., *Computational modelling of entrained flow slagging gasifiers*. 1900. xxv, 320 leaves.
118. De Lasa, H. and L.K. Mok, *Entrained coal gasifiers: Modeling the particle acceleration*. The Canadian Journal of Chemical Engineering, 1981. **59**(6): p. 658-661.
119. Celik, I. *Numerical simulation of coal gasification in an entrained-flow reactor*. 1990.
120. Govind, R. and J. Shah, *Modeling and simulation of an entrained flow coal gasifier*. AIChE Journal, 1984. **30**(1): p. 79-92.
121. Vamvuka, D., E.T. Woodburn, and P.R. Senior, *Modelling of an entrained flow coal gasifier. I. Development of the model and general predictions*. Fuel, 1995. **74**(10): p. 1452-1460.
122. Fletcher, D.F., et al., *A CFD based combustion model of an entrained flow biomass gasifier*. Applied Mathematical Modelling, 2000. **24**(3): p. 165-182.
123. Chen, C., M. Horio, and T. Kojima, *Numerical simulation of entrained flow coal gasifiers. Part I: Modeling of coal gasification in an entrained flow gasifier*. Chemical Engineering Science, 2000. **55**(18): p. 3861-3874.
124. Bockelie, M., et al. *Modeling entrained flow coal gasifiers*. 2008.
125. Watanabe, H. and M. Otaka, *Numerical simulation of coal gasification in entrained flow coal gasifier*. Fuel, 2006. **85**(12-13): p. 1935-1943.
126. Kajitani, S., et al., *CO gasification rate analysis of coal char in entrained flow coal gasifier*. Fuel, 2006. **85**(2): p. 163-169.
127. Choi, Y.C., et al., *Numerical study on the coal gasification characteristics in an entrained flow coal gasifier*. Fuel, 2001. **80**(15): p. 2193-2201.
128. Liu, G.S., et al., *Modelling of a pressurised entrained flow coal gasifier: the effect of reaction kinetics and char structure*. Fuel, 2000. **79**(14): p. 1767-1779.
129. Ajilkumar, A., U.S.P. Shet, and T. Sundararajan, *Numerical simulation of pressure effects on the gasification of australian and indian coals in a tubular gasifier*. Heat Transfer Engineering, 2010. **31**(6): p. 495-508.

130. Blake, T.R., D.H. Brownell Jr, and G.P. Schneyer, *Numerical simulation model for entrained flow coal gasification - 1. The hydrodynamical model*. 1978. v(7): p. 2971-3000.
131. Bouma, P.H., et al. *Numerical modelling of an entrained-flow gasification simulator*. 1999.
132. Janajreh, I., I. Talab, and R. Qudaih. *Numerical simulation of the flow inside the entrained flow gasifier*. 2009.
133. Qiang, X., et al., *Numerical simulation of trace element transport on subsurface environment pollution in coal mine spoil*. Journal of Trace Elements in Medicine and Biology, 2006. **20**(2): p. 97-104.
134. Lu, L., V. Sahajwalla, and D. Harris, *Characteristics of chars prepared from various pulverized coals at different temperatures using drop-tube furnace*. Energy and Fuels, 2000. **14**(4): p. 869-876.
135. Senneca, O., et al., *The relevance of thermal annealing to the evolution of coal char gasification reactivity*. Carbon, 1997. **35**(1): p. 141-151.
136. Cai, H.Y., et al., *Combustion reactivity and morphological change in coal chars: Effect of pyrolysis temperature, heating rate and pressure*. Fuel, 1996. **75**(1): p. 15-24.
137. Cetin, E., et al., *Influence of pyrolysis conditions on the structure and gasification reactivity of biomass chars*. Fuel, 2004. **83**(16): p. 2139-2150.
138. Majid, A.A., et al., *Further development of a suspension fired reactor to assess the relative performance and synergistic effects during the combustion of coal blends*. Energy and Fuels, 2005. **19**(3): p. 968-976.
139. Myers, R.H., *Response surface methodology*. 1971, Boston: Allyn and Bacon. 246.
140. Myers, R.H., D.C. Montgomery, and C.M. Anderson-Cook, *Response surface methodology : process and product optimization using designed experiments*. Wiley series in probability and statistics. Vol. 3rd. 2009, Hoboken, N.J: Wiley. 680.
141. Abghari, S.Z., et al., *Analysis of sulfur removal in gasoil hydrodesulfurization process by application of response surface methodology*. Korean Journal of Chemical Engineering, 2011. **28**(1): p. 93-98.

142. Ghasemi, E., F. Raofie, and N.M. Najafi, *Application of response surface methodology and central composite design for the optimisation of supercritical fluid extraction of essential oils from Myrtus communis L. leaves*. Food Chemistry, 2011. **126**(3): p. 1449-1453.
143. Silva, G.F., F.L. Camargo, and A.L.O. Ferreira, *Application of response surface methodology for optimization of biodiesel production by transesterification of soybean oil with ethanol*. Fuel Processing Technology, 2011. **92**(3): p. 407-413.
144. Feroso, J., et al., *Application of response surface methodology to assess the combined effect of operating variables on high-pressure coal gasification for H₂-rich gas production*. International Journal of Hydrogen Energy, 2010. **35**(3): p. 1191-1204.
145. Wen, C.Y. and T.Z. Chaung, *Entrainment coal gasification modeling*. Industrial and Engineering Chemistry Process Design and Development, 1979. **18**(4): p. 684-695.
146. Kim, Y.J., S.H. Lee, and S.D. Kim, *Coal gasification characteristics in a downer reactor*. Fuel, 2001. **80**(13): p. 1915-1922.
147. Feroso, J., et al., *Co-gasification of different rank coals with biomass and petroleum coke in a high-pressure reactor for H₂-rich gas production*. Bioresource Technology, 2010. **101**(9): p. 3230-3235.
148. Mills, S.J., et al., *Coal gasification and IGCC in Europe*. CCC (Series) (IEA Coal Research) ; 113; IEA Coal Research, The Clean Coal Centre, CCC113. 2006, London: IEA Clean Coal Centre ; Japan New Energy and Industrial Development Organization. 37.
149. Montagnaro, F. and P. Salatino, *Analysis of char–slag interaction and near-wall particle segregation in entrained-flow gasification of coal*. Combustion and Flame, 2010. **157**(5): p. 874-883.
150. Ollero, P., et al., *Diffusional effects in TGA gasification experiments for kinetic determination*. Fuel, 2002. **81**(15): p. 1989-2000.
151. Lowell, S., et al., *Characterization of porous solids and powders : surface area, pore size, and density*. Particle technology series. 2004, Dordrecht: Boston. xiv, 347 p.
152. Vishnyakov, A., P.I. Ravikovitch, and A.V. Neimark, *Molecular level models for CO₂ sorption in nanopores*. Langmuir, 1999. **15**(25): p. 8736-8742.

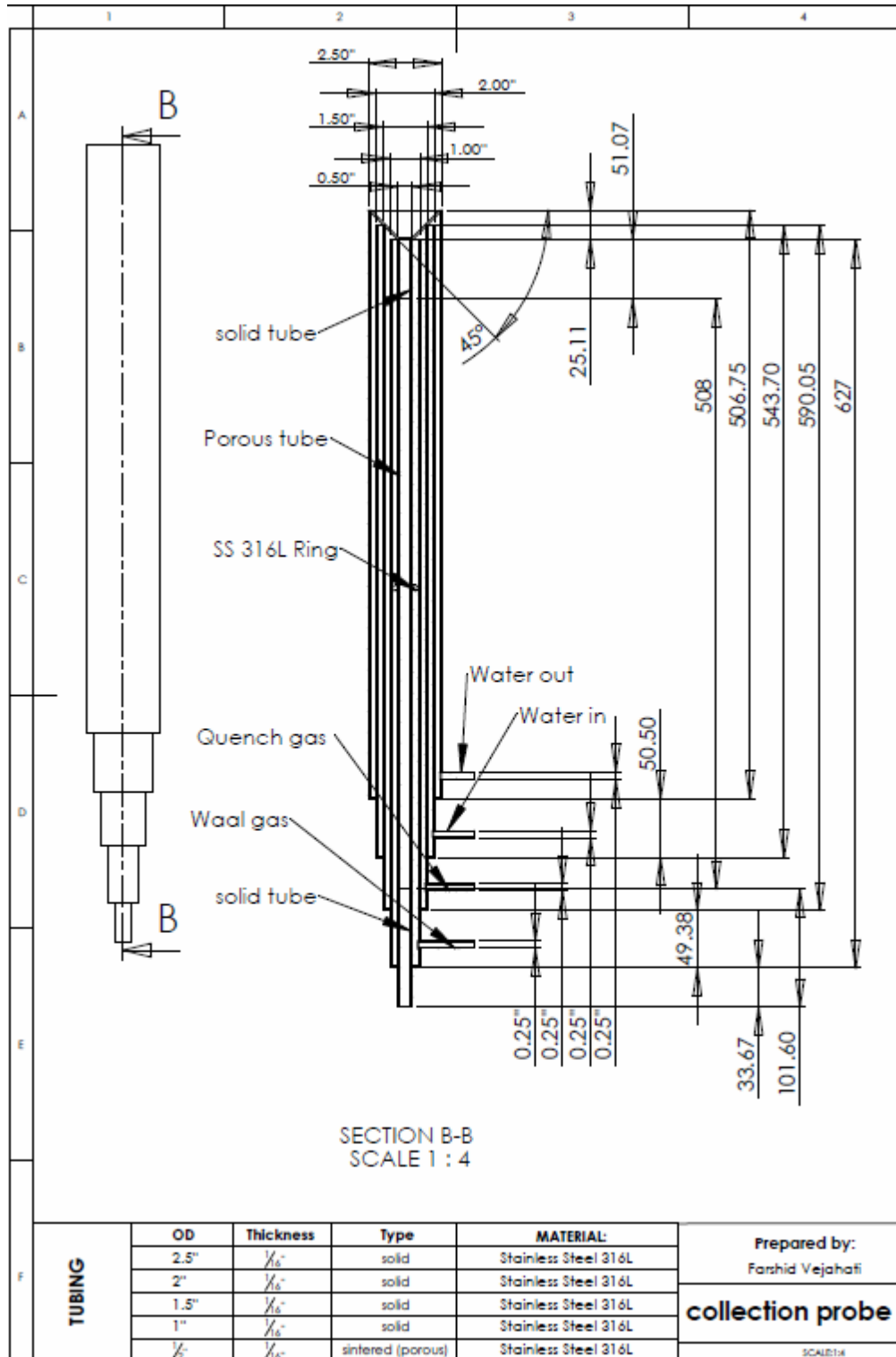
153. Harris, J.G. and K.H. Yung, *Carbon Dioxide's Liquid-Vapor Coexistence Curve And Critical Properties as Predicted by a Simple Molecular Model*. The Journal of Physical Chemistry, 1995. **99**(31): p. 12021-12024.
154. Olivier, J.P., W.B. Conklin, and M.v. Szombathely, *Determination of Pore Size Distribution from Density Functional Theory: A Comparison of Nitrogen and Argon Results*. 1994. p. 81-89.
155. Cyprès, R., D. Planchon, and C. Braekman-Danheux, *Evolution of pore structure and active surface areas of coal and char during hydrogenation*. Fuel, 1985. **64**(10): p. 1375-1378.
156. Cheng, A. and P. Harriott, *Kinetics of oxidation and chemisorption of oxygen for porous carbons with high surface area*. Carbon, 1986. **24**(2): p. 143-150.
157. Wen, C.Y., *Noncatalytic heterheneous solid-fluid reaction models*. Industrial & Engineering Chemistry, 1968. **60**(9): p. 34-54.
158. Weisz, P.B. and J.S. Hicks, *The behaviour of porous catalyst particles in view of internal mass and heat diffusion effects*. Chemical Engineering Science, 1962. **17**(4): p. 265-275.
159. Bischoff, K.B., *Accuracy of the pseudo steady state approximation for moving boundary diffusion problems*. Chemical Engineering Science, 1963. **18**(11): p. 711-713.
160. Srinivas, B. and N.R. Amundson, *A single-particle char gasification model*. AIChE Journal, 1980. **26**(3): p. 487-496.
161. 2010; Available from:
<http://www.netl.doe.gov/technologies/coalpower/gasification/worlddatabase/index.html>.
162. Channiwala, S.A. and P.P. Parikh, *A unified correlation for estimating HHV of solid, liquid and gaseous fuels*. Fuel, 2002. **81**(8): p. 1051-1063.
163. Westbrook, C.K. and F.L. Dryer, *Simplified reaction mechanisms for the oxidation of hydrocarbon fuels in flames*. Combustion Science and Technology, 1981. **27**(1-2): p. 31-43.
164. Jones, W.P. and R.P. Lindstedt, *Global reaction schemes for hydrocarbon combustion*. Combustion and Flame, 1988. **73**(3): p. 233-249.

165. Roberts, D.G., D.J. Harris, and T.F. Wall, *On the effects of high pressure and heating rate during coal pyrolysis on char gasification reactivity*. Energy and Fuels, 2003. **17**(4): p. 887-895.
166. Monaghan, R.F.D., et al. *Reduced order modeling of entrained flow solid fuel gasification*. 2010.
167. Liu, G.-S. and S. Niksa, *Coal conversion submodels for design applications at elevated pressures. Part II. Char gasification*. Progress in Energy and Combustion Science, 2004. **30**(6): p. 679-717.
168. Hla, S.S., Harris, D., Roberts, D., *Gasification conversion model- PEFR*. 2007, Cooperative Research Centre for coal in Sustainable Development (CCSD), Report 80.
169. Haynes, H.W., *An improved single particle char gasification model*. AIChE Journal, 1982. **28**(3): p. 517-521.
170. Levenspiel, O., *Chemical reaction engineering/ [Hauptbd.]*. 3rd. ed. 1999, New York: Weinheim. XVI, 668 S.
171. Brent, R., S. Winograd, and P. Wolfe, *Optimal iterative processes for root-finding*. Numerische Mathematik, 1972. **20**(5): p. 327-341.
172. *ANSYS FLUENT Theory Guide*. 2010, ANSYS, Inc. p. 752.
173. Launder, B.E. and D.B. Spalding, *The numerical computation of turbulent flows*. Computer Methods in Applied Mechanics and Engineering, 1974. **3**(2): p. 269-289.
174. Leckner, B., *Spectral and total emissivity of water vapor and carbon dioxide*. Combustion and Flame, 1972. **19**(1): p. 33-48.
175. Johnson, G., Massoudi, M., Rajagopal, K.R., *A review of interaction mechanisms of fluid-solid flows*, U.S. DOE. 1990.
176. Schlichting, H., *Boundary-layer theory*, in *McGraw-Hill series in mechanical engineering; Variation: McGraw-Hill series in mechanical engineering*. 1979, McGraw-Hill.
177. Ranade, V.V., *Computational flow modeling for chemical reactor engineering*, in *Process systems engineering series*. 2002, Academic Press.
178. Denson, C.D., E.B. Christiansen, and D.L. Salt, *Particle migration in shear fields*. AIChE Journal, 1966. **12**(3): p. 589-595.

179. Bretherton, F.P., *The motion of rigid particles in a shear flow at low Reynolds number*. Journal of Fluid Mechanics, 1962. **14**(2): p. 284-304.
180. Saffman, P.G., *The lift on a small sphere in slow shear flow*. J. Fluid Mech., 1965. **22**: p. 385-400.
181. Rubinow, S.I.a.K., J.B. , *The transverse force on a spinning sphere moving in a viscous fluid*. . J. Fluid Mech. , 1961. **11**: p. 447-459.
182. Swanson, W.M., *The Magnus effect: A summary of investigations to date*. . J. Basic Eng., 1961(25-67).
183. Tsuji, Y., Morikawa, Y. and Misuno, O. , *Experimental measurement of the Magnus force on a rotating sphere at low Reynolds numbers*. . Trans. ASME, J. Fluids Eng., 1985. **107**: p. 484-488.
184. Birkhoff, G., *Hydrodynamics*. 1960: Greenwood Press.
185. Lahey, R.T., *Virtual mass effects in two-phase flows - a review*. Trans. Am. Nuc. Soc., 1982. **42**: p. 665-666.
186. Happel, J.a.B., H. , *Low Reynolds Number Hydrodynamics*. 1973: Noordhoff Int. Pub.
187. Phillips, W.F., *Motion of aerosol particles in a temperature gradient*. Phys. Fluids, 1975. **18**: p. 144-147.
188. Talbot, L., Cheng, R.K., Schefer, R.W., and Willis, D.R. , *Thermophoresis of particles in a heated boundary layer* J. Fluid Mech., 1980. **101**: p. 737-758.
189. Patankar, S.V., *Numerical heat transfer and fluid flow*. 1980, hemisphere Publishing Corporation, Taylor & Francis group, New York.
190. Aarna, I. and E.M. Suuberg, *Changes in reactive surface area and porosity during char oxidation*. Symposium (International) on Combustion, 1998. **2**: p. 2933-2939.

APPENDIX A

Collection probe sketch



APPENDIX B

Surface area measurement

B1. BET method

The Brunauer-Emmett-Teller (BET) method is the most widely used procedure for the determination of the surface area of solid materials and involves the use of the BET equation:

$$\frac{1}{W\left(\frac{P_0}{P} - 1\right)} = \frac{1}{W_m C} + \frac{C - 1}{W_m C} \left(\frac{P}{P_0}\right) \quad (\text{B.1})$$

Where W is the weight of gas adsorbed at a relative pressure, P/P_0 , and W_m is the weight of adsorbate constituting a monolayer of surface coverage. The term C , the BET C constant, is related to the energy of adsorption in the first adsorbed layer and consequently its value is an indication of the magnitude of the adsorbent/adsorbate interactions.

B2. Multipoint BET Method

The BET equation requires a linear plot of $1/[W(P_0/P)-1]$ vs. P/P_0 which for most solids, using nitrogen as the adsorbate, is restricted to a limited region of the adsorption isotherm, usually in the P/P_0 range of 0.05 to 0.35. This linear region is shifted to lower relative pressures for micro-porous materials.

The standard multipoint BET procedure requires a minimum of three points in the appropriate relative pressure range. The weight of a monolayer of adsorbate W_m can then be obtained from the slope s and intercept I of the BET plot:

$$s = \frac{C - 1}{W_m C} \quad (\text{B.2})$$

$$I = \frac{1}{W_m C} \quad (\text{B.3})$$

So, the weight of monolayer W_m can be determined as:

$$W_m = \frac{1}{s + I} \quad (\text{B.4})$$

The second step in the application of the BET method is the calculation of the surface area. This requires knowledge of the molecular cross-sectional area A_{cs} of the adsorbate molecule. The total surface area S_t of the sample can be expressed as:

$$S_t = \frac{W_m N A_{cs}}{M} \quad (\text{B.5})$$

Where N is Avogadro's number (6.023×10^{23} molecules/mol) and M is the molecular weight of the adsorbate. Nitrogen is the most widely used gas for surface area determinations since it exhibits intermediate values for the C constant (50-250) on most solid surfaces. Since it has been established that the C constant influences the value of the cross-sectional area of an adsorbate, the acceptable range of C constants for nitrogen makes it possible to calculate its cross-sectional area from its bulk liquid properties. For the hexagonal close-packed nitrogen monolayer at 77 K, the cross-sectional area A_{cs} for nitrogen is 16.2 \AA^2 [151]

B3. Dubinin-Radushkevich (DR) Method

Based on the Polanyi potential theory of adsorption, Dubinin and Radushkevich postulated that the fraction of the adsorption volume V occupied by liquid adsorbate at various adsorption potentials ε can be expressed as a Gaussian function:

$$V = V_0 \exp \left[- \left(\frac{A}{\beta E_0} \right)^2 \right] \quad (\text{B.6})$$

Where A is the free energy of adsorption which in the early Dubinin's works was called adsorption potential ε :

$$A = RT \ln \left(\frac{P}{P_0} \right) \quad (\text{B.7})$$

V_0 represents micro-pore volume; E_0 is the so-called characteristic energy of adsorption and β is the affinity coefficient which can be approximated by a

ratio of the liquid molar volumes v of a given adsorbate and benzene used as the reference liquid:

$$\beta = \frac{v}{v_{C_6H_6}} \quad (B.8)$$

The distribution equation can be linearized as:

$$\log_{10} V = \log_{10} V_0 + 2.303 \left(\frac{RT}{\beta E_0} \right)^2 \log_{10} \left(\frac{P}{P_0} \right)^2 \quad (B.9)$$

which shows that micro-pore volume V_0 and E_0 parameter can be calculated from the linear fit of the isotherm data plotted as $\log(V)$ vs. $[\log(P/P_0)]^2$. Intercept of the fitted straight line gives $\log(V_0)$ while its slope m can be used to calculate E_0

$$E_0 = \frac{\sqrt{\frac{2.303}{m}} RT}{\beta} \quad (B.10)$$

The linear range for these plots is usually found at relative pressures of less than 10^{-2} .

Based on empirical studies it has been proposed that E_0 can be related to the characteristic micro-pore width for a carbonaceous adsorbent by the following simple formula:

$$\text{Pore Width} = 26 \left(\text{kJ} \frac{\text{nm}}{\text{mol}} \right) / E_0$$

The linear form of the DR equation can also be used to evaluate micro-pore surface area from the plot intercept, $\log(V_0)$ similar to BET method [151].

B4. Density Functional Theory (DFT) method

Classical macroscopic, theories like for instance the Dubinin-Radushkevich approach, and semi-empirical treatments such those of Horvath and Kawazoe (HK) do not give realistic description of the filling of micro-pores and even narrow meso-pores. They lead to an underestimation of pore sizes. In order to achieve a more realistic description, microscopic theories, which describe the sorption and phase behavior fluids in narrow pores on a molecular level, are necessary. Treatments as Density Functional Theory (DFT) or methods of

molecular simulation (Monte Carlo simulation (MC), Molecular Dynamics (MD)) provide a much more accurate approach for pore size analysis. Hence, such methods as the DFT of inhomogeneous fluids and Monte Carlo simulations bridge the gap between the molecular level and macroscopic approaches. The Non-Local Density Functional Theory (NLDFT) and the Grand Canonical Monte Carlo simulation (GCMC) methods correctly describe the local fluid structure near curved solid walls; adsorption isotherms in model pores are determined based on the intermolecular potentials of the fluid-fluid and solid-fluid interactions. The relation between isotherms determined by these microscopic approaches and the experimental isotherm on a porous solid can be interpreted in terms of a Generalized Adsorption Isotherm (GAI) equation:

$$N(P/P_0) = \int_{W_{min}}^{W_{max}} N(P/P_0, W) f(W) dW \quad (\text{B.11})$$

Where

$N(P/P_0)$ = experimental adsorption isotherm data

W = pore width

$N(P/P_0, W)$ = isotherm on a single pore of width W

$f(W)$ = pore size distribution function

The GAI equation reflects the assumption that the total isotherm consists of a number of individual “single pore” isotherms multiplied by their relative distribution, $f(W)$, over a range of pore sizes. The set of $N(P/P_0, W)$ isotherms (kernel) for a given system (adsorbate/adsorbent) can be obtained by either Density Functional Theory or by Monte Carlo computer simulation. The pore size distribution is then derived by solving the GAI equation numerically via a fast nonnegative least square algorithm. The DFT method has largely been applied to the characterization of micro- and mesoporous carbons using N_2 , CO_2 , and Ar adsorbates [31, 151, 152].

APPENDIX C

Response surface methodology

Response Surface Methodology (RSM) is a collection of statistical and mathematical techniques useful for developing, improving, and optimizing processes [140]. The applications of RSM are in the particular situations where several input variables (operating conditions) potentially influence some performance measure or quality characteristic of the process. Thus performance measure or quality characteristic is called the **response variable**. The input variables are sometimes called **independent variables, or experimental factors**; and they are subject to the control of the scientist or engineer. The response surface methodology consists of the experimental strategy for exploring the space of the process or independent variables (i.e. design of experiment, DOE), empirical statistical modeling to develop an appropriate approximating relationship between the response and the process variables, and optimization methods for finding the values of the process variables that produce desirable values of the response. The proper DOE is a key in RSM.

C1. Methodology

The design procedure of response surface methodology consists of the following steps:

- Statistical design of a series of experiments to adequately measure the effects of individual factors and their interactions on response variables.
- Developing a mathematical model for the response surface via multiple linear regression analysis and checking the goodness of fit using extensive statistical tests, and further model validation.

- Application of appropriate constrained linear/non-linear optimization algorithms to find the set of experimental parameters that produce a maximum or minimum value of response variables.
- Representation of the direct and interactive effects of process parameters through two and three dimensional plots.

Usually a second-order model is utilized in response surface methodology:

$$y = \beta_0 + \sum \beta_i x_i + \sum \beta_{ii} x_i^2 + \sum \sum \beta_{ij} x_i x_j \pm \varepsilon \quad (C.1)$$

Where ε is a random error. The coefficients are obtained by least square method.

C2. Estimation of the parameters

The method of least square is typically used to estimate the regression coefficients in a multiple linear regression model. Suppose $n > k$ observation on the response variables are available, say y_1, y_2, \dots, y_n . For each observed response y_i there is an observation on each regressor variable, let x_{ij} denoted by i^{th} observation or level of variable x_j .

The above second order equation can be rewritten as:

$$y = \beta_0 + \beta_1 x_{i1} + \beta_2 x_{i2} + \dots + \beta_k x_{ik} + \varepsilon_i \quad (C.2)$$

The objective is to find the vector of least squares estimators, b , that minimizes:

$$L = \sum_{i=1}^n \varepsilon_i^2 = \sum_{i=1}^n \left(y_i - \beta_0 - \sum_{j=1}^k \beta_j x_{ij} \right)^2 \quad (C.3)$$

The function L is to be minimized with respect to β_0, \dots, β_k . The **least square estimators** say b_0, \dots, b_k must satisfy:

$$\left. \frac{\partial L}{\partial \beta_0} \right|_{b_0, \dots, b_k} = -2 \sum_{i=1}^n \left(y_i - b_0 - \sum_{j=1}^k b_j x_{ij} \right) = 0 \quad (\text{C.4})$$

$$\left. \frac{\partial L}{\partial \beta_j} \right|_{b_0, \dots, b_k} = -2 \sum_{i=1}^n \left(y_i - b_0 - \sum_{j=1}^k b_j x_{ij} \right) x_{ij} = 0 \quad (\text{C.5})$$

These equations are called the **least squares normal equations**. Note that there are $p = k + 1$ normal equations, one for each of the unknown regression coefficients. The solution to the normal equations will be the least squares estimators of the regression coefficients b_0, \dots, b_k .

This set of equations can be rewritten in matrix form:

$$y = X\beta + \varepsilon \quad (\text{C.6})$$

Where

$$y = \begin{bmatrix} y_1 \\ \vdots \\ y_n \end{bmatrix}, \quad X = \begin{bmatrix} 1 & x_{11} & \dots & x_{1k} \\ 1 & x_{21} & \dots & x_{2k} \\ \vdots & \vdots & \ddots & \vdots \\ 1 & x_{n1} & \dots & x_{nk} \end{bmatrix}, \quad \beta = \begin{bmatrix} \beta_0 \\ \vdots \\ \beta_k \end{bmatrix}, \quad \text{and } \varepsilon = \begin{bmatrix} \varepsilon_1 \\ \vdots \\ \varepsilon_n \end{bmatrix}$$

We wish to find the vector of least squares estimators, b , that minimizes:

$$L = \sum_{i=1}^n \varepsilon_i^2 = \varepsilon' \varepsilon = (y - X\beta)'(y - X\beta) \quad (\text{C.7})$$

Note that L may be expressed as:

$$L = y'y - \beta'X'y - y'X\beta + \beta'X'X\beta = y'y - 2\beta'X'y + \beta'X'X\beta \quad (\text{C.8})$$

Since $\beta'X'y$ is a scalar, and its transpose $(\beta'X'y)' = y'X\beta$ is the same scalar. The least squares estimators must satisfy:

$$\left. \frac{\partial L}{\partial \beta} \right|_b = -2X'y + 2X'Xb = 0 \quad (\text{C.9})$$

This simplifies to:

$$X'Xb = X'y \quad (\text{C.10})$$

From this equation the least square estimator is obtained:

$$b = (X'X)^{-1}X'y \quad (\text{C.11})$$

Hence, the fitted regression model is:

$$\hat{y} = Xb \quad (\text{C.12})$$

The difference between the observation y_i ; and the fitted value \hat{y}_i ; is a **residual**:

$$e = y - \hat{y} \quad (\text{C.13})$$

C2.1 properties of least square estimators and estimation of σ^2

The method of least squares produces an **unbiased estimator** of the parameter β in the multiple linear regression models. This can be easily shown as follows:

$$\begin{aligned} E(b) &= E[(X'X)^{-1}X'y] = E[(X'X)^{-1}X'(X\beta + \varepsilon)] \\ &= E[(X'X)^{-1}X'X\beta + (X'X)^{-1}X'\varepsilon] = \beta \end{aligned} \quad (\text{C.14})$$

Since $E(\varepsilon) = 0$ and $(X'X)^{-1}X'X = I$. Thus b is an unbiased estimator of β .

The covariance matrix of b is:

$$\text{Cov}(b) = \sigma^2(X'X)^{-1} \quad (\text{C.15})$$

It is usually necessary to estimate σ^2 . For that consider the sum of squares of the residuals:

$$SS_E = \sum (y_i - \hat{y}_i)^2 = \sum e_i^2 = e'e \quad (\text{C.16})$$

We can derive a computational formula for SS_E :

$$SS_E = y'y - b'X'y \quad (\text{C.17})$$

This equation is called **error** or **residual sum of squares**, and it has $n-p$ degrees of freedom associated with it. It can be shown that:

$$E(SS_E) = \sigma^2(n - p) \quad (\text{C.18})$$

So an unbiased estimator of σ^2 is given by:

$$\hat{\sigma}^2 = \frac{SS_E}{n - p} \quad (\text{C.19})$$

C3. Hypothesis testing in multiple regression

In multiple linear regression problems, certain tests of hypotheses about the model parameters are helpful in measuring the usefulness of the model. These procedures require that the errors ε_i in the model be normally and independently distributed with mean zero and variance σ^2 , abbreviated as $\varepsilon \sim NID(0, \sigma^2)$. This results in the observations y_i to be normally and independently distributed with mean $\beta_0 + \sum_{j=1}^k \beta_j x_{ij}$ and variance σ^2 .

C3.1 Test for significance of regression

The test for significance of regression is a test to determine if there is a linear relationship between the response variable y and a subset of the regressor variables. The appropriate hypotheses are:

$$\begin{aligned} H_0: \beta_1 = \dots = \beta_k = 0 \\ H_1: \beta_j \neq 0 \text{ for at least one } j \end{aligned} \quad (\text{C.20})$$

Rejection of H_0 implies that at least one of the regressor variables x_1, \dots, x_k contributes significantly to the model. The test procedure involves partitioning the total sum of squares $SS_T = \sum_{i=1}^n (y_i - \bar{y})^2$ into a sum of squares due to the model (or to regression) and a sum of squares due to residual (or error):

$$SS_T = SS_R + SS_E \quad (\text{C.21})$$

One could use the P-value approach to hypothesis testing and, thus, reject H_0 if the P-value for the statistic $F_0 = \frac{SS_R}{k} / SS_E / (n - k - 1)$ is less than α . This test procedure is called an **analysis of variance (ANOVA)** because it is based on a decomposition of the total variability in the response variable y . Computational formula for SS_T is:

$$SS_R = b'X'y - \frac{(\sum_{i=1}^n y_i)^2}{n} \quad (\text{C.22})$$

The coefficient of multiple determinations R^2 is defined as:

$$R^2 = \frac{SS_R}{SS_T} = 1 - \frac{SS_E}{SS_T} \quad (\text{C.23})$$

However, a large value of R^2 does not necessarily imply that the regression model is good one. Adding a variable to the model will always increase R^2 , regardless of whether the additional variable is statistically significant or not. Thus it is possible for models that have large values of R^2 to yield poor predictions of new observations or estimates of the mean response. For this reason some regression model builders prefer to use an adjusted R^2 statistic defined as:

$$R_{adj}^2 = 1 - \frac{\frac{SS_E}{n-p}}{\frac{SS_T}{n-1}} \quad (C.24)$$

C4. Model adequacy checking

It is always necessary to (a) examine the fitted model to ensure that it provides an adequate approximation to the true system and (b) verify that none of the least squares regression assumptions are violated. Proceeding with exploration and optimization of a fitted response surface will likely give poor or misleading results unless the model provides an adequate fit.

C4.1 Residual analysis

The residuals from the least squares fit play an important role in judging model adequacy. A check of the normality assumption may be made by constructing a normal probability plot of the residuals. If the residuals plot approximately along a straight line, then the normality assumption is satisfied.

C4.2 Scaling residual

Many response surface analysts prefer to work with scaled residuals, as these scaled residuals often convey more information than do the ordinary least squares residuals.

One type of scaled residual is the standardized residual:

$$d_i = \frac{e_i}{\hat{\sigma}}, \quad i = 1, 2, \dots, n \quad (\text{C.25})$$

Where generally $\hat{\sigma} = \sqrt{MS_E}$. These standardized residuals have mean zero and approximately unit variance; consequently, they are useful in looking for outliers.

Most of the standardized residuals should lie in the interval $-3 < d_i < 3$, and any observation with a standardized residual outside of this interval is potentially unusual with respect to its observed response.

In some data sets, residuals may have standard deviations that differ greatly. So standard scaling is not very useful. To take this into account other scaling has been introduced.

The vector of fitted values \hat{y} corresponding to the observed values y is:

$$\hat{y} = Xb = X(X'X)^{-1}X'y = Hy \quad (\text{C.26})$$

The H matrix ($n \times n$) is called **hat matrix**. This matrix plays an important role in regression analysis.

The residual can be written as:

$$e = y - \hat{y} = y - Xb = y - Hy = (I - H)y \quad (\text{C.27})$$

The hat matrix has several useful properties. It is symmetric ($H' = H$) and idempotent ($HH = H$). Similarly the matrix $I - H$ is symmetric and idempotent.

The covariance matrix of the residual is:

$$\text{Var}(e) = \text{Var}[(I - H)y] = (I - H)\text{Var}(y)(I - H)' = \sigma^2(I - H) \quad (\text{C.28})$$

Because $\text{Var}(y) = \sigma^2 I$ and $I - H$ is symmetric and idempotent. The matrix $I - H$ is generally not diagonal, so the residual are correlated and have different variances. The variance of i^{th} residual is:

$$\text{Var}(e_i) = \sigma^2(1 - h_{ii}) \quad (\text{C.29})$$

Where h_{ii} is the i^{th} diagonal element of H .

As mentioned earlier to take into account the inequality of variances, residual can be scale using H matrix. This scale residual is called **studentized residuals**:

$$r_i = \frac{e_i}{\sqrt{\hat{\sigma}^2(1 - h_{ii})}}, \quad i = 1, \dots, n \quad (\text{C.30})$$

The studentized residuals have constant variance $Var(r_i) = 1$ regardless of the location of x_i ; when the form of the model is correct.

Another type of residual often used in RSM is called **PRESS residual (the prediction error sum of square)**:

$$PRESS = \sum_{i=1}^n e_{(i)}^2 \quad (C.31)$$

Where

$$e_{(i)} = \frac{e_i}{1 - h_{ii}} \quad (C.32)$$

Generally, a large difference between the ordinary residual and the PRESS residual will indicate a point where the model fits the data well, but a model built without that point predicts poorly. PRESS can also be used to compute an approximate R^2 for prediction:

$$R_{prediction}^2 = 1 - \frac{PRESS}{SS_T} \quad (C.33)$$

This statistic gives some indication of the predictive capability of the regression model.

C5. Standard error of predicted response

The most fundamental sampling property in any model building exercise is the standard error of the predicted response at some point of interest x , often denoted $S_{\hat{y}(x)}$, where in the most general framework:

$$\hat{y} = x^{(m)'}b \quad (C.34)$$

Here $b = (X'X)^{-1}X'y$. The vector $x^{(m)}$ is a function of the location at which one is predicting the response; the (m) indicates that $x^{(m)}$ is just x expanded to model space; that is, the vector reflects the form of the model as X does. For example, for $k = 2$ design variables and a second-order model we have

$$x^{(2)'} = [1, x_1, x_2, x_1^2, x_2^2, x_1x_2]$$

$$b = [b_0, b_1, b_2, b_{11}, b_{22}, b_{12}]$$

With the assumption of constant error variance σ^2 , we have

$$PV(x) = Var[\hat{y}(x)] = x^{(m)'}(X'X)^{-1}x^{(m)}\sigma^2 \quad (C.35)$$

As a result, an estimated standard error of $\hat{y}(x)$ is given by

$$S_{\hat{y}(x)} = s\sqrt{x^{(m)'}(X'X)^{-1}x^{(m)}} \quad (C.36)$$

Where $s = \sqrt{MS_E}$ is the square root of the mean square error of the fitted response surface that is, for a fitted model with p parameters,

$$s = \sqrt{\frac{\sum_{i=1}^k (y_i - \hat{y}_i)^2}{n - p}} \quad (C.37)$$

In studies that are done to compare designs, it is often convenient to scale the prediction variance, that is, work with the **scaled prediction variance**:

$$SPV(x) = \frac{N Var[\hat{y}(x)]}{\sigma^2} = N x^{(m)'}(X'X)^{-1}x^{(m)} \quad (C.38)$$

The division by σ^2 makes the quantity scale-free, and the multiplication by N allows the quantity to reflect variance on a per observation basis. That is, if two designs are being compared, the scaling by N automatically "punishes" the design with the larger sample size.

C6. Design moment and property of rotatability

Many of the properties of experimental designs are connected to the manner in which the points are distributed in the region of experimentation. Specifically, this distribution of points in space has a profound effect on the distribution of the scaled prediction variance. The distribution of design points is nicely quantified by its **design moment**. The term moments has the same conceptual meaning as the term sample moment that is taught in elementary statistics. We learn early in our training that the nature of the sample of the data is well characterized by its moments; for example, sample mean (first moment), sample variance (second moment). We also recall that symmetry in a sample is

quantified by the third moment. In the case of RSM, the moments that reflect important geometry in the design must also be a function of the model being fit.

Indeed the important moments come from the moment matrix

$$M = \frac{X'X}{N} \quad (\text{C.39})$$

The important variance properties of an experimental design are determined by the nature of the moment matrix:

$$\begin{aligned} SPV(x) &= N x^{(m)'} (X'X)^{-1} x^{(m)} = x^{(m)'} \left(\frac{X'X}{N} \right)^{-1} x^{(m)} \\ &= x^{(m)'} M^{-1} x^{(m)} \end{aligned} \quad (\text{C.40})$$

So the SPV is a quadratic form of the moment matrix, M . It is important for a second-order design to possess a reasonably stable distribution of the scaled prediction variance throughout the experimental design region. It must be clearly understood that the experimenter does not know at the outset where in the design space he or she may wish to predict, or where in the design space the optimum may lie. Thus, a reasonably stable scaled prediction variance provides insurance that the quality of the $\hat{y}(x)$ as a prediction of future response values is similar throughout the region of interest. To this end, the notion of design rotatability has been developed. A rotatable design is one for which the scaled prediction variance has the same value at any two locations that are the same distance from the design center. In other words, the scaled prediction variance is constant on spheres.

The importance of moment would be more clear noticing that an entire spectrum of optimality criteria, such as D-optimality, I-optimality, and A—optimality involve criteria that are related to norm.

C7. Practical Design optimality

In real cases where process is affected by more than 4 factors, in order for an experimenter to effectively cover all the direct and interactive effects of operating variables, the number of experiments grows exponentially in a way that researcher cannot afford the required number of runs. As a result, some

techniques have been developed over the years which can be effectively employed to thoroughly investigate the process for the effect of operating variables with much less number of runs. Of particular importance in this study the design based on optimality criteria can be cited.

Design optimality criteria are characterized by letters of the alphabet and as a result, are often called alphabetic optimality criteria. Some criteria focus on good estimation of model parameters, while others focus on good prediction in the design region.

In this study we have used a class of optimal design called **I-optimality** or **IV-optimality**. It addresses prediction variance. The attempt here is to generate a single measure of prediction performance through an averaging process; that is, $v(x)$ is averaged over some region of interest R . The averaging is accomplished via the integration over R . The corresponding division by the volume of R produces an average. The I-optimal design is given by:

$$\min_{\zeta} \frac{1}{K} \int_R v(x) dx \quad (C.41)$$

Where $K = \int_R dx$. We can write the criterion for a design as:

$$\min_{\zeta} \left[\frac{1}{K} \int_R x^{(m)'} M^{-1} x^{(m)} dx \right] \quad (C.42)$$

In this way the design is that in which the average scaled prediction variance is minimized. The IV-optimality criterion is conceptually a very reasonable device to use for choosing experimental designs, since selecting a design with good average prediction variance should produce satisfactory results throughout the design space.

C8. Computer-generated designs in RSM

Computer-generated design of experiments was the natural extension of design optimality as the computer era in statistics unfolded in the late 1960s and early 1970s. Today many computer packages generate designs for the user. With increased computer power, finding optimal designs has become more tractable.

Two types of exchange algorithms are common for creating experiment candidate points: **point exchange** and **coordinate exchange**. In the point exchange algorithm, a random design of the appropriate size is created from the set of candidate points. Then new designs are created by iteratively replacing individual points with the best replacement available from the candidates, conditional on the other points in the design. This is repeated for all points in the design until no improvements are possible. The entire process is repeated multiple times for different random initial designs, and the best overall design from all the starts is selected.

Coordinate exchange is a candidate-free approach, which begins with a random design of the appropriate size. Each coordinate for each factor for each design point is sequentially adjusted to its optimal value within the range of that factor, conditional on all other coordinates and points in the design. This is repeated for all coordinates in the design until no further improvements exist. As with the point exchange algorithm, multiple random initial designs are considered and the best overall design from all starts is chosen.

If IV-optimality is the selected criteria for the above algorithms, there are computationally efficient methods which can be used quickly and easily considering a large number of initial designs in a timely manner to create the design space.